Université de Mons - Faculté des Sciences
Laboratoire SYMBIOSE

The actin cortex acts as a mechanical memory of morphology in confined migrating cells

Dissertation originale présentée par

Yohalie KALUKULA

en vue de l'obtention du grade académique de Docteur en Sciences

dirigée par

Prof. Sylvain GABRIELE

soutenue le 28 novembre 2025 devant le jury composé de:

Prof. Mathieu SURIN	Université de Mons, Belgique
Prof. Lionel TAFFOREAU	Université de Mons, Belgique
Prof. Benoît LADOUX	MPZPM Erlangen, Allemagne
Prof. Sandrine ETIENNE-MANNEVILLE	CNRS Institut Pasteur, France
Prof. Sylvain GABRIELE	Université de Mons, Belgique

Yohalie KALUKULA
SYMBIOSE Lab,
Département de Chimie,
Université de Mons,
20, Place du Parc B-7000 Mons (Belgique).
November 2025

Email: Yohalie.KALUKULA@umons.ac.be

This research work was financially supported by the Fund for Research Training in Industry and Agriculture (FRIA).

ABSTRACT

Cell migration in narrow microenvironments occurs in numerous physiological processes. It involves successive cycles of confinement and release that drive significant morphological changes. However, it remains unclear whether migrating cells can retain a memory of their past morphological states that could potentially facilitate their navigation through confined spaces. We demonstrate that local geometry governs a switch between two cell morphologies, thereby facilitating cell passage through long and narrow gaps. We combined cell migration assays on standardized microsystems with biophysical modelling and biochemical perturbations to show that migrating cells have a long-term memory of past confinement events. The morphological cell states correlate across transitions through actin cortex remodelling. These findings suggest that mechanical memory in migrating cells plays an active role in their migratory potential in confined environments.

REMERCIEMENTS

J'ai l'intime conviction que derrière chaque grand accomplissement se cache un effort collectif, humain et synergique. Du moins, c'est le cas pour ces cinq années de thèse, qui trouvent aujourd'hui leur aboutissement.

J'aimerais tout d'abord partager une chose que ces dernières années m'ont apprise. Être un leader requiert avant tout un grand sens des relations humaines et une réelle intelligence émotionnelle.

Selon moi, un bon encadrant doit pouvoir faire preuve de patience, d'écoute, de confiance et de l'humilité nécessaire pour offrir à chacun l'espace et le temps dont il a besoin pour évoluer et atteindre son plein potentiel. En effet, cela repose sur la capacité à s'intéresser avec sincèrité aux autres, à les connaître suffisamment pour les apprécier à leur juste valeur, afin qu'ils deviennent ce pour quoi ils sont faits, et non ce que l'on aimerait qu'ils soient. C'est avoir un regard clairvoyant, savoir discerner les caractères et reconnaitre en chacun ce qu'il a d'unique.

J'ai appris à identifier et à reconnaître ces qualités grâce à mon promoteur de thèse, Sylvain Gabriele. Ce passage est avant tout l'occasion de le remercier et de le féliciter, car ce travail est aussi le sien. Merci d'avoir su

déceler en moi cette étincelle qui, aujourd'hui, continue d'alimenter ma passion pour la recherche. Merci pour ton soutien constant, ton mentorat bienveillant et ton accompagnement, qui m'ont permis d'acquérir une véritable maturité scientifique. Je t'en suis profondément reconnaissante, car je ne me vois pas m'épanouir ailleurs que dans la recherche fondamentale.

Partie de la chimie, j'ai eu la merveilleuse opportunité de découvrir un domaine multidisciplinaire, où la physique, la biologie et la chimie se rencontrent afin de révéler les fondements de la nature et du monde qui nous entoure. De là, née une synergie, une symbiose (clin d'oeil) entre les disciplines, qui nourrit chaque jour ma curiosité.

Enfin, merci pour ton bon sens des priorités, ta disponibilité et le temps que tu as toujours su m'accorder. J'ai pu apprendre la projection dans le temps et même l'espace, ce que je continue de travailler. Toutes des qualités qui sont profondément inspirantes.

En deuxième lieu, mais pas des moindres. J'aimerais remercier l'ensemble des membres de mon laboratoire Symbiose anciens comme actuels. Ma vision du fonctionnement d'un laboratoire est proche de celle d'une famille où chaque membre possède un rôle bien précis. Nous avons besoin les uns des autres. Personne n'est réellement dispensable lorsqu'il existe une véritable symbiose entre nous.

C'est en raison de cette cohésion, cette entraide et cette bienveillance partagée que je tiens à les remercier un par un. Merci à Marie, pour sa profonde gentillesse et le partage généreux de ses précieuses connaissances. Merci à Serge, pour nos nombreux éclats de rire et nos belles conversations. Merci à Dorothée, pour le partage de sa culture et sa présence toujours si agréable. Merci à Amandine, nous avons partagé cette aventure ensemble et en parallèle. Tu fais partie des personnes les plus adorables que je connaisse. Merci à Giuseppe, une rencontre merveilleuse, à la fois scientifique et humaine. Merci à Rémi, Roxanne et Maxime, je suis profondément reconnaissante de vous connaître. Vous êtes des personnes brillantes, simples, et ce fut un véritable plaisir de travailler à vos côtés. Merci à Lulu (Lucie), ma petite danseuse! Ta rigueur, ton sens de l'ordre

et ton talent sont une véritable source d'inspiration. Je crois que nous avons commencé à bâtir une belle amitié, et j'espère qu'elle continuera de grandir. Merci également à notre ZoZo (Zoé), l'un de mes prénom préféré, car il signifie vie en grec ancien. Tu es, toi aussi, une source d'inspiration : tant de talent, de profondeur et une liberté d'esprit rare. J'ai beaucoup aimé te découvrir et travailler à tes côtés.

Enfin, j'aimerai tellement remercier une personne que je trouve magnifique. Marine Luciano, merci pour la lueur d'espoir que tu représentes pour une jeune femme comme moi. Tes parcours personnel et professionel sont une grande source d'inspiration. Merci pour la personne entière que tu es et pour tout le soutien que tu m'apportes, je me réjouis de travailler encore avec toi à l'avenir.

Je tiens également à remercier les membres du laboratoire Influx à savoir Mary, Marco, Quentin T. et anciennement Guillaume. Ce fut un plaisir de partager le laboratoire avec vous, vous êtes de belles personnes et je vous souhaite le meilleur pour la suite. Je remercie également le professeur Pascal Damman pour ses enseignements précieux durant mon cursus académique.

Durant cette thèse, j'ai eu le plaisir d'encadrer plusieurs étudiants que j'aimerai remercier à savoir Clara Leens, Robin Deschamps et Evan Castiau. Votre curiosité et soif d'apprentissage a été et demeure une véritable bouffée d'air frais. Merci.

Mes remerciements vont également aux membres de mon jury, qui ont pris le temps d'examiner ce travail. Merci d'avoir fait preuve d'une grande implication et d'avoir fourni des retours riches lors de l'évaluation de ce travail. Je remercie les professeurs Sandrine Etienne-Manneville et Benoît Ladoux, mes rapporteurs externes, dont les carrières et les travaux ont été une source inspirante pour ce travail.

Je tiens à remercier le professeur Matthieu Surin pour l'ouverture du master en chimie bio-inspirée, qui m'a conduite jusqu'ici. Au sein de ton laboratoire, j'ai pu acquérir ma première expérience en recherche fondamentale. Merci également pour toutes les qualités humaines que tu possèdes. Merci également

au professeur Lionel Tafforeau qui m'a acceuilli à plusieurs reprises dans son laboratoire pour me transmettre ses connaissances et savoir faire en biologie cellulaire. De précieuses clefs pour mon future.

Je tiens également à remercier l'ensemble de mes collaborateurs pour la richesse de nos discussions et des projets que nous avons menés ensemble, parmi lesquels les professeurs Joachim Rädler, Jan Lammerding, Cynthia Reinhart-King, Matthieu Piel et Olivia Du Roure. Je souhaite également exprimer ma gratitude envers les étudiants qui m'ont beaucoup aidé dans l'apprentissage de nouvelles techniques, notamment Joseph Vermeil et Anumita Jawahar. Une attention particulière va au professeur David B. Brückner, un scientifique d'exception sans qui ce travail n'aurait pas pu atteindre son plein aboutissement. Mes remerciements vont également au professeur Martial Balland, pour ses qualités humaines et scientifiques uniques, ainsi qu'à Daniel Selma, pour son aide précieuse dans la mise au point d'un protocole de patterning. Enfin, je souhaite remercier Guillaume Charras et son postdoctorant Lucas Dent pour nos discussions enrichissantes et la collaboration actuelle, qui a permis de conclure ce travail de thèse en beauté tout en ouvrant de nouvelles perspectives.

Mes remerciements s'adressent également aux organismes de financement, notamment le Fonds de la recherche dans l'industrie et l'agriculture (FRIA), le Fonds de la recherche scientifique (FNRS) en Belgique, ainsi que le Fonds pour la recherche médicale en Hainaut, pour leur soutien sans lequel ce projet n'aurait pu voir le jour.

En dernier lieu, j'aimerais remercier les pilliers de ma vie, sans lesquels je n'aurais pu me construire. Premièrement, ma famille. Là où est ma paix. Merci à ma maman, mon pilier. Tu as été mon secours tant de fois. Tu m'as transmis ton éthique, ta rigueur et ton investissement dans le travail, des valeurs qui m'ont guidée tout au long de ces dernières années. Merci également à mon papa, je sais d'où tu viens, et cet accomplissement signifie beaucoup. Mon deuxième papa, Sylvian, te savoir fier de moi me pousse à vouloir donner le meilleur de moi-même. Merci à mes frères Yannick, Lenny, Noah, Corentin, Romaric, Helaury et soeurs, Vicky et Angélique, ainsi qu'à ma marraine et à

Zina. Sans vous, je ne serais pas celle que je suis et je n'aurais tout simplement pas le désir de poursuivre ces rêves.

Deuxièmement, je tiens à exprimer une profonde gratitude envers ma famille au sens élargi. En commençant par ma soeur de coeur et meilleure amie d'enfance Chloé Giangiordano. Ta présence a été un cadeau précieux.

Je terminerai par une citation, ou plutôt un célèbre verset biblique, tiré du livre Ecclésiaste et empreint de sagesse : « Mieux vaut la fin d'une chose que son commencement ; mieux vaut un esprit patient qu'un esprit hautain. » Ce sont souvent les derniers kilomètres d'une course d'endurance qui sont les plus difficiles. Ce verset nous encourage à finir les choses en beauté. Dans mon cas, Dieu a envoyé une armée « d'anges » pour me soutenir au moment où j'en avais le plus besoin : à la fin de cette thèse. Ma famille en Christ, un ensemble d'êtres humains exceptionnels, et une preuve concrète de la fidélité de Dieu dans ma vie.

Un énorme merci, rempli d'amour, à Christelle, Stéphane, Adrien, Francesca, Randy et toute la famille Caputo-D'Arcangelo. Ma deuxième famille, avec qui j'ai vécu ces derniers instants intenses. Merci également aux membres de mon église locale : Maman Colombe, Tryphène, Débo, Debby, Anthony (le Bishop), pour leur réelle attention et leurs prières autour de ce travail. Merci de partager cette victoire avec moi et pour votre soutien si précieux ; je le ressens dans mon coeur chaque jour.

A celui qui me connaissait avant même que je sois formée dans le ventre de ma mère, et qui a donné sa vie pour moi à la croix. Il est le fondement sur lequel j'ai choisi de bâtir ma vie depuis trois ans. Sans Lui, j'aurais abandonné à plusieurs reprises ; je me serais égarée. Merci à Dieu le Père, celui qui renouvelle mes forces au quotidien, et au Saint-Esprit, mon guide de chaque jour.

Peu importe où ce chemin me conduira, que toute la gloire revienne à Jésus-Christ, car il est le seul digne de la recevoir. Faire sa rencontre est le plus beau cadeau que l'on puisse recevoir.

LIST OF ABBREVIATIONS

1D	One-dimensional
2D	Two-dimensional
3D	Three-dimensional
A431	Human epidermoid carcinoma cell line
Actin-F	Filamentous actin (F-actin)
Actin-G	Globular actin (G-actin)
ADP	Adenosine diphosphate
AMPK	Adenosine Monophosphate-activated Protein Kinase
ARPC1B	Actin-related protein 2/3 complex subunit 1B
ATP	Adenosine triphosphate
BSA	Bovine serum albumin
BSI-sCMOS	Back-illuminated scientific complementary metal-oxide-semiconductor
DAPI	4',6-diamidino-2-phenylindole
DIC	Differential interference contrast microscopy
DMEM/F12	Dulbecco's Modified Eagle Medium / Ham's F-12 nutrient mixture
DLP	Digital Light Processing

DMD	Digital micromirror device
DMSO	Dimethyl sulfoxide
DN	Dominant negative
DNA	Deoxyribonucleic acid
ECM	Extracellular matrix
EMT	Epithelial–mesenchymal transition
FBS	Fetal bovine serum
FITC	Fluorescein isothiocyanate
FN	Fibronectin
GFP	Green fluorescent protein
HEPES	4-(2-hydroxyethyl)-1-piperazineethanesulfonic acid
LM	Laminin
MCF-10A	Michigan Cancer Foundation-10A
MCF7	Michigan Cancer Foundation-7, Human breast adenocarcinoma cell line
MDA-MB-321	MD Anderson - Mammary Breast - 231
MDCK	Madin-Darby canine kidney cells
MT	Microtubule
MTOC	Microtubule-organizing center
NIH3T3	Mouse embryonic fibroblast cell line
NSPARC	Nikon Spatial Array Confocal detector
PAF	Paraformaldehyde
PBS	Phosphate-buffered saline
PDMS	Poly(dimethylsiloxane)
RGD	Arginylglycylaspartic acid
DNA	Desoxyribonucleic acid
RT	Room temperature
RUNX2	Runt-related transcription factor 2
SEM	Scanning electron microscopy
SHG	Second-harmonic generation
siTTL	Small interfering RNA targeting tubulin–tyrosine ligase (TTL)
siVASH	Small interfering RNA targeting vasohibin (VASH)
TFM	Traction force microscopy

TRITC	Tetramethylrhodamine isothiocyanate
UV	Ultraviolet
WAVE	WASP family verprolin-homologous protein
YAP	Yes-associated protein
YFP-PBD	Yellow fluorescent protein fused to the p21-binding domain of Pak1

TABLE OF CONTENTS

CHAPTER 1

INTRODUCTION

1.1 Principles of individual cell migration

Cells are the fundamental units of all living systems. Gross estimations are obtained by dividing the estimated mean human body volume or weight by the corresponding volume or weight of a single cell, using as reference a standard male individual weighing 70 kg and measuring 1.72 m. On this basis, the adult human body is estimated to contain approximately 10^{13}, classified into at least 200 distinct cellular types and organized into more than twenty distinct structures and systems [1]. Owing to their remarkable complexity, cells have long been a central focus of research in mechanobiology—an interdisciplinary field exploring how mechanical forces and physical properties influence cellular behavior, development, physiology, and disease [2]. Among these behaviors, cell movement, an intrinsic property of living matter at the microscopic scale, has attracted particular attention. Cells are inherently dynamic, engaging in processes such as growth, death, division, changing their shape in response to external cues, and migration [3].

In this PhD work, we set out to investigate the mechanisms underlying the establishment of mechanical memory during confined cell migration, particularly in restrictive environments. To this end, this introductive chapter will first introduce the fundamental concepts of individual cell migration, then examine how migration is maintained over time through the spatial asymmetry of cellular structures, and finally how these processes are regulated under spatially constraining conditions.

1.1.1 Physiological and pathological context

Eukaryotic cell migration is a fundamental biological process playing a central role in both physiological and pathological contexts. It underpins tissue homeostasis from development through adulthood, and its dysregulation is implicated in a broad spectrum of diseases.

Embryogenesis is the process by which a multicellular organism with specialized tissues and organs develops. Cell migration plays a crucial role in shaping the three primary germ layers (ectoderm, mesoderm, and endoderm) each of

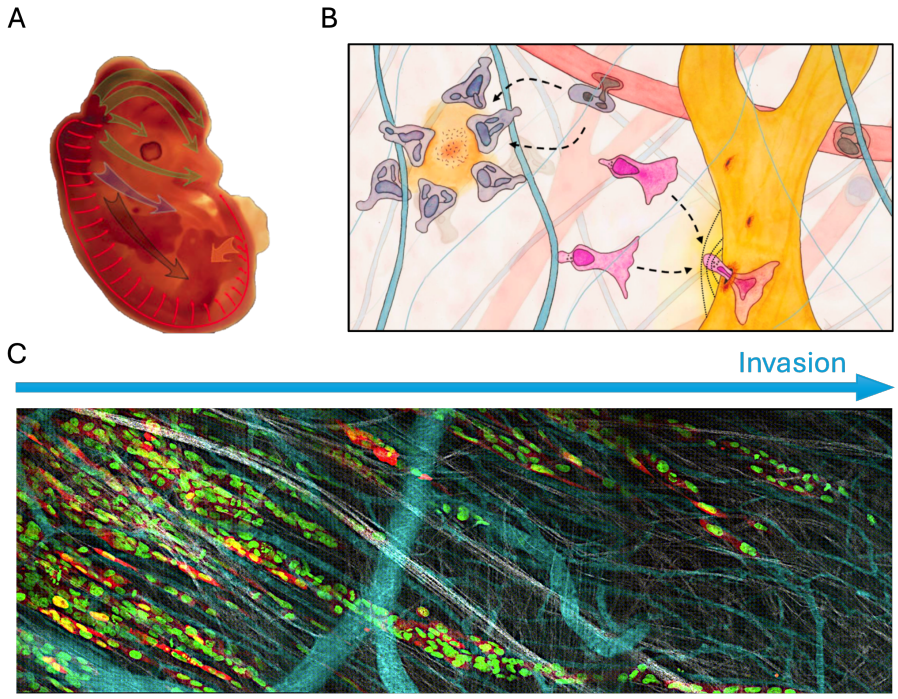

Figure 1.1: ***A.*** *Neural crest cells migrate from the dorsal part of the embryo toward the anterior region, adapted from [4].* ***B.*** *Neutrophils (grey) patrol the body through blood vessels (red). Inflammation also activates dendritic cells (pink), which detect infectious agents and migrate toward the lymphatic system (yellow), adapted from [5].* ***C.*** *Collective invasion of MV3 melanoma xenografts strands and single cells. Tumor cells express nuclear H2B-EGFP and cytoplasmic DsRed2.Dextran contrasts perfused blood vessels in cyan. Second harmonic generation (SHG) enables muscle and collagen fibers vizualiation in white [6].*

which gives rise to specific organs. A striking example is the migration of neural crest cells, which populate the early embryo and differentiate into neurons, glial cells of the peripheral nervous system, as well as connective tissues of the face, neck, and heart (Figure 1.1.A) [4].

In adults, cell migration remains essential for normal physiological functions. During wound healing, fibroblasts migrate through the extracellular matrix to close the wound, followed by epithelial cells that seal the surface. In inflammation, antigen-presenting cells travel to lymphoid organs to activate

lymphocytes, while macrophages move toward the inflammation site to mediate immune responses. Dysregulation of these migratory processes underlies diseases such as immunodeficiency, autoimmunity, and chronic inflammation (Figure 1.1B) [5].

Cancer further illustrates the importance of cell migration. Tumors are characterized by the uncontrolled proliferation of abnormal cells that invade surrounding tissues and can metastasize to distant organs. The mechanisms driving metastasis remain incompletely understood and differ across cancer types. Open questions in cancer biology include why certain non-motile cells acquire an invasive phenotype, and why some tumors regress while others become increasingly aggressive. Biophysical approaches are critical for addressing these questions. It is now evident that cell migration lies at the core of tumor progression (Figure 1.1C) [7].

1.1.2 Key components of the migratory machinery

Within a migrating cell, numerous molecular components collaborate to generate complex behaviors. In the following section, we examine how these components sustain cell migration in two-dimensional spaces. At the core of cellular motility is the cytoskeleton, which is a three-dimensional network of filamentous biopolymers belonging to three main families of protein filaments. Each family has distinct mechanical properties, dynamics, and biological functions. Together, they coordinate to spatial organization of the cell, define its mechanical properties, and regulate movement in response to external cues. Among these, the actin cytoskeleton is particularly important: the dynamic assembly and disassembly of actin filaments, controlled by a wide range of associated proteins, endows cells with both strength and adaptability.

The actin cytoskeleton

The actin cytoskeleton is built from actin microfilaments, or F-actin semi-flexible biopolymer composed of globular actin (G-actin), a 42-kDa protein. Three isoforms contribute to distinct acin-based networks: α-actin (found in contractile structures), β-actin (enriched in the cortical actin beneath the

plasma membrane), γ-actin (present in stress fibers and filaments extending from adhesions)[8].

In vitro measurements of single filaments have yielded characteristic mechanical parameters:

1. Persistence length: 8-17 μm, corresponding to the distance over which thermal fluctuations bend the filament. This relatively short persistence length explains why actin filaments are often found into interconnected bundles[9]. Nevertheless, confinement, cellular geometry, or by motor protein activity can bend filaments at the micron scale, well below their persistence length.

2. Young's modulus: approximately 10^9 Pa [10, 11] .

3. Buckling force: 0.4-1.6 pN is required to bend an actin filament [12]. Thus, allowing individual filaments to generate significant force before buckling [13].

Actin is one of the most abundant cytoplasmic proteins, reaching concentration up to 300 μM. In most eukaryotic cells, G-actin monomers first assemble into dimers and trimers, which then polymerize into a right-handed, double-stranded helical filament of 7 to 9 nm in diameter and up to 100 μm in length (Figure 1.2,A). Each actin subunits is rotated by 167° rotation and axially shifted by 2.7 nm relative to its neighbor. Beyond structural actin filaments provide tracks for intracellular transport of vesicles and molecules via motor proteins.

Actin filaments are intrinsically polar structures, with their dimeric subunits oriented uniformly along the filament axis (Figure 1.2,A). Actin filaments present two ends that are dynamically different. The plus-end, called the barbed, elongates roughly 10 times faster than the minus-end, called the pointed end (Figure 1.2,B). Actin polymerization, governed by a balance between monomer association and dissociation, proceed through two main phases: nucleation and elongation (Figure 1.3) [15].

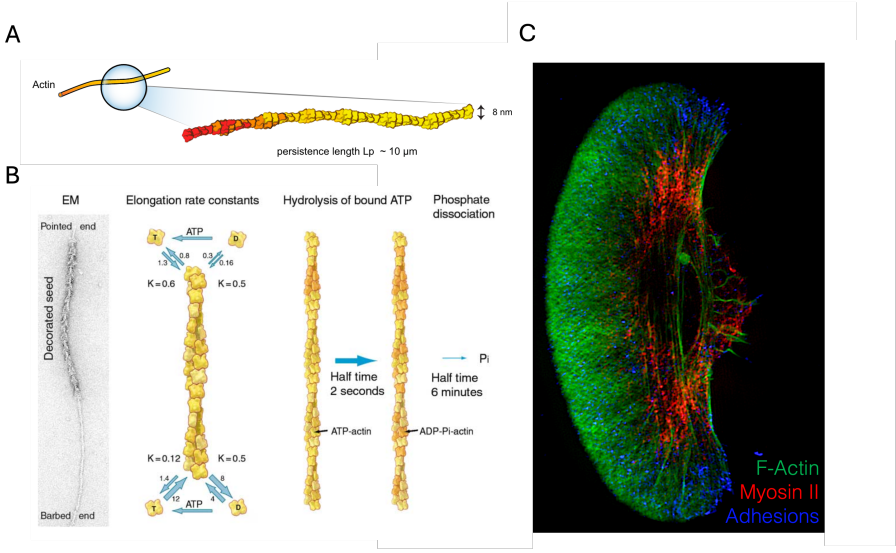

Figure 1.2: ***A.*** *Schematic representation of an actin filament, a polarized helical polymer with a diameter of 8 nm and a persistence length of 10 µm [9].* ***B.*** *Kinetic model of actin filament dynamics, including electron microscopy (EM) image of a filament "seed" (left), and the three major biochemical transitions involved in actin polymerization: nucleotide-dependent elongation at both barbed and pointed ends (left), ATP hydrolysis on filamentous actin (middle), and subsequent phosphate release (right). Actin monomers bound to ATP polymerize more rapidly than those bound to ADP, with distinct elongation rate constants at each end. ATP hydrolysis and phosphate dissociation introduce a biochemical gradient along the filament.* ***C.*** *Fluorescence image of a polarized migrating keratocyte showing the spatial distribution of cytoskeletal components: filamentous actin (F-actin, green), non-muscle myosin II (red), and focal adhesions (blue). F-actin is enriched at the cell front, myosin II localizes predominantly to the rear, and focal adhesions form at the leading edge and flanks, reflecting the coordinated organization required for directed migration[14].*

During elongation, ATP (adenosine triphosphate)-bound actin monomers are added to the (+) end, followed by ATP hydrolysis and phosphate group release (Figure 1.2,B). At the (–) end, ADP-actin monomers dissociate, leading to filament depolymerization. ADP in G-actin is then exchanged for ATP, recycling monomers for further polymerization. This continuous assembly–disassembly cycle, known as treadmilling, enables filament extension and generate protrusive forces at the cell leading edge (Figure 1.2,C) [15].

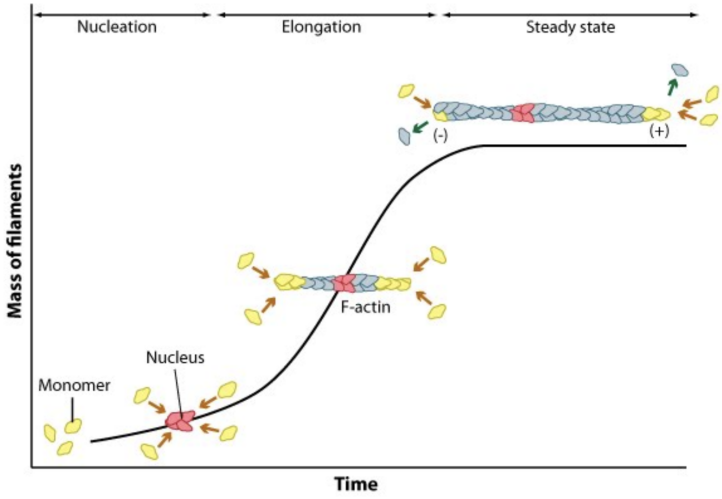

Figure 1.3: *Nucleation, elongation, and steady state phase of actin filament assembly. Source : Mechanobiology Institute, National University of Singapore.*

Filament length and turnover are regulated by capping proteins, which bind to either filament end and block subunit addition or removal [16]. Within cells, actin assembles into network with diverse architectures, depending on the action of regulatory proteins. These networks differ in their local mechanical properties, which are tuned by actin nucleators and crosslinkers (such as non-muscle myosin II, $\alpha - actinin$, Arp2/3) [15].

Actomyosin contractility

Molecular motors, such as myosins, kinesins, and dyneins, are essential components of the cell migration machinery, driving cytoskeletal reorganization, force generation, and intracellular transport to coordinate and propel cell movement.

Non-muscle myosin II (NM II)— a members of the myosin superfamily—is an important molecular motor involved in the cell migration machinery, as it generates contractile forces that regulate cytoskeletal dynamics, adhesion turnover, and rear retraction[17]. Depending on their structure, myosin motors are involved in different processes such as the cross-linking of F-actin with the

cell membrane (class I), the contraction of actin filaments (class II), or the transport of vesicles along them (class V), for the most conventional myosins [18].

NM II molecules present as hexamers and consist of three pairs of peptides: two 230 kDa heavy chains, two 20 kDa regulatory light chains (RLCs) that control NM II activity, and two 17 kDa essential light chains (ELCs) that stabilize the heavy chain structure (Figure 1.4,A) [19, 20]. Myosin II molecules can walk along actin filaments toward the barbed-end (plus), propel their sliding, or generate tension, processes that require energy from ATP hydrolysis and depend on catalytic sites with ATPase activity (Figure 1.4,A) [17].

High-resolution light microscopy has revealed that NM II tail domains self-associate in both parallel and antiparallel orientations to form 300 nm-long bipolar filaments, characterized by clusters of motor domains at both ends and overlapping tail domains centralized in the filament core (Figure 1.4,B) [20]. Once assembled, the motor domains located at the two opposing ends engage with antiparallel actin filaments and hydrolyze ATP, generating contractile forces essential for cellular tension and reorganization [20].

The motor activity of myosin is a multi-step process consisting of binding to F-actin, subsequent hydrolysis of ATP and a resulting power stroke. This process is referred to as the mechano-chemical cycle of Myosin II (Figure 1.4,C). It describes how myosin converts the chemical energy from ATP into mechanical force to move along actin filaments and generate tension [20]. In summary, the cycle starts with myosin engaging their ATPase cycle in a nucleotide-free state and strongly bound to actin (actin-bound myosin, AM) (Figure 1.4C). Upon binding with ATP to give AM-ATP, myosin enters a weak actin-binding state where it can detach from actin. Subsequent, ATP hydrolysis leads to the release of ADP and regeneration of the initial nucleotide-free myosin (Figure 1.4,C) [20].

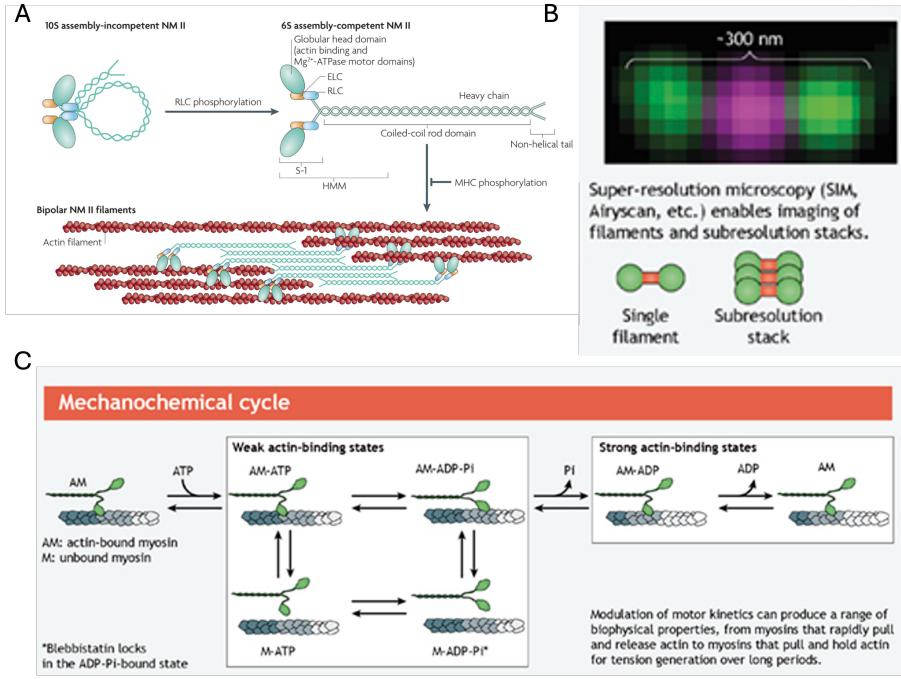

Figure 1.4: *Structural assembly and mechanochemical function of non-muscle myosin II (NMII). (A) RLC phosphorylation converts NMII from an inactive folded 10S conformation to an extended, assembly-competent 6S form that polymerizes into bipolar filaments capable of interacting with actin. (B) Super-resolution microscopy enables visualization of individual NMII filaments and subresolution stacks (300 nm). (C) NMII mechanochemical cycle: ATP binding, hydrolysis, and product release drive transitions between weak and strong actin-binding states, enabling force generation and filament sliding. Adapted from [19, 20].*

Cell-matrix adhesions

Eukaryotic cells constantly interact with the extracellular matrix (ECM), which exerts a profound influence on them via transmembrane adhesion proteins that act as receptors. Through these adhesion sites, ECM components can modulate nearly every aspect of cell behavior, including migration [21]. Various classes of molecules can act as ECM receptors or co-receptors, including transmembrane proteoglycans, integrins, and other related proteins [22].

Integrins are transmembrane receptors that assemble as heterodimers composed of one α (alpha) and one β (beta) glycoprotein subunit, which associate non-covalently (Figure 1.5,A-B). The extracellular domains of the integrin heterodimer bind to components of the extracellular matrix (ECM), such as collagen, laminin, and fibronectin, by recognizing short amino acid motifs, the most well-known being the RGD sequence (arginine–glycine–aspartic acid) [22]. Most of the integrin structure extends into the extracellular space, while the cytoplasmic domains are relatively short, typically consisting of 10-70 amino acids. The transmembrane regions of both subunits are short, helical segments. To date, 18 α-subunits and 8 β-subunits have been identified (Figure 1.5,A), which can combine to form up to 24 distinct functional heterodimers. Each cell type expresses a characteristic repertoire of integrins, determining the subset of ECM components it can recognize and bind to, thereby influencing cell behavior and fate decisions [23].

To initiate adhesion during migration, a sufficient density of adhesion proteins is required at the contact site. Shortly after integrins accumulate there, numerous intracellular proteins are recruited to form a nascent adhesion, which is a minimal structure that connects the cell to the ECM (Figure 1.6). These

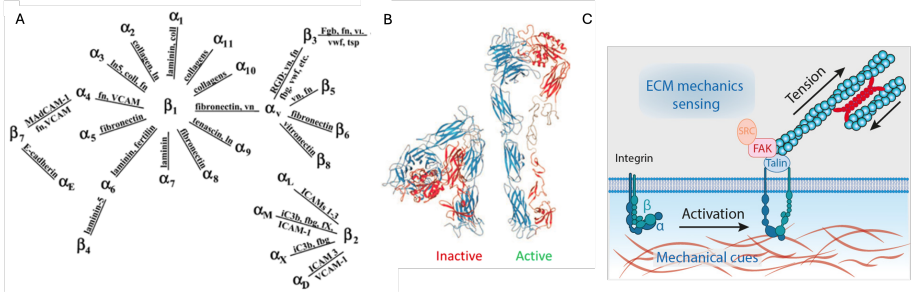

Figure 1.5: ***A.*** *Overview of integrin α and β subunit pairings and their primary extracellular matrix (ECM) ligands. Integrins form heterodimers (e.g., $\alpha 5\beta 1$, $\alpha v\beta 3$) that mediate specific adhesion to ECM components such as fibronectin (fn), laminin (ln), and collagen.* ***B.*** *Structural models of integrins in their inactive (bent) and active (extended) conformations.* ***C.*** *Mechanosensing by integrins. Mechanical cues from the ECM trigger integrin activation via talin binding and recruitment of focal adhesion kinase (FAK) and SRC, allowing transmission of intracellular tension and modulation of downstream signaling pathways. Adapted from [22]*

nascent adhesions can withstand only very small traction forces (2 pN) [24]. The tension generated by cytoskeletal filaments can then promote their maturation into larger focal adhesions [22].

Among the best-studied components of these adhesions are structural proteins such as talin and vinculin, as well as signaling molecules like focal adhesion kinase (FAK) and Src-family tyrosine kinases, which regulate adhesion dynamics and signaling during cell migration (Figure 1.5,C). These proteins are not randomly distributed but instead organize into discrete vertical layers, spanning from the extracellular matrix to the cytoplasmic side, enabling efficiently transduction of mechanical forces and biochemical signals (Figure 1.6) [25].

A migrating cell must be able to form and disassemble adhesions with their substrate. At adhesion sites, integrin dimers at adhesion sites can switch between two conformations: an inactive (closed and bent) state with low ECM affinity, and an active (open and extended) state with high ECM affinity (Figure 1.5,B) [21]. This conformational change is regulated by interactions with intracellular or membrane-associated proteins. For example, cytoskeletal components such as talin, which links to actin filaments, can bind to the cytoplasmic tail of the β subunit and activate the receptor. integrin activation also promotes clustering, thereby amplifying downstream signaling.

Because adhesions can exist at different stages of maturation, they are classified according to their size and structure. Initially, a small nascent adhesion ($<$0.5 μm^2) grows into a focal complex (FC; 0.5–1 μm^2). These circular mature structures can then develops into larger and elongated focal adhesions (FA; $>$1 μm^2) [26], which anchor stress fibers at the adhesion site (Figure 1.6,A). The transition from FC to FA depends on the force applied to the nascent adhesion. At a maturation stage, fibrillar adhesions form, characterized by an integrin composition favoring fibronectin binding [22].

The magnitude of the traction forces exerted by the cytoskeleton on adhesion sites depends on the size of the adhesion complex. Measurements from human fibroblasts on deformable substrates have shown a relatively constant stress of about 5.5$\pm$2 nN/μm^2 exerted by focal adhesions. A comparable level (4.8

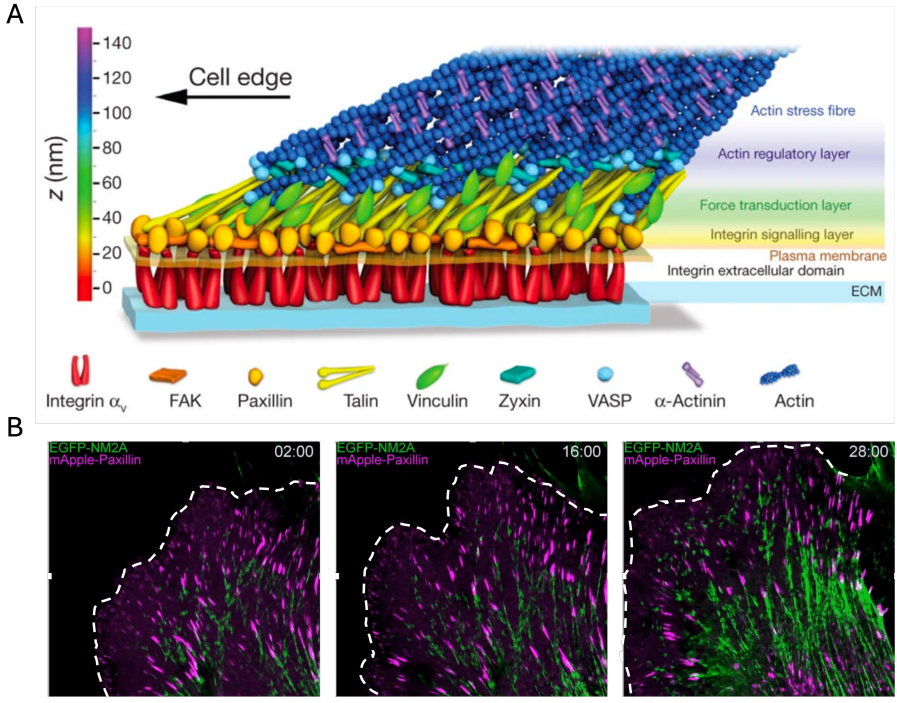

Figure 1.6: ***A.*** *Schematic of the vertical stratification of a mature focal adhesion complex. Distinct functional layers are organized along the z-axis, from the extracellular matrix (ECM) to the actin cytoskeleton. The integrin extracellular domains connect the ECM to the intracellular signaling layer (e.g., FAK, paxillin), force-transduction layer (e.g., talin, vinculin), and actin-regulatory structures (e.g., α-actinin, VASP, and actin stress fibers).* ***B.*** *Time-lapse imaging of a migrating cell expressing EGFP-tagged non-muscle myosin IIA (NM2A, green) and mApple-tagged paxillin (magenta), visualizing the spatiotemporal coordination between actomyosin contractility and focal adhesion dynamics during cell edge advancement. Time is indicated in minutes; cell edge outlined in dashed white. Adapted from [25]*

$\mathrm{nN}/\mu\mathrm{m}^2$) has been observed in muscle cells, despite morphological differences between the two cell types[22, 27]. Notably, force generated by actin retrograde flow alone can be sufficient to open integrins and maintain nascent adhesions and focal contacts independently of NM II [28, 29].

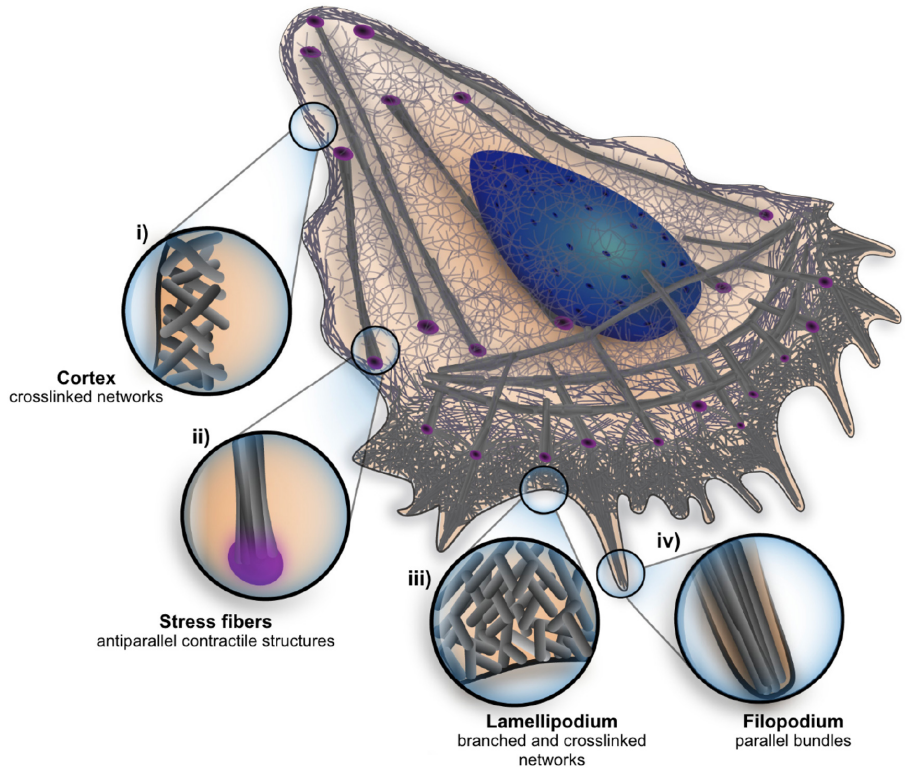

Figure 1.7: *Schematic representation of various actin cytoskeleton structures in a motile cell : the cortex, stress fibers, lamellipodium and filopodium. The nucleus is represented in blue and focal adhesions in purple [9].*

1.2 Actin-based protrusions and organization

In vitro, actin polymerization dynamics are controlled by actin concentration. In cells, however, polymerization must be tightly regulated by numerous binding partners that interact with actin monomers or filaments. Most cells contain over a hundred distinct actin-binding proteins. Collectively, this group of proteins orchestrate the dynamic remodeling of the actin cytoskeleton, a central process forming cellular protrusions such as lamellipodia and filopodia, as well as stress fibers and the actin cortex (Figure 1.7) [16].

A key step in this process is actin nucleation corresponding to the formation of new actin filaments from monomeric G-actin. Because spontaneous nucleation is energetically unfavorable, cells rely on specialized actin nucleators to initiate and organize filament growth at the leading edge. Two major classes of actin nucleators coordinate the architecture and dynamics of actin networks during protrusion formation: the Arp2/3 and Formins [16]. Together, they control the spatial and temporal assembly of actin structures that drive membrane protrusions, a critical step in cell migration, tissue remodeling, and development.

1.2.1 Branched Actin networks and Arp2/3

Lamellipodia

A key actin architecture driving force generation for cell movement and shape changes is the branched actin network, initiated by the Arp2/3 complex—a seven-protein assembly consisting of two actin-related proteins (Arp2 and Arp3), a seven-blade β-propeller subunit (ARPC1A and ARPC1B in mammalians), and four distinct subunits (ARPC2–5) that support and stabilize the complex initiated by a complex made of seven proteins: the Arp2/3 complex (Figure 1.8,A)[30].

The Arp2/3 complex mediated nucleation is essential for forming broad, sheet-like lamellipodia (Figure 1.8,B). It requires activation by nucleation-promoting factors (NPFs) such as WAVE or N-WASP[1], which are recruited downstream of signaling pathways like Rac1[2] (Figure 1.8,A) [31]. By mimicking the geometry of actin dimers, Arp2/3 promote polymerization and generate branches at approximately 70° (Figure 1.8,A)[8], enabling filament growth close to the plasma membrane. Rho-GTPases[3] regulate this network by acti-

[1]The Wiskott-Aldrich syndrome protein (WASP) and WASP-family verprolin-homologous protein (WAVE) family proteins are fundamental cortical actin organizers, involved in signal transduction from the cell surface to the actin cytoskeleton.

[2]Rac1 (Ras-related C3 botulinum toxin substrate 1) is a small signaling GTPase belonging to the Rho family.

[3]Rho GTPases are a family of small (21 kDa) signaling G proteins belonging to the Ras superfamily. They act as molecular switches cycling between an inactive GDP-bound state and an active GTP-bound state.

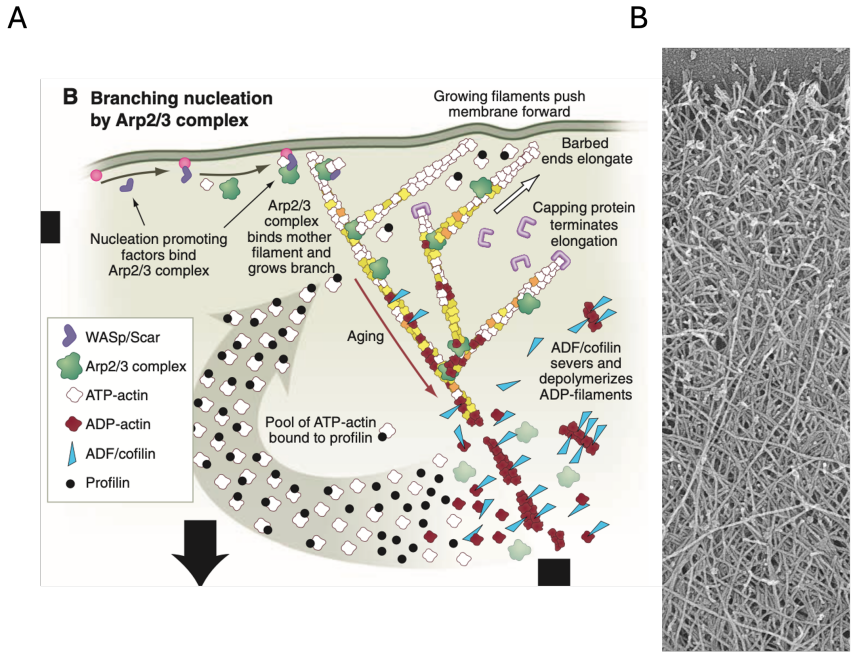

Figure 1.8: *Branched actin network formation driven by the Arp2/3 complex. Nucleation promoting factors (e.g., WASp/Scar) activate Arp2/3, which binds to the side of a pre-existing filament to nucleate a new branch. Actin polymerization at the barbed ends pushes the membrane forward, while filament aging leads to ADF/cofilin-mediated disassembly. Right, transmission electron micrograph shows a dense branched actin network similar to that found in lamellipodia. Adapted from [32, 9]*

vating Arp2/3 and stabilizing newly formed filaments through the inhibition of filament-dissociation factors. [31].

Filopodia

Formins promote the nucleation and elongation of linear, unbranched actin filaments, typically associated with filopodia, stress fibers, and contractile structures [9]. Remaining processively bound to the barbed end of actin filaments, they protect filaments from capping and enable rapid elongation, often under the control of Rho GTPases such as RhoA [9]. Filopodia are slender, actin-rich projections of the plasma membrane (Figure 1.9) [9], usually initiated at the leading edge. They consist of parallel bundles of unbranched actin filaments

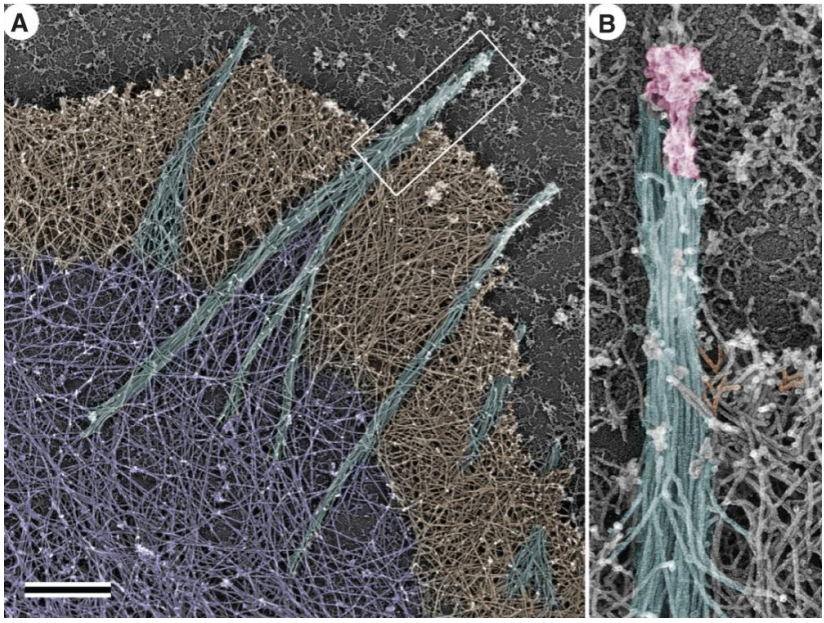

Figure 1.9: *Scanning electron microscopy (SEM) images showing the ultrastructure of the actin cytoskeleton at the cell periphery.* ***A.*** *Color-enhanced overview showing multiple structural domains: lamellipodial meshwork (brown), filopodial bundles (cyan), and retrograde actin network (purple).* ***B.*** *Zoomed-in view of a filopodium with actin bundles (cyan), membrane (pink), and potential linkage to underlying network (orange arrows).Scale bar, 500 nm [33].*

with barbed ends facing the membrane, stabilized by transcient crosslinking from proteins such as α-actinin and fascin, whose binding dynamics, on the order of seconds, are sensitive to mechanical load[9].

Although the mechanism underlying filopodia elongation is well established, their initiation remains a matter of debate. The prevailing model proposes that filopodia arise from the actin network through the convergence of branched filaments generated by the Arp2/3 complex. These filaments are subsequently elongated by formins[4] and other regulatory proteins into straight filaments [33]. These elongated filaments are then bundled and stabilized by fascin, which increases stiffness and mechanical resilience. However, the precise contribution

[4]nucleator proteins that promote actin filament growth at the barbed end

of the Arp2/3 complex to filopodia initiation remains uncertain and warrant further investigations [33].

Like branched-actin networks, elongating actin bundles can generate forces sufficient to drive protrusion [34]. Optical tweezer experiments have quantified the force exerted by individual filopodia with millisecond resolution, revealing that a single filopodium can generate forces up to ∼3 pN. These forces are solely powered by actin polymerization. Larger forces, by contrast, require the additional contribution of microtubule polymerization[34]. Importantly, filopodia dynamics rely entirely on actin assembly and turnover.

Beyond their role in migration, filopodia contribute to environmental sensing, the initiation of cell-cell contacts, and intercellular signaling. Notably, enhanced actin polymerization alone is not sufficient to initiate protrusion formation. The initiation of lamellipodia and other actin-rich protrusions has long been attributed to local increases in actin polymerization [35]. However, this view has been recently challenged by studies showing that local detachment of the plasma membrane from the underlying cortex is also an essential prerequisite for initiating actin-rich protrusions [36, 37].

The Actin cortex

Dynamic changes in cell shape are fundamental to diverse biological processes such as migration, division, and morphogenesis. In animal cells, these changes are primarily mediated by the actin cortex—a thin, dense network of actin filaments and myosin motors located immediately beneath the plasma membrane [38, 39] (Figure 1.10,A-B). The cortex generates cortical tension, a key mechanical property that shapes cells by establishing spatial gradients across the cell [40].

Cortical tension primarily arises from the activity of non-muscle myosin-2, which assembles into bipolar minifilaments that contract the actin network [41] (Figure 1.10,C-D). Yet, recent work emphasizes that the organization and dynamics of cortical actin are equally critical. Actin filament length, and connectivity strongly influence how contractile forces are generated and transmitted

throughout the cortex [42].

Cortex assembly relies on the coordinated activity of actin nucleators, in particular the formin mDia1 and the Arp2/3 complex, which drive the formation of linear and branched filaments, respectively [43]. These nucleators shape cortex architecture and mechanical properties, with mDia1 playing a central role in filament elongation and cortex thickening, especially during mitotis[42]. In the absence of formins the cortex becomes irregular, with regions of varying filament density, whereas loss of Arp2/3 results in notably longer filaments.

Beyond nucleation, the actin cortex contains numerous crosslinking and bundling proteins—including α-actinin, filamin, and fascin—that modulate network organization. Crosslinkers such as filamin generate isotropic networks, whereas bundlers like fascin align filaments into parallel arrays [39]. This filament architecture directly impacts cortical mechanics, with higher connectivity generally correlating with increased contractile tension [41].

Cortical F-actin is anchored to the plasma membrane through linker proteins such as ERM proteins[5] and myosin-1 motors (Figure 1.10,A). While these do not always directly affect cortical tension, they regulate plasma membrane tension, thereby modulating how easily the membrane deforms during shape changes [46].

The nanoscale thickness (typically 100–400 nm) and high density of the cortex present major challenges for imaging and structural analysis (Figure 1.10,A). Although electron microscopy and super-resolution methods have provided valuable insights, the 3D architecture of the cortex remains incompletely resolved [47, 48] (Figure 1.10). This lack of structural clarity limits the precision of theoretical models of cortical tension, which often rely on assumptions about actin filament organization [49].

[5]Ezrin, Radixin, and Moesin (ERM) are membrane–cytoskeleton linkers that connect the actin cytoskeleton to the plasma membrane, regulating cell shape, adhesion, and signaling.

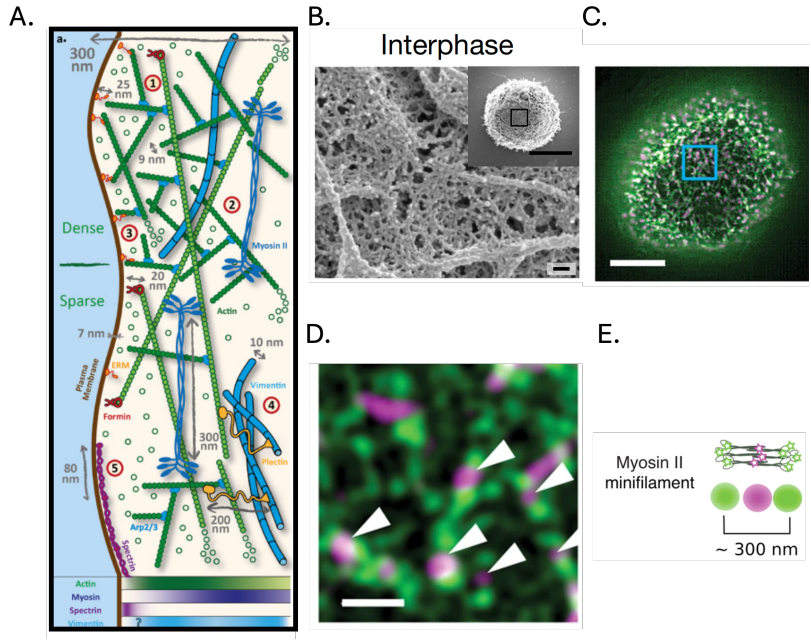

Figure 1.10: *Architecture of the actin cortex during interphase.* ***A.*** *Schematic representation of the actin cortex highlighting its dense submembrane organization. The cortex consists of a dense actin meshwork (100–300 nm thick) beneath the plasma membrane, crosslinked by myosin II minifilaments, ERM proteins, and other actin-binding factors such as formins and Arp2/3. Spectrin, vimentin, and plectin also contribute to cortex organization and connectivity with intermediate filaments.* ***B.*** *High-resolution electron microscopy (EM) and super-resolution fluorescence* ***(C)*** *imaging of interphase cells reveals the nanoscale organization of the actin cortex and the distribution of myosin II minifilaments (green) and associated structures (magenta)* ***(D-E)****. Scale bars, 5 µm and 500 nm. Adapted from [44, 45, 42].*

ERM proteins in actin cortex organization

ERM proteins—ezrin, radixin, and moesin—are conserved membrane-cytoskeleton linkers with essential roles in organizing the actin cortex and specialized membrane domains [50] (Figure 1.11,A). By connecting filamentous actin to transmembrane and membrane-associated proteins, ERM contribute to membrane stability, cortical tension, and dynamic shape remodeling (Figure 1.11,B). Their activity is regulated by a head-to-tail folding mechanism, regulated by phosphatidylinositol (4,5)-bisphosphate and phosphorylation of a conserved C-termi-nal threonine (e.g., T567 in ezrin, T558 in moesin)[50] (Figure 1.11,A).

Upon activation, ERMs localize to the cortex, strengthening actin-membrane attachment and participating in cell polarity, adhesion, and migration [50]. During mitosis, moesin is required for cortical stiffening, bleb retraction, and proper spindle positioning, its dephosphorylation at anaphase promotes cortex relaxation and elongation [50] (Figure 1.11,B).

ERMs proteins also function as signaling integrators. Ezrin regulates Rho, PI3K/Akt, and Cdc42 signaling pathways, with phosphorylation regulated by Rho-activated kinases such as SLK and LOK [51]. It recruits Rho GEFs like Dbl, enabling Cdc42 activation in lipid rafts, which are critical for directional migration and front-rear polarity in carcinoma cells [52]. Radixin, regulates Rac1 through Vav GEF activity, thereby influencing cell area and motility [53]. Importantly, active ERMs can suppress RhoA activity, whereas inactive ERMs correlate with increased RhoA signaling and myosin II phosphorylation, highlighting reciprocal regulation between ERM activation and cortical contractility[54] (Figure 1.11,C).

Pharmacological inhibition further demonstrates ERM functionality. NSC668394 directly binds ERMs, preventing phosphorylation of their regulatory threonine residues and disrupting actin binding [50, 56]. This inhibition impairs ezrin-mediated motility and migration in vitro and in vivo, while reducing cortical tension by uncoupling moesin from F-actin. Clinically, high ezrin expression is associated with poor prognosis and metastasis in breast cancer, correlating with increased motility, cadherin mislocalization, and HER2 positivity [57, 56].

Among ERM proteins, moesin play a particularly prominent role in coordinating cytoskeletal dynamics during cell migration. Moesin localized to the cortical actin dome during early adhesion, where it regulates Rho activation and Myosin II–driven contractility, driving cortical polarization and the transition from a rounded to an elongated migratory morphology [58]. During migration, moesin undergoes phosphorylation-dependent membrane association and is transported rearward via lamellar actin flow, integrating into a dual actin network [55] (Figure 1.11,D). This coupling of cortical and lamellar networks modulated by moesin ensures feedback regulation of actin flow and leading-edge dynamics, underscoring moesin's central role in maintaining migratory

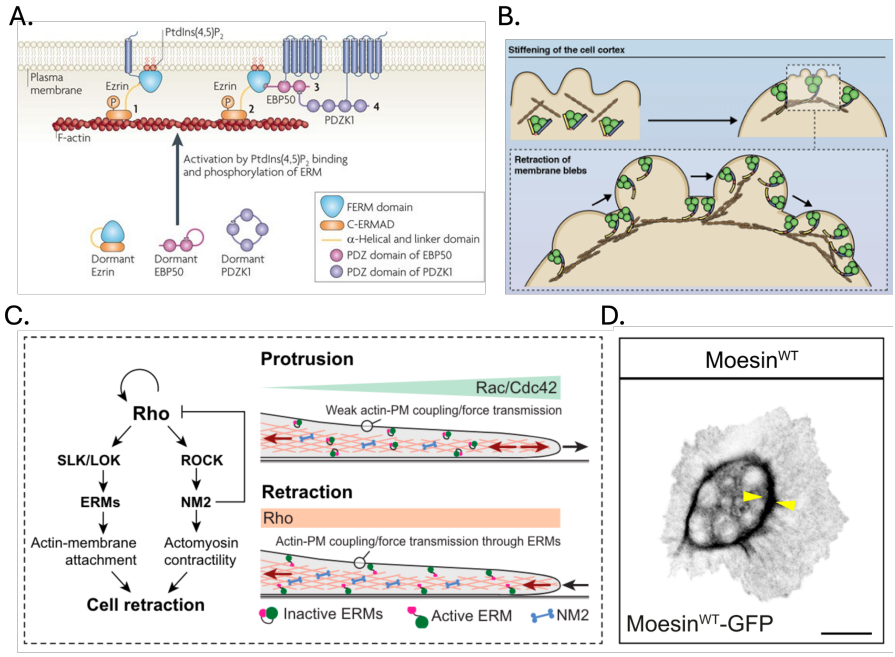

Figure 1.11: *Regulation and function of ERM proteins in actin–membrane coupling.* ***(A)*** *Schematic of ERM protein activation. ERM proteins (ezrin, radixin, moesin) are initially in a dormant conformation and become activated via binding to PtdIns(4,5)P_2 at the plasma membrane, followed by phosphorylation.* ***(B)*** *ERM-mediated actin–membrane coupling contributes to cortical stiffening and is essential for membrane bleb retraction.* ***(C)*** *Rho GTPase signaling coordinates ERM activation and actomyosin contractility through kinases such as SLK/LOK and ROCK. ERMs and non-muscle myosin II (NM2) cooperate to drive cell rear retraction.* ***(D)*** *Moesin distribution visualized using GFP-tagged constructs in migrating hemocyte. Moesin is enriched at the cortex and colocalizes with regions of high cortical tension, as indicated by the yellow arrowheads. Adapted from [50, 55, 54].*

efficiency (Figure 1.11,D).

1.3 Mechanics of individual cell migration

In the 1970s, pioneering work by Abercrombie and colleagues laid the foundation for our current understanding of cell crawling on two-dimensional sub-

strates. Using detailed phase-contrast imaging of fibroblast-like cells, they proposed the «contractile model» of migration, which remains highly influencial today [59, 60]. The term "cell crawling" describes cell locomotion as a multistep, highly orchestrated process, emphasizing that cells must generate and transmit mechanical forces against their environment to propel themselves forward [61].

1.3.1 Steps of cell migration

Cell migration is a cyclic and tightly coordinated process that depends on a dense actin network beneath the plasma membrane [62, 63]. Movement involves the coordination of five major steps (Figure 1.12):

1. **Protrusion projection**: At the leading edge, lamellipodia and filopodia extend as actin polymerization pushes against the plasma membrane. Protrusive forces at the front of the cell have been quantified using atomic force microscopy (AFM). In keratocytes, AFM tip deflection values revealed an average force of ∼8 pN per actin filament [64].

2. **Attachment**: Nascent adhesions form at the front, anchoring the actin cytoskeleton to the substrate via integrins, and assembling into adhesion complexes [65].

3. **Contraction**: Actomyosin contractility generates tension within the cell body, promoting rear retraction, and driving cytoplasm flow forward. Traction force microscopy (TFM) has been used to quantifiy these forces: during fibroblast migration, average traction stresses of ∼3 kPa are observed [27].

4. **Release**: Rear adhesions disassemble, stress fiber tension is relieved, and actin filaments undergo depolymerization [66].

5. **Recycling**: Actin monomers and adhesion components are recycled and transported to the leading edge, ensuring sustained migration [63].

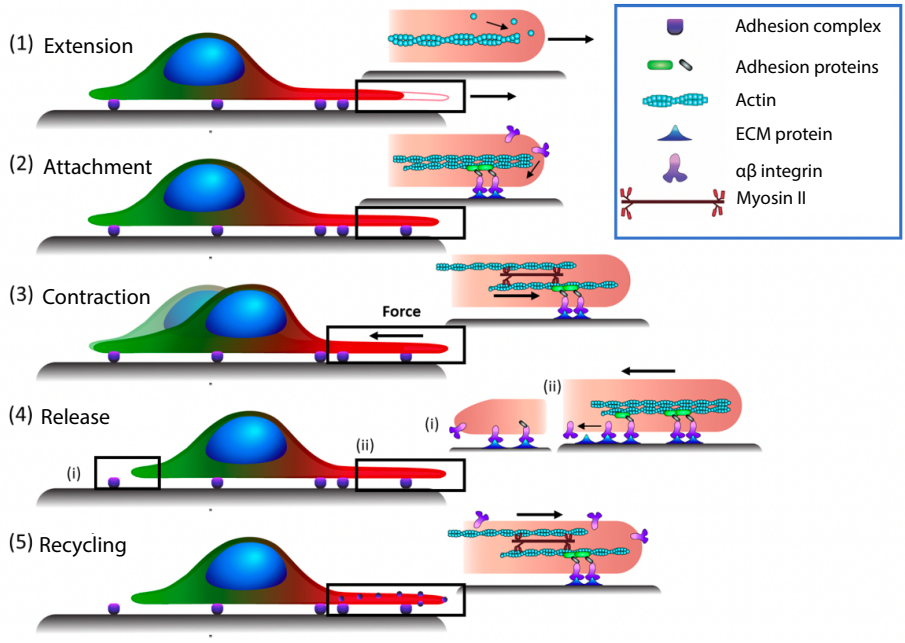

Figure 1.12: *Schematic representation of the main steps in the cell migration cycle, including protrusion, adhesion, contraction, release, and recycling. Key molecular components are indicated in the inset.*

1.3.2 Forces transmission during migration

Although numerous studies have shown that force are transmitted to the substrate through focal adhesions, the spatiotemporal regulation of these forces, and how they drive persistent, directional migration, remains only partially understood[67]. To explain how cells dynamically couple cytoskeletal forces to adhesion sites, Giannone et al. proposed the molecular clutch model, drawing an analogy to the engagement and disengagement mechanism of a car clutch [68].

Brief description of the molecular clutch

The molecular clutch refers to a set of proteins located at adhesion complexes that modulate the mechanical coupling between the actin cytoskeleton and the extracellular substrate. In this model, F-actin retrograde flow, generated by

actin polymerization at the leading edge and myosin II–mediated contractility in the lamella, serves as the motor driving force [68].

When adhesions are absent or weak, retrograde actin flow proceeds unrestricted, and membrane protrusion is inefficient (Figure 1.13,A). By contrast, when adhesion molecules engage to the ECM, the retrograde flow slows due to mechanical resistance, analogous to engaging a car clutch. This engagement transfers cytoskeletal tension to the substrate, enabling effective traction force generation and forward protrusion (Figure 1.13,B). As adhesions mature, they recruit structural and signaling proteins and are reinforced by actin bundles, thereby increasing their load-bearing capacity, similar to shifting gears to transmit greater force.

Biophysically, the clutch model treats actin–substrate links as dynamic molecular springs. The probability of bond formation (k_{on}) is constant (Figure 1.13,C), while detachment (k_{off}) increases with load (Figure 1.13,C)[69] . On stiff substrates, rapid loading cause frequent slipping and inefficient traction, whereas on compliant substrates gradual loading can lead to cooperative clutch rupture, producing oscillatory or irregular migration. Importantly, this principle applies not only to branched actin networks in lamellipodia, but also to stress fiber–associated adhesions where tension derives from myosin II contractility. In both cases, focal adhesions act as mechanosensitive elements that regulate force transmission and allow cells to probe the mechanical properties of their environment [69] .

Membrane tension as a regulator of cell migration

The plasma membrane is not a passive boundary but an active regulator of cell shape, polarity, and motility. Migration arises from the dynamic interplay between membrane tension and actin cytoskeleton assembly, which together coordinate protrusion, adhesion, and retraction cycles [70, 71]. Typical membrane tension ranges from 2×10^{-5} to 4×10^{-4} N/m, acting as a resistive force against deformation and reflecting the energetic cost of coupling to the underlying cytoskeleton [72]. Because tension propagates across the membrane on millisecond timescales, it provides rapid mechanical feedback that link local

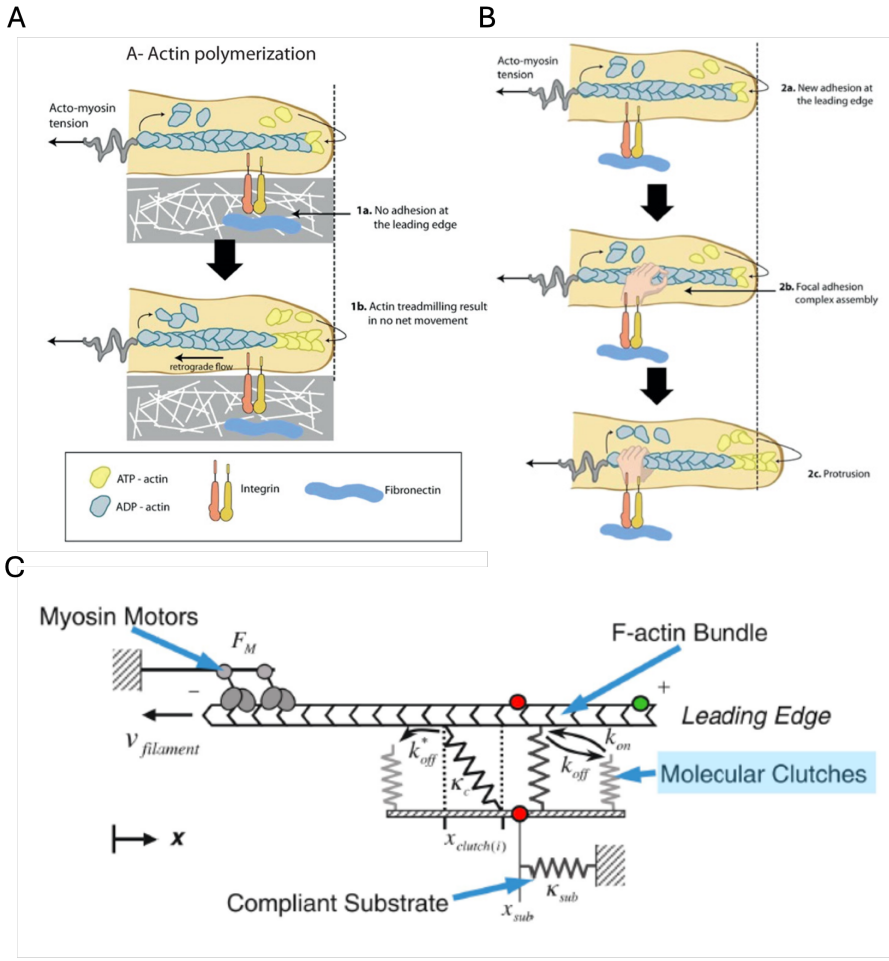

Figure 1.13: *The molecular clutch model.* ***A.*** *Schematic of actin polymerization, retrograde flow, and adhesion engagement during cell migration. When adhesions are absent, actin treadmilling does not result in net protrusion.* ***B.*** *Adhesion engagement at the leading edge slows actin flow and enables protrusion.* ***C.*** *Biophysical model of the molecular clutch as a set of spring-like couplings between the actin cytoskeleton and a compliant substrate, illustrating the dynamics of bond engagement and force transmission. Adapted from [68].*

protrusions with global migratory behavior.

As a global mechanical constraint, membrane tension modulates actin dynamics at the cortex (Figure 1.14). By imposing load on the actin network, high tension opposes lamellipodial expansion, whereas low tension facilitates spreading and protrusion (Figure 1.14) [73].

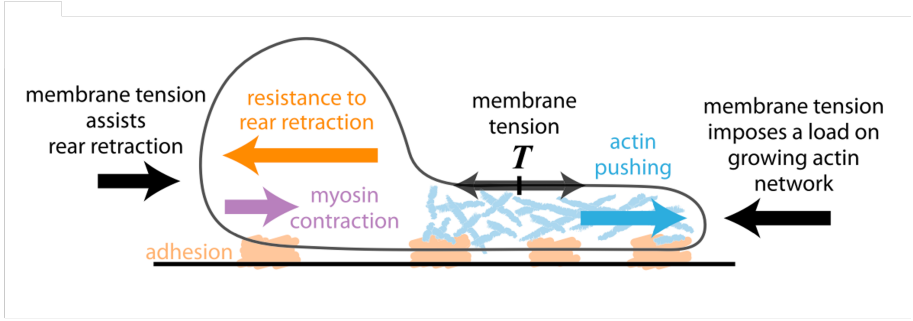

Figure 1.14: *Membrane tension balances forces during cell migration. Tension resists actin-driven protrusion at the front, imposes a load on the actin network, and aids rear retraction by opposing cortical resistance. Adapted from [71].*

Coupling between the lipid bilayer and the actin cortex generates tension gradients across the cell. These gradients spatially restrict actin polymerization and adhesion formation, effectively acting as "mechanical fences" that bias protrusive activity and promote directional migration [71].

Membrane tension also regulates actin assembly indirectly by modulating the localization and activity of actin nucleators such as WAVE and the Arp2/3 complex. These proteins are recruited to curved or tensed regions, coupling physical membrane states to intracellular signaling cascades. This feedback loop between mechanics and biochemistry stabilizes front–rear polarity [73]. Functionally, membrane tension tunes protrusion dynamics (Figure 1.15,A): low tension allows multiple lamellipodia, causing unstable polarity and inefficient migration. Moderate membrane tension promotes a single dominant protrusion, maximizing migration speed; while excessive tension suppresses actin polymerization and slows movement [74] (Figure 1.15,B).

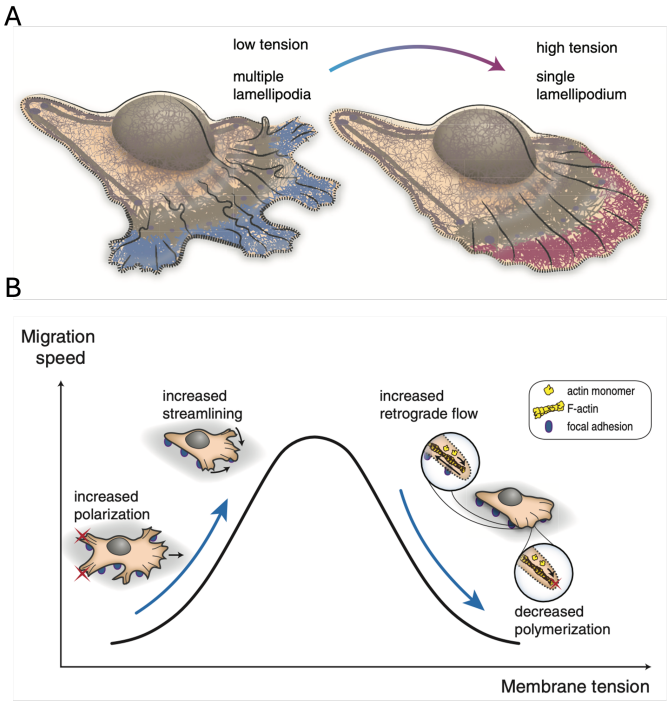

Figure 1.15: *Membrane tension coordinates polarization and motility.* ***A.*** *Low tension allows multiple lamellipodia, whereas high tension favors a dominant front.* ***B.*** *Cell migration speed follows a biphasic response to membrane tension. Adapted from [74].*

1.4 Maintenance of front-rear polarization

A fundamental requirement for cell migration is the establishment of front–rear cell polarity. This polarity arises from an intrinsic cellular asymmetry manifested in distinct structural, morphological, and functional organizations along a single axis [62]. It reflects the polarized distribution of intracellular components, cytoskeletal elements, and signaling cascades that collectively define leading and trailing edges.

Polarity is initiated through symmetry breaking, triggered either by extracellular cues such as chemotactic gradients or by stochastic fluctuations in signaling networks [75]. Once established, polarity must be maintained by spatial and temporal control of molecular activity, sustaining asymmetry in signaling,

cytoskeletal architecture, and adhesion dynamics [76].

1.4.1 Protein Activity: Rho GTPases

The Rho family of small GTPases (21kDa) function as molecular switches that regulate cytoskeletal dynamics, cell migration, vesicular trafficking, and other fundamental cellular processes [77, 78]. Anchored to the inner leaflet of the plasma membrane, these proteins cycle between an active GTP-bound conformation and an inactive GDP-bound state (Figure 1.16,A). In their active form, they bind specific effectors until inactivation by GTP hydrolysis. Guanine nucleotide exchange factors (GEFs) promote GDP-GTP exchange, switching the proteins "on," while guanine nucleotide dissociation inhibitors sequester them in the cytosol (Figure 1.16,A)[79].

Among the best-characterized members, Rac1 stimulates actin polymerization at the cell periphery through the Arp2/3 complex, leading to lamellipodia formation. Cdc42 promotes filopodia assembly and contributes to directional sensing, whereas RhoA induces actomyosin contractility via ROCK, bundling actin filaments into stress fibers and promoting focal adhesion maturation (Figure 1.16,A-B)[80, 81].

Front–rear polarity emerges from the spatial segregation of Rho family GTPase activity: Cdc42 and Rac1 dominate at the leading edge to drive actin-rich protrusions, while RhoA predominates at the rear, generating contractile forces [82]. This distribution is maintained by localized GEF and GAP (GTPase-activating proteins) activity, reinforced by feedback loops linking cytoskeletal dynamics with adhesion signaling. Microtubule-based trafficking further stabilizes this organization, supporting persistent migration and long-term polarity maintenance [82].

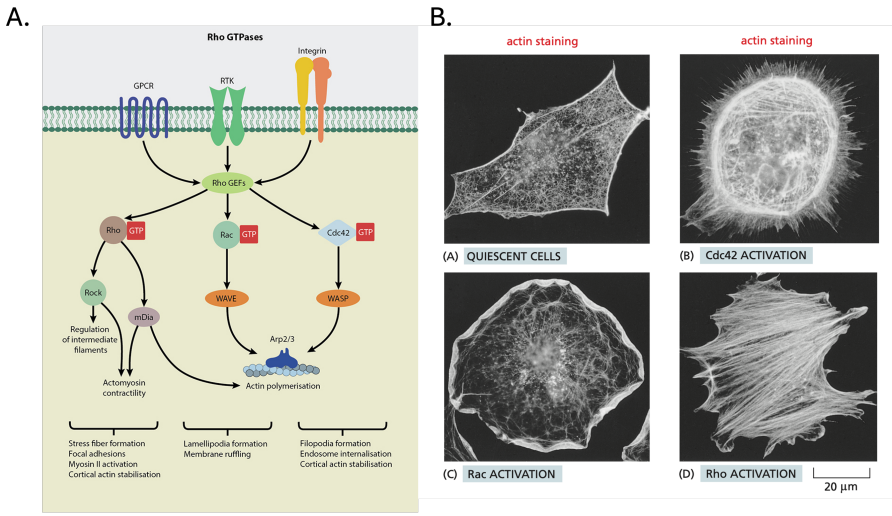

Figure 1.16: *Rho GTPase signaling pathways and effects on the actin cytoskeleton.* ***A.*** *Rho GTPases are activated downstream of GPCRs, RTKs, and integrins via Rho GEFs.* ***B.*** *Representative actin staining in fibroblasts illustrating Rho GTPase-induced cytoskeletal phenotypes. (A) Quiescent cells display diffuse actin networks. (B) Cdc42 activation induces filopodia. (C) Rac1 activation results in lamellipodial protrusions. (D) RhoA activation promotes strong stress fibers and contractility. Adapted from [78].*

1.4.2 Microtubules in polarization

Microtubules (MTs), along with actin filaments and intermediate filaments, form the three major components of the cytoskeleton. Structurally, they are hollow, rigid cylinders of α- and β-tubulin heterodimers with an outer diameter of 25 nm (Figure 1.17,A) [16]. Owing to their larger diameter and high persistence length—often reaching several millimeters—microtubules are far stiffer than actin filaments (persistence length ∼15–20 μm) and intermediate filaments, enabling them to resist compressive forces and contribute to cellular mechanical integrity (Figure 1.17,A)[22].

Beyond their architectural role, microtubules are crucial regulators of polarity and migration. Their intrinsic polarity, with minus ends anchored at microtubule-organizing centers (MTOCs) and plus ends dynamically extending toward the cell periphery, supports directional trafficking and spatial cytoplasmic organization (Figure 1.17,B) [83].

In migrating mesenchymal cells, the centrosomal MTOC aligns with the nucleus–Golgi axis, organizing microtubules in a radial array oriented toward the leading edge (Figure 1.17,C)[84]. This organization enables polarized delivery of vesicles, organelles, and signaling complexes, reinforcing cell polarity and sustaining directed migration.

Microtubules and Rho GTPases regulate one another in a reciprocal feedback loop. RhoA, Rac1, and Cdc42 influence microtubule behavior through cortical effector proteins that capture and stabilize microtubule plus ends [85]. Conversely, microtubule depolymerization releases GEF-H1, a guanine nucleotide exchange (GEF) factor that activates RhoA, thereby enhancing contractility and focal adhesion maturation at the cell rear [86]. At the leading edge, dynamic microtubule growth promotes Rac1 activation, supporting actin polymerization and focal adhesion turnover[87, 88].

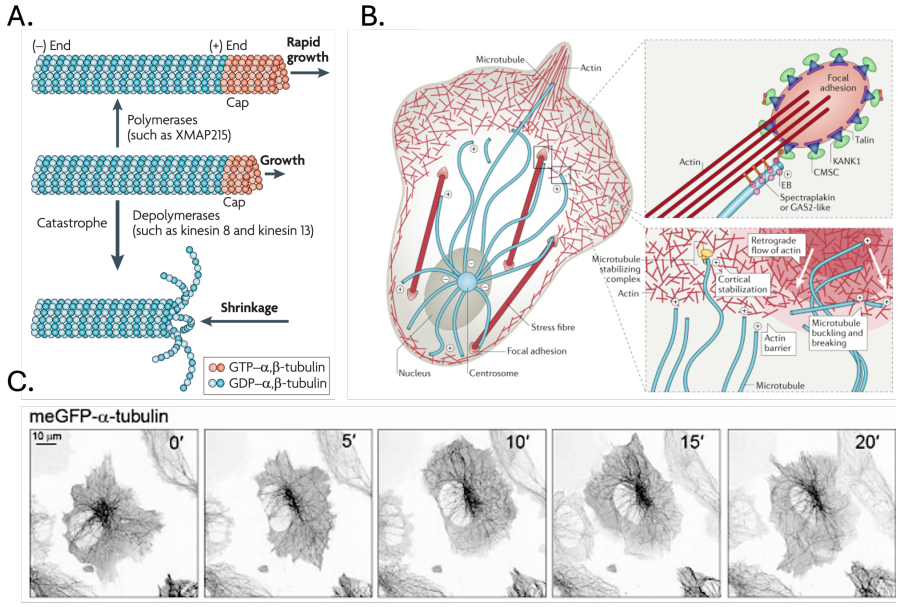

Figure 1.17: *Microtubule dynamics and role in cell polarity and migration.* ***(A)*** *Schematic of microtubule dynamic instability. Microtubules polymerize at their plus ends through the addition of GTP-bound tubulin dimers and undergo dynamic transitions between phases of growth and shrinkage, controlled by regulatory proteins. GTP-tubulin forms a stabilizing cap, while hydrolysis to GDP-tubulin leads to destabilization and shrinkage via catastrophe events.* ***(B)*** *Microtubule organization in a migrating mesenchymal cell. The centrosome reorients to face the leading edge, directing radial microtubule growth. Insets show focal adhesion-associated microtubule capture and cortical microtubule stabilization complexes (CMSC), as well as microtubule buckling and actin barrier formation at the cell front. Microtubules modulate focal adhesion turnover and support polarized trafficking.* ***(C)*** *Time-lapse fluorescence images of a cell expressing meGFP–α-tubulin, illustrating microtubule reorganization over a 20-minute period. Microtubules dynamically extend and rearrange toward the cell periphery, supporting centrosome repositioning and front–rear polarization. Adapted from [89, 90, 91]*

Microtubules further support front–rear polarization through several interconnected mechanisms:

1. **Directed vesicle and organelle transport**: MTs serve as tracks for kinesin and dynein motor proteins to deliver vesicles from the Golgi to the leading edge and recycle cargo toward the rear [87].

2. **Spatial control of signaling**: MTs transport GEFs and GAPs for Rho

GTPases to specific subcellular locations, reinforcing localized activation of stabilizing polarity [92].

3. **Microtubule plus-end capture at focal adhesions**: plus-end tracking proteins (+TIPs) such as CLASP, together with cortical tethers such as KANK1, anchor growing microtubule plus ends at adhesion sites, promoting adhesion disassembly and reorientation of the polarity axis (Figure 1.17,B) [90].

4. **Support of symmetry breaking**: uring processes such as epithelial-to-mesenchymal transition (EMT), cells reorganize from apicobasal polarity with non-centrosomal MTOCs to a front–rear polarity with a single centrosomal MTOC. This enables radial microtubule extension toward the leading edge, driving symmetry breaking and persistent migration[93].

Altogether, the microtubule (MT) network acts as both a mechanical scaffold and a dynamic signaling hub coordinating cell polarity, force generation, and adhesion dynamics. Its asymmetric organization establishes front–rear polarity by coupling intracellular transport, signaling, and cytoskeletal remodeling at distinct cell locations [94, 95].

From the molecular point of view, MTs mediate cross-talk between the actin cytoskeleton and focal adhesions (FAs). Growing MT plus ends, enriched in +TIP complexes, concentrate signaling molecules and actin assembly factors. MTs are captured near FAs through CLASP–KANK complexes, which stabilize their plus ends, while proteins such as APC (Adenomatous polyposis coli) and mDia (formin) cooperate to reinforce actin nucleation and MT stability [94, 95].

MT dynamics directly regulate Rho GTPase activity. The Rho GEF (GEF-H1), sequestered on MTs, is released upon depolymerization to activate RhoA, stimulating myosin II–driven contractility via ROCK activation and thus, participating to FAs stabilization. On the other hand, MT polymerization activates Rac1 via specific GEFs, promoting protrusive activity at the leading edge [96, 94, 95].

Dynamic targeting of FAs by MTs triggers adhesion relaxation and disassembly through kinesin-dependent delivery of factors such as APC, and via FAK–Src–paxillin signaling cascades that regulate both MT stability and FA turnover [96, 94, 95].

Through these coupled mechanical and signaling functions, MT growth and shrinkage balance actin dynamics, contractility, and adhesion turnover; thereby sustaining polarity and directed cell migration.

1.4.3 Organelle positioning

Establishing and maintaining cell polarity requires the coordinated organization of intracellular organelles—particularly the Golgi apparatus and the centrosome—along the axis of protrusion [97]. The nucleus–Golgi axis typically aligns with the leading edge, supporting polarized vesicular trafficking toward protrusions with a delay of 20 min (Figure 1.18,A)[98]. Disruption of this axis or vesicle delivery reduces migration persistence, even when protrusion speed remains unaffected [84, 99]. Recent reviews emphasize that organelle positioning is an active, regulated process—rather than a passive one—and is essential for directional migration[100]. Within motile cells, organelles are actively transported, anchored, and spatially organized to reinforce front–rear identity (Figure 1.18,B).

Nucleus and MTOC–Golgi axis

In mesenchymal cells, the microtubule-organizing center (MTOC), often associated with the centrosome, repositions anteriorly toward the leading edge, ahead of the nucleus. The Golgi aligns with this relocated MTOC, organizing a radial microtubule network that directs vesicle trafficking toward the front. Concurrently, the nucleus shifts rearward. This coordinated architecture enables efficient delivery of Golgi-derived cargo required for membrane extension and sustained polarized migration (Figure 1.18)[84, 97].

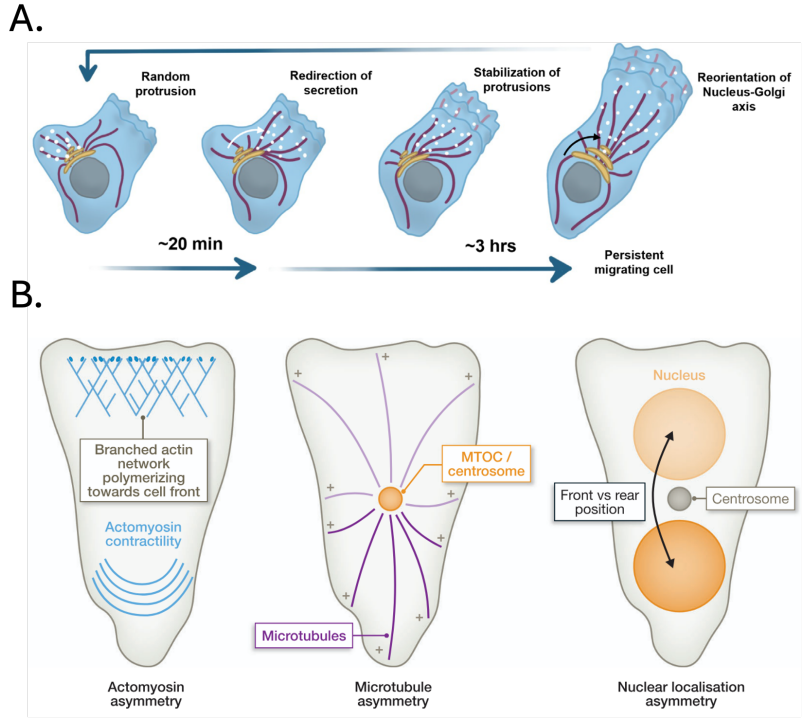

Figure 1.18: *Organelle repositioning and cytoskeletal asymmetry during establishment of front–rear polarity in migrating cells. (**A.**) Schematic of polarity establishment over time. Cells initially display random protrusive activity and unpolarized secretion. Within ∼20 minutes, secretion is redirected toward a dominant protrusion, which is then stabilized. Over a period of ∼3 hours, the Nucleus–Golgi–MTOC axis aligns along the direction of migration.(**B.**)Intracellular asymmetry underlie polarized migration: (1) asymmetric actomyosin contractility with a branched actin network oriented toward the front and cortical contraction at the rear, (2) polarized microtubule network emanating from the centrosome/MTOC toward the leading edge, and (3) spatial separation between the centrosome and nucleus along the migration axis, with the centrosome leading and the nucleus trailing. Adapted from [98, 100].*

Dynamic redistribution and polarity switching

Highly motile cells often generate multiple protrusions before selecting a dominant "winning" front. In these cases, the centrosome reorients into the selected protrusion, anchoring microtubules and stabilizing its cytoskeletal structure. Organelles within retracting branches are repositioned accordingly, reinforcing

polarity and allowing adaptive responses to environmental cues [101].

Positioning of the nucleus, centrosome/MTOC, Golgi apparatus, mitochondria, and lysosomes is mediated by cytoskeletal and anchoring mechanisms that align organelles with either the leading or trailing edge, depending on functional needs. This spatial organization governs energy supply, vesicle transport, contractility, and mechanical interactions with the extracellular matrix, thereby supporting persistent and adaptive polarized migration [84, 100].

1.4.4 Front–rear coupling

Persistent directional migration requires tight coupling between membrane protrusion and organelle polarity. Protrusive signaling via Cdc42/Rac1 shapes the internal axis (nucleus–Golgi alignment), while polarized trafficking from the Golgi reinforces protrusion stability. This bidirectional feedback connects protrusive initiation with axis reorientation, thereby governing persistence and directionality [102].

Mechanical coordination across the cell further contributes to polarity maintenance. Optogenetic activation of actin-driven protrusion or Rho-mediated contractility showed that cortical force generation rapidly increases global membrane tension within less than one second (Figure 1.19). In contrast, direct mechanical force applied to the plasma membrane—without engaging the actin cortex—failed to induce this effect (Figure 1.19,A). These findings support a model in which cortex-generated forces propagate through the membrane, integrating local protrusive and contractile events into a unified cell-scale response [103].

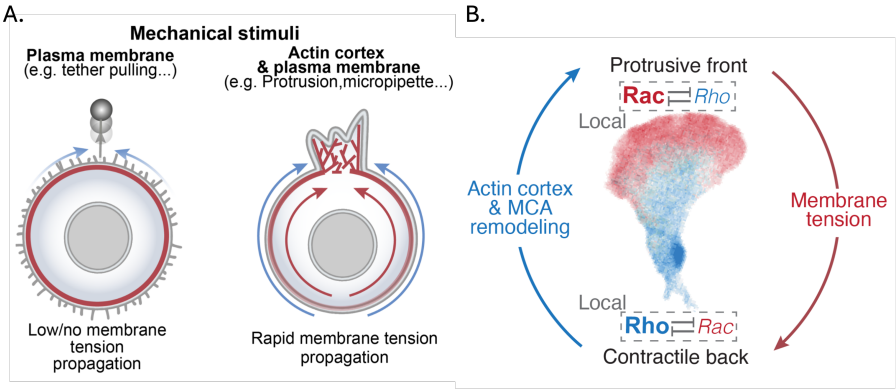

Figure 1.19: *Long-range front–rear coupling via membrane tension propagation and Rho GTPase crosstalk. (**A.**) Comparison of mechanical stimuli affecting membrane tension propagation. Tether pulling on the plasma membrane alone results in minimal or no long-range propagation of membrane tension. In contrast, mechanical stimulation that deforms both the plasma membrane and the underlying actin cortex such as a protrusion leads to rapid, global propagation of membrane tension across the cell surface. (**B.**) Schematic of feedback loop between membrane tension and cortical actin remodeling. Local activation of Rac at the leading edge and Rho at the rear establishes a front–rear polarity. Localized actomyosin-driven events induce global increases in membrane tension that propagate through the actin cortex, facilitating the reinforcement of Rac–Rho polarity. Adapted from [103, 104].*

Cortical force propagation also modulates Rho GTPase activity: local Rac1 activation at the front promotes protrusion, while RhoA-mediated contractility enhances rear detachment and cortical tension (Figure 1.19B). In this framework, membrane tension acts as a fast, cell-spanning integrator that synchronizes Rac–Rho signaling between front and rear, thereby maintaining polarity and ensuring robust directional migration [103, 104, 62].

1.5 Spatially constrained cell migration

In vivo, cell migration rarely occurs on flat, homogeneous surfaces. Instead, cells typically migrate within geometrically and mechanically complex environments defined by tissue architecture and extracellular matrix organization. Migration spans a continuum of spatial contexts, from one-dimensional (1D) tracks to fully three-dimensional (3D) matrices (Figure 1.20) [105, 106].

1D and 2D migration: One-dimensional migration occurs along narrow, linear substrates—such as collagen fibers or microfabricated lines—where the cell elongate and follow a predefined path. Two-dimensional (2D) migration, widely studied in vitro, occurs on planar surfaces such as culture dishes or epithelial layers. This mode is physiologically relevant to processes such as wound re-epithelialization and leukocyte scanning behavior along endothelial surfaces (Figure 1.20,A) [107].

2.5D migration: Intermediate "2.5D" environments include migration along tissue interfaces (e.g., between muscle fibers or adipocytes) or ECM-coated micropatterns. These contexts combine the flatness of 2D substrates with the topographic complexity and partial confinement of 3D tissue environments [108].

3D migration: Three-dimensional migration is the most physiologically representative mode, where cells must navigate through dense ECM networks or compact tissues. These environments impose mechanical constraints such as narrow pores, variable stiffness, and matrix anisotropy [109]. Unlike in 2D settings, cells in 3D must deform, squeeze, or switch migration strategies to overcome spatial constraints (Figure 1.20,B).

Under confinement, migration becomes increasingly dependent on the integration of intrinsic mechanical properties and environmental cues. Cells adapt by switching among migration modes—mesenchymal, amoeboid, lobopodial, or collective—depending on ECM structure, pore size, stiffness, and adhesiveness (Figure 1.20,C).

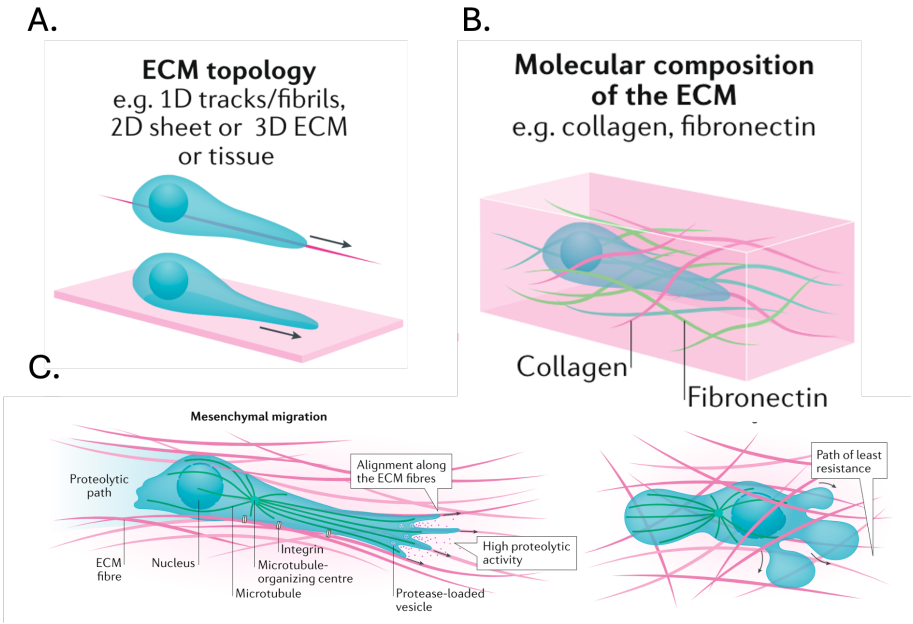

Figure 1.20: *Environmental and cellular determinants of 3D migration modes.* ***A.*** *ECM topology includes one-dimensional (1D) fibrillar tracks, two-dimensional (2D) planar surfaces, and fully embedded three-dimensional (3D) tissue environments. Cells adapt their shape and migration strategies to these spatial geometries.* ***B.*** *Molecular composition of the ECM, such as collagen and fibronectin networks, modulates integrin engagement, signaling, and matrix degradation.* ***C.*** *Cells use distinct migration strategies based on ECM properties. In mesenchymal migration (bottom left), cells elongate and align along ECM fibers, polarizing organelles (MTOC, nucleus) and secreting protease-loaded vesicles to degrade ECM and create paths of least resistance. This migration mode relies heavily on integrin–ECM interactions and microtubule-dependent trafficking. In contrast, in confined 3D environments, cells may switch to amoeboid migration (bottom right), in which they deform and squeeze through ECM gaps without significant proteolysis, navigating primarily via mechanical sensing and actomyosin contractility to find the path of least resistance. Adapted from [110]*

1.5.1 Cell migration modes

Migration modes were first described based on morphology, but modern classifications incooporate cytoskeletal architecture, force generation, and cell–ECM interactions. The key distinction lies between individually cell migration—amoeboid or mesenchymal strategies—and collectively migration, where cells remain interconnected [110].

Amoeboid migration (Figure 1.21A): Amoeboid cells are weakly adhesive and adopt rounded or ellipsoidal shapes. Two subtypes exist: (1) bleb-driven migration, powered by intracellular pressure, and (2) actin-rich filopodial protrusions engaging weak ECM contacts. Amoeboid migration typically involves low adhesion, minimal protease activity, and strong RhoA–ROCK–Myosin II contractility. Bleb-based movement is particularly suited to confined or low-adhesive environments and is largely independent of integrins or ECM remodeling [111].

Mesenchymal migration (Figure 1.21B): This mode relies on lamellipodia or filopodia at the front, driven by Arp2/3-mediated actin polymerization, and a contractile uropod at the rear. Migration proceeds through five coordinated steps: protrusion, adhesion, ECM remodeling, contraction, and retraction. Matrix degradation via proteolysis (e.g., Matrix metalloproteinase—MMPs) enables cells to overcome physical barriers, a hallmark of mesenchymal migration in 3D environments. Blocking proteolysis often forces cells to switch to amoeboid motility [112].

Lobopodial migration (Figure 1.21C): This intermediate mode features cylindrical, blunt protrusions (lobopodia) driven by nuclear piston-like movement[113]. It arises under conditions of high contractility and intermediate adhesion, with limited dependence on proteases. The nucleus and centrosome are centrally positionned and reinforced by a vimentin cage, which helps to generate pressure gradients that drive nuclear translocation and forward protrusion [95]

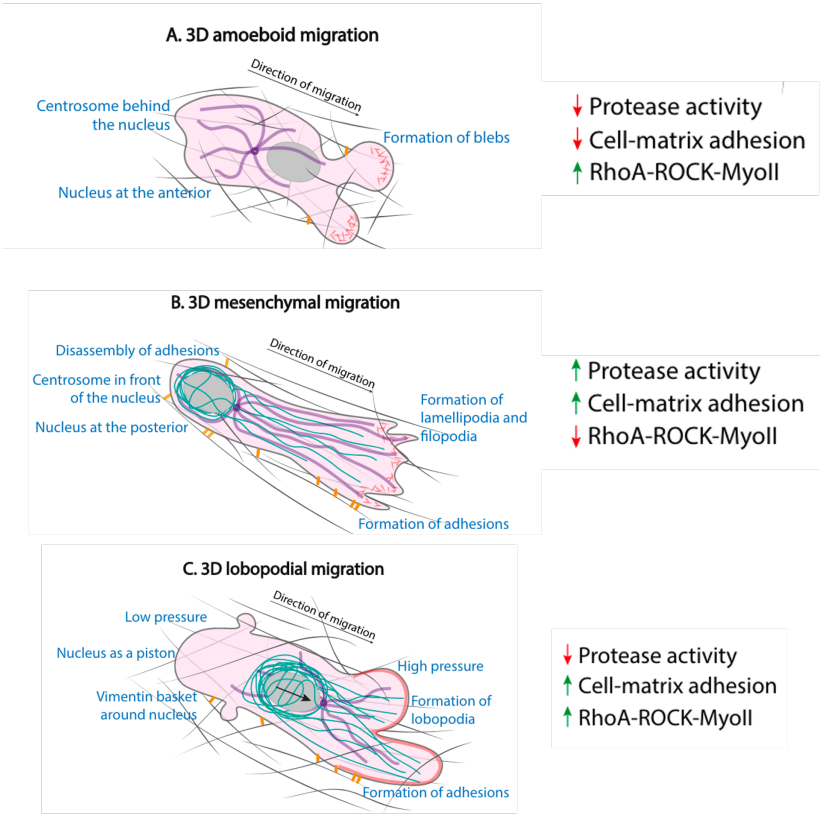

Figure 1.21: *Comparison of distinct 3D migration modes.* ***A. Amoeboid migration:*** *Characterized by bleb-based movement with low adhesion and minimal proteolytic activity, driven by high cortical contractility (RhoA–ROCK–Myosin II).* ***B. Mesenchymal migration:*** *Involves the formation of lamellipodia/filopodia, strong adhesion, and high matrix degradation, but lower actomyosin contractility.* ***C. Lobopodial migration:*** *Relies on pressure-driven protrusions (lobopodia), high RhoA–ROCK–Myosin II activity, and strong adhesion, with the nucleus acting as a piston.*

Collective Migration: Cells migrate as cohesive groups while maintaining intercellular adhesions. Leader cells generate protrusive and contractile forces, while follower cells reinforce cohesion through cadherins and coordinated actomyosin contraction[114].

Although most mechanistic insights derive from 2D systems, migration in 3D is far more representative of in vivo contexts. Within tissues, cells encounter heterogeneous microenvironments that demand a high degree of adaptability. Importantly, cells exhibit migration plasticity—the ability to switch between modes in response to environmental changes [115]. A competence cells must exploit in vivo to adapt and remain motile. Understanding how cells navigate these complex landscapes is fundamental for processes such as development, immune surveillance, and cancer invasion [109, 93].

We have summarized the mechanisms underlying persistent cell migration, emphasizing the integration of cytoskeletal dynamics, organelle repositioning, and spatiotemporal signaling. We highlighted how microtubules, actomyosin contractility, and membrane tension coordinate front–rear polarity with intracellular organization. Finally, we examined how physical constraints in 3D environments influence migratory modes, underscoring the remarkable plasticity that allow cells to adapt to diverse extracellular architectures and mechanical challenges. Together, these insights provide a comprehensive framework for understanding how cells preserved directionality and coherence during migration in complex environments.

In the following chapters of this thesis, these insights will serve to investigate the mechanisms by which epithelial cells migrate within highly confined environments and to explore the hypothesis that the establishment of a mechanical memory may promote efficient migration through extracellular matrices characterized by alternating constricted and dilated regions.

CHAPTER 2

STATE OF THE ART

Over the past decades, advances in cell mechanobiology has improved our understanding of how mechanical confinement regulates cell migration[110]. In vitro assays that recapitulate the physical constraints of the in vivo microenvironment have demonstrated that cells rely on active force generation, mechanosensing pathways, and cytoskeleton remodeling to navigate confined spaces [116, 117, 118]. Consistent with in vivo observations, it is now well-established that cells dynamically adapt both their morphology and mode of migration in response to external physical constraints imposed by their surrounding environment[119]. However, the mechanism by which cells switch between shapes and migratory behaviour in response to environmental stimuli remains incompletely understood.

This capacity for adaptive switching, commonly referred to as "migratory plasticity", is a hallmark of metastatic cancer cells. Emerging evidence highlights mechanical memory as a crucial facet of this adaptive behavior [120]. Mechanical memory refers to a cell's ability to retain biophysical adaptations from past mechanical stimuli and modulate future responses accordingly. While numerous studies have shed light on the establishment of mechanical memory over long timescales [120, 121], most of them have focused micro-environmental cues such as matrix stiffness and topography. In contrast, the impact of physical confinement and whether it can induce mechanical memory over short timescales—remains largely unexplored.

2.1 In vivo confined cell migration

Confined cell migration is a fundamental biological process underpinning embryonic development, immune surveillance, and tumor progression. In particular, tumor metastasis relies critically on the ability of cancer cell to migrate through physically confined anatomical structures[122]. Despite its major clinical importance, metastasis remains poorly understood due to its complexity and inherent inaccessibility of the tumor microenvironment for direct observations [123]. On their way to target sites, invading tumor cells face a variety of versatile environments.

A systematic understanding of the strategies of how cells perceive and navigate these constraints is necessary to decipher the principles behind their motility and plasticity.

These challenges have motivated growing efforts to characterize the physicochemical microenvironment encountered by metastasizing cells. In the following section, we review foundational studies that employed in vivo tissue imaging to investigate confined cell migration and identify key environmental elements guiding these behaviors.

2.1.1 Spatial confinement and directional cues in vivo

The visualization of confined cell migration in dense tissues has been greatly facilitated by recent advances in deep-tissue, time-lapse imaging, particularly through the development of intravital microscopy[124, 125, 126]. These techniques have revealed the clinical relevance of structurally confined migration pathways, such as aligned fibrous tracks and tumor stroma interfaces.

Peter Friedl's group has extensively used intravital microscopy to uncover mechanism of cell migration plasticity. Using this technique, they have generated valuable data by imaging melanoma cells invasion through the mice dorsal skin [127]. They identified two major categories of topographic migration routes employed by invading mouse melanoma cells (Figure 2.1,A)[127].

- The first category is characterized by discontinuous, loosely confined spaces within random fibrillar collagen networks (Figure 2.1,A1-A2), comprising trails of thin fibrils or thicker fibers bundles that enclose discontinuous inter fibril spaces ranging from ∼5 to 30 μm in diameter. These structures support the invasion of single cells as well as weakly connected stream of cells oriented in the direction of the matrix structure (Figure 2.1,A).
- The second category is characterized by irregular or linear tracks identified within fat tissues and formed by interfaces between neighboring adipocytes, basement membranes, myofibers or bundled collagen fibers

(Figure 2.1,A3-A4), creating irregular 3D slit-like cavities of 2-10 μm diameter that promote collective migration.

Overall, these findings suggest that migrating cells experience a multidimensional physical landscape composed of 1D, 2D and 3D structural scaffolds, varying in alignment and density—that collectively shape in vivo migratory routes[127].

2.1.2 Tissue remodeling and track formation in vivo

These scaffolds may either arise from pre-existing tracks and trails created by anatomical structures or naturally emerge from dynamic remodeling of the tissue matrix. Comparison between tumor-free tissues and tumor cell containing tracks allowed to estimate the extent of this remodeling. Near-identical cross-section of tumor-free tracks and infiltrating tumor cell bodies were observed during melanoma invasion of collagen networks, perineural, and adipose tissues, suggesting a small contribution of microscopic tissue deformation in that case [127].

In contrast, Ilina et al. observed in breast cancer models that both tumor-free and tumor-associated tracks exhibited marked widening, driven by a combination of mechanical deformation and proteolytic matrix remodeling (Figure 2.1,B)[125]. These observations corroborate earlier studies showing that collagen reorganization, particularly at the tumor-stromal interface, facilitates local invasion[128] and correlates with metastatic risk in breast cancer[129].

2.1.3 In vivo mimicking strategies

In vitro assays replicating the conditions of aligned collagen matrices similarly demonstrate that intravasation of metastatic breast cancer cells was enhanced by orientated fibers[130]. A recent study that decoupled collagen fiber alignment from matrix tension found that cells preferentially migrate along the axis of highest tension, rather than merely along alignment, suggesting that cells seek path that minimize the energy required to deform the matrix[131].

Other in vitro platforms using aligned fibrillar networks have revealed a bimodal, switch-like migration behavior: cells alternate between moving parallel

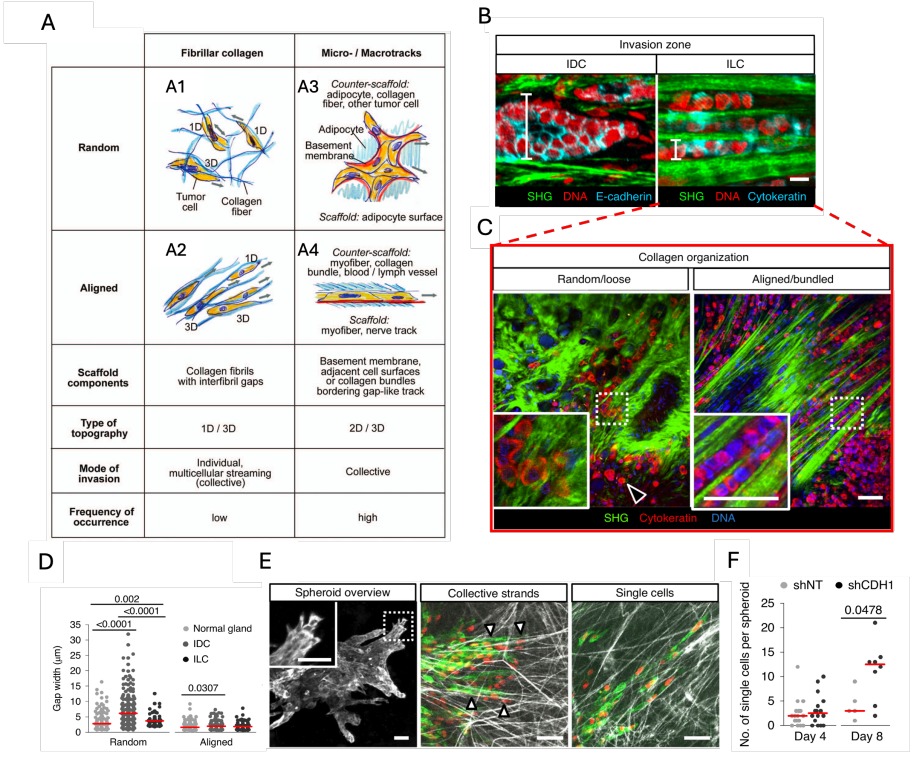

Figure 2.1: *Modes of tumor cell invasion in vivo and their classification. (A) Schematic representation of invasion modes in fibrillar collagen (A1–A2) and micro-/macrotracks (A3–A4), comparing random versus aligned matrix organization. Scaffold components, topographies, invasion modes, and frequencies of occurrence are summarized. (B) Representative images of the invasion zone in invasive ductal carcinoma (IDC, left) and invasive lobular carcinoma (ILC, right), showing differences in collagen organization and epithelial markers (SHG: green; DNA: red; E-cadherin or cytokeratin: cyan). Scale bar, 10 µm. (C) Images of collagen organization in tumors, comparing random/loose versus aligned/bundled architectures. Insets highlight tumor cell–collagen interactions. Scale bar, 50 µm. (D) Quantification of inter-fibrillar gap widths in normal glands, IDC, and ILC across random and aligned collagen organizations. (E) Spheroid invasion assays illustrating collective invasion through aligned bundles versus dissemination of single cells into collagen. Scale bar, 50 µm. (F) Quantification of single-cell dissemination per spheroid in shNT (control) and shCDH1 (E-cadherin knockdown) conditions at day 4 and day 8. Scale bars: 20 µm unless otherwise indicated. Adapted from [125] and [127].*

or perpendicular to fibers alignment, depending on the organization of their cytoskeletal network. Key player in the f-actin architecture regulation were identified. Specifically, formins-mediated linear actin networks promote migration parallel to fibers, whereas Arp2/3-driven branched actin networks supports perpendicular migration [132].

These minimalist discrete systems, with controlled microstructure and fiber stress states, have provided key mechanistic insights into how extracellular physical cues govern both collective and single-cell migration.

2.1.4 In vivo migratory strategies

Tissue remodeling is an important aspect of breast cancer metastasis, mediated through proteolytic matrix degradation, mechanical deformation, and collagen realignment. These processes generate permissive tracks that support both collective and single-cell migration. Collective invasion often initiates matrix remodeling after which single cells may detach and disseminate along the newly formed paths. The stromal architecture, its density, alignment, and composition, dynamically regulates the balance between collective and individual migration mode. In fact, tumor invasion and metastasis are not solely collective phenomena. Indeed, they also rely on the capacity of individual cancer cells to detach and migrate through the extracellular matrix. The intrinsic property of tumors such as its epithelial or mesenchymal character is determinant of its invasion mode. Epithelial tumors predominantly adopt collective invasion, wherein sustained cell-cell adhesions allow coordinated movement of cell clusters[133]. While mesenchymal tumors, often subjected to high tissue confinement, form invasive multicellular clusters with low-cohesiveness, which results in individualized and scattered invasion patterns [133, 134].

Multiphoton microscopy of multicellular spheroids implanted into mice mammary fat pad has revealed that invasive lobular carcinoma (ILC) samples, unlike invasive ductal carcinoma (IDC), shows a distinct pattern of cell individualization (Figure 2.1,B-C) [125]. This behavior stems from the weakening of E-cadherin-mediated adherens junctions, a hallmark of ILC progression[135]. These regions often contain distinct invasive zones associated with randomly

organized and aligned collagen fibers (Figure 2.1,C). These regions are characterized by subset of fully individualized cells and thin multicellular strands, both expressing cytokeratin, markers of epithelial origin and disease progression (Figure 2.1,B-C). In both tumor-free and peritumoral stroma, gap widths between ECM fibers range from 0.7 to 32 μm but are smaller in regions of collagen alignment (Figure 2.1,D).

Experimental models using E-cadherin knockdown cells (4T1-shCDH1) have demonstrated that individual cells are capable of migrating through regions of reduced porosity. These findings suggest that dowregulation of E-cadherin facilitates migration through more confining environments by enabling cells to deform and squeeze through smaller ECM pores (Figure 2.1,E-F)[125].

Analogous to glassy materials, cellular monolayers are known to undergo a jamming-unjamming transition, which describes a reversible switch from a solid-like, low motility state to a more fluid-like, dynamic state often regulated by cell density[134]. Ilina et al. demonstrated that this transition is not governed by density alone but also by the interplay between three-dimensional spatial restriction and the stability of cell-cell junction [125]. This transition is often interpreted as a key mechanism by which otherwise stationary epithelia monolayer initiate migratory behavior.

Recent work from La Porta's group introduced a novel theoretical framework, inspired by liquid crystal physics, to interpret collective cell migration in vivo. Using intravital microscopy of metastatic progression in deep dermis of mice, they revealed the emergence of dynamic cellular flow patterns within confined interstitial spaces, reminiscent of active nematic turbulence [126]. These flow organized into persistent antiparallel cell tracks were reminiscent of organized flow patterns due to confinement, a well-established phenomenon in active matter[136]. The authors developed a model of active nematic fluids turbulence allowing to make insightful predictions, further confirmed by experiments. In agreement with experiments and theory, the persistence time —a measure of cellular flow stability— is inversely proportional to the channel width, highlighting the relevance of the spatial confinement. Together, these results reveal that confined migration in vivo occurs in a turbulent regime,

driven by spatial confinement and a loss of intercellular cohesion that disrupts nematic order[126].

Further intravital observations revealed that carcinoma cells within metastatic tumors exhibit their highest migration velocities when moving along linear ECM fibers, emphasizing the role of ECM architecture in guiding single-cell movement [124]. These cells displayed a strong tendency to align their migration with pre-existing topographies [124]. Importantly, physical confinement and matrix alignment act as instructive biophysical cues that steer both collective and single-cell migration in vivo. However, the intracellular signaling pathways that mediate these effects remain to be fully elucidated.

2.2 Impact of confinement on cell migration

In vivo, spatial confinement resulting from tissue crowding and ECM geometry shapes cell migration, invasion, and cell fate decisions. These spatial restrictions emerge with complex 1D, 2D, and 3D architecture, making it challenging to observe and decipher the mechanism of migration. To overcome this, in vitro micropatterning approaches—first introduced by chemist George Whitesides and later adapted for biological systems—have been developed [137, 138, 139]. These platforms consist of micrometer-scale adhesive protein islands of defined shape and size, allowing precise control of cell spreading area, specific ECM interactions, and global geometry. The present work builds on a broad body of literature using such microfabricated tools to investigate confined migration across multiple scales.

In the sections that follow, we first explore how lateral confinement modulates coordinated collective movement of epithelial cells. Then, we examine how spatial restriction affects individual cell speed, morphology, and migration dynamics. Finally, we conclude with a focus on fiber-mimicking micropatterns as a platform to study high-speed directional migration and discuss symmetry breaking at the onset of confined migration.

2.2.1 Confined migration with collective support

Physiological and pathological scenarios often involved small autonomous cell clusters navigating through complex environment. The size of these migrating clusters varies widely, from tens of cells in border cell migration of Drosophila, to hundreds of cells during the migration of zebrafish lateral line primordium [140]. In human epithelial cancers, polarized and persistent tumoral clusters containing as few as eight cells have been observed to invade collectively [141, 142]. Recent studies have begun to probe how confinement influences the efficiency, organization, and dynamics of such multicellular units.

Vercruysse et al. cultured fish scales with primary epithelial monolayers on fibronectin-coated stripes of varying widths (15 μm to 100 μm wide) to generate minimal migrating clusters (Figure 2.2,A) [143]. As these tissue migrated, they fragmented into cell strands and ultimately into organized trains of varying size and aspect ratio (Figure 2.2,B). Surprisingly, trains composed of 2–10 cells migrated at the same speed as individual cells on 15 μm-wide stripes, regardless of train length (Figure 2.2,C).

This observation suggest that maximum migration speed is constrained by intrinsic single cell properties. This observation raises important questions about whether other dynamic parameters, such as persistence and directionality, exhibit similar behavior when comparing single cells to clusters. These results challenge the classical leader–follower model, which assumes that traction forces are primarily generated by leader cells that drag followers forward [144]. Recent optogenetic studies indicate that while leader cells contribute to collective directionality, sustained migration requires global mechanical coordination throughout the cluster[145]. Moreover, the mechanosentivity of leader cells to aligned collagen appears crucial for the formation of finger-like protrusions that initiates collective invasion [146]. Within migrating trains, all cells maintained high mitochondrial activity and stable polarization over time (Figure 2.2,D), suggesting that each cell actively contribute to motion. In contrast, larger clusters with stronger intercellular adhesion accumulated contractile forces (Figure 2.2,F) and lateral stresses (Figure 2.2,G) perpendicular to the cell migration axis, which reduced migration efficiency (Figure 2.2,E). These cell trains relied

on cytoskeletal and organelle polarity, such as Golgi alignment (Figure 2.2,H), microtubule orientation, and the formation of cryptic lamellipodia to facilitate forward movement (Figure 2.2,I), forming compact, cohesive, and polarized units that move as fast as single cells [143].

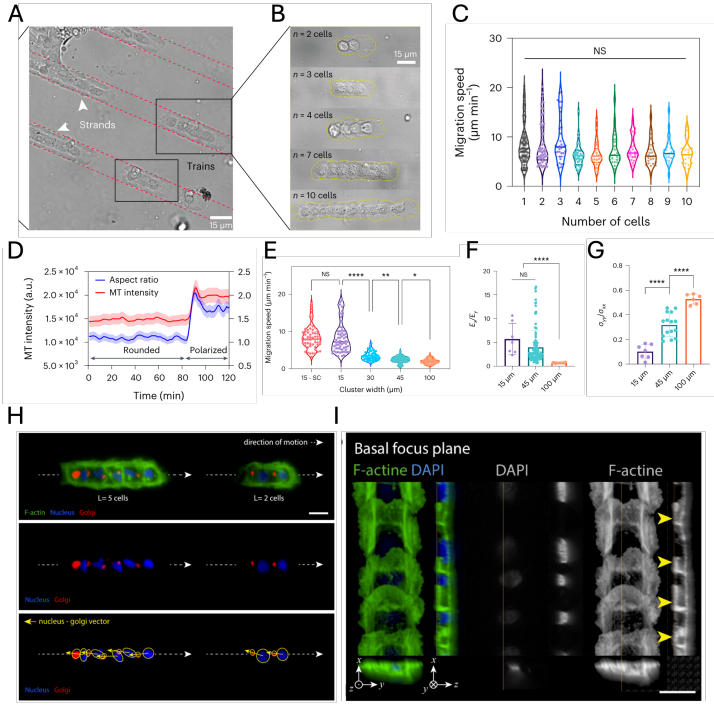

Figure 2.2: *Minimal cellular cluster dynamics in confined tracks. (A) Phase-contrast image of cell strands ("trains") migrating along micropatterned linear tracks (dashed red lines). (B) Representative examples of trains of increasing sizes (2–10 cells). (C) Migration speed as a function of the number of cells per train, showing no significant dependence. (D) Time-dependent evolution of cell aspect ratio and mitochondria (MT) intensity during transitions from rounded to polarized states. (E) Migration speed as a function of cluster width. (F–G) Quantification of the ratio between the axial (E_x) and lateral (E_y) components of the total strain energy and the ratio between the axial ($\sigma_x x$) and lateral ($\sigma_y y$) internal stress components for cell trains 15 µm wide (light purple) and epithelial clusters 45 µm wide (light green) or 100 µm wide (light orange). Force fluctuations increase with track width. (H) Immunofluorescence images of migrating clusters: F-actin (green), nuclei (blue), and Golgi (red), showing front–rear polarity and nucleus–Golgi alignment in migrating strands. (I) Basal-plane reveals actin-rich protrusions at the cell–substrate interface : cryptic lamellipodia (yellow arrowheads). Scale bars, 15 µm.*

Another study reported the extension of cryptic lamellipodia beneath adjacent cells confirming front-rear polarization as key to the coordinated rotational movement of epithelial cell trains (Figure 2.3,A-B). Such rotating movements are observed in vitro in cellular monolayers and in vivo in genital and follicular rotation [147, 148]. Jain et al. confined epithelial cells (MDCK) to one dimensional ring-shaped patterns and observed right after confluency the emergence of a persistent coordinated movement (Figure 2.3,A)[149]. This behavior depends on the strength of cell-cell junctions, which creates a mechanical continuum that promotes efficient force transmission. The maintenance of a rotating movement requires a Rac1-dependent front–rear polarity within each individual cell (Figure 2.3,A-B). Although, the initiation of coordinated rotational movement requires cell-cell junctions to establish, its maintenance does not require their continual integrity. This was evidenced by the maintenance of front-rear polarization in single cells breaking away from sub-confluent migrating trains (Figure 2.3,C). In contrary to isolated cells that struggle to acquire a polarized state, single cell that originate from trains retain the polarity axis and remain persistence (Figure 2.3,D).

These results suggest a potential memory of polarity that could support highly persistent migration. An open question remains: if the single encounters a more confined track, will it be able to maintain its directional movement while adapting to the confinement. In conclusion, being part of a monolayer appears to facilitate the establishment of a stable polarity axis and sustained persistence.

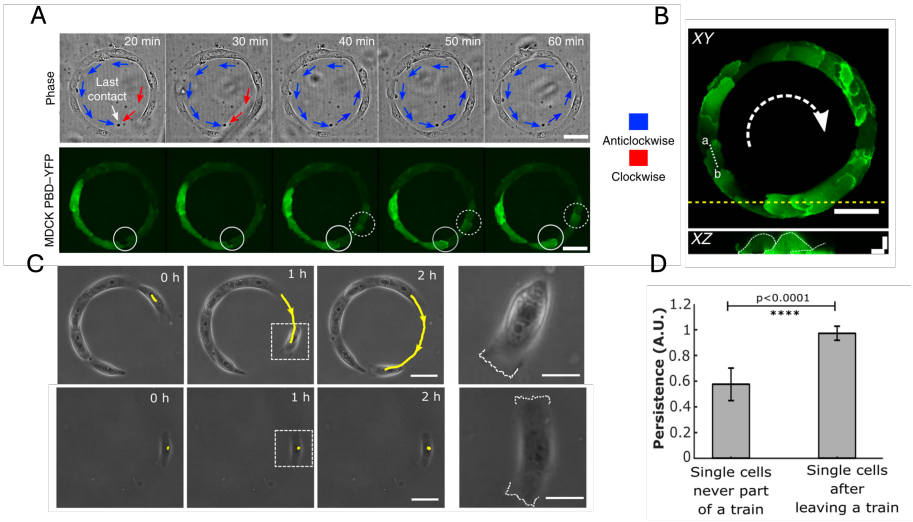

Figure 2.3: *Collective and single-cell coordinated dynamics on circular tracks. (A) Time-lapse sequence of MDCK cells migrating collectively on circular micropatterns. Phase-contrast images (top) show alternating clockwise (red arrows) and anticlockwise (blue arrows) rotations. Corresponding PBD–YFP biosensor signal images (bottom) highlight dynamic front–rear polarity within migrating trains. Scale bar, 50 µm. (B) Confocal microscopy of a migrating cell train (XY and XZ views) showing confinement within the circular track showing PBD–YFP biosensor signal distribution. Scale bar, 4 µm. (C) Phase-contrast images of cells migrating in circular tracks (top row: collective train; bottom row: single cells). Yellow arrows indicate migration trajectories of single cells, and magnified views (right panels) show edges of the cell protrusion(s) morphology. (D) Persistence of the cell movement for isolated single cells and single cells previously part of a sub-confluent train. Adapted from [149].*

2.2.2 Single cell migration under lateral confinement

To further investigate how individual cells respond to spatial confinement in the absence of a monolayer, the following section examines how spatial constraints influence migration speed and polarity. Within a crowded monolayer, cells are able to sense spatial confinement and adapt their migration speed to the available space.

Mohammed et al. studied the migration of individually migrating epithelial fish keratocytes on fibronectin micropatterns consisting of five interconnected stripes of varying widths (from 5 to 21μm) [64], mimicking a single cell escaping

from a monolayer (Figure 2.4,A-B). They found that migration speed decreased drastically with increased confinement (Figure 2.4,C). Cell velocity was directly correlated with the adhesive area of focal adhesions (Figure 2.4,D). Confined cells exerted approximately half the contractile stress of unconfined cells, which reached a plateau at around 9 kPa of total stress (Figure 2.4,E-F). Lateral confinement also altered the spatial distribution of traction of forces exerted on the substrate. Intense contractile forces, initially concentrated at the leading-edge region of confined cells, gradually shifted toward the trailing edge during the escape process (Figure 2.4,E).

In addition, to modulating the balance of forces and migration speed, confinement induces a change in 3D cell morphology (Figure 2.5,A-B). Thickening of the lamellipodia under confinement was associated with reduced protrusive forces and slower cell velocity (Figure 2.5,C). Later on, this morphological adaptation has been linked to decreased intracellular diffusion, which defines a fast and slow migration mode in keratocytes (Figure 2.5,D)[150]. Limited intracellular diffusion leads to increased molecular crowding (Figure 2.5,E-F). Slow membrane expansion at the leading edge, induced by dragging forces such as those measured by Mohammed et al., may allow more actin filaments, oriented over a wider angular range to maintain contact with the slowed membrane and continue polymerizing. This results in a denser actin network within the lamellipodium of slower-moving cells.

These two studies are complementary: the increased frontward traction forces observed by Mohammed et al. are consistent with the model proposed by Jiang et al., linking slowed membrane dynamics to molecular crowding and lamellipodium thickening [64, 150].

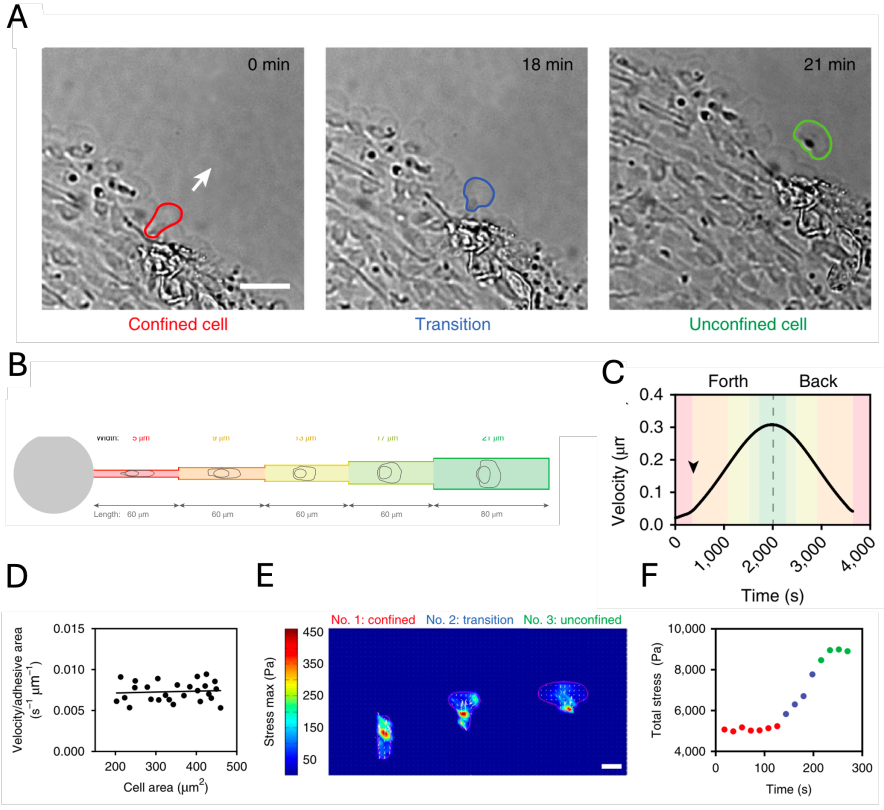

Figure 2.4: *Single cell migration during confinement escape. (A) DIC time series of a single keratocyte escaping from a tissue, showing three morphological stages: confined (red), through an intermediate state (blue) and unconfined migration (green). Scale bar, 30 µm. (B) Schematic of the confinement release assay featuring progressively widening channels. (C) Migration velocity profile over time, showing acceleration (forth motion) and deceleration phases (back motion). (D) Relationship between cell area and normalized velocity/adhesive area ratio. (E) Sequence of traction force maps of cells in confined, transition, and unconfined states, color-coded for stress magnitude. Scale bar, 15 µm. (F) Quantification of total traction stress over time, from confined (red) to unconfined (green). Adapted from [64].*

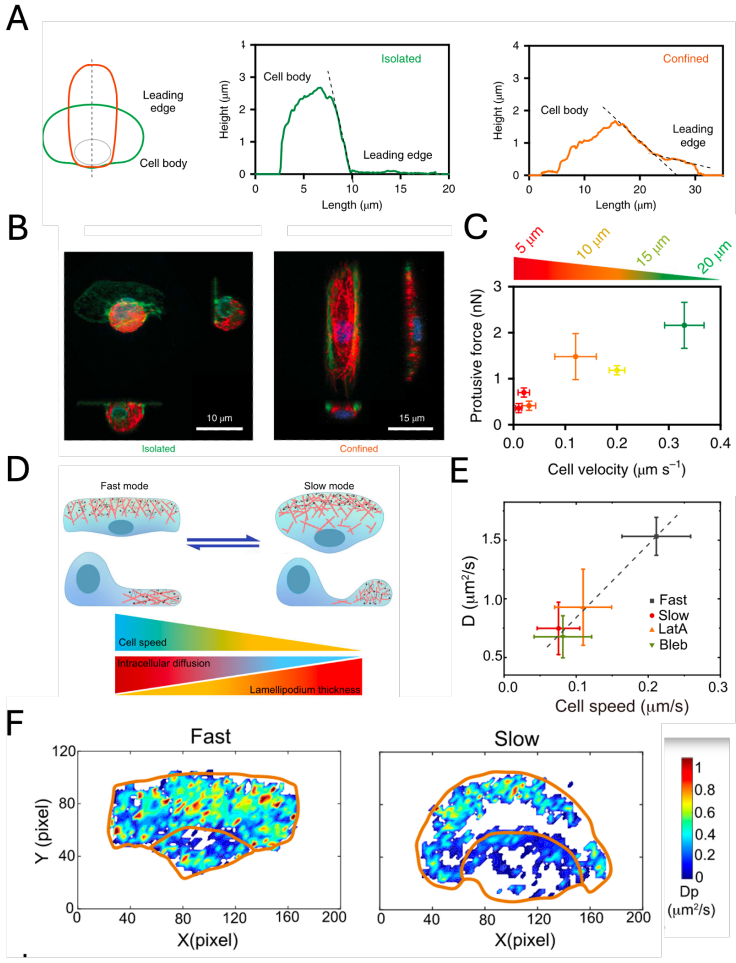

Figure 2.5: *Lamellipodia thickening during confined cell migration. (A–B) Schematic and cross-sectional profiles of isolated (green) and confined (orange) cells showing differences in height and leading-edge morphology. Representative fluorescence images illustrate isolated (left) versus confined phenotypes (right) (actin: green, nucleus: blue, microtubules: red). (C) Relationship between protrusive force and migration velocity across confinement widths (5–20 μm). (D) Model of fast versus slow migration modes for fish kerocytes, with corresponding changes in lamellipodium thickness, intracellular diffusion and cell speed. (E) Correlation between cell speed and intracellular diffusion coefficient (D), comparing fast, slow, Latrunculin A-treated, and blebbistatin treated cells. (F) Diffusion maps of fast- and slow-migrating keratocytes, color-coded for local diffusion coefficient (Dp). Scale bar, 10 μm (isolated), 15 μm (confined). Adapted from [64] and [150].*

2.2.3 Confined migration on two-state systems

Whether in physiological or pathological context, single migrating cells face common physical challenges. What distinguishes them is their ability to adapt based on unique cytoskeletal architecture and signaling regulation. One such recurring scenario is the alternation between cycles of confinement and release, which requires dynamic cytoskeleton remodeling to maintain directed migration.

Brückner et al. have developed a minimal system to investigate the dynamics of confined cell migration in structured environment using both invasive mesenchymal and normal epithelial mammary cells [151]. This system consists of two-state micropatterns: two adhesive islands connected by a thin adhesive bridge, enabling cells to perform repeated stochastic transitions between the two sites (Figure 2.6,A). Entry into the narrow bridge promotes protrusion formation, which is sustained until the cell reaches the opposite island (Figure 2.6,B). The dwell time—defined as the time between successive transitions—follow a broad distribution, reflecting both intercellular heterogeneity and intrinsic fluctuations at the single cell level (Figure 2.6,C).

Remarkably, despite the variability inherent to living cells, the authors extracted an emergent dynamical law under control boundary conditions from a large set of single-cell trajectories. The inferred equation of motion separates deterministic[1] and the stochastic[2] components contributing to migration. Cells deterministically initiate migration into the thin bridge, and their motion is further accelerated by intrinsic noise, with a characteristic timescale τ governed by the bridge length. This time scale was found to scale linearly with the bridge length (Figure 2.6,D). Interestingly, nuclear translocation often the rate-limiting process— accounted only for 30% of the increase suggesting that cells crossing longer bridges also spend more time on the island. This finding raises intriguing questions about how bridge geometry influences the internal cellular machinery and the capacity to reestablish front-rear polarity.

[1]Deterministic, describes a process or system in which outcomes are fully determined by initial conditions, with no randomness involved.

[2]stochastic, refers to a process that involves randomness or probability, where outcomes cannot be predicted with certainty but instead follow statistical distributions.

Both MDA-MB-231 and MCF10A cells exhibited a deterministic driving force that guided them through the thin constriction[151]. This behavior likely reflects the interplay between the microscopic cytoskeleton machinery and intracellular signaling, modulated by stochastic fluctuations, and varying across cell types. Such micropatterned platform thus offer a powerful approach to discriminate between cell types of different invasiveness and provides a versatile framework for studying migration dynamics under more complex and physiologically relevant constraints.

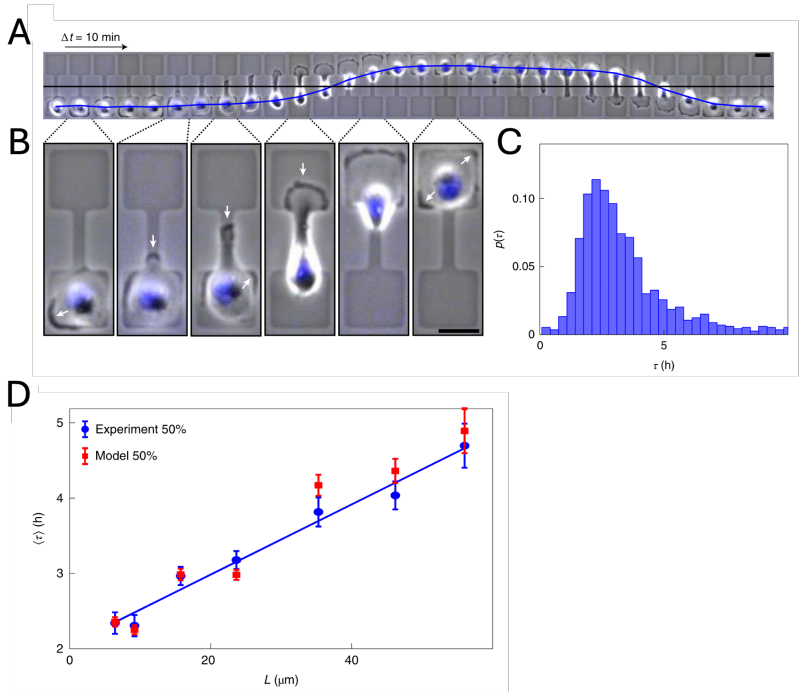

Figure 2.6: *Single cell migration on two-state micropatterns (A) Time-lapse sequence of a single-cell track on a micropattern with bridge length $L = 35$ μm, the nucleus is in blue. Scale bar, 25 μm. (B) Magnifications showing the transition process through the bridge. White arrows indicate the direction of protrusion extensions. (C) Probability distribution of residence times, τ (defined as the time between subsequent transitions of the cell nucleus across the bridge centre). (D) Linear scaling of the mean residence time $\langle\tau\rangle$ as a function of constriction length (L), comparing experimental data (blue) with model predictions (red). Adapted from [151].*

Work from the same group introduced additional complexity by employing asymmetric micropatterns and anisotropic island shapes to study cell migration dynamics [152]. These geometrical features led to asymmetric occupancy, with cells exhibiting longer dwell times on larger adhesive area (Figure 2.7,A), indicating a tendency to exit more confined regions. Anisotropy-introduced through triangular and diamond-shaped islands biased both the spatial distribution of adhesive contacts and actin distribution (Figure 2.7,B). In contrast, vertically oriented rectangular islands influenced the alignment of stress fibers and were associated with shorten dwell times (Figure 2.7,C).

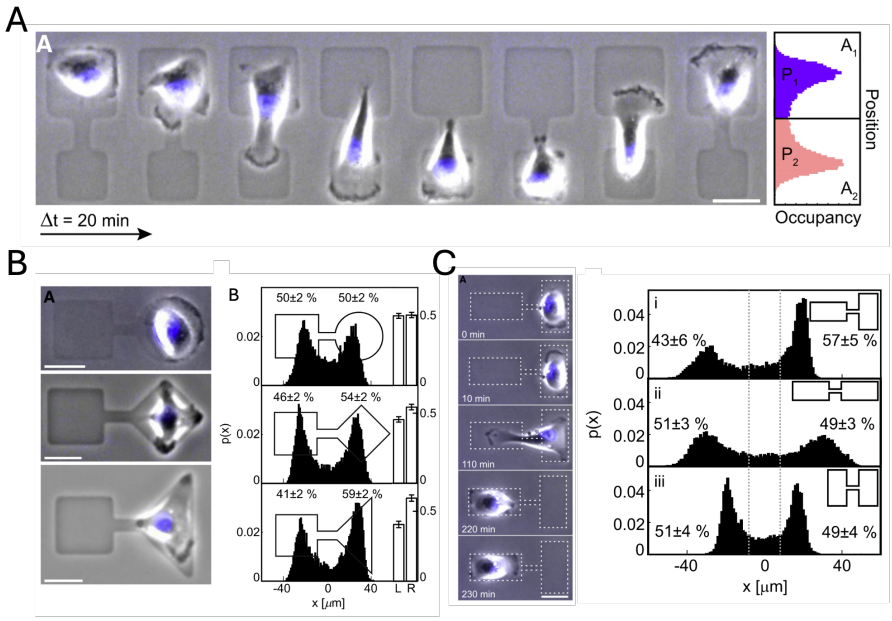

Figure 2.7: *Area and geometry dependence on two-state micropatterns. (A) Time-lapse sequences of a single MDA-MB-321 cell migrating between two distinctly sized square sites. The right panel shows the nuclear position probability distributions (P_1, P_2) on two stable occupancy sites (A_1, A_2). (B) Representative examples of MDA-MB-321 cells confined to different pattern geometries (A,top to bottom) and corresponding left/right occupancy distributions. Bar plots indicate left/right occupancy fractions. (C) Time-lapse sequence of a confined cell transitioning between rectangular micropatterns of orthogonal orientation. Dotted boxes highlight pattern edges. Right, probability distributions and left-right occupancies on two-state patterns with equally sized but differently oriented rectangles (i–iii). Scale bars, 25 μm. Adapted from [152].*

These findings highlight the pivotal role of adhesive island geometry in guiding cytoskeletal remodeling, which in turn modulates the probability of transition between islands. This work also identifies the conditions that favor more efficient transient migration through narrow passages[152].

2.2.4 1D lines that mimic fibrillar migration

Further reducing the width of micropatterned stripes brings us to a category referred to as one-dimensional (1D) lines. Previous studies have revealed that 1D cell migration could recapitulate the cellular morphology observed during 3D cell migration on suspended fibers (Figure 2.8,A) [153, 154]. In addition, Doyle et al. revealed that both migration mode share common features such as fast and directional migration, contractile dependent migration, microtubule-dependent migration, posterior centrosome position, independent matrix ligand density[153].

Guetta-Terrier et al. compared two reductionist approaches that can mimic 3D fibrillar migration: 1D micropatterned lines and 3D electrospun polycaprolactone nanofibers (Figure 2.8,B)[155]. Interestingly, mesenchymal cells migrating on 4 μm-wide line and 1.3 μm wide fibers presented similar cellular morphology and an average migration speed of $\sim 40 \mu$m/h (Figure 2.8,C). Migration on fibers was characterized by the formation and propagation of wave-like cellular protrusions (Figure 2.8,D). These actin-based protrusions originated from the leading edge and were transmitted to the back of the cell through actomyosin contractility allowing force generation. Thus, efficient forward translocation requires the right balance between contractility and protrusion (Figure 2.8,E). Cells generate these waves through balanced activation of the Rac1/N-WASP/Arp2/3 and Rho/formins pathways (Figure 2.8,D). Lateral actin-based waves have been observed in various cell types, indicating that they constitute a common mechanism of fibrillar migration[155].

The observed efficiency of fibrillar migration highlights the need to deepen our understanding of contact guidance sensing mechanism. To address this, Tabdanov et al. developed engineered nanotextured platforms with tunable stiffness to mimic aligned extracellular matrix fibers [156]. They demonstrated

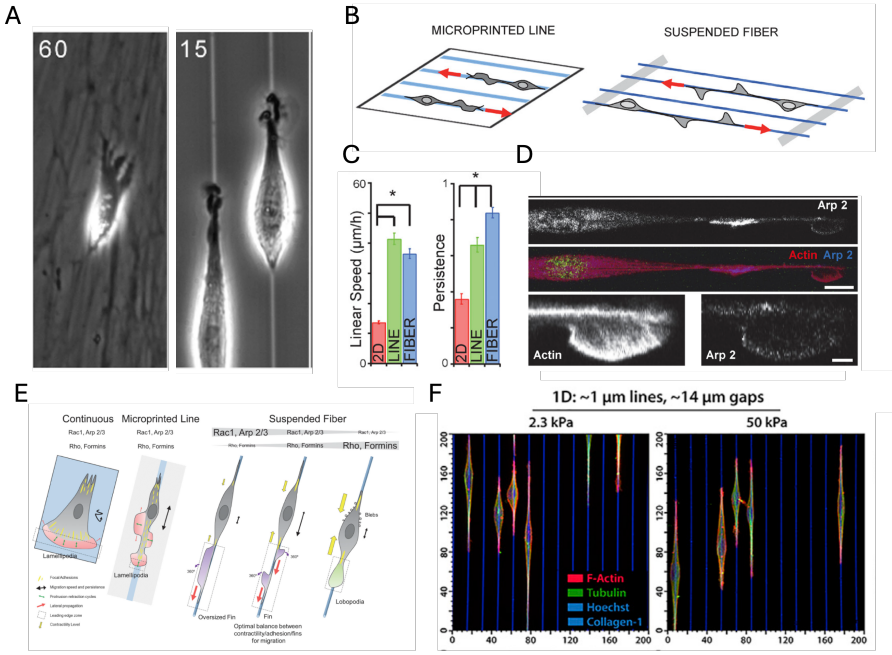

Figure 2.8: *1D confined cell migration dynamics. (A) Phase-contrast images of fibroblast cells migrating through a 3D cell-derived matrix (left) and a 1.5 µm microprinted lines (right). (B) Schematic illustrating differences between micropatterned lines and suspended fibers.(C) Quantification of linear speed (left) and persistence (right) for continuous surface (red), line (green), and fiber (blue) (*$p < 0.05$). (D) Fluorescence imaging of GFP-actin (red) and mCherry-Arp2/3 (blue) distribution on fibers. scale bar, 10 µm.(E) Schematic summary of actin regulators (Rac1, Arp2/3, Rho, Formins) driving distinct protrusion dynamics and migration strategies on 2D substrates, microprinted lines, and suspended fibers. (F) Confocal images of cells migrating along 1D microprinted lines (1 µm wide) under different substrate stiffness (2.3 kPa vs 50 kPa). Stainings show F-actin (red), tubulin (green), nuclei (Hoechst, blue), and collagen-I (cyan). Adapted from [153], [155] and [156].*

that contact guidance requires the mechanical cooperation between microtubules (MT) and actomyosin cytoskeleton (Figure 2.8,F). MT networks serve as an intracellular mechanical scaffold that can mechanically compete for actomyosin contractile energy. On 1D lines, MTs scaffolding render protrusions insensitive to external contact guidance cue rigidity. Their data also reveal that distinct Arp2/3- and formin dependent actin structures guide microtubule-driven protrusions and enhance contact guidance sensing. Overall, their work provides a mechanistic framework suggesting a physical MT-actomyosin link where actomyosin-generated forces are mechanically adsorbed by both an MT intracellular scaffold and ECM[156].

2.2.5 Symmetry breaking and polarization at 1D

Beyond playing a crucial role in cell alignment and ECM topography sensing, microtubules (MT) post-translational modifications are a prerequisite to trigger the initial "symmetry event" at the onset of migration. Recent studies have described, this symmetry breaking using a "stick-slip" model in migrating mesenchymal and epithelial cells [157]. According to this model, cells initially start symmetrically elongated thereby increasing their contractile stress (stick phase) until focal adhesions on one extremity and stochastically detaches due to increased contractility, initiating the retraction of the cell rear (slip phase) and subsequent cell body translocation (Figure 2.9,A-B). This reveals an inverse relation between cell length and speed (Figure 2.9,C). In this model, cell motion does not require a pre-established rear-front polarity but instead arise from instabilities in the mechanochemical coupling between the cell and its environment.

More recently, Lavrsen et al. showed that microtubule detyrosination[3] drive epithelial cell polarization by guiding kinesin-1- based transport of stabilizing MT factors to cortical sites (Figure 2.9,D)[158]. By stabilizing MT and reinforcing polarity, this mechanism acts as positive feedback loop. Consistent with the "stick-slip" model, the biphasic behavior of migrating cells relies on microtubule (MT) detyrosination. In the absence of an asymmetric distribu-

[3]It depicts a type post-translational modification occurring on α-tubulin. It consists in the cleavage of the C-terminal tyrosine to leave a glutamate at the newly formed C-terminus.

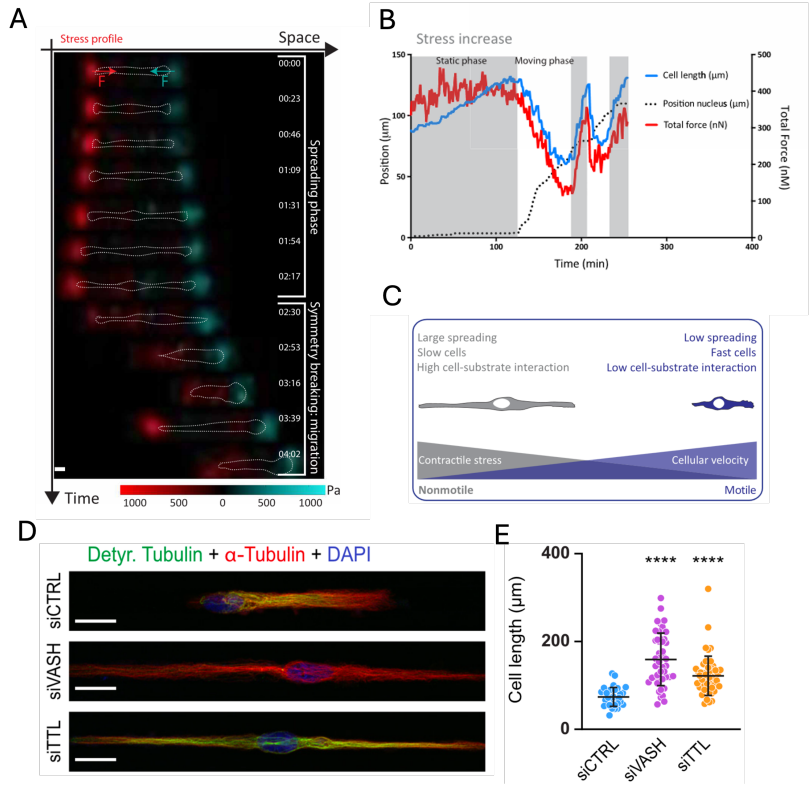

Figure 2.9: *Symmetry breaking and stick-slip model on 1D micropatterns. (A) Time-lapse sequence and corresponding stress profile extracted from TFM during single epithelial cell migration. Dotted white line indicate cell outline; color-coded stress profile depending on the direction of applied traction forces (color scale in Pascal). Scale bar, 10 µm. (B) Quantification of stress evolution over time. Curves show changes in cell length (blue), nucleus position (black dotted line), and total force (red) across static and motile phases (grey shaded areas). (C) Schematic model linking spreading state, contractile stress, and motility.(D) Immunofluorescence images of control cells (siCTRL) and knockdown of VASH (siVASH) or TTL (siTTL), stained for detyrosinated tubulin (green), α-tubulin (red), and nuclei (blue, DAPI). Scale bars, 20 µm. (E) Quantification of cell length under different knockdown conditions, siCTRL in blue, siVASH in pink and siTTL in orange. Adapted from [157] and [158].*

tion of MT detyrosination — caused by depletion of either VASHs or TTL — the stick-slip behavior cannot occur for two reasons (Figure 2.9,E). First, the symmetric kinesin-1–mediated transport of microtubule-stabilizing factors

promotes elongation at each end of the cell. Second, the symmetric dynamics of focal adhesions (FAs) and the even distribution of myosin prevent detachment and retraction at either end. Altogether, these data demonstrated that adhesion dynamics and contractility but also MTs post translational state are essential to generate spontaneous polarization and drive efficient 1D migration on fibrillar substrates. In addition, MT detyrosination was found essential for directional 3D cell migration within the ECM. Thereby, the mechanism is generally conserved during 3D cell migration. [157, 158].

2.3 The morphological switch on fibers

Micropatterns provide a controlled platform to study how cells establish front–rear polarity and have revealed that symmetry-breaking events serve as the initiation step of directed cell migration. The stick–slip behavior observed on linear micropatterns is thought to recapitulate key aspects of 3D migration along ECM fibers, where cells alternately adhere, generate tension, and release in order to move forward. Interestingly, on real 3D fibers, cells also undergo morphological transitions, such as switching between elongated and more rounded shapes.

In the following section, we present recent findings on the occurence of such morphological switches during fibrillar migration and examine their role in enabling efficient navigation through confined environments.

Sharma et al. found that during the migration of mesenchymal cells monolayer on aligned fibers, single cells initiate the invasion on fibers by detaching from the monolayer[159]. These cells were identified to translocate onto the fibers by a mechanism of spreading and recoil allowing them to adopt high speed, and travel longer distances from the monolayer (Figure 2.10,A). While the spreading phase was quite stationary with symmetric morphology of the cell, the recoil phase was associated with a rounded cell body and an unidirectional movement.

Another group, originally investigating epithelial collective movement on glass wires, also reported this behavior. Yevick et al. observed single cells migrating on a glass wire speeding up by adopting a characteristic "rounded up" shape that minimized the contact area with the wire (Figure 2.10,B)[160]. Interestingly, they found that cell long axis under 40 μm corresponded to the maximal migrating speed (Figure 2.10,D). The morphological switch is not solely restricted to single fibers and occurs within dense matrices of aligned fibers.

Recently, Wang et al. have developed synthetic 3D aligned matrix fibers with defined stiffness (Figure 2.10,C)[161]. While fiber alignment enhances speed and directionality of mesenchymal cells, the relationship between cell contractility and stiffness defines the optimal migration mode. They identified a unique mode of migration altering stretch and recoil called slingshot in only deformable matrices. This mode allows cell to reach high migration speed by a sudden recoil of the matrix after adhesion failure at the cell's trailing edge and simultaneous translocation of the cell body forward along the axis of fiber alignment (Figure 2.10,E)[161].

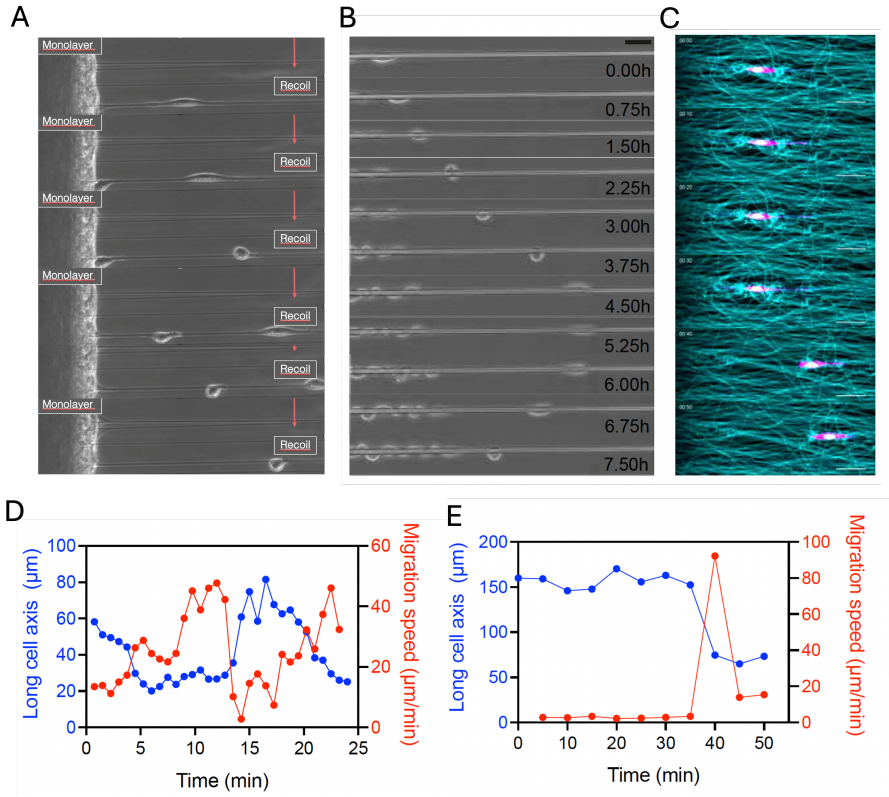

Figure 2.10: *Examples of morphological switch on glass fiber and in 3D collagen fiber matrix. (A) Time-lapse sequence of a single fibroblast (NIH3T3) escaping from a monolayer. Recoiling, and rounding of the cell body during migration along a single fiber. (B) Time-lapse sequence of a single MDCK epithelial cell migrating on a smooth glass wire (diameter = 5.3 µm). After detaching from the tissue, the epithelial cell rounds up and migrate on the glass fiber. Scale bar, 50 µm. (C) Time-lapse sequence of a single fibroblast (NIH3T3) migrating in a 3D matrix composed of aligned collagen fibers. Scale bar, 50 µm. (D) Temporal evolution of the long cell axis and the migration speed indicating that the cell morphological switch from an elongated to a compacted morphology is associated with an increase in migration speed. (E) Temporal evolution of the long cell axis and the migration speed indicating that the cell morphological switch from an elongated to a compacted morphology is associated with an increase in migration speed with a maximum speed around 80 µm/min. Adapted with permission from [159], [160] and [161].*

2.4 Mechanical memory in migrating cells

Growing evidence suggests that adherent cells can retain a memory of the mechanical characteristics of their environment after prolonged exposure, ranging from a few days to several weeks, through alterations in transcription factor activity, post-translational modifications and epigenetic changes [120]. In confined 1D and 3D environments, migrating cells exhibit important and successice morphological switches, raising the question of what governs the persistence of these morphologies and whether their behavior reflects a form of mechanical memory. In the following section, we review recent studies that have explored the concept of mechanical memory in the context of cell migration, highlighting how past mechanical cues can influence cell fate.

2.4.1 Mechanical memory associated to ECM features

The process of metastasis is particularly relevant to the concept of mechanical memory as the tumor microenvironment undergoes multiple mechanical modifications during disease progression. These modifications range from stiffening to changes in topography, solid stresses and composition[120]. One hypothesis suggests that the ability of tumor cells to survive the metastatic process is enhanced by mechanical stresses in the primary tumor microenvironment that select for well-adapted cells[120]. A current hypothesis suggests that the resulting biophysical adaptations favorable for metastasis can be retained via mechanical memory.

A general mechanism for the establishment of mechanical memory in cancer metastasis was recently proposed (Figure 2.11) [120]. On the timescale of minutes to hours, cells read out mechanical cues such high matrix stiffness through specific $\beta 1$ based integrins. The specific signalling coming from integrin triggers subsequent cytoskeleton remodelling and epigenetic changes, the priming time is initiated. After a few days or weeks, mechanical memory is imprinted through persistent molecular mechanism. Two transcription factors were identified as key players in the priming process: YAP, a well-known mechanotransducer, and RUNX2[4], which influences migration and invasion (Figure 2.11). However, how

[4]It is a key transcriptional factor associated with osteoblast differentiation.

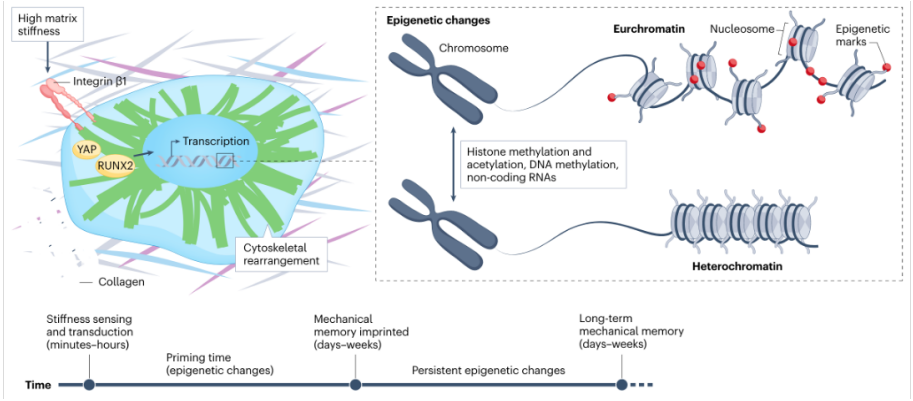

Figure 2.11: *Mechanical memory of matrix stiffness imprinted through persistent epigenetic changes. High matrix stiffness is sensed through integrin β1, leading to cytoskeletal rearrangements and nuclear translocation of YAP and RUNX2, activation of transcriptional programs, and priming of epigenetic changes. (Right) Epigenetic modifications such as histone methylation/acetylation and DNA methylation regulate chromatin state, shifting between euchromatin (open, transcriptionally active) and heterochromatin (compact, transcriptionally repressed). (Bottom) Timeline of mechanical memory imprinting: stiffness sensing and transduction occurs within minutes to hours, followed by a priming phase (epigenetic changes). Mechanical memory is imprinted over days to weeks, maintained by persistent epigenetic changes, and can result in long-term mechanical memory spanning extended time scales. Adapted from [120]* .

mechanical memory is molecularly retained remains poorly understood.

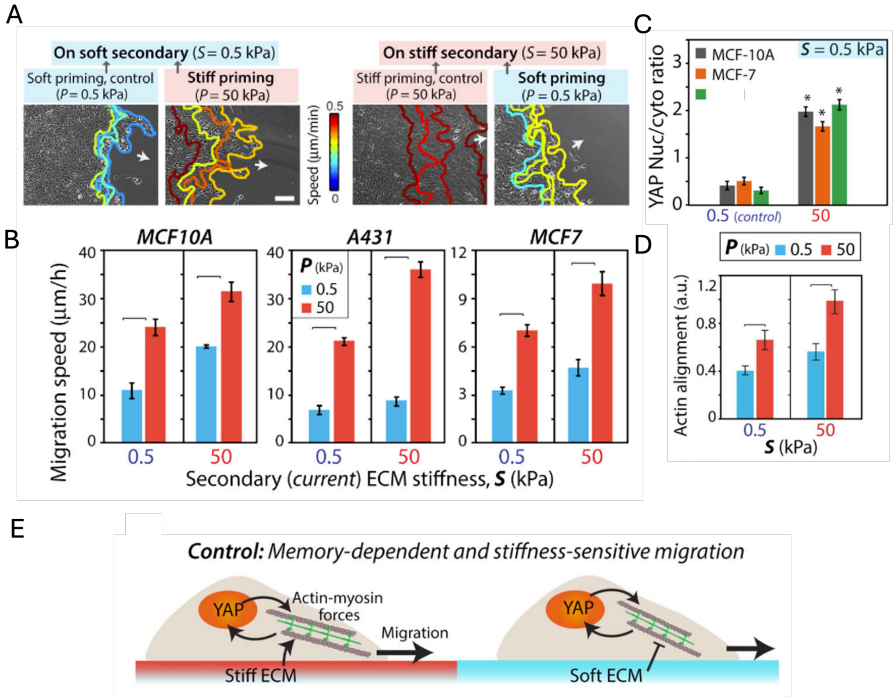

Figure 2.12: *Mechanical memory and stiffness-sensitive migration. (A) Leading-edge tracks of MCF10A monolayers recorded for 12 hours in the secondary ECM after 3-day priming on soft (0.5 kPa) or stiff substrates (50 kPa), with color-coding for migration speed. Arrows indicate direction of migration. Scale bar, 100 µm. (B) Leading-edge migration speed of MCF10A, A431, and MCF7 cells on secondary ECM (S=0.5, 50 kPa) after defined priming (P=0.5, 50 kPa). (C) YAP nuclear-to-cytoplasmic ratio of MCF10A, A431, and MCF7 cells on soft secondary ECM, after stiff priming. (D) Actin fibers alignment of MCF10A cells. (E) Schematic model of memory-dependent migration: cells primed on a stiff matrix activate YAP and actin–myosin forces, sustaining high motility even after transitioned to a soft matrix. Adapted from [162].*

Nasrollahi et al. used engineered substrate with distinct soft (0.5 kPa) and stiff (50 kPa) regions to reveal that prime epithelial monolayers primed on a stiff matrix migrate significantly faster, even after transitionning to a softer substrate, than those primed on a soft matrix (Figure 2.12,B)[162]. This enhanced migration was associated with sustained nuclear localization of YAP and was abolished under YAP depletion (Figure 2.12,C). The mechanical memory also encoded enhanced actin alignment within the stiff primed monolayer indicat-

ing permanent cytoskeleton remodelling, key for the process of cell migration (Figure 2.12,D).

The mechanical memory effect was both time and stiffness dependent, requiring at least 2–3 days of exposure to the stiff matrix to establish long-lasting mechanical adaptations. These findings expand our traditional view of mechanosensitive migration, demonstrating that not only current matrix cues matters but also past mechanical cues encoded in the epigenetic landscape of primed cells (Figure 2.12,E).

Stiff matrix priming also confers an advantage to cells in more complex environment, such as fibrillar collagen network. Recent work demonstrated that human breast epithelial cells pre-conditionned for five days on a stiff matrix expressed higher level of RhoA and Rac1, key GTPases player in fibrillar migration ((Figure 2.13,A)[163]. This acquired mechanical memory enabled cells to generate higher level of forces, remodel collagen fibers more effectively, and promote invasion (Figure 2.13,B-E). Consistent with previous findings, the memory effect was abolished by YAP depletion but remained intact following Myosin II inhibition, suggesting that the mechanism requires epigenetic modifications and is not solely dependent on cytoskeletal activity[163].

Another key modification of the ECM feature during tumor progression is its spatial organization. Maiques et al. identified three characteristic ECM organizational patterns in both human and mouse tumours [164]. They classified tumor regions into (1) the tumour body (TB), (2) the proximal invasive front (PIF), and (3) the distal invasive front (DIF) in models of melanoma and breast cancer (Figure 2.14,A). Notably, the PIF region exhibited enhanced matrix alignment.

To investigate whether cells retain a mechanical memory of matrix organization at their site of origin, the authors cultured cells—isolated from these distinct tumor regions on ex vivo collagen I networks. Interestingly, cells retained cytoskeletal features reflective of their original tumor location, including increased cell rounding and elevated myosin levels.

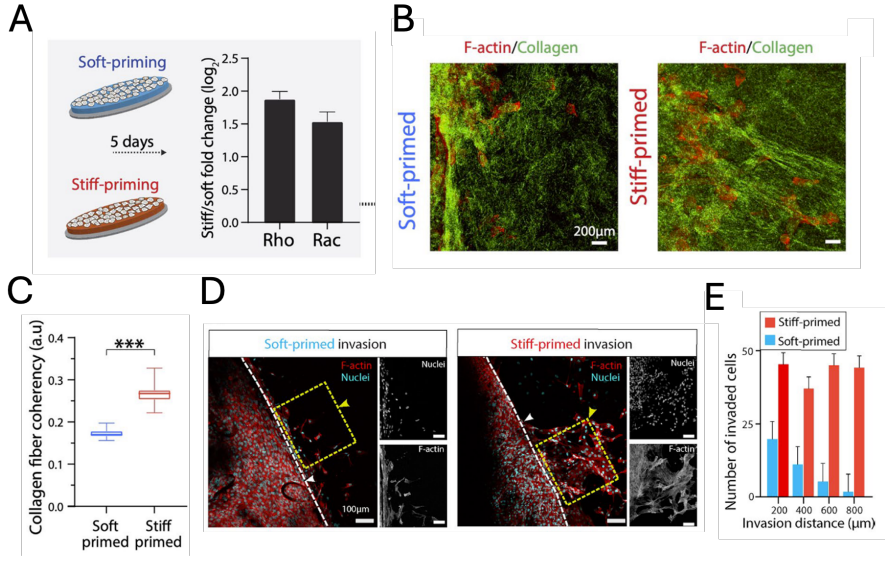

Figure 2.13: *Stiffness priming promotes collagen remodeling and cell invasion. (A) Schematic of 5 days soft- or stiff-priming. Fold change in Rho and Rac activity (log_2) shows upregulation in stiff-primed cells compared to soft-primed controls. (B) Representative immunofluorescence images of F-actin (red) and collagen (green) reflectance[5] in MCF10A cells after 5 days of soft or stiff priming and 3 days of invasion into collagen. Scale bars, 200 μm. (C) Collagen fiber coherency reveals significantly increased alignment in stiff-primed matrices. (D) Invasion assays comparing soft- and stiff-primed cells embedded in 3D collagen matrices. Insets show higher magnification of nuclei (cyan) and F-actin (red) at the invasive front. Scale bars, 100 μm. (E) Quantification of invasion depth for soft- and stiff-primed cells. Adapted from [163].*

Importantly, cells originating from the invasive front—those most likely to form metastases in vivo—maintained these cytoskeletal features and exhibited enhanced survival and migratory capacity, traveling the longest distances within the ex vivo collagen (Figure 2.14,B-C)[164].

[5]Reflectance designate the fraction of light that is reflected back from tissue. In collagen, it mainly arises from its fibrillar structure, making reflectance sensitive to collagen density and organization.

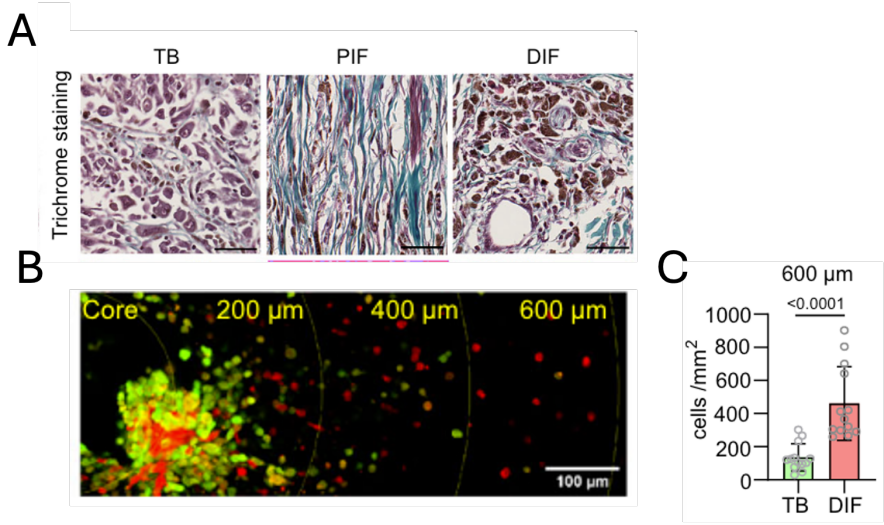

Figure 2.14: *Matrix organization endows tumour cells with Mechanical memory. (A) Region of interests from Tumour Body (TB) and Proximal Invasive Front (PIF) and Distal Invasive Front (DIF) of primary melanoma: trichrome staining. Collagen fibers are more aligned in PIF and DIF compared to TB. Scale bars, 50 µm. (B) Fluorescence imaging of invasive cells spreading from the tumor core into a collagen matrix. Distance from the core (200, 400, 600 µm) is indicated, with cells originating from TB marked in green and cells from DIF in red. Scale bar, 100 µm. (C) Quantification of invasive cells at 600 µm shows significantly higher density in DIF compared to TB. Adapted from [164].*

2.4.2 Mechanical memory of space and confinement

While it is established that microenvironmental cues can encode mechanical memory in migrating cells, the impact of self-induced environmental perturbations—such as the deposition of biochemical signals or mechanical remodeling of the extracellular matrix—on cell trajectories remains an open challenge.

Recent work using in vitro setups featuring 1D micropatterned lines has demonstrated that migrating cells leave behind physicochemical footprints along their path—through biochemical deposition—which encode a form of spatial memory [165]. These conclusions arose from the observation that isolated cells exhibited regular oscillatory migration patterns, which became more pronounced over extended timescales (48-60h) (Figure 2.15,A-B).

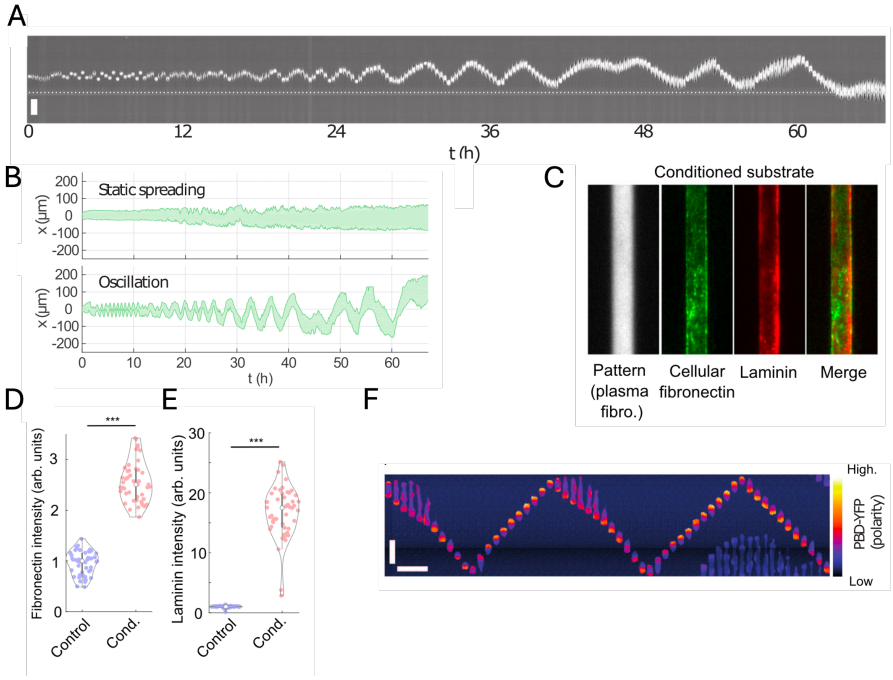

Figure 2.15: *Long-live spatial memory on linear micropatterns. (A) Kymograph of a single MDCK cell oscillatory migration. Scale bar, 20 µm. (B) Typical kymographs showing static spreading (top) and oscillatory migration (bottom) with amplitude fluctuations over time. (C) Fluorescence images of conditioned substrates showing deposition of cellular fibronectin (green) and laminin (red) onto human plasma fibronectin micropatterns (grey). Quantification of fibronectin (D) and laminin (E) fluorescence intensity showing deposition on conditioned substrates compared to controls. (F) Kymograph of a MDCK cell expressing PBD-YFP (reporter of Rac1/Cdc42 activation). Color-scale reports activity from low to high. Oscillatory migration illustrates the periodic changes in front–rear polarity. Scale bar, 20 µm. Adapted from [165].*

In a complementary experiment, a substrate was first conditioned by culturing a dense layer of cells. After removing this layer, isolated cells were replated onto the pre-conditioned substrate to observe their behavior. Analysis of the conditioned surface revealed the presence of cellular fibronectin and laminin, key components of the cellular footprint (Figure 2.15,C-E). These deposits appeared to create local polarity cues that enhanced Rac-1 mediated cell polarization (Figure 2.15,D), directing cells preferentially toward previously visited

regions and resulting in oscillatory migration behavior[165].

The spatial memory encoded in these self-deposited footprints has significant implications for how cells explore their environment. It may influence not only path selection but also the persistence and directionality of movement. These findings could be particularly for understanding fibrillar migration and matrix invasion. However, whether such self-generated spatial memory also occurs along individual matrix fibers or within fully three-dimensional environments remains to be elucidated.

It remains unclear how the concept of mechanical memory, previously established in the context of substrate stiffness, extends to physical confinement. Mosier et al. addressed this question by investigating how transient confinement affects the migratory behavior of metastatic breast cancer cells (MDA-MB-231)[166]. Using microfabricated collagen microtracks, they exposed cells to narrow constrictions followed by wider regions to determine whether prior confinement influences future migration (Figure 2.16,A).

These results revealed that cells not only accelerate within confined sections but also retain this increased migration speed after transitioning into less restricted areas, thereby demonstrating a form of confinement-induced mechanical memory (Figure 2.16,B-C). Moreover, confined cells exhibited persistent polarization of migratory features, including actin and active mitochondria, toward the leading edge. Remarkably, this polarized distribution was maintained even after exiting the constricted zones (Figure 2.16,D-E), suggesting a spatial relocalization of energy production toward mechanically demanding cytoskeletal regions.

This study also underscore the central role of focal adhesions. Disruption of vinculin, a key focal adhesion component, abolished both mitochondrial polarization and the post-confinement enhancement of migration speed. These findings implicate focal adhesion–mediated mechanotransduction as essential for encoding this confinement-induced mechanical memory[166].

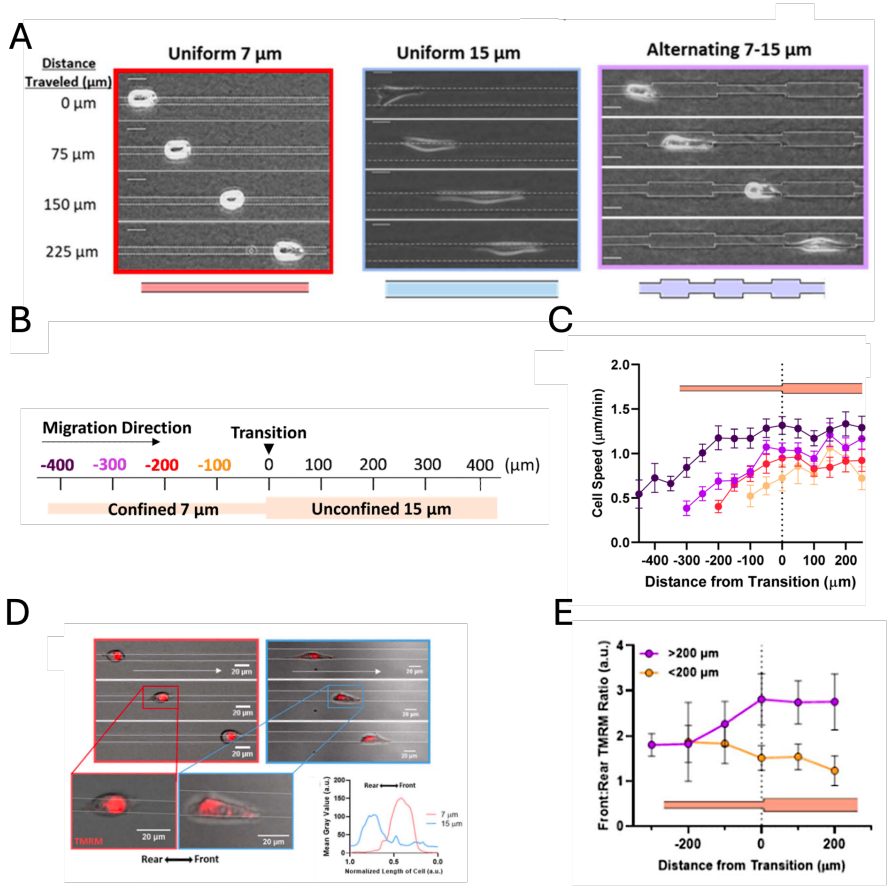

Figure 2.16: *Cell speed regulation and mitochondria polarization by spatial confinement priming. (A) Time-lapse images of cells migrating through micro-channels with uniform confinement (7 μm, red; 15 μm, blue) and alternating confinement (7–15 μm, purple). (B) Schematic of confinement transition from narrow (7 μm) to wide (15 μm) channels. (C) Cell speed as a function of distance from the transition. Colors indicate origin distance from transition: 100 μm (yellow), 200 μm (red), 300 μm (purple), 400 μm (dark purple). (D) Representative images of cells stained with TMRM (tetramethylrhodamine, methyl ester) to assess mitochondrial activity along confined (7 μm) and unconfined (15 μm) channels. Plot shows average fluorescence distribution along the cell body. Scale bars, 20 μm. (E) Front:rear TMRM ratio relative to transition zones. Colors indicate origin distance from transition: >200 μm (purple) and <200 μm (orange).*

Previous work from the same group investigated how spatially complex microenvironments that present directional choices under confinement affect the

energetic costs of migration[167]. These energetic costs arise from the mechanical work required to deform both the cell and the microtrack. The authors showed that confined cells upregulated both ATP production and glucose uptake to sustain fast migration.

By confronting unconfined cells with bifurcating collagen tracks featuring both narrow and wide branches, they demonstrated that cells preferentially select the path of least resistance to minimize energy expenditure[167]. This raises an intriguing question: do cells emerging from prior confinement continue to favor energetically optimal paths, or are they better equipped to navigate confined environments due to confinement-induced mechanical memory encoded in the bioenergetic and cytoskeletal machinery?

In this PhD work, we developed an in vitro cell migration assay using standardized fibronectin-coated two-state micropatterns. These microsystems provide a versatile platform with tunable geometries, enabling the investigation of long-term memory effects of past confinement events in migrating epithelial cells. The geometric flexibility of the patterns allows for precise control of cell morphology and facilitates the induction of specific morphological transitions.

Long-term time-lapse video microscopy enabled the collection of an extensive dataset of migration trajectories, capturing parameters such as cell speed, morphology, and actin organization over time. Combined with biophysical modeling and targeted biochemical perturbations, this strategy revealed the emergence of a mechanical memory of the migratory mode adopted by cells as they transitioned across narrow micro-bridges.

CHAPTER 3

GOALS AND STRATEGIES

The actin cytoskeleton plays a central role in in shaping cellular morphology and orchestrating the dynamic responses of migrating cells. In confined microenvironments, cells frequently undergo successive cycles of constriction and release, which drive profound morphological adaptations. While it is well established that adherent cells can retain a long-term memory of mechanical stimuli at the transcriptional or epigenetic level, it remains unclear whether cells also preserve a short-term memory of such morphological adaptations across repetitive confinement events, and how this memory contributes to migration efficiency. In particular, the potential role of the cytoskeleton as a structural support for such a mechanical memory has not yet been investigated.

The overarching goal of this PhD work is to elucidate the cellular mechanisms by which confinement-induced morphological states are maintained and transmitted across successive transitions, and to determine whether components of the cytoskeletal machinery encode a mechanical memory that optimizes migration through narrow environments. To address this challenge, we combined microfabricated confinement assays, live-cell imaging, high-resolution confocal microscopy, and pharmacological perturbations. In addition, we established a collaboration to confront our experimental findings with a theoretical model, thereby bridging quantitative measurements with predictive simulations.

Our experimental strategy relies on the use of micropatterned fibronectin substrates with precisely defined geometries, allowing us to impose successive cycles of confinement and deconfinement on individual epithelial cells. We employed adhesive micropatterns featuring a dumbbell geometry, which consists of a narrow FN-coated passage, 6 μm in width, with a variable length systematically increased from 40 μm to 80 μm, 120 μm, 160 μm, and 320 μm. These dimensions are physiologically relevant, as they approximate the size of interstitial spaces encountered in skin and breast tissues, which are typically less than 10 μm in diameter and can extend over more than 150 μm in length. Each end of the narrow bridge is connected to a large square adhesive area (40 $\times$ 40 μm^2), allowing cells to spread, repolarize, and reinitiate migration before traversing the confined passage again. Time-lapse imaging was used to track morphological transitions and quantify migration dynamics across the different confinement lengths. In parallel, high-resolution microscopy enabled us to ana-

lyze actin cortex organization and microtubule distribution, thereby identifying structural correlates of morphological memory. Time-lapse imaging was used to track morphological switches and quantify migration dynamics across different confinement length. In parallel high-resolution microscopy further enabled us to analyze actin cortex organization and microtubule distribution, thereby identifying structural correlates of morphological memory.

To establish causal links, we perturb the cytoskeleton using pharmacological agents that weaken or stabilize the actin cortex, or disrupt microtubule dynamics. This approach allows us to dissect the respective contributions of cortical actin and microtubules to the maintenance of compacted morphologies. Furthermore, we systematically vary the geometry of confinement and deconfinement sites to determine how spatial parameters influence resident time, shape retention, and migration efficiency. We demonstrate that local geometry governs a switch between two cell morphologies (elongated vs compacted), thereby facilitating cell passage through long and narrow gaps.

Finally, we integrated our experimental findings with a minimal theoretical model developped by our collaborators, which captures the stochastic switching dynamics between elongated and compacted states under confinement. We then challenged the theoretical model by modifying the size of the square relaxation areas, in order to either promote the maintenance of a compact cellular morphology or, conversely, an elongated morphology. This modeling framework enabled us to test the hypothesis that geometry-sensitive switching, reinforced by actin cortex remodeling, constitutes the fundamental basis of a cytoskeletal mechanical memory.

By using a multidisciplinary approach, this work aims to provide direct evidence that the actin cortex encodes a mechanical memory of past morphological states, thereby promoting efficient migration in confined environment. Such a mechanoadaptive process is expected to have broad implications for understanding cell navigation during embryonic development, immune surveillance, wound healing, and metastatic invasion.

CHAPTER 4

MATERIALS AND METHODS

4.1 Cell culture

The cellular model

Figure 4.1: *Epifluorescence image of MCF-10A cells cultured on a flat substrate. Scale bar : 300 μm.*

This PhD work is based on the MCF-10A cellular model (Figure 4.1) and incorporates two additional derivatives of this line, genetically modified to express specific proteins of interest. Each of these variants will be described in the following section. The MCF10A human mammary epithelial cell line was originally established from the mammary gland of a 36-year-old woman with fibrocystic disease and constitute a widely used in vitro model of non-tumorigenic breast epithelium. MCF10A cells provide a reference system for studying epithelial cell function, malignant transformation, and the epithelial-to-mesenchymal transition (EMT) associated with invasive breast carcinoma. Although classified as basal-like, MCF10A cells express a combination of luminal and stem-like markers together with epithelial proteins such as cytokeratins and milk proteins, making them a versatile model for probing mammary cell biology and early tumor progression [168].As shown in Figure 4.1, MCF-10A

cells cultured on fibronectin-coated glass substrates display heterogeneous morphologies. When isolated, they are well spread and form broad lamellipodia, a characteristic feature of individual epithelial cells. The measured mean cell area was 1167 ± 545 μm^2, which served as a useful reference for the design of experiments during this thesis work (Figure 4.2).

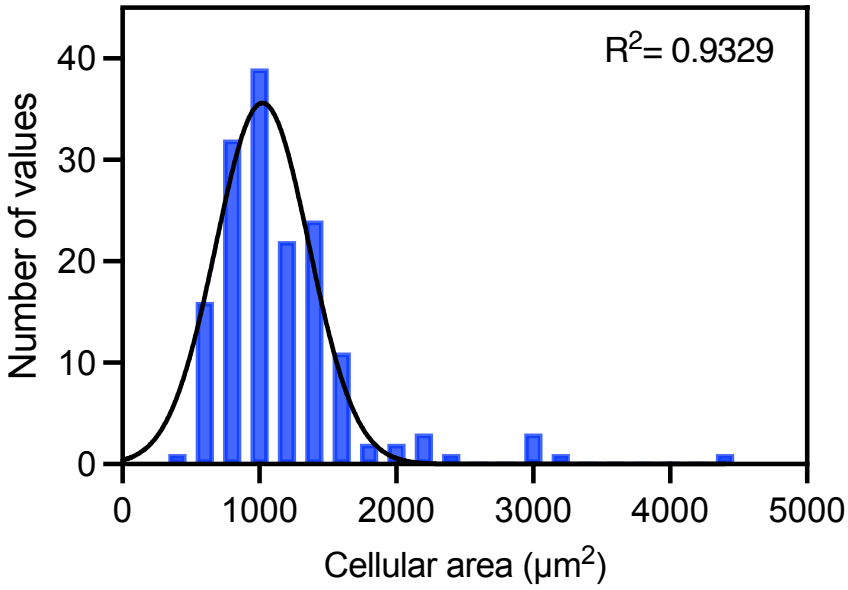

Figure 4.2: *Distribution of MCF-10A cell areas. Cell area was quantified from segmented actin images of cells cultured on fibronectin-coated glass for 24 h. n = 158 cells; mean ± SD = 1167 ± 545 μm^2.*

We collaborated with Guillaume Charras' laboratory at University college of London (UK), which generated two MCF-10A mutant cell lines.

To generate MCF-10A cells with endogenously tagged ARPC1B, the mScarlet fluorescent protein has been inserted at the N-terminus of ARPC1B using CRISPR genome editing. The donor plasmid consisted of homology arms, a hygromycin resistance gene, a self-cleaving T2A peptide, and the mScarlet protein. Following electroporation of the cells with the sgRNA, the donor plasmid, and a plasmid encoding Cas9 (Addgene #42230), cells were first selected with

hygromycin (20 µg/mL) for 7-10 days before enrichment by flow cytometry. The repetition of these passages eventually introduces genetic drift into the cell population. In order to limit the effects of this process, the use of was systematically stopped at 35 passages.

The second derivative is an MCF-10A dominant-negative ezrin cell line, engineered to express a truncated ERM construct consisting of only the N-terminal FERM domain fused to GFP. In wild-type ERM proteins, the FERM domain anchors the protein to the plasma membrane while the C-terminal domain binds F-actin. The ERM-GFP construct retains membrane binding but lacks the actin-binding site, therefore it outcompetes endogenous ERMs for membrane localization while disrupting the normal membrane–actin linkage.

Cell culture and growing conditions

MCF-10A cells were cultured in DMEM/F-12 (ThermoFisher) supplemented with 5% horse serum (ThermoFisher), 20 ng/mL epidermal growth factor (EGF) (Peprotech), 0.5 mg/mL hydrocortisone (Merck), 100 ng/mL cholera toxin (Enzo Life Sciences), 10 µg/mL insulin from bovine pancreas (Merck), and 0.1% penicillin/streptomycin (Pen/Strep, Merck). DMEM/F-12 uses a sodium bicarbonate buffer (3.7 g/L) and requires 5% CO_2 to maintain physiological pH at 37°C. Cells were passaged every 3-4 days upon reaching confluence and plated at a 1:4 dilution (∼1 million cells/T75 flask). For cell passaging, culture medium was aspirated and cells were washed with 10 mL of 1× PBS. After aspirating the PBS, cells were incubated with 2 mL of 0.25% trypsin (Merck) at 37°C for 10 minutes. Trypsinization was halted by adding 4 mL of medium, and cells were centrifuged at 1300 rpm for 5 minutes in a 15 mL Falcon tube to obtain a pellet. The supernatant was removed, and cells were resuspended in 1 mL of fresh medium before replating. MCF-10A cells were used up to a maximum of 15 passages.

Cells were cryopreserved in liquid nitrogen at −196°C to prevent senescence, reduce contamination risks, and minimize genetic drift. Dimethyl sulfoxide (DMSO) was used as a cryoprotective agent at −80°C at least 24 hours prior to transfer into liquid nitrogen, as it lowers the freezing point and reduces ice

crystal formation during gradual cooling. For recovery, cryovials were rapidly thawed and DMSO was removed within 24 hours, since it is cytotoxic above 4°C. Cells were diluted in pre-warmed DMEM/F-12 culture media to minimize DMSO exposure.

4.2 Protein micropatterning

Micropatterns were fabricated by light-induced molecular adsorption using the PRIMO system (Alvéole, France) on glass substrates [169], rather than microcontact printing[170, 171, 143, 172]. Light-Induced Molecular Adsorption of Proteins (LIMAP) is a micropatterning technique originally developed by Vincent Studer and colleagues in Bordeaux. It relies on a water-soluble photoinitiator that, upon near-UV illumination, locally modifies the antifouling properties of PEG-based polymer brushes through a photoscission mechanism

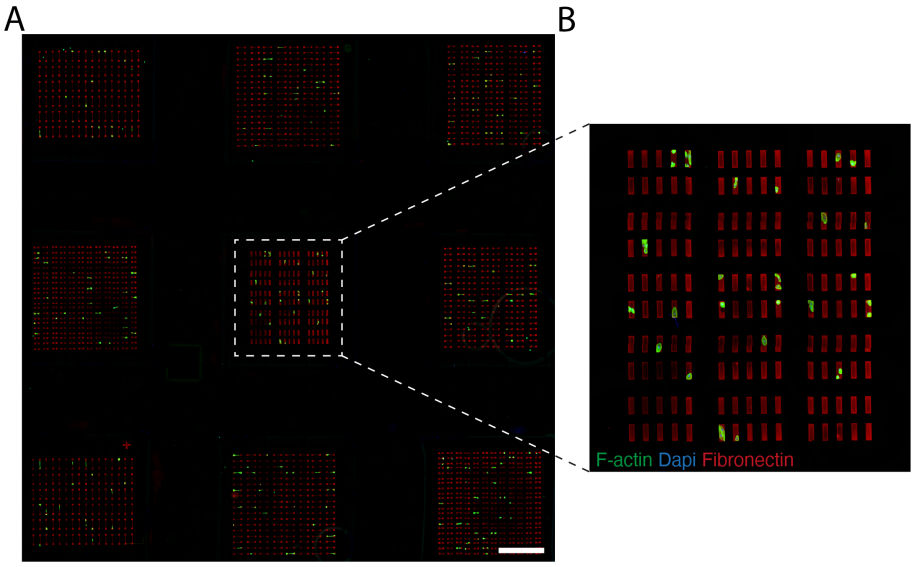

Figure 4.3: *(A) Large-scale view of micropattern arrays featuring various geometries generated on glass-bottom dishes. The large image was generate from stitching of 40x magnification images. (B) Magnified view of the region highlighted in (A). Cells were stained for F-actin (green, phalloidin), nuclei (blue, DAPI) and patterns (Red, fibronectin rhodamine). Scale bar, 1 mm.*

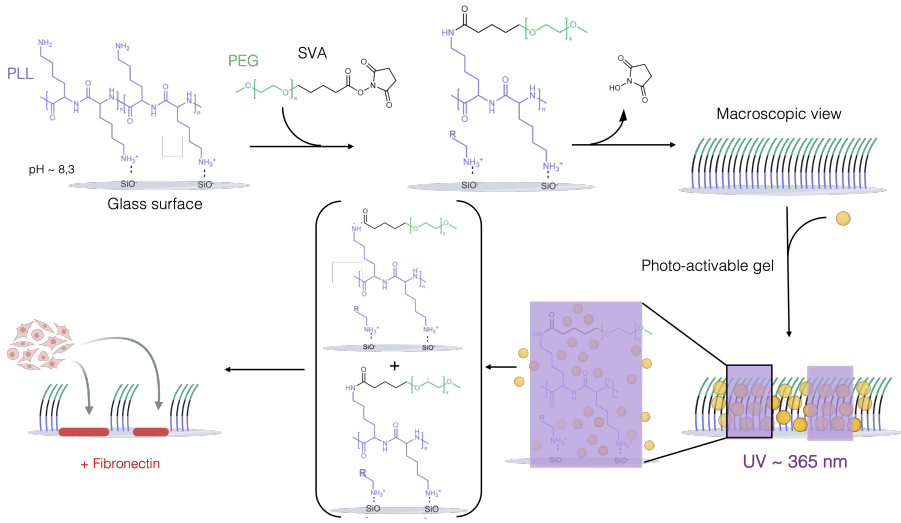

Figure 4.4: *Principle of micropatterning method (LIMAP) based on the PRIMO system. Glass substrates were first coated with poly-L-lysine (PLL) and polyethylene glycol (PEG) to create an anti-fouling surface. A photosensitive initiator was then activated by illuminating selected regions patterned UV light (λ=365 nm) using a digital micromirror device (DMD). Local photo-degradation of PEG created adhesive zones that allowed controlled adsorption of fibronectin (red zones). Cells subsequently adhered only to fibronectin-coated regions, enabling spatially defined organization.*

[173]. This controlled photo-degradation exposes adhesive regions where selected proteins can be adsorbed, enabling the generation of a large array of stable, high-resolution micropatterns with sub-micrometer precision (Figure 4.3).

The experimental procedure was adapted from Alvéole's original protocol and performed as follows: glass-bottom dishes (Cellvis) and PDMS stencils were plasma-activated for 3 min (Harrick Plasma) prior to assembly. Glass was coated with 0.1% (m/v) poly-L-lysine for 30 min, followed by 100 mg/mL PEG-SVA solution for 1 h (Figure 4.4). Surfaces were then treated with PLLP-gel photoinitiator, surfactant, and 70% ethanol, dried, and exposed to 375 nm UV light (100 mJ/mm^2, 20× objective) via a DMD projector (Figure 4.4). Regions were subsequently coated with 15 μg/mL fibronectin (Sigma) containing 5 μg/mL fluorescent fibronectin for 5 min (Figure 4.4). Patterned surfaces were

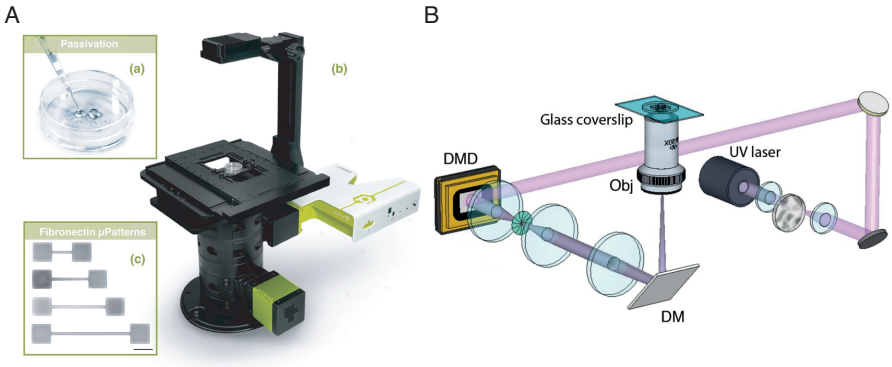

Figure 4.5: *PRIMO maskless photopatterning system.(Aa) Snapshot describing the coating procedure of a glass-bottom dishes with a PDMS stencil. (Ab) Openframe microscope system mounted with the Primo module and camera. (Ac) Dumbbell fibronectin micropatterns (in grey) obtained using the Primo technique. Scale bar, 40 µm. (B) Schematic of the optical setup used for DMD-based UV patterned illumination. The system allows to project spatially modulated UV light onto the sample through a set of focusing lenses, mirrors, and a dichroic mirror (DM). Obj: microscope objective. Adapted from [169].*

either used immediately or stored at 4°C in 0.1 M $NaHCO_3$ (pH 8.3) for up to 24 h.

Micropatterns were generated using maskless photopatterning through UV light projection (Figure 4.5). The technology consists of a high-contrast, wide-field projection module coupled to OpenFrame modular inverted microscope (Cairn Research, UK). UV illumination is provided by a Digital Light Processing (DLP) device equipped with a digital micromirror device (DMD). The DMD contains a 1824 × 1140 array of micromirrors, which can be individually switched to spatially modulate excitation light (Figure 4.5B) [169].

This maskless illumination scheme allows the direct projection of arbitrary grayscale UV patterns onto the sample plane with submicrometer resolution. According to litterature patterns dimensions ranging from 500 nm up to 1 mm can be printed in a single step, enabling rapid fabrication of adhesive patterns of diverse geometries without the need for physical photomasks [169].

4.3 Immunocytochemistry and live staining

MCF-10A epithelial cells were fixed with 4% paraformaldehyde (PFA) in PBS for 15 min at room temperature after cell migration experiments. Subsequently, cells were washed three times with PBS, with the last wash lasting for 5 min, and permeabilized using 0.05% Triton X-100 in PBS for 15 min at room temperature. After another round of three washes in PBS, permeabilized cells were blocked with a solution of 5% (v/v) fetal bovine serum (FBS, Gibco) and 1% (w/v) bovine serum albumin (BSA, Merck) in PBS for 30 min at room temperature. Actin filaments were stained with AlexaFluor 488 phalloidin (Invitrogen, 1:200), the nucleus with 4',6-diamidino-2-phenylindole (DAPI; Invitrogen, 1:200), microtubules with an anti-tubulin antibody produced in mouse (Sigma-Aldrich, 1:200), and phosphorylated myosin light chain (p-MLC) was stained using an anti-pMLC antibody in rabbit (Cell Signaling #3674, 1:200). Finally, phosphorylated ERM proteins were stained using an anti-phosphorylated Ezrin (Thr567)/Radixin (Thr564)/Moesin (Thr558) antibody produced in rabbit (Cell Signaling #3726, 1:200). For live labelling of the Golgi apparatus, cells were incubated overnight at 37°C, 5% CO_2, using the CellLight Golgi GFP BacMan 2.0 probe (Thermo Fisher C10592, 1:1000). Following incubation, cells were washed with PBS, and nuclei were stained with Hoechst (15 min at 1 μg/mL) before imaging.

Physicochemical footprints

To assess the biochemical remodeling of fibronectin (FN) micropatterns, samples were fixed at 5 h and 24 h incubation with cells and immunostained for laminins (anti-laminin, Sigma-Aldrich L9393) and cell-derived fibronectin (anti-IST9, Santa Cruz Biotechnology) after removal of cells. Controls (CTRL) were subjected to the same treatment without contact with cells. Immunostaining followed previously described protocols [165].

F-actin flow experiments

MCF-10A cells were incubated with SPY555-FastAct™ (Spirochrome) for 2 h at 37°C following the manufacturer's instructions (1:1000 dilution). Live actin imaging was performed in confocal mode with a Nikon A1R HD25 Ti2

microscope equipped with a 100×/1.35 silicone objective. All time-lapse experiments were performed with phenol red–free culture medium (DMEM/F12 from FisherScientific). An incubation chamber maintained 5% CO_2 and 37°C. Images were acquired every 1.25 s for 5 min. Data were recorded and processed using NIS-Elements (Nikon, Advanced Research v4.5, Japan).

4.4 Drug treatments

Cytoskeletal perturbations were induced using the following pharmacological agents: 20 nM latrunculin B (actin depolymerization), 10 μM Y27632 (ROCK inhibition), 2.5 μM nocodazole (microtubule depolymerization), and 50 μM NSC668394 (ERM protein inhibition). Drugs were added after 4 h of time-lapse imaging, and imaging was continued for an additional 20h in their presence. Actin stabilization was performed with 1 nM jasplakinolide, added 30 min prior to imaging. Latrunculin B, nocodazole, and jasplakinolide were dissolved in DMSO, whereas Y27632 was dissolved in water.

4.5 Image analysis

Actin fluorescence analysis

To quantify actin filament intensity, time-lapse images of SPY555-FastAct™-stained cells were converted to 8-bit, thresholded, binarized, and analyzed with the Particle Analysis tool in Fiji. Background intensity was measured in non-thresholded areas and subtracted. For cells fully spanning the micropattern bridge, fluorescence intensity was normalized to the mean intensity of the same cell in square regions at both ends of the dumbbells, accounting for inter-cell variability.

Cell tracking

Fluorescence time-lapse images were analyzed to track the individual cell nuclei over time using ImageJ. To reduce noise prior to segmentation, a Gaussian blur filter ($\sigma = 2$ pixels) was applied. Images were then thresholded using standard binarization procedures to isolate nuclei and track each nucleus across

successive frames. Following thresholding, the "Analyze Particles" function in ImageJ was employed to identify and track each nucleus across successive frames.

For cell contour segmentation and tracking, time-lapse DIC sequences (20 h, 3 min intervals, ∼400 frames/experiment) were analyzed with Cellpose 2.0 [174] integrated into the TrackMate plugin (Fiji).

Cellpose is a deep learning–based algorithm developed by Carsen Stringer and Marius Pachitariu. Desinged to generalize across diverse microscopy modalities, it automatically segments single cells, thereby improving throughput and reducing inter-operator variability. In this study, we employed the pretrained neural network models available in the Cellpose detector module integrated into TrackMate. The algorithm, implemented in Python 3, was trained on large datasets of manually segmented images, enabling accurate recognition and segment of new, unseen data. This automated approach minimizes manual effort and reduces operator bias, thereby increasing both the efficiency and reproducibility.

Following automated images analysis, all cell contours were manually verified. Trajectories were then analyzed to extract spreading area, perimeter, and the coordinates of front, rear, and center of mass. A passage was classified as *failed* if the cell reversed before its center of mass reached the opposite square; otherwise, it was considered *successful*.

Cell shape index (CSI)

Cell areas (A) and perimeters (P) were measured with ImageJ. The CSI was defined as:

$$\mathrm{CSI} = \frac{4\pi A}{P^2}$$

Values range from 1 (circular) to 0 (elongated).

Sliding standard deviation (SSD)

To quantify the magnitude of cell motion during migration, we calculated the sliding standard deviation (SSD) of the nucleus center of mass trajectories. The SSD is calculated as the standard deviation of the values within a given time window, and $\bar{x}$ is their mean. We chose a fixed sliding window of 20 frames (1 hour) using the mean nuclear positions of cells migrating on the micropatterns. For an experimental sample of n points, the standard deviation SSD was computed as:

$$\text{SSD} = \sqrt{\frac{\sum_{i=1}^{n}(x_i - \bar{x})^2}{n-1}}.$$

Retrograde actin flow determination

To quantify retrograde actin flow at lamellipodia, time-lapse sequences were converted to 8-bit format, underwent background subtraction and contrast enhancement, and were smoothed using a Gaussian blur filter ($\sigma = 1.5$). Kymographs were generated in Fiji using the reslice tool on 1-pixel wide lines drawn across lamellipodia (three per lamellipodium). Slopes of kymograph traces were used to calculate flow speeds:

$$v = \frac{x_2 - x_1}{t_2 - t_1}$$

in units of µm/s, later converted to nm/s.

Focal adhesions analysis

Focal adhesion images were first pre-processed in Fiji following a protocol adapted from a previously published method [175]. Subsequently, focal adhesions were quantified using the Focal Adhesion Analysis Server, an online tool developed by Shawn Gomez's laboratory at the University of North Carolina [176]. The image processing workflow was as follows: images were first converted to 8-bit and cropped to isolate single cells. Background was removed using the sliding paraboloid algorithm with a rolling ball radius of 50. Contrast was then enhanced by applying CLAHE (block size = 19, histogram bins = 256, maximum slope = 6). To further reduce background, an exponential

transformation was applied. The processed images were subsequently analyzed using the Focal Adhesion Analysis Server (FAAS), and segmentation quality was manually verified.

4.6 Optical microscopy

4.6.1 Differential interference contrast (DIC)

Differential Interference Contrast (DIC) microscopy, originally developed by Georges Nomarski in the 1950s, was designed to enhance contrast in unstained and optically transparent samples [177]. The technique relies on the principle of interferometry, allowing the detection of differences in optical path length within the specimen and thereby rendering otherwise "invisible" structures visible. DIC produces images where objects appear in shades ranging from black to white on a uniform grey background. The resulting image shares similarities with phase contrast microscopy but avoids the characteristic bright diffraction halos that often obscure fine details.

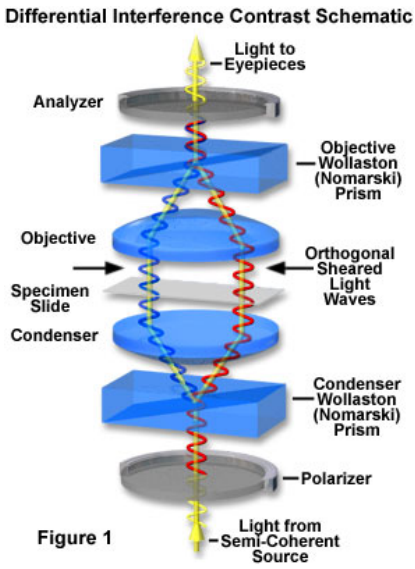

Figure 4.6: *Schematic of the optical path through a differential inferential contrast microscope configuration [178]. Source: Nikon*

The optical pathway in DIC microscopy begins with the polarization of light using polarizing filters (Figure 4.6). The polarized beam is then divided into two rays of identical wavelength but slightly displaced optical paths by a Nomarski prism made of birefringent crystals. These two rays are separated laterally by a fraction of the wavelength. As they pass through the sample, the rays undergo phase shifts that depend on the local refractive index. For example, in a living cell, one ray may traverse the cytoplasm while the other passes through the nucleus, each encountering distinct compositions and optical properties. After transmission, the rays are collected by the objective lens and recombined by a second prism. Their interference at the final polarizer converts these phase differences into variations in intensity, thereby generating image contrast.

DIC microscopy is particularly valuable in cell biology because it accentuates structures with refractive indices different from that of the surrounding cytoplasm. This makes it a powerful tool for studying living cells without the need for staining, preserving their physiological state while revealing subcellular organization.

4.6.2 Epifluorescence Microscopy

Fluorescence microscopy

Fluorescence microscopy was employed to observe and image cellular structures in both fixed and living cells. Fluorophores, once excited by a specific wavelength of light, emit photons at a longer wavelength. This fundamental principle of fluorescence is summarized in the Jablonski diagram (Fig. 4.7) [179].

Upon excitation, a fluorophore absorbs a photon and an electron is promoted from the ground state (S_0) to an excited state (S_2). Following vibrational relaxation, the electron relaxes to a lower excited state (S_1). The return to the ground state (S_0) is accompanied by the emission of light at a longer wavelength (red-shifted spectrum), which corresponds to fluorescence [179].

Protein visualization in cells was carried out using an inverted epifluorescence microscope (Nikon A1R HD25 Ti2, Japan) equipped with a broad-spectrum

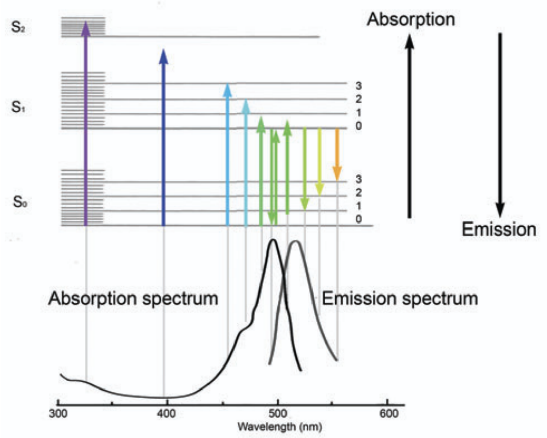

Figure 4.7: *Jablonski diagram showing the different energy transitions of a fluorophore's electrons during absorption and emmission of light. The spectrum display absorption and emission signals as a function of wavelength. The shift towards high wavelengths indicate a loss of energy [179].*

LED illumination (CoolLED pE-300white). Excitation filters were used to select the incident wavelengths, while emission filters isolated the emitted fluorescence. Filter sets were chosen according to the fluorochromes used (AlexaFluor, tetramethylrhodamine, and DAPI), each consisting of an excitation filter, a dichroic mirror, and an emission filter.

In epifluorescence mode, the selected excitation light is reflected at 90° by the dichroic mirror onto the sample. Emitted fluorescence then passes back through the dichroic mirror and is collected by the objective lens (Fig. 4.8). Images were acquired using a Prime 95B camera (Photometrics, Tucson, AZ) equipped with a highly sensitive back-illuminated scientific complementary metal–oxide–semiconductor (BSI-sCMOS) sensor. The sensor comprised 1200×1200 pixels of $11 \times 11 \mu$m each, cooled to $-25°$C to minimize background noise and enable the detection of weak fluorescent signals.

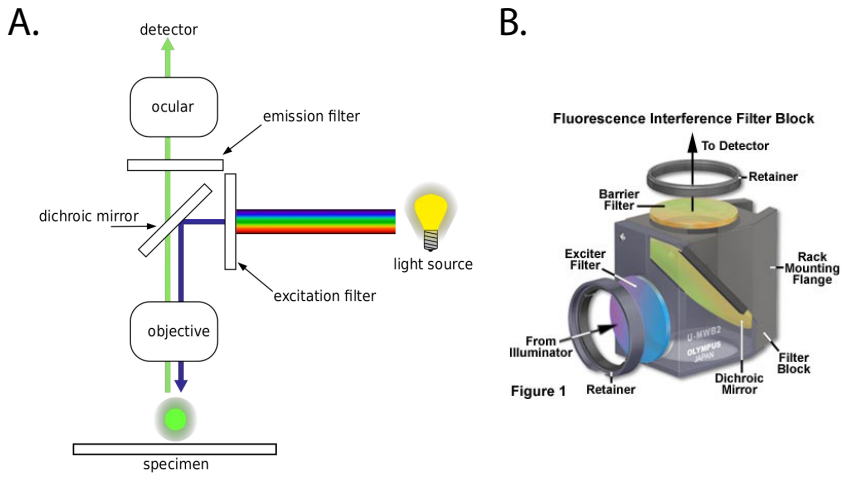

Figure 4.8: *(A) Schematic diagram of the working principle of an epifluorescence microscope, showing the excitation light directed through the objective onto the specimen and the emitted fluorescence collected back through the same objective to the ocular. (B) Fluorescence interference filter cube showing the arrangement of the exciter filter, dichroic mirror, and barrier filter, which together direct excitation light to the specimen and transmit emitted fluorescence to the detector. Adapted from [180] and [178].*

4.6.3 Time-lapse imaging

For launching time-lapse experiments, we proceeded as follows: 5–6 hours prior, sub-confluent MCF-10A cells were split (as previously described) and homogeneously seeded onto micropatterned samples at a concentration of 10,000 cells/ml in 3 ml of culture medium suitable for fluorescence microscopy. Cells were allowed to sediment and attache onto micropatterns before launching the experiment. The nucleus was labelled following the previously described protocol. Cell migration on dumbbell micropatterns was imaged at 40× magnification with a Photometrics Prime 95B camera (Photometrics, Tucson, AZ) mounted on a Nikon A1R HD25 Ti2 motorized inverted microscope (Nikon, Japan). An incubation chamber (Okolab, Italy) maintained 5% CO_2 and 37°C throughout imaging. Time-lapse sequences were acquired in DIC mode for 20 h at 3 min intervals and processed in NIS-Elements (Nikon, Advanced Research v4.5, Japan).

4.6.4 Confocal Microscopy

Confocal microscopy, introduced by Marvin Minsky in 1955, was developed to address the shortcomings of conventional wide-field fluorescence microscopy[181]. In standard fluorescence imaging, resolution is compromised by the presence of out-of-focus light that overlaps with the focal plane. By contrast, confocal imaging minimizes background interference from non-focal layers, thereby enhancing clarity. This technique captures images as a series of thin optical sections, with each frame representing fluorescence exclusively from a single focal plane. These slices can then be computationally combined to reconstruct a three-dimensional view of the sample.

Confocal systems employ lasers as excitation sources (Figure 4.9). Lasers produce monochromatic light at defined wavelengths, which is narrowed through the excitation diaphragm and focused onto a precise region within the specimen. Emitted fluorescence is subsequently filtered through an emission diaphragm, which selectively transmits light from the focal plane. This reduces out-of-focus contributions and significantly improves image contrast.

During this PhD work, confocal imaging was carried out using the Nikon A1R HD25 motorized inverted microscope equipped with 20×, 40×, and 60× Plan Apo objectives (NA 1.45, oil immersion), as well as a 100× Plan Apo silicone objective. Excitation was provided by a suite of lasers covering the violet (405 and 440 nm), blue (457, 477, 488 nm), green (514 and 543 nm), yellow-orange (568 and 594 nm), and red (633 and 647 nm) spectral ranges. High-resolution confocal images were captured with the 100× silicone lens in galvanometric scanning mode, using fine z-steps (0.1 μm) and a pinhole aperture of 12 μm. Data collection and processing were performed with NIS-Elements software (Nikon, Advanced Research v4.5).

4.6.5 High-resolution confocal microscopy

The actin cytoskeleton and microtubule networks of MCF-10A cells were imaged in high-resolution confocal mode with a Nikon AX Ti2 confocal microscope (Nikon, Japan) combined with the Nikon Spatial Array Confocal (NSPARC) detector. Z-stacks were acquired with a Galvano scanner using a 60×/1.42

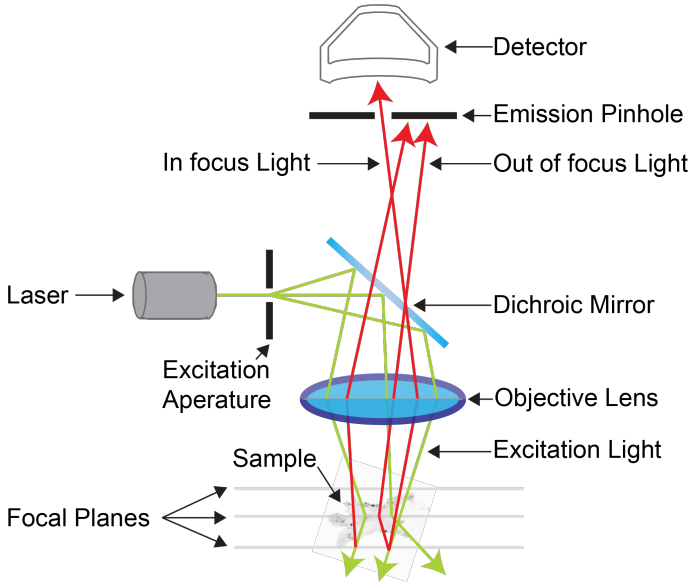

Figure 4.9: *Optical pathway of a confocal microscope. Laser light (green) is focused onto the sample through the objective lens, and emitted fluorescence (red) is collected back through the same lens. The dichroic mirror separates excitation and emission paths, while the pinhole ensures that only in-focus light reaches the detector, thereby rejecting out-of-focus fluorescence [178]. Source: Nikon.*

Plan Apo oil immersion objective and a step size of 0.17 μm for three channels (DAPI, TRITC, and FITC). Images were processed in NIS-Elements (Nikon, Advanced Research v4.5, Japan), applying Richardson-Lucy deconvolution to remove out-of-focus signal.

4.7 Statistical analysis

Each experiment was repeated at least three times. Normality was tested with the d'Agostino-Pearson test in Prism v10 (GraphPad Software). For normally distributed paired data, Student's two-tailed t-test (unequal variances) was used; otherwise, the Mann–Whitney test was applied. For multiple non-normal comparisons, the Kruskal–Wallis test was used, with Dunn's post-test when significant ($p<0.05$). Data are presented as mean ±s.d., unless stated otherwise. Box plots were generated in Prism v10, showing medians, interquartile

ranges (IQR), whiskers (min–max), and outliers. Significance levels are denoted as *p $<$ 0.05, **p $<$ 0.01, ***p $<$ 0.001, ****p $<$ 0.0001, and n.s. = not significant.

CHAPTER 5

MECHANICAL MEMORY IN CONFINED MIGRATION

As described in the preceding chapters, cell migration through narrow microenvironments is a hallmark of many physiological processes. It relies on successive cycles of confinement and release that induce marked morphological changes. Yet, it remains unclear whether migrating cells can retain a memory of their past morphological states that could potentially facilitate their navigation through confined spaces. The goal of this chapter is to demonstrate experimentally how local geometry governs the switching between distinct cell morphologies, thereby enabling more efficient transitions through long and narrow gaps. To address this, we developed an experimental strategy that integrates standardized microfabricated migration assays with biophysical modeling and targeted biochemical perturbations. Using this approach, we show that migrating cells exhibit a long-term memory of past confinement events. This memory enhances their migratory efficiency in restrictive environments and represents a fundamental mechanoadaptive property of the cytoskeleton

5.1 A morphological switch enables efficient passage through narrow gaps

To study cell shape changes during confined migration under standardized and reproducible conditions, we employed a well-established system of adhesive micropatterns featuring a dumbbell geometry, as introduced previously [151, 152, 182, 183]. This system consists of a narrow fibronectin (FN) passage, 6 μm in width, with variable lengths systematically increased from an initial 40 μm up to 80, 120, 160, and 320 μm (Figure 5.1A). These dimensions correspond to those of interstitial spaces found for instance in skin [127] and breast tissues [125], which are less than 10 μm in diameter and can extend over 150 μm in length [121]. Each end of the narrow bridge is connected to a large square area (40×40 μm^2), allowing the cell to spread and repolarize before traversing the confined passage again.

As previously discussed, it has been demonstrated that one-dimensional (1D) micro-stripes, similar to those used for the bridge, can effectively replicate many characteristics of the rapid, uniaxial migration phenotype observed in fibrillar three-dimensional (3D) cell-derived matrices [153]. Quantifying the cell shape

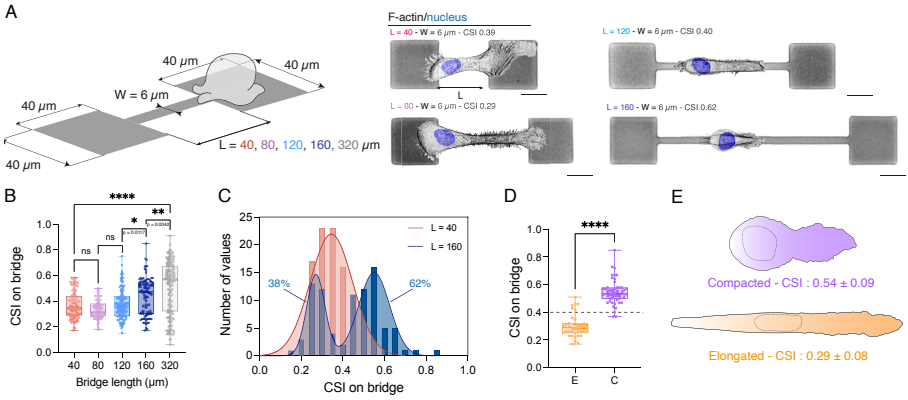

Figure 5.1: *A morphological switch ensures a successful crossing on long bridges.* ***(A)*** *Schematic representation and typical microscopy images of single epithelial cells (MCF-10A) navigating through a narrow passage represented by a dumbbell micropattern. The fibronectin-coated micropattern consists of two square islands of 40 μm × 40 μm connected to a narrow bridge of a constant width (W = 6 μm) and varying lengths (L= 40, 80, 120, 160 and 320 μm). The nucleus is stained with Hoechst and actin filaments are stained with phalloidin (colors inverted). The cell shape index (CSI) is indicated for each bridge length. Scale bars, 20 μm.* ***(B)*** *CSI on bridge versus bridge length (n = 116 for 40 μm, n=76 for 80 μm, n=109 for 120 μm, n=87 for 160 μm and n=184 for 320 μm from N≥3). *p=0.0117, **p=0.0042, ****p< 0.0001.* ***(C)*** *Distribution of the CSI on bridge for L=40 μm (in red) and L=160 μm (in blue).* ***(D)*** *CSI on bridge for elongated (E, n=37) and compacted (C, n=50) epithelial cell morphologies on L=160 μm.* ***(E)*** *Schematic representation of the typical morphology of a compacted (CSI: 0.54±0.09) and an elongated (CSI: 0.29±0.08) cells.*

index (CSI, see material and methods) [184] of mammary epithelial cells (MCF-10A) within these confined bridges (Figure 5.1B) based on automatic tracking of 20 hours time-lapse experiments revealed a surprising bimodal distribution for the longest length (160 μm, Figure 5.1C). This suggests the presence of two distinct sub-populations of cell morphologies with CSI either below or above 0.4 (Figure 5.1D) (Supp. Movie S1), corresponding to elongated (≈38%) or compacted (≈62%) morphologies, respectively (Figure 5.1E). As shown in Figure 5.2, bridges of 120 μm yielded a unimodal Gaussian CSI distribution (CSI = 0.34 ± 0.09, R^2=0.8257), whereas bridges of 160 and 320 μm consistently exhibited bimodal distributions. For these longer bridges, the subpopulation means remained remarkably consistent: 0.27 ± 0.04 and 0.55 ± 0.08 for 160 μm (R^2 = 0.8445), and 0.27 ± 0.08 and 0.55 ± 0.10 for 320 μm (R^2 = 0.9492).

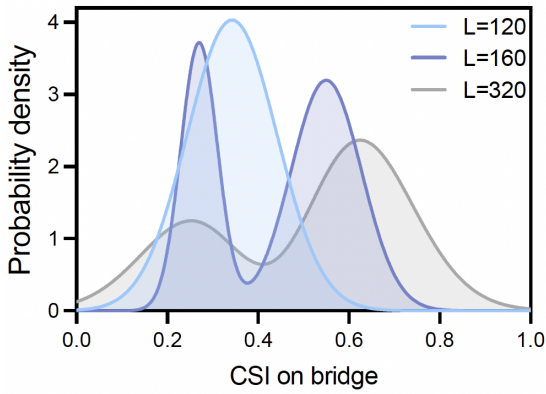

Figure 5.2: *Probability density of cell shape index. Gaussian fits of the probability density of cell shape index (CSI) for bridge lengths: L=120 (light blue, R^2=0.8257), L=160 (dark blue, R^2=0.8257), and L=320 µm (grey, R^2=0.9492), from N≥3 replicates for each condition.*

These distinct CSI subpopulations suggest the coexistence of different migratory phenotypes, which may reflect underlying differences in cell contractility—major regulator of cell shape. Amoeboid phenotypes are typically associated with strong rear-localized phosphorylated Myosin Light Chain (pMLC) staining, whereas mesenchymal states exhibit more homogeneous pMLC distribution. To investigate whether these morphological differences reflect pre-existing heterogeneity in cellular contractility, we performed immunostaining for pMLC, a key regulator of contractility and actin–myosin cytoskeletal dynamics (Figure 5.3A).

To evaluate the intrinsic contractile state of the initial non-confined cell population, we cultured MCF-10A cells on glass surfaces functionalized with the same concentration of fibronectin used for micropatterns. Immunostainings revealed a unimodal distribution of pMLC fluorescence intensity (Figure 5.3B), indicating a continuum of contractility levels rather than discrete subpopulations. After 24 h, most of the cell population was well spread and exhibited actin stress fibers containing myosin II, indicative of a mesenchymal migratory phenotype[119]. We speculate that rounder cells corresponded to those in mitosis, either about to enter or just exiting the process. These results suggest that the initial MCF-10A population does not exhibit inherent heterogeneity in contractility.

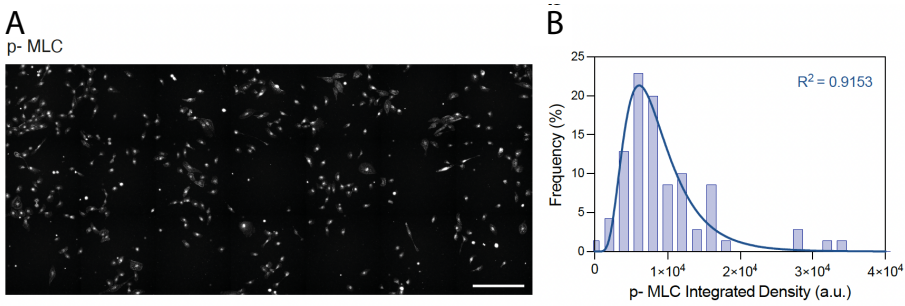

Figure 5.3: *Distribution of pMLC expression in MCF-10A cells.* ***(A)*** *Large microscopy image of individual MCF-10A immunostained for the phosphorylated form of the myosin light chain (pMLC) after 24 hours of culture on an FN-coated glass coverslip. Scale bar, 300 μm.* ***(B)*** *Distribution of pMLC in a population of MCF-10A cells (n = 77).*

Furthermore, not all crossings were successful, and success appeared correlated with CSI. To quantify this observation, we tracked back-and-forth motions by time-lapse imaging for the different bridge lengths. This enabled quantification of the percentage of failed passages (Figure 5.4A), during which cells reversed direction before reaching the square at the opposite end, versus successful passages (Figure 5.4B), during which cells successfully traversed the entire bridge before spreading in the opposite square. Interestingly, we observed that cells crossed longer bridges more efficiently: the probability of an attempt (defined as a protrusion entering the bridge) to result in a successful transition increased with bridge length, reaching ≈91.6 % on the longest bridges of 160 μm (Figure 5.4C). Surprisingly, this high rate of successful crossings is directly linked to the compacted morphology, which appears to be much more effective for navigating through long and narrow environments (Figure 5.4D).

Together, these findings reveal that the emergence of two discrete morphological states—elongated and compacted—occurs only beyond a critical bridge length of 120 μm, which notably exceeds the average maximum elongation capacity of MCF-10A cells (≈100 μm). This morphological switch likely reflects an adaptive response to persistent confinement and is associated with efficient migration through long, narrow gaps.

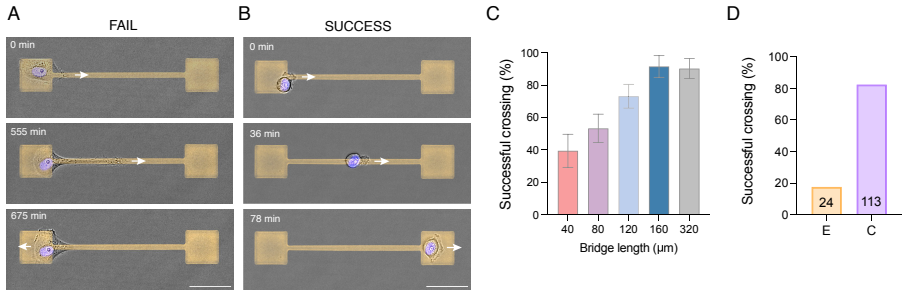

Figure 5.4: *Time-lapse sequence of* ***(A)*** *a failed and* ***(B)*** *a successful crossing on a bridge of W=6 µm and L=160 µm. Arrows show the direction of migration. Scale bar, 50 µm. Percentage of successful crossings for* ***(C)*** *bridges of varying lengths (n = 116 for 40 µm, n=76 for 80 µm, n=109 for 120 µm, n=87 for 160 µm and n=184 for 320 µm from N≥3 replicates per condition) and* ***(D)*** *elongated (n=24) versus compacted (n=113) morphologies on L=160 µm. Error bars represent the standard deviation (SD) in* ***(C)****. *p< 0.05, **p< 0.01, ****p< 0.0001, n.s. = not significant (Student's t-test, two-tailed, unequal variances). Boxplots range from the first quartile (Q1) to the third quartile (Q3), with the median (50th percentile) indicated by a line. Whiskers extend from the box to the minimum and maximum data points within* 1.5 *times the interquartile range.*

5.2 Symmetry breaking and polarization drive cell shape dynamics.

To explore the link between cell morphology and confined migration efficiency—measured by the percentage of successful crossings—we quantified back-and-forth cell movements over a 20-hour period and color-coded the trajectories based on CSI (Figure 5.4A-D), revealing striking differences in migration dynamics between the two morphologies (Figure 5.5A). Compacted cells exhibited an average crossing speed three times faster than elongated morphologies Figure 5.5B) and three times shorter dwell times—defined as the time spent on the square areas—compared to elongated cells (Figure 5.5C). Actin flow analysis in the lamellipodia (Figure 5.5D) of both morphologies revealed a significantly higher retrograde flow in compacted cells (Figure 5.5E-F), a hallmark of fast-migrating cells[185]. Interestingly, morphological switches from an elongated to a more compacted state have been previously observed during the migration of breast epithelial cells in collagen microtracks with a high level of spatial confinement[166]. Furthermore, the intrinsic relationship between

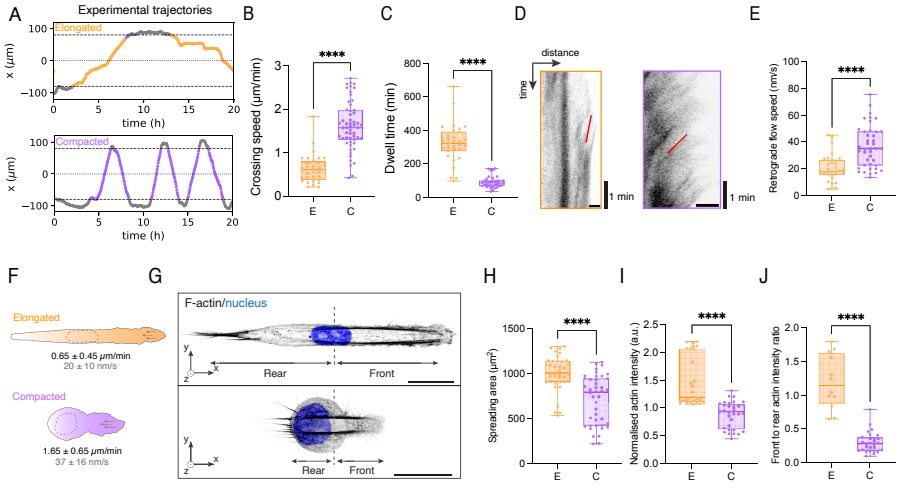

Figure 5.5: *Impact of symmetry breaking and polarization states on cell dynamics.* ***(A)*** *Experimental trajectories for an elongated (top) and a compacted (bottom) cell morphology on a micropatterned dumbbell (160 μm long, 6 μm wide). Trajectories are color-coded to show square zones, elongated (CSI<0.4), and compacted morphologies (CSI>0.4).* ***(B)*** *Crossing speed (n=32 for elongated, n=55 for compacted, and N=16) and* ***(C)*** *dwell time for elongated (n=31 and N=16) and compacted (n=36 and N=16) cell morphologies.* ***(D)*** *Kymographs of the actin flow (Scale bars, 2 μm) and* ***(E)*** *quantification of the retrograde actin flow speed in the lamellipodia elongated and compacted cells.* ***(F)*** *Representative sketch of elongated (n=32, N=3) and compacted (n=4, N=3) morphologies with their associated mean cell speed and retrograde actin flow. Arrows show the direction of the retrograde flow.* ***(G)*** *Representative confocal image in super-resolution mode of elongated (top) and compacted (bottom) morphologies of MCF-10A cells. Scale bars: 20 μm (top) and 25 μm (bottom).* ***(H)*** *Spreading area (n=37 for elongated, n=42 for compacted, N=3),* ***(I)*** *normalized actin density (n=28 for elongated, n=33 for compacted, N=3).* ***(J)*** *Front-to-rear actin intensity ratio (n=12 for elongated, n=28 for compacted, N=3).*

adopting a compacted mode and the increase in migration speed has been observed for other cell types in different confinement situations, such as migration on glass fibers with a diameter similar to the bridge[160] width (Figure 5.6A) or within collagen matrices[161] (Figure 5.6B).

High-resolution confocal microscopy (Figure 5.5G) revealed that elongated cells are larger, display a relatively uniform F-actin distribution along their length, and contain a higher overall density of actin filaments (Figure 5.5H-I) compared to compacted cells. While some front–rear asymmetries can be

observed, such as F-actin enrichment at the leading edge and a stem-like rear, the overall morphology remains less polarized than that of compacted cells. In contrast, compacted cells adopt a highly asymmetric shape characteristic of migrating cells, with a broad leading edge and a rounded rear (Figure 5.5G, bottom), as well as significantly smaller spreading areas (Figure 5.5H) and lower total actin filament density (Figure 5.5I). Pronounced F-actin asymmetry in compacted cells (Figure 5.5J) further reinforces their polarized morphology, a hallmark of fast migration[157].

In collaboration with David Brückner, we used a theoretical model to test the hypothesis that the distinct migratory dynamics of compacted versus elongated cells arise from a symmetry-breaking event in cell polarity. The modeling approach developed by David Brückner has two key goals: first, to identify a minimal description of the polarity dynamics of elongated vs compacted cells that quantitatively captures the key experimental statistics. Second, to provide a framework to test the predicted statistics of various implementation of the dynamic switching between these to morphological states that we can compare to experiment. In this context, we explored a minimal biophysical model of active migration under confinement. In the following sections, we present the key elements of David Brückner's model, enabling the reader to appreciate the role of critical parameters and to assess how its predictions compare with our experimental findings.

Specifically, cells were modeled as polar particles exerting active migration forces in a direction of polarity $p = (p_x, p_y)$. The dynamics of cell position x(t) are then described by $\frac{dx}{dt} = p_x + F(x)$, where F(x) is a repulsive force arising at the left and right edge of the micro-pattern to ensure confinement, reflecting the absence of ECM adhesion outside the adhesive track and ensuring confinement consistent with the experimental setup (see Supp. Theory Note in [186] for further details). To describe the dynamics of cell polarity, a minimal model was used that allows both states in which cells are unpolarized (corresponding to morphologies with two opposing protrusions), and states in which cells are highly polarized in the direction of a single protrusion. Specifically, it was

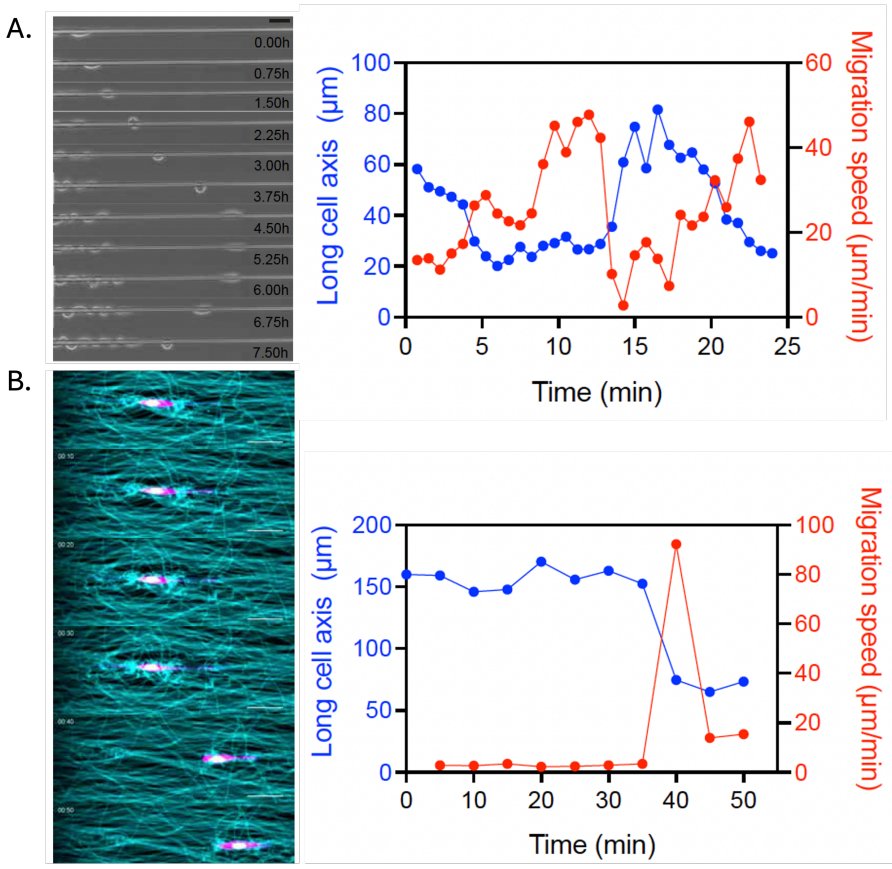

Figure 5.6: *Examples of morphological switch on glass fiber and in 3D collagen fiber matrix.* ***(A)*** *Time-lapse sequence of a single MDCK epithelial cell migrating on a smooth glass wire (diameter = 5.3 µm). After detaching from the tissue, the epithelial cell rounds up and migrate on the glass fiber. The temporal evolution of the long cell axis and the migration speed indicates that the cell morphological switch from an elongated to a compacted morphology is associated with an increase in migration speed. Scale bar, 50 µm. Adapted with permission from [160].* ***(B)*** *Time-lapse sequence of a single fibroblast (NIH3T3) migrating in a 3D matrix composed of aligned collagen fibers. Scale bar, 50 µm. The temporal evolution of the long cell axis and the migration speed indicates that the cell morphological switch from an elongated to a compacted morphology is associated with an increase in migration speed with a maximum speed around 80 µm/min. Adapted with permission from [161].*

hypothesized that the dynamics of cell polarity follow

$$\dot{p} = (-\beta|p|^2 - \alpha)p + \gamma F(x) + \sigma\xi(t)$$

with β>0, where γ quantifies the tendency of cells to repolarize upon contact with the micropattern boundary, and ξ(t) is a Gaussian white noise modeling fluctuations of the cell polarization. Different states of polarization are determined by the parameter α: for positive α, the cell polarization stochastically fluctuates around a mean-zero polarization state (Figure 5.7A—Top). For negative α, the cell is highly polarized, with a non-zero mean polarity (Figure 5.7A—Top). Simulations of the model with positive and negative α produced trajectories in close agreement with those observed for elongated and compacted cell morphologies, respectively (Figure 5.7B) (Supp. Movie S1). Fitting α-values to the experimentally measured crossing speeds, we indeed find positive and negative α for elongated and compacted cells, respectively (see Supp. Theory Note in [186] for further details). This model correctly captures that compacted cells were faster (Figure 5.7C) and spend less time on the square islands between transitions, as quantified by the dwell time(Figure 5.7D). Furthermore, this model captures key features of the qualitative nature of the nonlinear dynamics of elongated and compacted cells during their transition across the bridge. Elongated cells should exhibit a stable fixed point at vanishing speed v=0, indicating that they are susceptible to stochastic fluctuations, leading to frequent changes in direction (Figure 5.7E). Compacted cells exhibit two stable fixed points at finite speed, leading to a highly persistent crossing of the bridge at a fixed speed. These modeled dynamics can be measured experimentally by inferring the cell's average acceleration as a function of its velocity for elongated and compacted cells[187] (Figure 5.7F) (see Supp. Theory Note in [186] for further details).

This result confirmed the hypothesized qualitative difference in nonlinear dynamics, with compacted cells exhibiting a pronounced separation of two stable fixed points at finite speeds v $\approx$ 2 μm/min, closely matching the typical measured crossing velocity. Collectively, our findings demonstrate that compacted and elongated morphologies are associated with distinct migratory behaviors, governed by different polarization states under confinement.

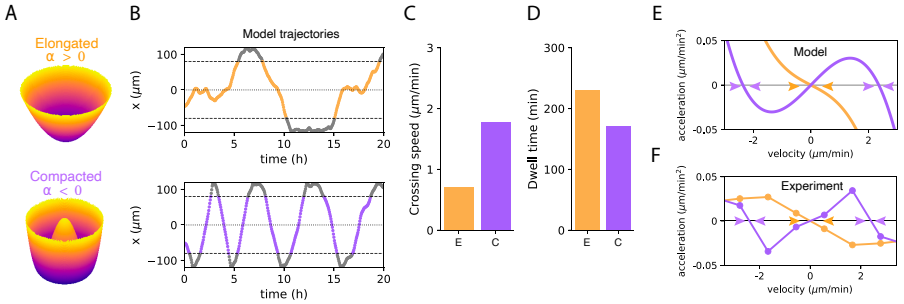

Figure 5.7: ***(A)*** *Representation of cell polarity dynamics with $\alpha>0$ when cell polarization stochastically fluctuates around a zero-mean polarization state (top), and $\alpha<0$ when the cell is highly polarized (bottom), with a non-zero mean polarity.* ***(B)*** *Representative trajectories,* ***(C)*** *crossing speed and* ***(D)*** *dwell time estimated by the model. Cell morphologies and time spent on squares are color-coded. Average acceleration of elongated vs compacted cells as a function of the cell velocity as* ***(E)*** *estimated by the model and* ***(F)*** *measured experimentally ($n=57$ cells, $N=16$). Purple arrows show the presence of stable fixed points at finite speeds $v\approx 2$ μm/min close to experimental crossing speed values, while orange arrows show $v=0$ where both curves cross each other. $****p < 0.0001$ (Student's t-test or Kruskal-Wallis test). Boxplots range from the first quartile (Q1) to the third quartile (Q3), with the median (50th percentile) indicated by a line. Whiskers extend from the box to the minimum and maximum data points within 1.5 times the interquartile range.*

To investigate molecular differences between polarization states, we analyzed key markers involved in cell polarity, including vinculin-containing adhesion sites, Golgi positioning, β-tubulin distribution, and Arp2/3 fluorescence intensity. Both elongated (Figure 5.8A) and compacted (Figure 5.8B) cells exhibited actin filament accumulation and vinculin-rich adhesions at the leading edge, primarily at the cell periphery. This peripheral localization is consistent with a highly motile phenotype, where cells typically form smaller, more dynamic adhesion complexes. Adhesion sites were classified into three categories based on area: nascent adhesions (NAs; <0.5 μmμm^2), focal complexes (FCs; 0.5–1 μm^2), and focal adhesions (FAs; >1 μm^2). Elongated cells displayed a comparable proportion of NAs and FCs, but a lower frequency of FAs. In contrast, compacted cells exhibited a higher proportion of NAs, a similar proportion of FCs, and significantly fewer FAs compared to elongated cells (Figure 5.8C-D).

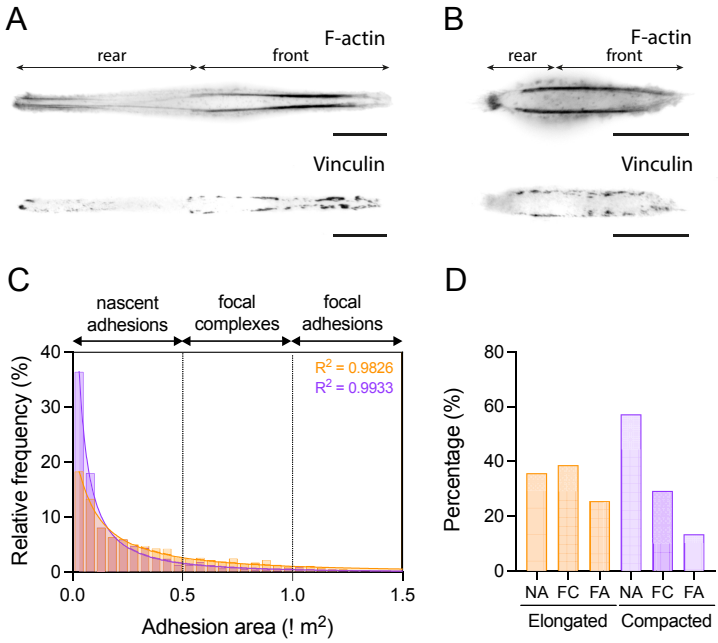

Figure 5.8: *Polarization markers in elongated and compacted cells. Typical images of the spatial distribution of actin filaments (top) and vinculin-containing adhesions (bottom) in* ***(A)*** *elongated and* ***(B)*** *compacted MCF-10A cells migrating on an FN dumbbell, 160 µm in length.* ***(C)*** *Distribution and* ***(D)*** *percentage of nascent adhesions (NA<0.5 µm^2), focal complexes (0.5 µm^2<FCs<1 µm^2), and focal adhesions (FA>1 µm^2) in elongated in orange (n = 1484 adhesions, N = 3) and compacted in purple (n = 727 adhesions, N = 3) cells.*

The spatial distribution of adhesions was similarly front-biased in both morphologies, with 77.3±16.7% in elongated cells and 82.0±11.7% in compacted cells (Figure 5.9A), with no statistically significant difference. The adhesive area at the front accounted for 2.3±1.2% and 1.6±0.9% of the total spreading area in elongated and compacted cells, respectively (Figure 5.9B). At the rear, this area was reduced to 1.0±0.9% in elongated cells and 0.5±0.3% in compacted cells (Figure 5.9C), a distribution consistent with that observed in fast-migrating phenotypes. This observation aligns with previous studies of polarized migration on micro-patterns[188], reinforcing the idea that compacted morphologies exhibit a higher degree of polarization.

To further characterize these polarization states, we examined Golgi apparatus positioning, a well-established readout of front–rear polarity during directed migration. In elongated, less polarized cells, the Golgi was typically positioned toward the leading edge, whereas in compacted, more polarized cells, it was relocated behind the nucleus (Figure 5.10A-D). This posterior positioning of the Golgi is characteristic of cells undergoing persistent migration and has been linked to enhanced directional stability. Supporting this, super-resolution imaging revealed a strong accumulation of microtubules at the leading edge in compacted cells (Figure 5.10E), consistent with recent evidence that microtubule enrichment at the front is essential for maintaining persistent polarized migration[189, 87]. In polarized cells, the Arp2/3 complex accumulates at the leading edge, where it nucleates branched actin networks that support lamellipodial protrusion; by contrast, reduced polarity is often associated with a diffuse cytoplasmic distribution of Arp2/3[190].

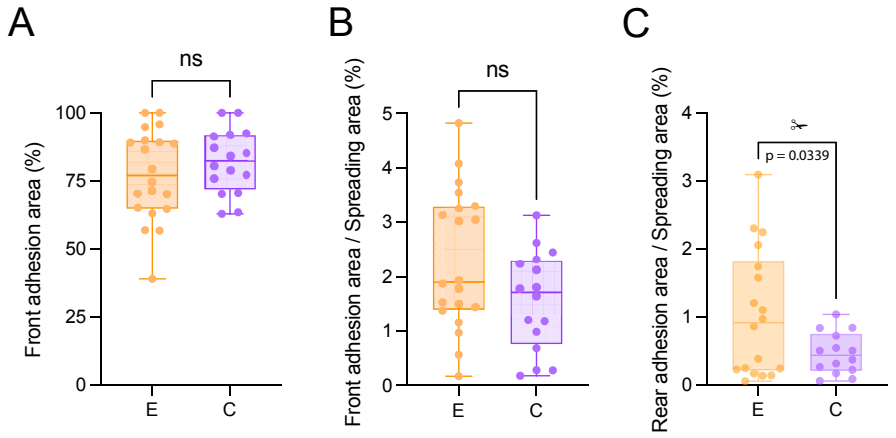

Figure 5.9: *Distribution of* ***(A)*** *the percentage of adhesion area at the front edge,* ***(B)*** *the ratio between the adhesion area at the front edge and the total spreading area (n = 20 for elongated, n = 16 for compacted N = 3), and* ***(C)*** *the ratio between the adhesion area at the rear edge and the total spreading area for elongated in orange (n = 18, N = 3), and compacted in purple (n = 14, N = 3) cell morphologies with p=0.0339. Boxplots range from the first quartile (Q1) to the third quartile (Q3), with the median (50th percentile) indicated by a line. Whiskers extend from the box to the minimum and maximum data points within 1.5 times the interquartile range. *p < 0.05 and n.s. is not significant.*

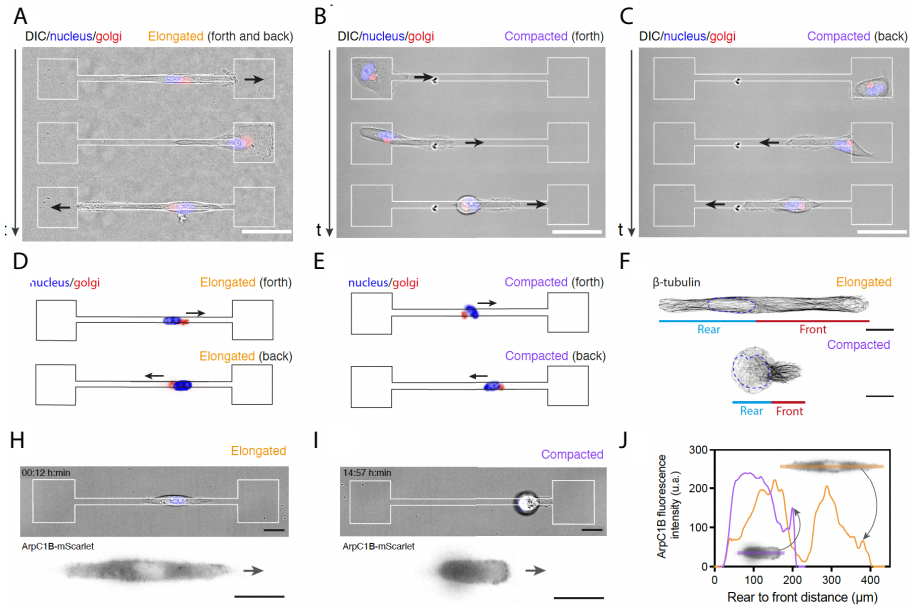

Figure 5.10: *Markers of polarity states in elongated and compacted morphologies. Representative sequence of Golgi positioning during the back-and-forth motion of an MCF-10A cell migrating on a dumbbell-shaped micropattern, adopting either* ***(A)*** *an elongated or* ***(B-C)*** *a compacted morphology. The cell is imaged in DIC mode, the nucleus is shown in blue and the Golgi in red. Scale bars, 50 μm. Representative spatial distribution of the Golgi apparatus located in front of the nucleus in* ***(D)*** *elongated cells and behind the nucleus in* ***(E)*** *compacted cells.* ***(F)*** *Representative spatial distribution of β-tubulin in the front and rear regions of elongated and compacted cells. Scale bar, 10 μm. ArpC1B-mscarlet is homogeneously distributed in* ***(H)*** *elongated cells, whereas in* ***(I)*** *compacted cells it accumulates in the cell body and is enriched at the front of the lamellipodia.* ***(J)*** *Superimposed intensity profiles of ArpC1B–mScarlet in elongated (orange) and compacted (purple) morphologies reveal an accumulation of Arp2/3 at the leading edge of compacted cells. Profiles are those for the cells in* ***(H)*** *and* ***(I)****.*

To further evaluate front–rear polarity, we performed time-lapse imaging of MCF-10A cells expressing ArpC1B–mScarlet cultured on dumbbell-shaped micropatterns (Figure 5.10F-G). In compacted cells, Arp2/3 fluorescence was significantly enriched at the leading edge (Figure 5.10H), consistent with its well-established role in driving lamellipodial protrusion and maintaining directional migration[191]. We also analyzed the temporal dynamics of Arp2/3 activity during back-and-forth migration events (Figure 5.11A). Notably, Arp2/3

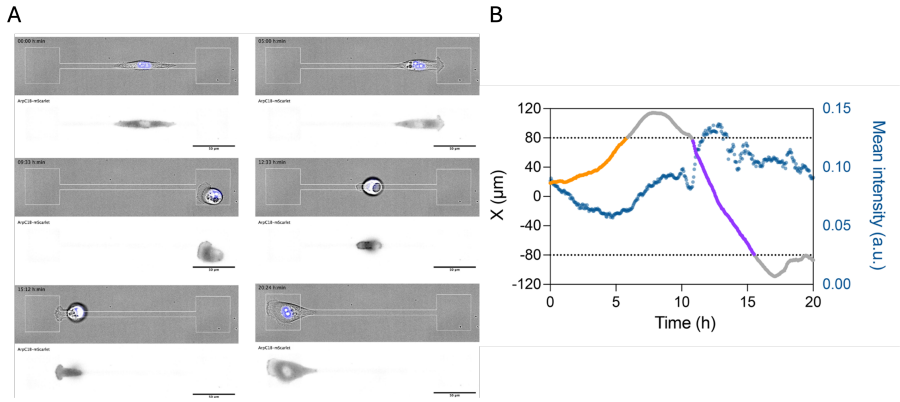

Figure 5.11: *Arp2/3 localization during a morphological switch.* ***(A)*** *Typical sequence extracted from a time-lapse experiment with an MCF-10A cell expressing ArpC1B tagged with mScarlet, migrating for 22 hours on a dumbbell micropattern 160 µm in length. Scale bar, 50 µm. The top images show the cell in Differential Interference Contrast (DIC) mode, while the bottom images display the fluorescence signal of ArpC1B, a subunit of the Arp2/3 complex, which is critical for actin filament nucleation and branching.* ***(B)*** *Evolution of the mean cell intensity (in blue) over time, superimposed with the color-coded trajectory of the MCF-10A cell expressing ArpC1B. The trajectory is represented as elongated (orange), compacted (purple), and positions within the square zone (gray).*

fluorescence intensity increased significantly during morphological transitions from the elongated to the compacted state (Figure 5.11B), indicating a shift toward enhanced front–rear polarization. Altogether, these findings demonstrate that compacted cells exhibit a higher degree of front–rear polarity compared to elongated cells, consistent with our theoretical model, in which cells are modeled as active particles capable of adopting either a high-polarity (compacted) or low-polarity (elongated) state.

5.3 Dynamic morphological switch is controlled by local geometry.

Importantly, single cells migrating in a confined environment can alternate between elongated and compacted morphologies. This leads to morphological switch events during migration (Figure 5.12 and Figure 5.13A), which are accompanied by an immediate change in migration speed, consistent with our previous results (Figure 5.5B).

This raises a central question: what are the statistical rules of cells switching between these two distinct morphological states? To address this question, we analyzed the evolution of cell shape over time during crossing events (Figure 5.13B), using numerous experimental trajectories extracted from 20-hour time-lapse movies. Based on the CSI, we automatically assigned in these trajectories the time spent in the elongated mode (orange), compacted mode (purple), and on the deconfinement squares (gray) (Figure 5.13C). Interestingly, we found that the percentage of compacted cells, defined as having an average CSI on the bridge greater than 0.4 (Figure 5.13D), strongly increased with the bridge length, reaching ≈58% for a bridge length of 160 μm (Figure 5.13B).

Previous theoretical work suggests that the polarity dynamics of cells adapt to local micropattern geometry[192], raising the question of whether a dependence of dynamical switching on local confinement could explain the dependence of morphological states on bridge length. Since a model with con-

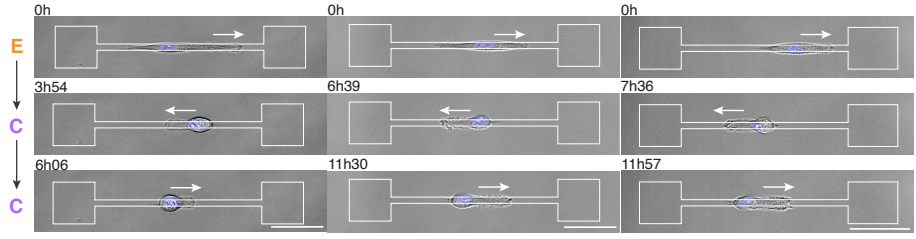

Figure 5.12: *Representative examples of morphological switches. Three representative examples of cells transitioning from an elongated to a compact state during back-and-forth migration on fibronectin-coated dumbbell-shaped micropatterns (160 μm-long and 6 μm-wide bridge). Scale bar, 50 μm.*

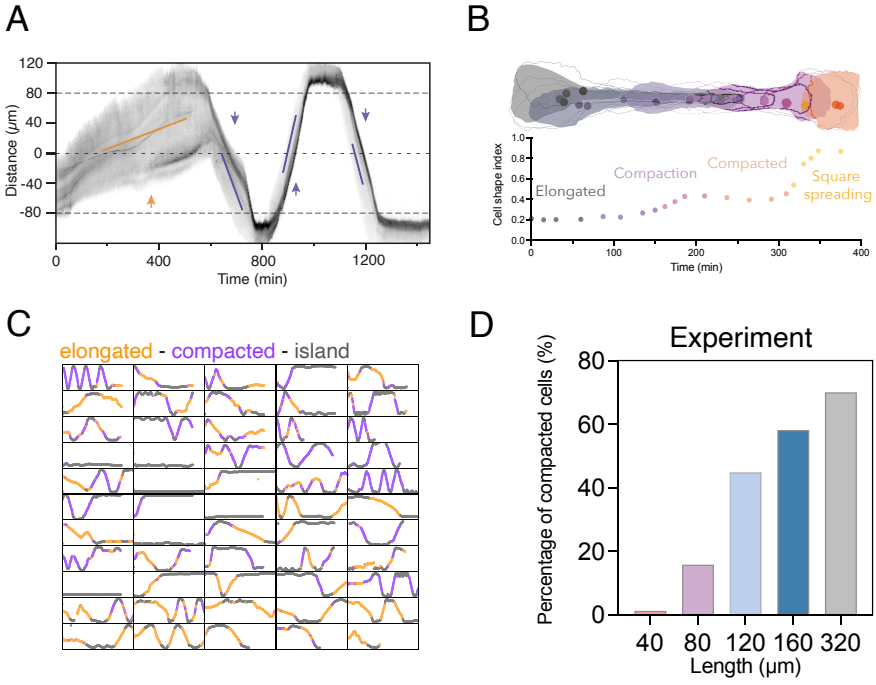

Figure 5.13: *Morphological switch dynamics and mechanical memory.* ***(A)*** *Representative kymograph of a migrating cell tagged for actin with Spy555-FastAct, showing a transition from an elongated to a compacted state over a 24-hour time lapse.* ***(B)*** *Representative color-coded outline of an MCF-10A cell undergoing a morphological switch on a dumbbell micropattern, alongside the corresponding evolution of the CSI vs time.* ***(C)*** *Selection color-coded cell trajectories (n=55, N=11) of individual MCF-10A cells migrating on FN dumbbell micropatterns for 20 hours. Trajectories are color-coded to represent square zones (islands), elongated (CSI<0.4), and compacted (CSI>0.4) morphologies.* ***(D)*** *Percentage of compacted cells for varying bridge lengths (n=116 for L=40 μm, n=76 for 80 μm, n=109 for 120 μm and n=87 for 160 μm, from N≥3).*

stant fixed switching rate cannot capture the length-dependence of compacted states, the Brückner's group extended their model to include geometry-sensitive stochastic switching between elongated and compacted cells (Figure 5.14A). Motivated by the idea that lateral confinement could drive shape adaptation in cells, we hypothesized that cells are more likely to transition to a polarized ($\alpha<0$), compacted, state when they were highly confined on the bridge and more likely to revert to an unpolarized ($\alpha>0$), elongated state upon reaching the

island. To model this, we assumed that the switching rates between the morphological states depend on the lateral width of the pattern (Figure 5.14A)(see Supp. Theory Note of [186]): the transition rate from elongated to compacted $r_{E\to C}$, increases proportionally as the width decreases when the cell moves from island into the confining bridge. Conversely, we assume that the rate of switching from compacted to elongated $r_{C\to E}$ increases proportionally with width when the cell exits the bridge and spreads onto the island. While we cannot rule out more complex dependencies of the switching rates on local width, such as different dependencies for compacted vs elongated cells, this provides a minimal model for the geometry-sensitive nature of the switch and is implemented through position-dependent switching rates $r_{E\to C}$ (x), and $r_{E\to C}$ (x), as illustrated in Figure 5.14A.

This minimal model captured an increase in the percentage of compacted morphologies with bridge length (Figure 5.14B), as observed experimentally (Figure 5.13D). Furthermore, the model suggested a further increase in the percentage of compacted cells in confining systems without islands (to 70%, Figure 5.15A). To test this, we confined cells to 1D micro-patterned lines of 500 μm long (Figure 5.15B) and we analyzed their shape during their back-and-forth motion (Figure 5.15C), indicating an increase of the percentage of compacted cells (Figure 5.15D), in agreement with the model's outcome.

Together, these findings indicate that cells dynamically switch between elongated and compacted morphologies in a geometry-sensitive manner.

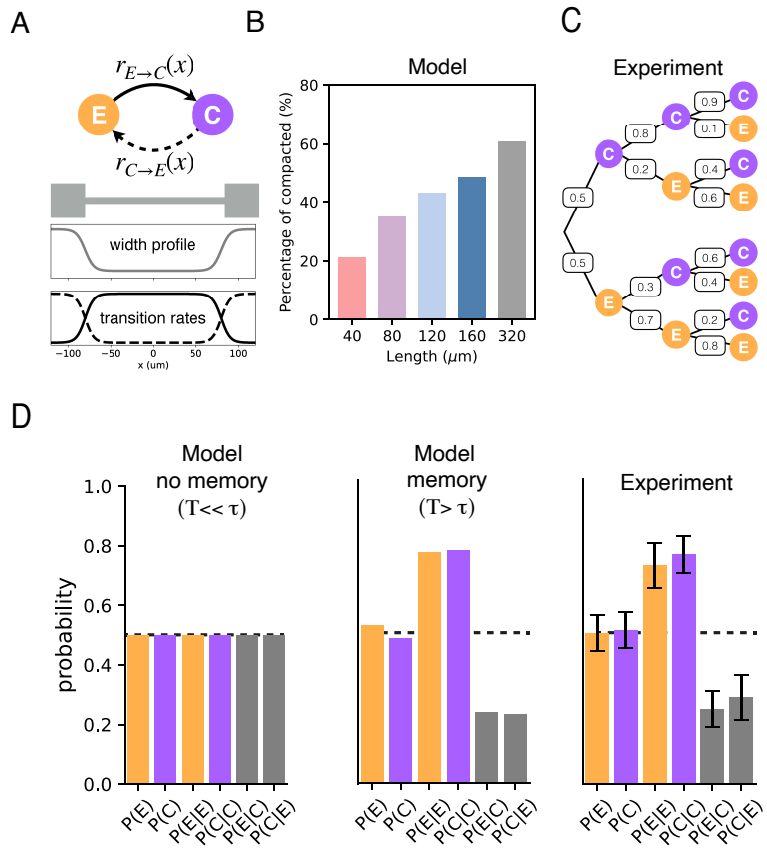

Figure 5.14: *Morphological switch dynamics and mechanical memory.* ***(A)*** *Sketch of the geometry-sensitive stochastic switching between elongated and compacted cells, including the spatial dependence of the normalized switching rates.* ***(B)*** *Model estimation of the percentage of compacted cells for varying bridge lengths.* ***(C)*** *Statistical tree representation of the experimental probabilities for elongated and compacted states over three generation of successive crossings.* ***(D)*** *Histogram representation of the probabilities for elongated, P(E), and compacted, P(C), states for various combinations of morphological switches: elongated to elongated P(E|E), compacted to compacted P(C|C), elongated to compacted P(E|C) and compacted to elongated P(C|E). Error bars represent SD (n=55, N=11).*

5.4 Cell memory links morphological states across transitions.

We next investigated the overall timescales of the switching process. A key parameter in the theoretical model is the average timescale between switches, T. If this timescale exceeds the average dwell time τ, the morphological state

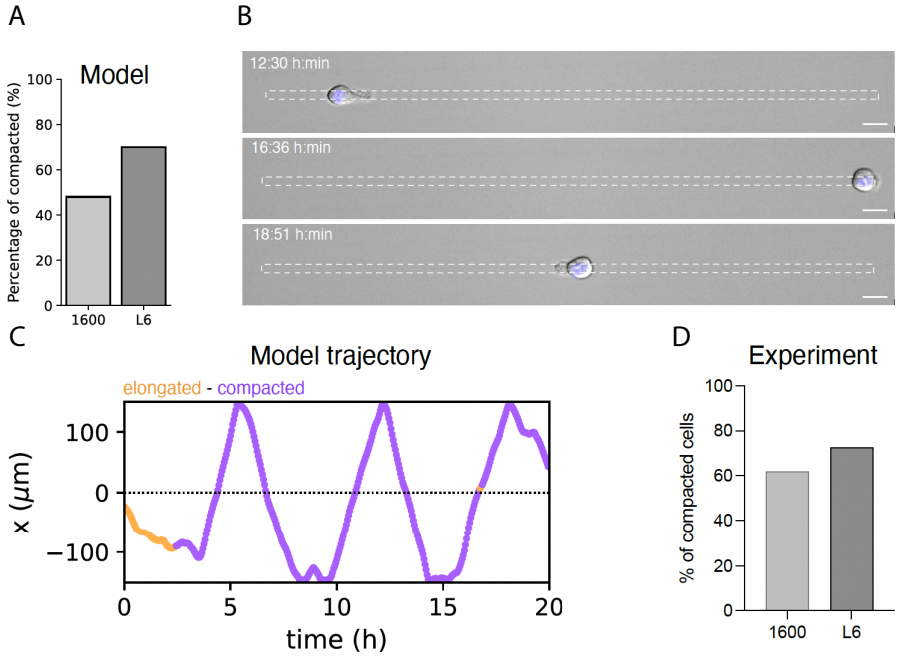

Figure 5.15: *Semi-infinite narrow segments.* ***(A)*** *Theoretical expectation of the percentage of compacted cell on the bridge of dumbbells (W=6 μm and L=160 μm) with square area of 1600 μm^2 versus 1D semi-infinite line of W=6 μm and L=500 μm. On 6 μm line, percentage of compacted cell is expressed as the percentage of time spent under the compacted morphology over a 20-hour time-lapse.* ***(B)*** *Time-lapse sequence of a compacted cell morphology migrating on a one-dimensional (1D) micropatterned line of W=6 μm and L=500 μm. Scale bar, 20 μm.* ***(C)*** *Representative color-coded trajectories with elongated (CSI<0.4) and compacted (CSI>0.4) morphologies.* ***(D)*** *Percentage of compacted cells on the bridge of dumbbells (W=6 μm and L=160 μm) with square area of 1600 μm^2 (n= 56, N = 16) versus 1D semi-infinite line of W=6 μm and L=500 μm (n=10, N = 2). On 6 μm line, percentage of compacted cell is expressed as the percentage of time spent under the compacted morphology over a 20-hour time-lapse.*

of cells in subsequent transitions is expected to be correlated.

During any given transition, the probability of a cell being either elongated or compacted is 50% ($L = 160\mu$m, Figure 5.14C-D and Figure 5.16). In the absence of long-term memory ($T \ll \tau$), we expect these probabilities to be independent of the morphological state during the previous transition (Figure 5.14D). In the case where $T > \tau$, cells are more likely to remain in the same morphological state (Figure 5.14D).

Experimentally, we found strong correlations across transitions: after a compacted transition, $75 \pm 5\%$ of cells remained compacted in the subsequent transition, while $72 \pm 6\%$ of previously elongated cells retained their elongated state (Figure 5.14C-D). In contrast, a memory-free process determined by the probabilities of the first passage would predict only $50 \pm 5\%$ retention. Similarly, the third consecutive transition also exhibits memory effects, with probabilities of $88 \pm 6\%$ for compacted cells and $78 \pm 8\%$ for elongated cells (Figure 5.14C).

These correlations across transitions are quantitatively captured by our model for a switching time $T \approx 2.3\tau \approx 10$ h. Given that the percentage of successful crossings is highest on 160 and 320 μm bridges (Figure 5.4H), and that cells retain their morphological state across transitions on 160 μm bridges, we next investigated the memory process on 320 μm bridges by tracking cell morphology over time in 50 time-lapse experiments, each lasting 40 hours (Figure 5.17A).

We used the Cell Shape Index (CSI) to automatically quantify, for each trajectory, the time spent in the elongated state (orange), the compacted state (purple), and within the deconfinement zones (grey) (Figure 5.17B). As observed on 160 μm bridges, we found strong correlations across transitions (Figure 5.17C). Following a compacted transition, $71 \pm 5\%$ of cells remained compacted in the subsequent transition, while $60 \pm 3\%$ of previously elongated cells retained their elongated state (Figure 5.17D), in agreement with the theoretical model.

Together, these findings demonstrate that cells "memorize" their morphological state across transitions. This raises a key question: how is this memory

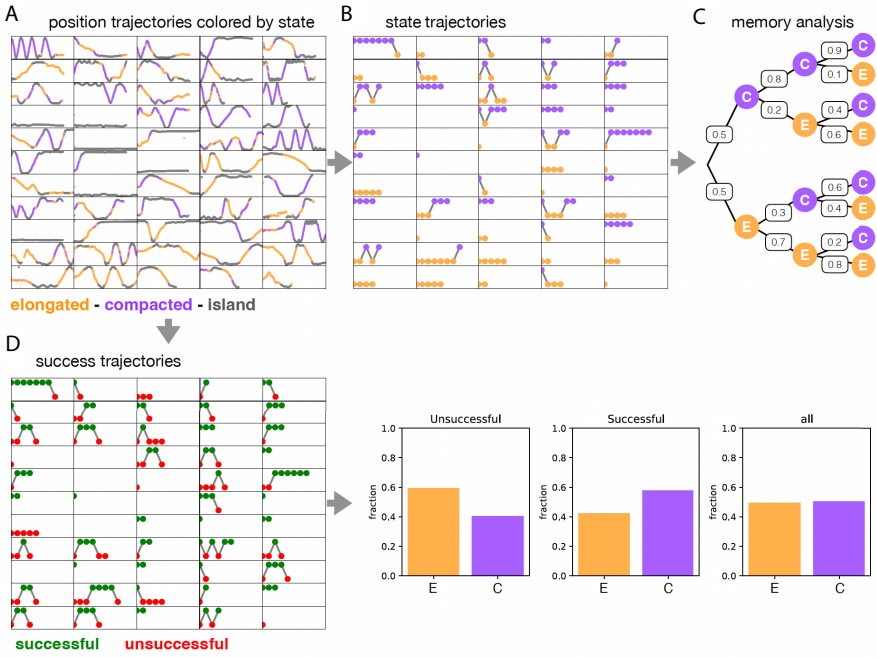

Figure 5.16: *Analysis of memory dynamics from cell trajectories.* ***(A)*** *Selection of n=55 color-coded single cell trajectories of individual MCF-10A cells migrating on FN dumbbell micropatterns for 20 hours. Trajectories on the bridge are color-coded by state: elongated (CSI<0.4) and compacted (CSI>0.4) morphologies.* ***(B)*** *State trajectories computed from position trajectories in* ***(A)****. A morphological state is assigned to each transition on the bridge, based on the morphological state adopted for most time-points during each transition.* ***(C)*** *Memory analysis tree diagram for events C (compacted transition) and E (elongated transition) obtained from state trajectories in* ***(B)****. Numbers of the branches indicate probabilities.* ***(D)*** *Trajectories of successful and unsuccessful transitions, defined as follows: in successful transitions, the cell (nucleus) enters the bridge and transmigrates to the other island. In unsuccessful transitions, the nucleus enters the bridge and returns to the same island. Fraction of unsuccessful, successful and total transition, which are repartitioned into two categories, elongated and compacted.*

achieved, given that entry into the square is expected to lead to cell spreading and loss of polarization?

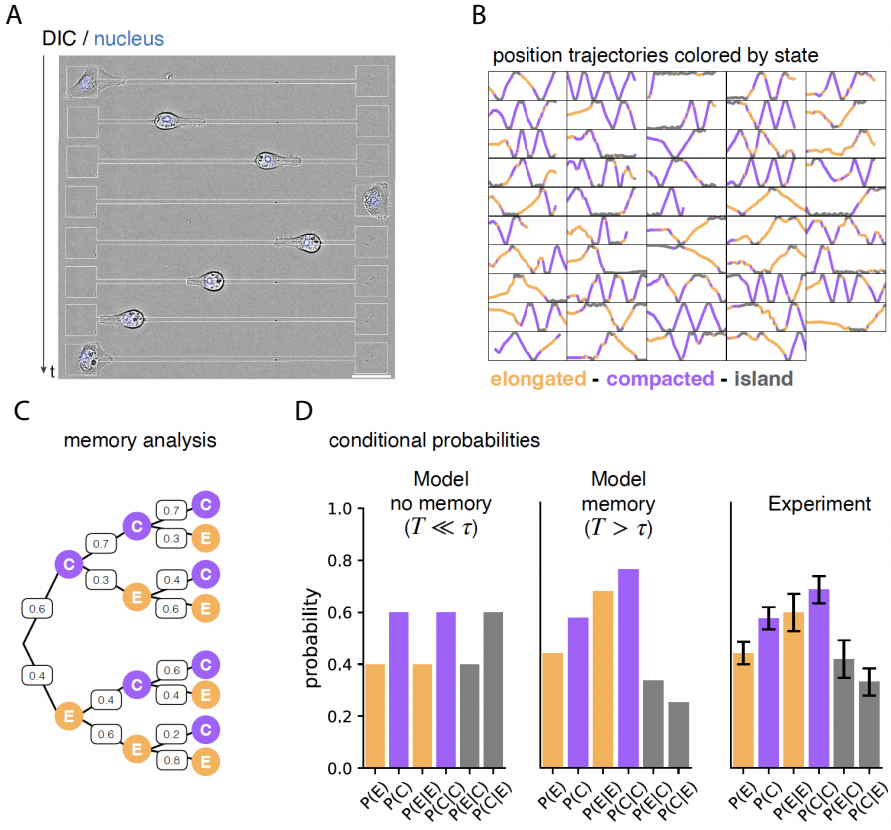

Figure 5.17: *Morphological switching dynamics and mechanical memory on 320 µm-long bridges.* ***(A)*** *Representative sequence of a back-and-forth motion of an individual MCF-10A cell migrating on an FN dumbbell micropattern with a 320 µm-long bridge.* ***(B)*** *Selection of n=50 color-coded cell trajectories of individual MCF-10A cells migrating on FN dumbbell micropatterns for 30 hours. Trajectories on the bridge are color-coded with elongated (CSI<0.4) and compacted (CSI>0.4) morphologies, and square zones.* ***(C)*** *Statistical tree representation of the experimental probabilities for elongated and compacted states over three generation of successive crossings (N≥3 replicates for each condition).* ***(D)*** *Histogram representation of the probabilities for elongated, P(E), and compacted, P(C), states for various combinations of morphological switches: elongated to elongated P(E|E), compacted to compacted P(C|C), elongated to compacted P(E|C) and compacted to elongated P(C|E). Data are presented as mean values ± SD.*

5.5 Compacted cells have a thicker actin cortex.

To identify the origin of the long-term memory of short-term confining events over short periods of time, we first hypothesized that migrating cells can remodel their matrix by secreting ECM proteins. We therefore investigated the possibility of physicochemical footprints left by cells during migration, which could potentially result in history-dependence of migration behaviors over an extended period.

We analyzed the biochemical composition of the FN micropattern after 5 hours of incubation with cells and at the end of the 20-hour imaging period (Figure 5.18A), using immunostaining for pre-coated and cell-produced laminin (Figure 5.18B-C), as well as fibronectin (Figure 5.18B-D). Our findings indicated no statistical difference in fibronectin or laminin intensity between the different conditions, suggesting no direct relation to a biochemical remodeling of the surface.

We therefore hypothesized that the organization of the cytoskeleton could give rise to a mechanical memory across transitions. To test this, we used super-resolution confocal microscopy to examine the architecture of the cytoskeleton, focusing on microtubules[193] and the actin cortex[194], which are key regulators of cell polarization and shape remodeling in confined environments.

In elongated cells, microtubules were uniformly distributed and aligned along the bridge axis (Figure 5.19A). In contrast, compacted cells exhibited a striking redistribution of microtubules toward the rear (Figure 5.19B). While both morphologies showed preferential microtubule alignment along the bridge axis at the front (Figure 5.19C), compacted cells displayed enhanced alignment along the vertical axis at the rear (Figure 5.19D), resulting in pronounced spatial asymmetry (Figure 5.19E).

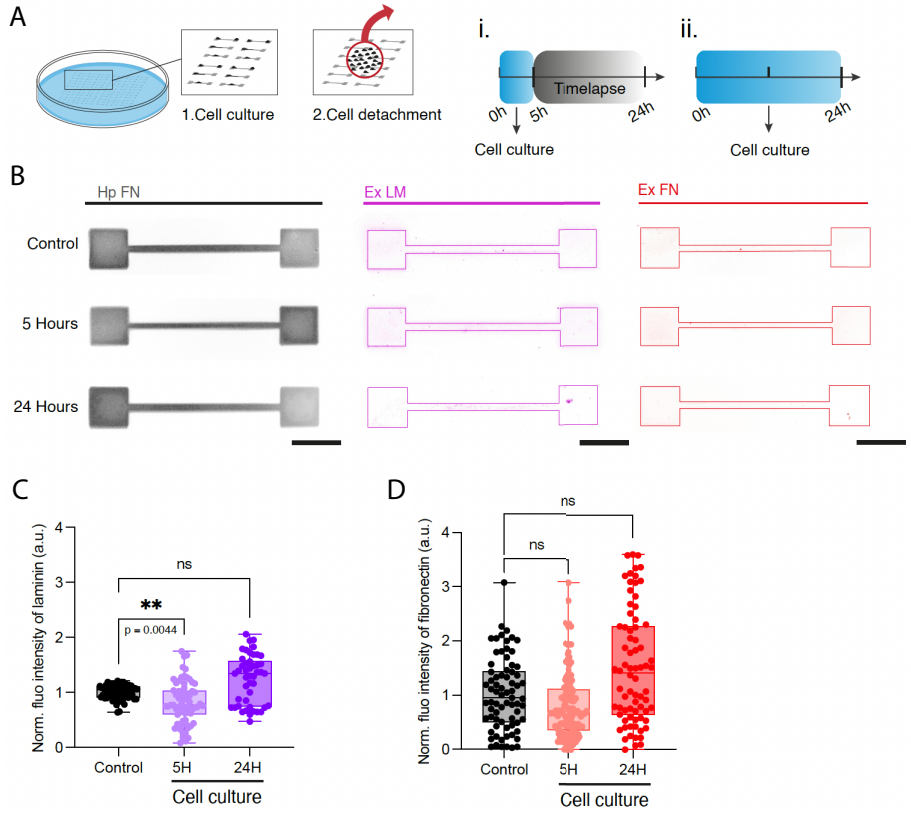

Figure 5.18: *Physico-chemical footprints.* ***(A)*** *Schematic representation of the two experimental procedures used to assess pattern conditioning by migrating cells. Cells were seeded on human plasma (hp) fibronectin (FN) micropattern, then detached and fixed either (i) after 5 hours (before the time-lapse) or (ii) 24 hours (after the time-lapse) of culture on micropatterns.* ***(B)*** *Epifluorescence images showing human plasma fibronectin, cellular laminin and cellular FN in control conditions after t=5h and t=24h of cell culture (top to bottom). Scale bar, 50 µm.* ***(C)*** *Normalized laminin intensity for control (n=62 patterns, N=3), 5-hour conditioning (n = 67 patterns, N=3), and 24-hour conditioning (n=46 patterns, N=3).* ***(D)*** *Normalized fibronectin intensity from control (n = 73 patterns, N=3), 5-hour conditioning (n=125 patterns, N=3), and 24 hour-conditioning (n=74 patterns, N=3). Boxplots range from the first quartile (Q1) to the third quartile (Q3), with the median (50th percentile) indicated by a line. Whiskers extend from the box to the minimum and maximum data points within* 1.5 *times the interquartile range.**$p < 0.01$, ns = not significant (Kruskal-Wallis test).*

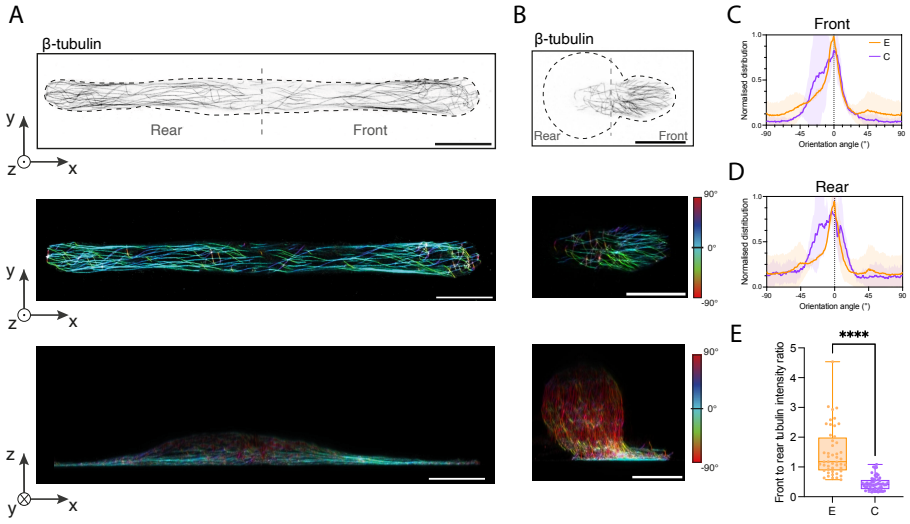

Figure 5.19: *Spatial distribution of microtubule filaments. Confocal microscopy images in super-resolution mode of the basal planes of* ***(A)*** *elongated (left) and* ***(B)*** *compacted (right) cell morphologies. β-tubulin staining (inverted image) and the cell body outline is represented with a black dashed line. Scale bar, 20 µm. In bottom images, β-tubulin filaments in elongated and compacted cells were color-coded according to their spatial orientation. Scale bar, 20 µm. Distribution of the normalized intensity of microtubules* ***(C)*** *at the front and* ***(D)*** *at the rear of elongated (n=3, N = 2) and compacted (n=2, N = 2) cell morphologies.* ***(E)*** *Front-to-rear tubulin intensity ratio of elongated (n=48, N=3) and compacted (n=54, N=3) morphologies during crossing events. Boxplots range from the first quartile (Q1) to the third quartile (Q3), with the median (50th percentile) indicated by a line. Whiskers extend from the box to the minimum and maximum data points within 1.5 times the interquartile range. ****p<0.0001 (Student's t test).*

Surprisingly, we found that actin cortex organization also varied significantly between morphologies. High-resolution imaging of elongated (Figure 5.20A) and compacted (Figure 5.20B) morphologies revealed that cortex thickness was nearly doubled in compacted cells (Figure 5.20C-D). This observation is consistent with recent findings suggesting that cortex thickness regulates internal stress and cortical tension, thereby influencing cell shape[44]. Furthermore, deeper penetration of myosin filaments into the actin cortex of compacted cells has been proposed to enhance cortical tension in this state[45].

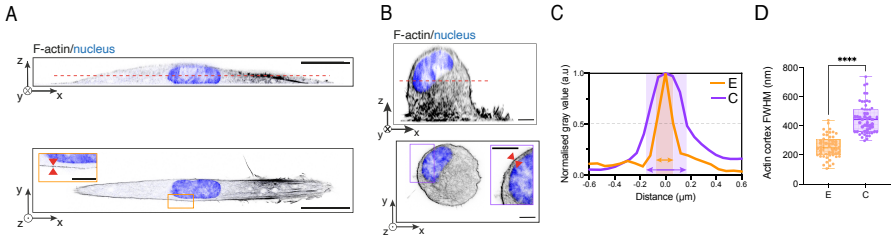

Figure 5.20: *Confocal microscopy images in super-resolution mode of side and top views of* ***(A)*** *elongated and* ***(B)*** *compacted cell morphologies. The zoom shows the thickening of the actin cortex in compacted cells. Scale bars, 20 µm for* ***(A)*** *and 5 µm for* ***(B)****.* ***(C)*** *Plot profile of the normalized actin intensity in the actin cortex for elongated and compacted cells. The light purple zone indicates the distance corresponding to the full width at half maximum (FWHM) in compacted cells.* ***(D)*** *FWHM for elongated (n=34, E) and compacted (n=35, C) cells. ****$p < 0.0001$ *(Student's t-test, two-tailed, unequal variances). Boxplots range from the first quartile (Q1) to the third quartile (Q3), with the median (50th percentile) indicated by a line. Whiskers extend from the box to the minimum and maximum data points within* 1.5 *times the interquartile range.*

To explore this mechanism, we examined using super-resolution microscopy the spatial distribution of phosphorylated myosin light chain (p-MLC) at the actin cortex in elongated (Figure 5.21A-B) and compacted (Figure 5.21C-D) morphologies. In compacted cells, our results confirmed cortical thickening (Figure 5.21E) and revealed substantial colocalization with actin (Figure 5.21D), suggesting increased myosin infiltration into the cortex.

Together, these results support the idea that cortex thickening acts as a mechanical memory of prior confined events, stabilizing the compacted morphology over time.

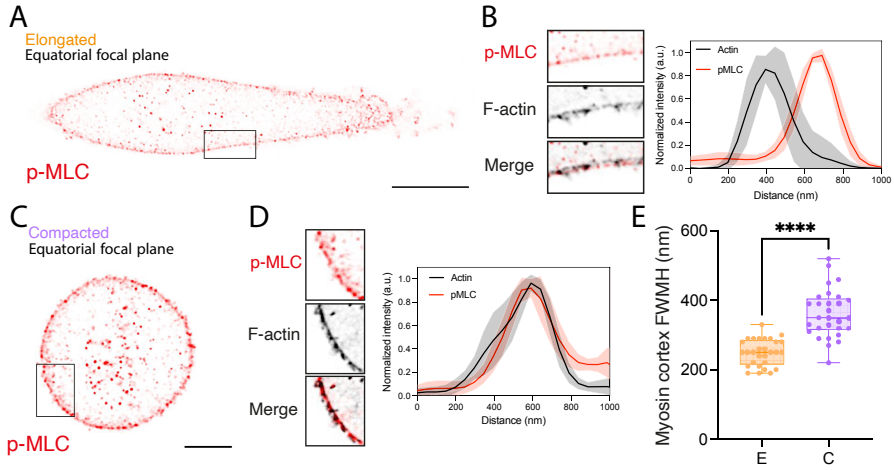

Figure 5.21: *Myosin cortex in elongated and compacted cells. Typical equatorial focal plane obtained in super-resolution microscopy showing the spatial distribution of phosphorylated myosin light chain (p-MLC) at the actin cortex in (**(A-B)**) elongated and **(C-D)** compacted cells. Plot profiles in (b) and (c) shows the normalized intensity of actin and p-MLC as a function of the distance from the membrane. **(E)** Full width at half maximum (FWHM) for myosin cortex in elongated (orange, $n = 29$) and compacted (purple, $n = 29$) cells. Boxplots range from the first quartile (Q1) to the third quartile (Q3), with the median (50th percentile) indicated by a line. Whiskers extend from the box to the minimum and maximum data points within* 1.5 *times the interquartile range. ****$p < 0.0001$ (Student's t test). Scale bars, 10 μm.*

Mechanical memory is controlled by the actin cortex

Assuming that mechanical memory is associated with reinforced front-rear polarity, microtubules and the actin cortex are likely candidates to explain the origin of this mechanical memory. Indeed, it is well established that microtubules play a pivotal role in the establishment of cell polarity [195], while cortex thickening can stabilize the compacted cell shape, generate long-range membrane tension propagation [196], and therefore contribute to the maintenance of cell polarity [39].

To test these hypotheses, we first treated cells with nocodazole, which disrupts microtubule dynamics by binding to tubulin and leading to microtubule

depolymerization (Figure 5.22A). Tubulin-treated cells exhibited a similar CSI on the bridge to control cells (Extended Data Fig. 8b), a similar area on squares (Figure 5.22C), but a very low success crossing rate (Figure 5.22D) and a very high dwell time (Figure 5.22E). Indeed, nocodazole-treated cells mostly became unable to migrate into the bridge and to maintain sufficient polarization to migrate within the confined area. Altogether, these results demonstrated that microtubules are not involved in the mechanical memory process related to maintaining the compacted shape, but they are necessary for enabling the passage of epithelial cells in narrow environments.

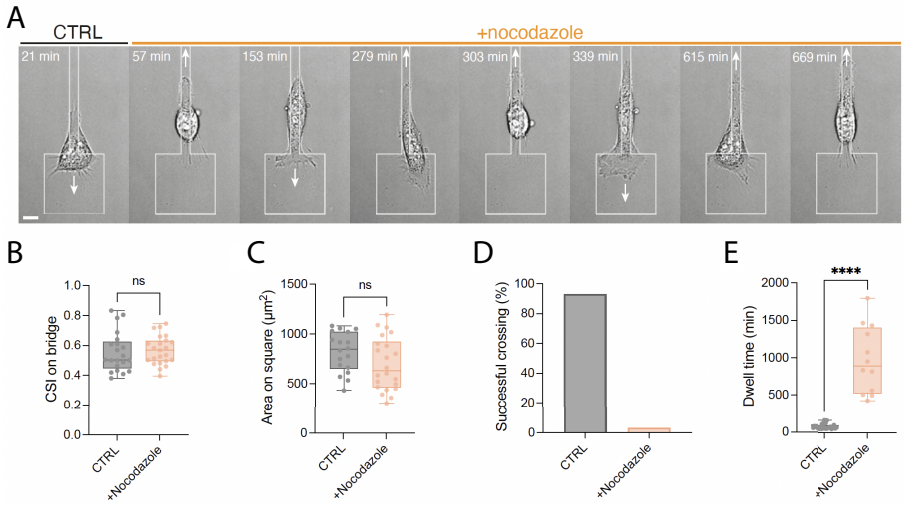

Figure 5.22: *Effect of a nocodazole treatment on confined migration.* ***(A)*** *Time-lapse sequence of a compacted cell entering a bridge before (control, CTRL) and after treatment with nocodazole (orange). CTRL is DMSO for nocodazole experiments. Scale bar, 10 µm. White arrows show the direction of migration.* ***(B)*** *Cell shape index on bridge for CTRL (n=21, N=5) and nocodazole-treated cells (n = 23, N=6).* ***(C)*** *Cell area on square for CTRL (n=18, N=6) and nocodazole-treated cells (n=22, N=7).* ***(D)*** *Successful crossing percentage for CTRL (n=146, N=18) and nocodazole-treated cells (n=33, N=8) and* ***(E)*** *dwell time on square for CTRL (n=22, grey) and nocodazole-treated cells (n=12, light orange). Boxplots range from the first quartile (Q1) to the third quartile (Q3), with the median (50th percentile) indicated by a line. Whiskers extend from the box to the minimum and maximum data points within* 1.5 *times the interquartile range.* $****p < 0.0001$ *and n.s. = not significant (Student's t test).*

In the next step, cells were treated either with a low concentration (20 nM) of Latrunculin B (LatB, Figure 5.23A-D) and to weaken cortical F-actin, or with Y27632 (Figure 5.23E-H), which inhibits Rho-associated protein kinase (ROCK), a key regulator of actin cortical tension, leading to a significant decrease in cortex elasticity [197]. Interestingly, cortical tension is higher in cells with elevated ROCK activity compared to those with higher Rac1 activity, suggesting that cortical tension increases when contractility dominates over actin polymerization [198].

We quantified back-and-forth cell movements during an initial 4-hour control period, followed by an additional 20-hour period after adding one of the pharmacological agents (Figure 5.23B and F). Cells treated with LatB and Y27632 were significantly slower (Figure 5.23C and G), exhibited a very low shape index on the bridge (Figure 5.23D, CSI ≈ 0.2), characteristic of an extended morphology, and a much lower rate of successful passage (Figure 5.23H). These findings collectively demonstrate the major role of the actin cortex and the associated ROCK contraction pathway in maintaining the compacted shape.

Perturbing the mechanical memory dynamics

Our finding that the morphological states of cells on the confining bridge are correlated across transitions suggests that cells can retain memory of previous states during periods of unconfinement on the square islands. Indeed, the spreading rate on the square islands (Figure 5.24A-B) can significantly affect actin cortex thickness (Figure 5.24C) and thus perturb mechanical memory. This raises the question of whether the two morphological states lead to distinct cytoskeletal organization during the unconfining event on the islands.

By studying transitions between two elongated (E/E, Figure 5.26A) or two compacted (C/C, Figure 5.26B) shapes, we observed that the cell area on squares of 1600 μm^2 was statistically larger for E/E than for C/C (Figure 5.26C), with a transition occurring at a cell area of around 1000 μm^2. Addition-

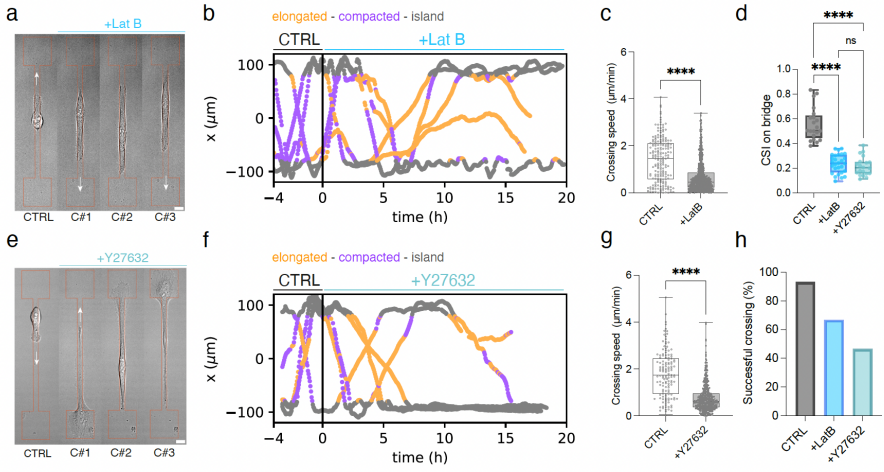

Figure 5.23: *Pharmacological perturbation of mechanical memory dynamics.* ***(A)*** *Sequence showing typical cell morphology during three successive crossings (C#1, C#2, and C#3) after treatment with LatB.* ***(B)*** *Representative trajectories of cells treated with LatB at t=0 during their migration on a dumbbell pattern with a 160 µm long bridge. Elongated morphologies, compacted morphologies, square zones (islands) are color-coded. CTRL is DMSO for LatB.* ***(C)*** *Mean crossing speed for cells before and after treatment with LatB (n=5, N=4).* ***(D)*** *Cell Shape Index on bridge for CTRL (n=21) and LatB-treated cells (n=28, N=8).* ***(E)*** *Sequence showing typical cell morphology during three successive crossings (C#1, C#2, and C#3) after treatment with Y27632.* ***(F)*** *Representative trajectories of cells treated with Y27632 at t=0 during their migration on a dumbbell pattern with a 160 µm long bridge. Elongated morphologies, compacted morphologies, square zones (islands) are color-coded. CTRL is water for Y27632.* ***(G)*** *Mean crossing speed for cells before and after treatment with Y27632 (n=20 for Y27632, N=8).* ***(H)*** *Successful crossing rate for CTRL n=146, LatB (n=65), and Y27632 (n=58), N≥8 for all. ****p < 0.0001 and n.s. not significant (Student's t-test, two-tailed, unequal variances or Kruskal-Wallis test). Boxplots range from the first quartile (Q1) to the third quartile (Q3), with the median (50th percentile) indicated by a line. Whiskers extend from the box to the minimum and maximum data points within 1.5 times the interquartile range.*

ally, we found that LatB- and Y27632-treated cells exhibited larger spreading areas (Figure 5.26D) and larger dwell times (Figure 5.26E) on squares compared to compacted cells.

Interestingly, we observed a continuous decrease of CSI (Figure 5.25A-B) and crossing velocity (Figure 5.25C-D) after each crossing for LatB- and Y27632-treated cells, while the spreading area on squares increased continu-

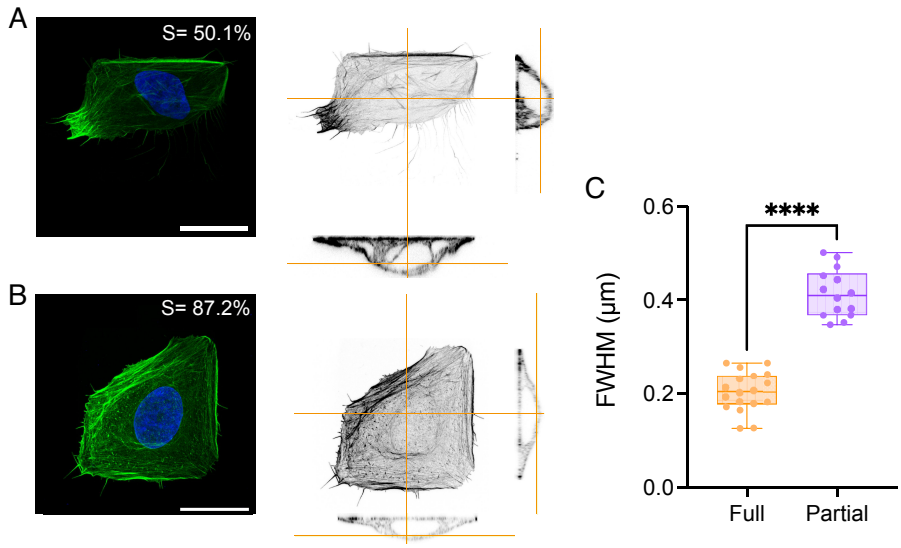

Figure 5.24: *Thickness of the actin cortex in cells spread on squares. Super-resolution confocal images of* ***(A)*** *a partial spreading and* ***(B)*** *a full spreading of epithelial cells on FN square of 1600 μm^2. Cells are immunostained for F-actin with phalloidin (in green) and DNA with DAPI (in bue). Inverted images show normal and side views of the actin cytoskeleton at the apical side. The spreading rate is 50.1% for partial spreading (A) and 87.2% for full spreading* ***(B)****. Scale bars, 20 µm.* ***(C)*** *Full width at half maximum (FWHM) represents the actin cortex thickness for partial (n=18, N=4) and full (n=18, N=4) spreading conditions. Boxplots range from the first quartile (Q1) to the third quartile (Q3), with the median (50th percentile) indicated by a line. Whiskers extend from the box to the minimum and maximum data points within 1.5 times the interquartile range. ****$p < 0.0001$ (Student's t test).*

ously in both conditions (Figure 5.25E-F). Altogether, these results demonstrate that both the actin cytoskeleton and the ROCK contraction pathway control dwell times through cell spreading and actin cortex remodeling.

To test the role of available spreading area in the memory of morphological switching, we designed two new dumbbell geometries: one with squares of 900 μm^2 (below the transition threshold of 1000 μm^2,Figure 5.26C), and another with squares of 2500 μm^2 (larger than the maximal spreading area post-drug treatment, Figure 5.26D).

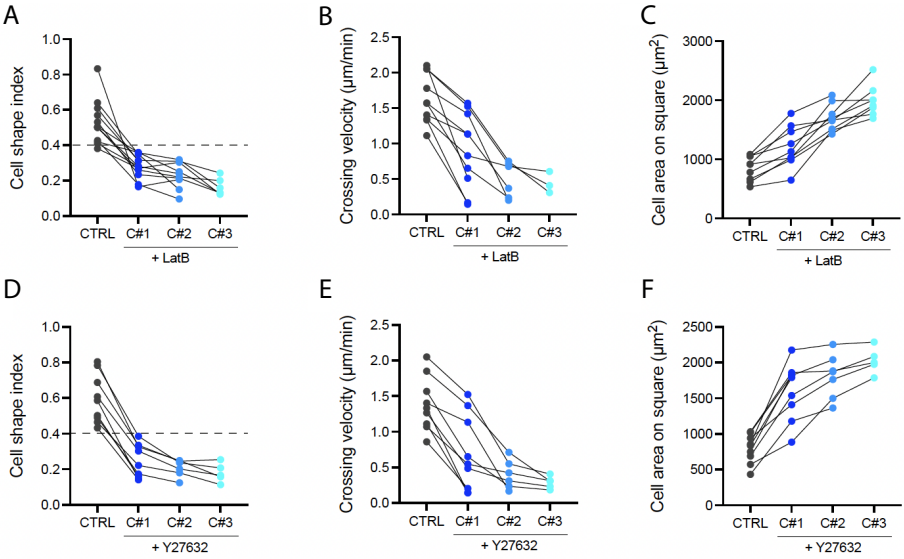

Figure 5.25: *Evolution of the cell shape index, the crossing velocity and the cell area on square in response to Latrunculin B and Y27632 treatments.* ***(A)*** *Cell shape index (n=11, N=4),* ***(B)*** *crossing speed (n = 10, N = 4), and* ***(C)*** *and cell area on square (n = 9, N = 4) before (control, CTRL) and after treatment with latrunculin B (LatB, shades of blue).* ***(D)*** *Cell shape index (n=8, N=3),* ***(E)*** *crossing speed (n=9, N=4), and* ***(F)*** *cell area on square (n=9, N=3) before (control, CTRL) and after treatment with Y27632 (shades of blue). Data from the same cell are connected by black lines. C#1, C#2, C#3 refer to the transition number after addition of the drug.*

By tracking back-and-forth motions on these geometries (Figure 5.26F) (Supp. Movies-S2 and S3), we observed that the mean CSI on bridges connected to 900 μm^2 squares (0.56 ± 0.16) was higher than that on bridges connected to 1600 μm^2 squares (0.44 ± 0.15), while cells on 2500 μm^2 squares exhibited a lower CSI (0.29 ± 0.12, Figure 5.26G), suggesting that the larger the square, the lower the CSI (Figure 5.28A). The percentage of compacted cells was also highest on 900 μm^2 squares and decreased with increasing square area (Figure 5.26H). Moreover, increasing the square area led to proportionally longer dwell times (Figure 5.27A and Figure 5.28B).

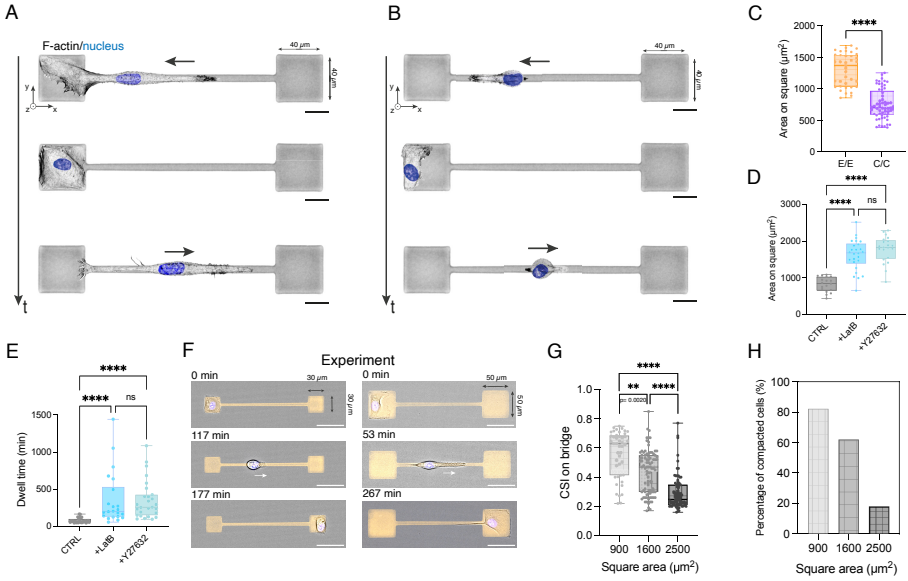

Figure 5.26: *Geometrical perturbation of the mechanical memory dynamics. Representative sequence showing a transition between* ***(A)*** *two elongated states (E/E) and* ***(B)*** *two compacted states (C/C).* ***(C)*** *Spreading area on 1600 μm^2) squares during a transition between two elongated states (E/E, n = 37, and N=3) and two compacted states (C/C, n=61, and N=3), indicating a transition around 1000 μm^2.* ***(D)*** *Mean cell area and* ***(E)*** *dwell time on 1600 μm^2 squares for control (n=27, N$\geq$4), LatB-treated cells (n=22, N$\geq$4), and Y27632-treated (n=27, N$\geq$4) cells.* ***(F)*** *Representative sequence showing a crossing event on a bridge (L=160 μm, W=6 μm) connected to squares of 900 μm^2 (left) and 2500 μm^2 (right).* ***(G)*** *Cell shape index and* ***(H)*** *percentage of compacted cells on a bridge of 160 μm long and 6 μm wide for dumbbell geometries with squares of 900 μm^2 (n=45, N=3), 1600 μm^2 (N=87, N=14), and 2500 μm^2 (n=72, N=3).*

We then extended our model to replicate these new geometries. The model predicted that larger square areas result in fewer compacted cells (Figure 5.27B) and longer dwell times (Figure 5.27C), matching our experimental findings and supporting the model's robustness.

To further confirm the role of the actin cortex in shape memory, we treated cells on 2500 μm^2 squares with Jasplakinolide, a drug that stabilizes actin filaments. A moderate Jas concentration was used to thicken the cortex without impeding lamellipodial dynamics [47]. Jas-treated cells maintained compact shapes (CSI $= 0.51 \pm 0.13$, Figure 5.27D) and had shorter residence times ($\tau =$

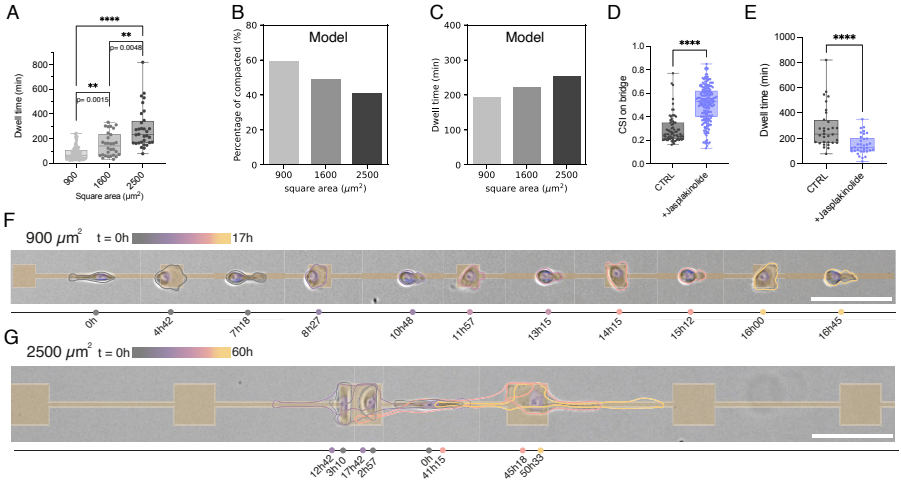

Figure 5.27: ***(A)*** *Dwell time observed on squares of 900 μm^2 (n=45, N=2), 1600 μm^2 (n=87, N=16), and 2500 μm^2 (n=13, N=3). Simulated behavior of* ***(B)*** *the percentage of compacted cells on a bridge of 160 μm long and 6 μm wide for dumbbell geometries with squares of 900 μm^2, 1600 μm^2, and 2500 μm^2 and* ***(C)*** *the dwell time on squares of 900 μm^2, 1600 μm^2, and 2500 μm^2.* ***(D)*** *Cell shape index for control cells (n=13, N=4) and jasplakinolide-treated cells (n=207, N=4). CTRL is DMSO for jasplakinolide experiments.* ***(E)*** *Dwell time for control cells (n=31, N=4) and jasplakinolide-treated cells (n=34 and N=4, purple). Representative time-lapse sequence of a single MCF-10A cell migrating on an interconnected dumbbell-shaped micropattern featuring 160 μm-long bridges and square deconfinement zones of* ***(F)*** *900 μm^2 and* ***(G)*** *2500 μm^2. Color-coded, time-dependent cell outlines are shown alongside. Scale bar, 100 μm. ***$p < 0.001$, ****$p < 0.0001$; n.s. = not significant (Student's t-test, two-tailed, unequal variances or Kruskal-Wallis test). Boxplots range from the first quartile (Q1) to the third quartile (Q3), with the median (50th percentile) indicated by a line. Whiskers extend from the box to the minimum and maximum data points within 1.5 times the interquartile range.*

151 ± 67 min, Figure 5.27E), indicating that reinforcing the cortex promotes memory retention in otherwise elongating conditions.

To test memory independently of the necessity for cells to re-polarize at each ends of the pattern, thus engaging cells in the opposite direction. We conducted a final experiment that explicitly reveal the correlation between morphological states across transitions as a function of the available square area. We used concatenated dumbbells with 900 μm^2 (Figure 5.27F) or 2500 μm^2 (Figure 5.27G) squares (Supp.Movies S4). Cells on 900 μm^2 patterns stayed

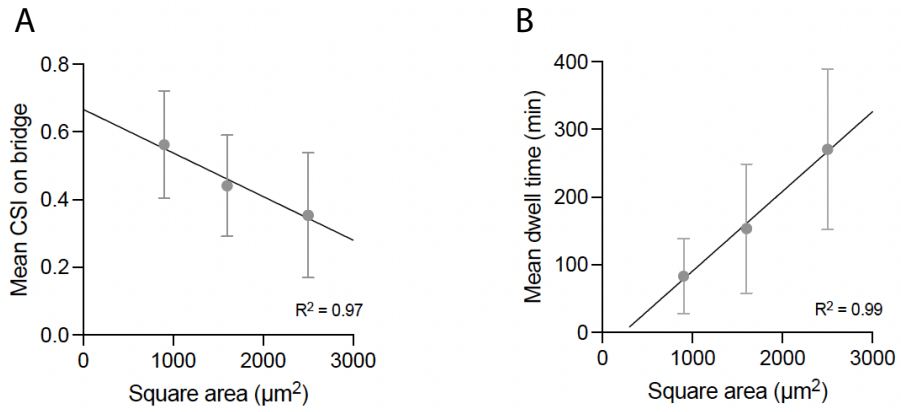

Figure 5.28: *Relation between cell shape index, dwell time and square area.* ***(A)*** *Linear correlation between the mean cell shape index on bridge and the area of the square at each end (R^2=0.9723).* ***(B)*** *Linear correlation between the mean dwell time on the square and the area of the square (R^2=0.9951). Data are presented as mean values ± SD. from N≥3 replicates.*

compact, crossed 10 motifs in under 17 hours. On 2500 μm^2 patterns, cells elongated, lost directionality, and struggled to cross even one motif in over 60 consecutive hours. Our model reproduced these behaviors, matching experimental crossing rates and polarization events (Figure 5.29A-D), validating its predictive power. Together, these data confirm the role of lateral confinement in shaping cell migratory behavior. Smaller areas promote highly persistent compacted migrating cells that rapidly explore their surrounding environment.

Collectively, our data identify a morphological switch in confined migration and establish a mechanical memory function of the actin cortex. The dynamic switching between compacted and elongated morphologies allows cells to alternate between highly polarized, directed and more exploratory, undirected motility. This adaptability probably plays a key role in navigating through heterogeneous matrices and narrow constrictions, which is relevant to various physiological processes, such as immune cell patrolling, progenitor cell motility during development and cancer cell invasion.

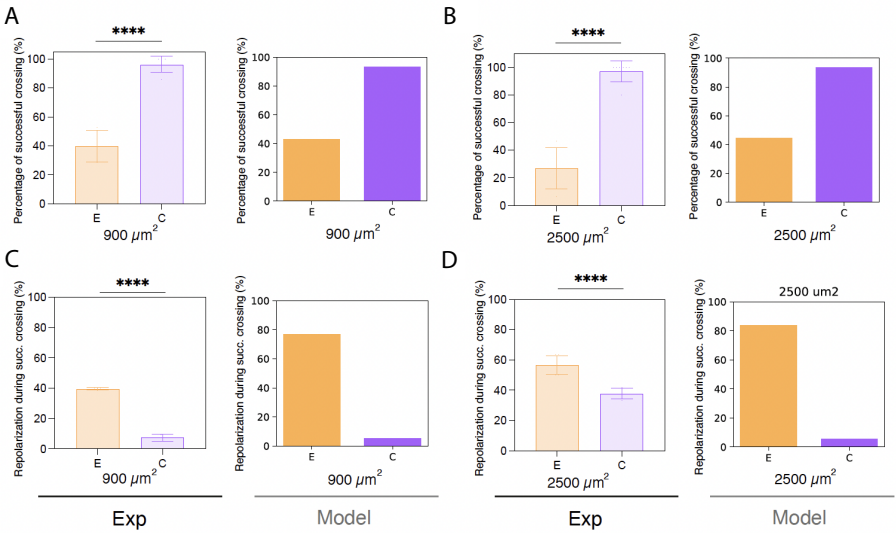

Figure 5.29: *Experimentally measured and simulated percentages of successful crossing on interconnected dumbbell micropattern. Percentages of successful crossing with* ***(A)*** *900 μmathrmm² squares for elongated (E, n=34, N=3) and compacted (C, n=34, N=3) and* ***(B)*** *2500 μm² squares for elongated (E, n=50, N=3) and compacted (C, n=50, N=3). Experimentally measured and model-estimated percentages of repolarization during successful crossing on interconnected dumbbell micropattern with* ***(C)*** *900 μm² squares for elongated (E, n=21, N=3) and compacted (C, n = 30 cells, N=3) cells and* ***(D)*** *2500 μm² squares for elongated (E, n = 41, N=3) and compacted (C, n=27 cells, N=3) cells. Data are presented as mean values ± SD. ****p < 0.0001 (Student's t test).*

The mechanical memory we describe allows cells to retain a record of their previous morphological state, even as they transition through subsequent cycles of confinement and unconfinement. This memory is encoded by the organization of the actin cortex and enables cells to maintain a compacted morphology during temporary unconfinement events. The relationship between cortex thickness and mechanical properties is cell-type dependent. Although cortical thickening in oocytes has been associated with reduced cortical tension due to disproportionate actin polymerization over myosin contractility[199], our findings for MCF-10A epithelial cells align with previous reports indicating that cortex thickening correlates with increased cortical tension and enhanced migratory capacity[39].

Our findings support this epithelial-specific mechanism and highlight cortical thickening as a mechanical memory that sustains efficient migration under confinement. The retention of memory from previous confining events may allow cells to traverse heterogenous confinements such as interstitial spaces without having to pause to reorganize their shape each time they encounter an unconfined space.

Notably this mechanical memory preserves a compacted, highly polarized state, which promotes rapid exploration through persistent motion and efficient navigation at dead ends. The bimodal transition between elongated and compacted morphologies arises from a coupling between confinement, actin cortex remodeling and polarity feedback. Increased confinement promotes front–rear polarization and cortex thickening, which reinforces the compacted state, whereas less-constrained regions allow more symmetrical spreading. This bistability is further enhanced by mechanical memory, as cells tend to maintain the compacted morphology even after leaving confinement, which enhances migratory efficiency.

CHAPTER 6

CONCLUSIONS

Accumulating evidence demonstrates that migrating cells are exquisitely sensitive to the physico-chemical properties of their microenvironment. Beyond biochemical signaling, mechanical and topographical cues strongly influence cellular responses. To optimize motility, cell remodel their migratory machinery by reorganizing the cytoskeleton, adhesion, and polarity. In confined environments, where tissues present heterogeneous features such as interfaces, aligned fibers, and narrow tracks, cells must adopt versatile strategies to overcome physical constraint. A striking example is found in vivo, where single cells migrate along matrix fibers within the tumor stroma with remarkable speed and persistence, behaviors tightly linked to metastatic potential. Motivated by these observations, this PhD work investigated whether biophysical adaptations of single migrating cells can be stored as a form of mechanical memory to subsequently modulate migration efficiency.

To address this question, we established migration assays with epithelial MCF-10A cells on standardized micropatterns designed to alternate confinement and release (Figure 6.1a). This reductionist platform enabled systematic analysis of how epithelial cells adapt to physical constraints. We identified two discrete morphological states—elongated and compacted—that emerged beyond a critical bridge length of 120 μm, notably exceeding the intrinsic elongation capacity of MCF-10A cells (≈100 μm) (Figure 6.1a).

Compacted morphologies increased in frequency with bridge length and were strongly associated with a higher crossing success. These cells migrated nearly three times faster than elongated ones, exhibited shorter dwell times (≈ 100 min), and displayed hallmarks of strong polarization, including rearward-biased actin distribution and rapid retrograde flow. A minimal theoretical model developed by David Brückner (University of Basel) based on active particle theory confirmed that elongated and compacted states represent distinct polarity regimes that govern migratory dynamics (Figure 6.1b). Molecular analyses further revealed that compacted cells exhibited microtubule alignment, Golgi positioning, and Arp2/3 localization consistent with a polarized and persistent phenotype.

Long-term single-cell tracking revealed that cells dynamically switch between compacted and elongated states, alternating directed migration and exploratory migration (Figure 6.1a-b). This plasticity enables cells to overcome obstacles such as narrow constrictions and likely represents an adaptive response to persistent confinement. Quantitative analyses showed that confinement promotes front–rear polarization and cortex thickening, reinforcing compact morphologies, whereas release favored spreading and elongated states (Figure 6.1c). Together with theoretical modeling, these experimental results underscore polarity dynamics and cortical remodeling as the basis of morphological switching and highlight geometry as a stabilizer of migration phenotypes.

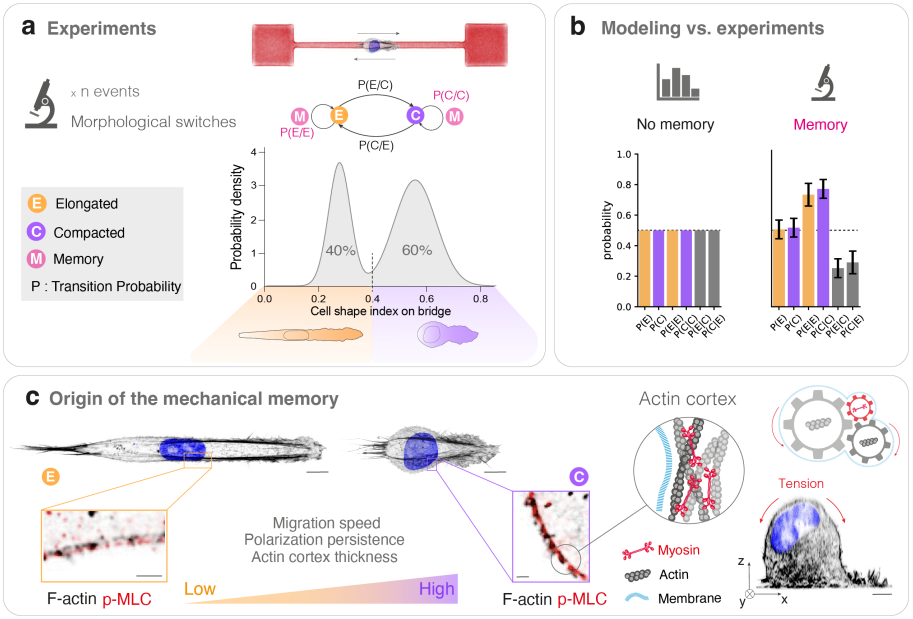

Figure 6.1: *The actin cortex act as mechanical memory of past morphologies during confined cell migration. a. From top to bottom, schematic of the experimental strategy, using microdumbbells enabling back-and-forth cell migration. Time-lapse microscopy captures a large number of morphological switches events from elongated shape (E, orange) to compacted shape (C, purple) and vice versa with associated probability P(E/C), P(C/E) or P(C/C), P(E/E) corresponding to memory. Probability density distribution of the cellular shape index, showing bimodal distribution. (b) Histogram representation of the probabilities for elongated, P(E), and compacted, P(C), states for various combinations of morphological switches for model (no memory) and experiments (with memory). Error bars represent SD (n=55, N=11). (c) From left to right, representative confocal images in super-resolution mode of elongated (left) and compacted (right) morphologies of MCF-10A cells (Actin in black and nucleus in blue). Inserts show actin (black) and phospho-myosin light chain cortex (red). Right, Schematic of actin cortex composition responsible for mechanical memory and confocal side view of compacted MCF-10A showing tension on the cell cortex. Scale bar, 5 μm.*

Crucially, we demonstrated that cells retain information from prior confinement events. Compacted and elongated states persisted across cycles of confinement and release, establishing a form of mechanical memory. This memory is encoded by the actin cortex: compact morphologies exhibited cortical thickening and enhanced myosin activity that persisted even after transient release.

Perturbation experiments with cytoskeletal drugs confirmed the central role of actin organization and ROCK-dependent contractility in maintaining memory. Beyond stabilizing morphology, this memory enhanced migratory efficiency, with compacted cells remaining faster and more persistent upon re-confinement.

Confinement-induced memory thus emerges as a fundamental adaptation with both biological and translational relevance. At tumor–stroma interfaces, where fibrillar ECM and dynamic remodeling prevail, such these strategies likely endow invasive cells with persistence despite fluctuating environments. This may help explain the aggressive behavior of invasive front cells, which retain high levels of phosphorylated myosin light chain and rounding capacity ex vivo [164]. These findings resonate with in vivo reports of rapid migration along ECM fibers, where Rac, Arp2/3, and microtubules direct polarity and protrusion dynamics [163].

In this thesis, we identify the actin cortex as the structural basis of confinement-induced memory, adding a new layer to the broader concept of cellular memory. Previous studies have described distinct mechanisms: for instance, cells can leave physicochemical footprints—extracellular matrix (ECM) deposits that bias subsequent trajectories and thereby encode short-term migratory memory in space [165]. In contrast, stiff substrates have been shown to induce a matrix stiffness memory mediated by YAP-dependent transcriptional programs, enabling long-term persistence of mechanosensitive phenotypes even after transfer to softer environments [162]. Furthermore, the nucleus itself plays a critical biophysical role in confined migration: dispensable in 2D but essential in 3D, where it contributes to force generation and movement [200, 201]. Future work combining our model with enucleated cells, namely cytoplast should clarify how nuclear mechanotransduction and epigenetic changes interact with cortical remodeling to establish and retain memory. Compared with these ECM- and nucleus-based mechanisms, cortex-encoded memory operates on the cytoskeletal level, directly coupling intracellular mechanics and polarity to past confinement history. Together, these complementary strategies illustrate how cells exploit multiple, timescale-dependent layers of memory—from extracellular footprints to nuclear reprogramming—to adapt migration in complex microenvironments.

Taken together, this Phd thesis identifies confinement-induced morphological switching and actin cortex–based memory as fundamental principles of migration plasticity. Cells perceive confinement not merely as a barrier but as an instructive cue, encoding past experiences into structural states that enhance migration. These insights refine theoretical models of migration, extend the concept of memory beyond biochemical signaling, and highlight the cytoskeleton as a central integrator of physical adaptation. From a translational perspective, our standardized micropattern platforms constitute robust tools for probing migration strategies across cell types, with direct implications for drug discovery and therapies targeting invasive persistence in cancer and other diseases.

This work also raises several key open questions, for instance:

- What is the characteristic relaxation timescale of the mechanical memory encoded in the actin cortex, and which molecular components regulate this process?
- How do cell–substrate adhesion dynamics contribute to the establishment of actin-based mechanical memory?
- What is the relevance of mechanical memory in more physiologically confined environments?
- What molecular mechanisms sustain mechanical memory in cells? In particular, what role do actin–membrane crosslinkers play in stabilizing the actin cortex and thereby contributing to the persistence of mechanical memory?
- Could these mechanisms be relevant to cancer progression, offering insight into how cells transition from a static to an invasive state?

In conclusion, the study of migration-associated mechanical memory opens new perspectives on how cells integrate geometry, mechanics, and history to navigate the complexity of living tissues.

CHAPTER 7

OUTLOOKS

Over the past decade, mechanical memory has emerged as a central topic in mechanobiology. Whether cells can retain a record of past mechanical experiences is now a major question. The concept was first introduced by Balestrini et al. in 2012 with the discovery of stiffness priming in fibroblasts. Since then, most studies have focused on how matrix properties—such as stiffness or structural organization—imprint mechanical memory over timescales of hours to days, often through stable epigenetic modifications. However, whether mechanical memory can also be encoded directly within the cytoskeleton to support rapid, short-term adaptation remains less well understood, and the molecular determinants of cytoskeletal memory timescales are still unclear.

This PhD work provides that migrating epithelial cells can store and recall confinement-induced memory. Unlike stiffnes- or matrix-encoded memory rooted in gene expression, this form of mecahnical memory is cytoskeleton-based, enabling cells to maintain a compact, polarized shape after transient release. Such mechanism may represent a physiological strategy to facilitate mi-

gration through dense tissues or, in pathological contexts, to enable metastatic cancer cells to traverse fibrotic barriers enriched in aligned ECM fibers.

The timescale of mechanical memory

A key question concerns the timescale of mechanical memory establishment and maintenance. Our theoretical model that the average time between morphological switches, T, must be on the order of 2.3τ ($\approx$ 10 h) to reproduce the persistence of memory observed experimentally. We hypothesize that this timescale reflects the lifetime of cytoskeletal structures undergoing continous-remodeling. Likely contributors include regulators of polarity and shape maintenance suchg as the RhoA signaling pathway, cortical actin filament regulators, and myosin assemblies. Supporting this hypothesis, our data show that T is sensitive to local geometry (lateral confinement) and is regulated by the acto–myosin contractile state. However, the current experimental setup does not allow us direct interrogation of the molecular events that define this timescale.

Addressing this challenge will be crucial to identify the molecular players governing cytoskeletal memory, and may also have translational relevance by opening therapeutic strategies to modulate migration persistence. Furthermore, it raises broader questions: for instance, whether mechanical memory can be transmitted to daughter cells after mitosis, thereby influencing tissue-level dynamics.

Experiments in this work were performed on static adhesive micropatterns, which limit the ability to probe cytoskeletal adaptations under dynamic conditions. To overcome this limitation, we initiated a collaboration with Johanna Ivaska's group in Türku (Finland) to implement dynamic micropatterning[202]. This approach uses deep-UV photopatterning of biotinylated polyethyleneglycol–grafted poly-L-lysine (PLL-g-PEG), compatible with diverse streptavidin-conjugated ligands, and allows precise spatiotemporal control of adhesion sites (Figure 7.1). This technique, initially developed during a Master's internship, has now been successfully adapted our laboratory.

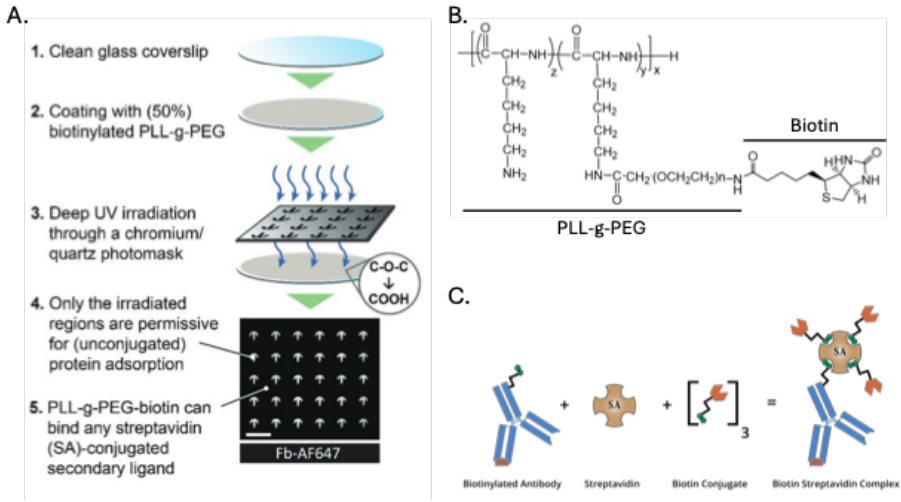

Figure 7.1: *Schematic of the dynamic micropatterning strategy. (A) Clean glass coverslips are coated with biotinylated PLL-g-PEG. Then, deep UV irradiation through a chromium/quartz photomask rendering exposed regions permissive for protein adsorption. In these regions, PLL-g-PEG-biotin can subsequently bind any streptavidin-conjugated secondary ligand, enabling spatially controlled protein patterning on the surface and allowing fouling regions to become permissive to cellular adhesion. (B) Chemical structure of PLL-g-PEG functionalized with biotin. (C) Schematic representation of biotin–streptavidin interactions enabling the immobilization of specific ligands (e.g., protein, antibodies) The polyvalent properties of streptavidin allows interaction with up to four biotin molecules with a high degree of affinity. Adapted from [202]*

This system enables controlled confinement-release cycles, with tunable duration and geometry. For example, cells can be seeded on compact dumbbell patterns (e.g, ≈900 µm^2 squares) to induce polarization, then release after defined intervals. By varying confinement time, degree of restriction, and release geometry, we can directly quantify how prior confinement influences subsequent migration. Time-lapse imaging will provide dynamic readout of memory relaxation, while markers of polarity and F-actin distribution [37] will reveal how cytoskeletal asymmetries reorganize. Such experiments will help determine which cytoskeletal components—myosin assemblies, microtubules, or upstream RhoA regulators- set the timescale of memory. Ultimately, this strategy will be essential to establish the hierarchy of cytoskeletal processes that define the duration, stability, and consistency of mechanical memory.

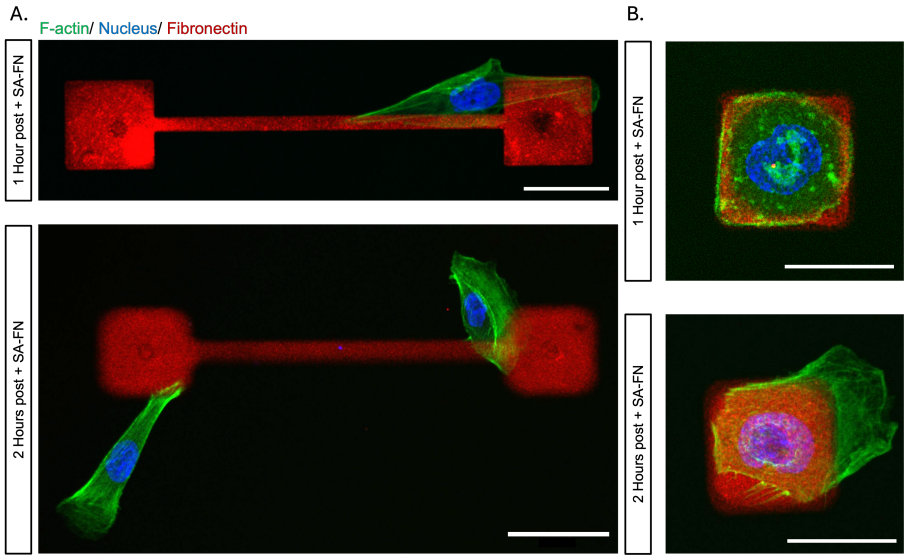

Figure 7.2: *(A) Epifluorescence images of MCF-10A cells cultured on fibronectin micro-dumbbells consisting of 40 × 40 µm square islands connected by a 6 × 160 µm bridge. The top panel shows a cell 1 h after fibronectin–streptavidin addition (release), and the bottom panel shows cells 2 h after release. (B) Epifluorescence images of MCF-10A cells on 30 × 30 µm square micropatterns. The top panel corresponds to 1 h after release, and the bottom panel to 2 h after release. Fibronectin–rhodamine is shown in red, F-actin stained with phalloidin in green, and nuclei stained with DAPI in blue. Scale bars, 50 µm. Adapted from Clara Leens's master thesis (2025).*

The role of adhesion dynamics

A second perspective emerging from our data concerns the role of adhesion dynamics in mechanical memory. Analyses of vinculin-based adhesion and actin retrograde flow revealed that compacted cells exhibit a higher proportion of nascent adhesions compared to elongated cells, together with elevated retrograde flow. Because nascent adhesions are short-lived and promote rapid migration, these findings suggest that adhesion turnover may be central to memory-dependent regulation of migration speed. This raises the broader question of whether mechanical memory is progressively encoded through adhesion sensing and turnover. Supporting this idea, Mosier et al. demonstrated

that confinement memory, coupled with polarized mitochondrial activity, is abolished in the absence of vinculin—underscoring the pivotal role of focal adhesions in memory encoding [166].

In line with this, recent work has identified AMPK as an adhesion-sensing mechano-metabolic hub that coordinates mitochondrial dynamics with cytoskeletal remodeling. In low-adhesion, fast-migrating amoeboid cells, AMPK activation links reduced mitochondrial ATP production with enhanced Myosin II–dependent contractility, thereby promoting migration in confined environments [203]. Within this framework, it is tempting to speculate, though still highly hypothetical, that mechanical memory may arise from an adhesion-metabolism-cytoskeleton feedback loop. In this scenario, focal adhesion turnover would not only encode past confinement experiences but also tunes energetic pathways to regulate future migration strategies.

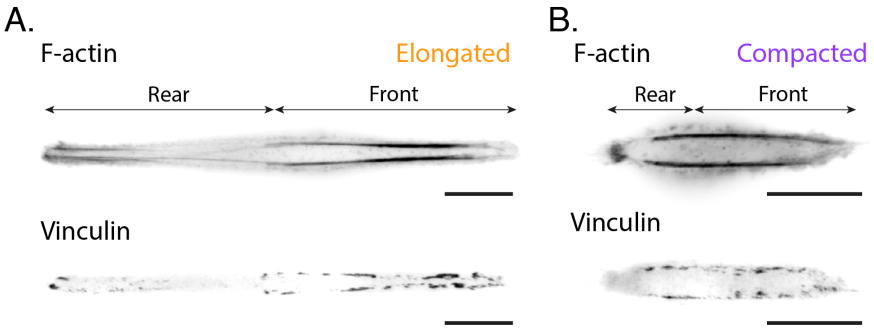

Figure 7.3: *Distribution of F-actin and vinculin in MCF-10A cells displaying elongated and compacted morphologies. (A) F-actin (top) and vinculin (bottom) polarized along the front–rear axis in a elongated cell. (B) F-actin (top) and vinculin (bottom) polarized along the front–rear axis in a compacted cell. Scale bars, 10 µm (A) and 20 µm (B).*

Future experiments could test this hypothesis by employing live imaging of talin, a key protein in focal adhesion assembly and mechanosensing. Combining talin dynamics with traction force microscopy (TFM) and the PercevalHR ATP probe[167] would us to directly assess whether mechanical memory modulates adhesion behavior, and toprobe how adhesion-mediated forces and metabolic states are coupled during memory encoding.

In parallel, cells migrating on substrates have been shown to deposit characteristic physicochemical footprints after prolonged migration [165]. With the timeframe of our experiments, we did find a significant contribution of such an extracellular imprinting for MCF10A cells. However, it will be valuable to investigate whether this mechanism becomes relevant for MCF-10A cells over longer timescales, and whether these footprints could reinforce mechanical memory by amplifying polarity cues such as Rac-1 signaling. This line of research would bridge extracellular environmental remodeling, highlighting a potential interplay between mechanical memory and ECM imprinting.

Towards more physiologically relevant conditions

Another perspective is to extend our findings obtain on 2D adhesive micropatterns toward more physiologically relevant conditions. While our current system using narrow microstripes can simplify in vitro the complexity of the 3D tissue environment, in vivo migrating cells face a wider spectrum of mechanical inputs, including matrix stiffness, ongoing remodeling, biochemical gradients, and compressive forces. A natural question is whether cells also rely on actin cortex-based memory to guide migration along fibers or within tightly confined intestitial spaces.

A promising direction involves the use of vertical confiners, which impose an additional dimension of confinement via Z-axis compression [119, 204]. Microsystems based on PDMS or agarose soft confiners enable vertical compression while allowing nutrient diffusion, making them compatible with long-term cell migration studies of cell migration[205]. Interestingly, compacted and elongated cells adopt distinct 3D morphologies, suggesting that vertical confinement will affect these phenotypes differently. Previous studies demonstrated that vertical compression can activate nuclear responses that increase contractility, effectively promoting migration as an escape mechanism [204, 206].

To date, however, vertical confinement has not been combined with micropatterning. Coupling these strategies could provide a powerful system to mimic the multidimensional mechanical landscapes encountered by cells in vivo. Such an approach would allow us to test whether confinement-induced memory en-

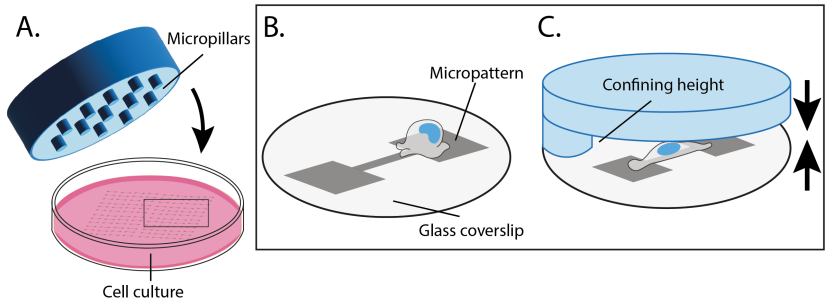

Figure 7.4: *Experimental strategies for combining micropatterned substrates to vertical compression. (A) Arrays of micropillars with controlled height integrated into cell culture device. (B) Schematic of a cell confined on a dumbbell micropattern before vertical compression. (C) Vertical confinement device imposes a controlled height to cell confined on micropatterns.*

hances cellular adaptation under more realistic tissue-like conditions, thereby revealing how past mechanical experiences are integrated with concurrent environmental cues.

Finally, the most accessible and short-term perspective is to dissect the molecular mechanisms that sustain mechanical memory. From a translational angle, it will also be important to assess how these mechanisms contribute to cancer progression. In this context, we have established collaborations with Giorgio Scita's laboratory (IFOM, Milan), which investigates tumor cell migration during early carcinogenesis, and maintained our collaboration with Guillaume Charras' group (University College London), which provides a panel of genetically modified MCF-10A cell lines. Together, these resources will allow us to explore the molecular principles underpinning mechanical memory at higher resolution.

Building on our hypothesis that the actin cortex acts as a reservoir of mechanical memory, and supported by previous work identifying long-lived cytoskeletal structures as drivers of directional memory [207], we focused on actin–membrane crosslinkers of the ERM Ezrin–Radixin–Moesin) protein family.

The ERM protein family

ERM proteins are particularly compelling candidates in this context. As central organizers of the actin cortex, they anchor F-actin to the plasma membrane, regulate membrane tension, and coordinate the balance between cortical and lamellar actin (Figure 7.5,A) [50]. Activated by phospholipid binding and phosphorylation, ERM proteins connect transmembrane receptors to actin filaments and regulate membrane domain organization [50]. Their dual role in mechanotransduction and cytoskeletal architecture positions them as strong candidates for encoding and maintaining mechanical memory.

To investigate this possibility, we performed preliminary experiments usng MCF-10A cells expressing a mutant Ezrin construct unable to anchor F-actin to the membrane (see description Materials and Methods). Migration was monitored on dumbbell micropatterns (bridges of 160 μm length and 6 μm width) and on 900 μm^2 square islands using 20 h time-lapse imaging. Results were compared with wild-type MCF-10A cells and with MCF-10A cells treated with the ERM phosphorylation inhibitor NSC668394, which is a small-molecule inhibitor that interferes with ERM (Ezrin–Radixin–Moesin) protein activation. NSC668394 prevents the phosphorylation of the regulatory threonine by blocking access of kinases (such as ROCK or PKC). Indeed, ERM proteins are auto-inhibited in their closed conformation. They become active when their C-terminal actin-binding site is exposed, which requires phosphorylation of a conserved threonine residue (e.g., Ezrin T567, Radixin T564, Moesin T558). This phosphorylation stabilizes the open conformation, allowing ERMs to link F-actin to the plasma membrane and regulate cortical mechanics. As a result: ERMs remain in their closed, inactive conformation, the link between actin filaments and the plasma membrane is destabilized, and cortical stiffness and membrane tension are reduced.

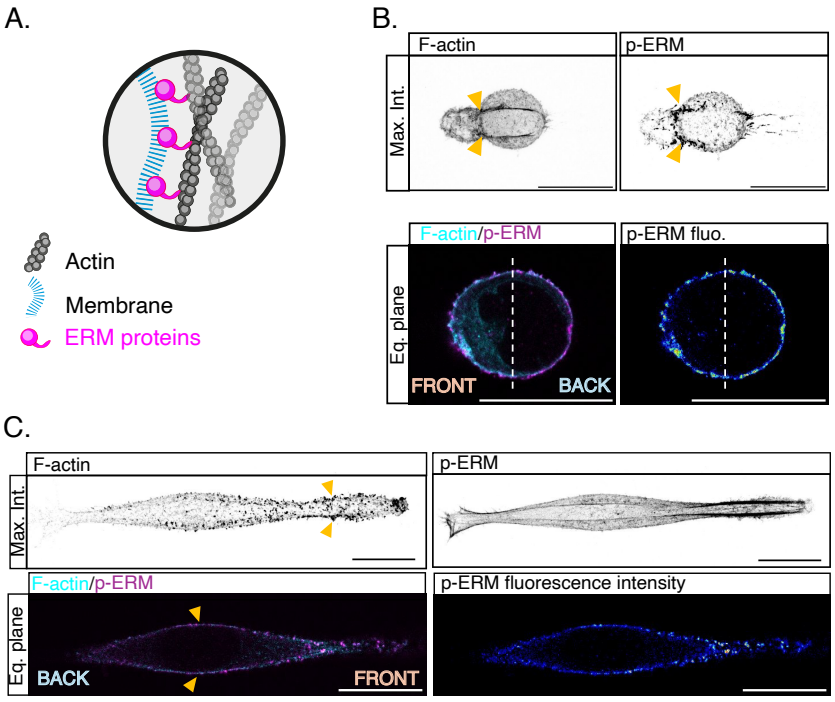

Figure 7.5: *Localization of phosphorylated ERM (p-ERM) in compacted and elongated MCF-10A cells. (A) Schematic representation of ERM proteins linking the plasma membrane to the actin cortex. (B) and (C) Representative confocal images showing maximal intensity projection of F-actin (phalloidin staining) and phosphorylated ERM (p-ERM) in compacted (B) and elongated cells (C). Below, single equatorial plane of merged F-actin and phosphorylated ERM (left). Color-coded p-ERM fluorecence intensity signal, white regions indicate maximal fluorescence intensity signal (right). Scale bar, 20 µm*

In compacted wild-type MCF-10A cells, phosphorylated ERM (p-ERM) accumulated strongly at the transition between cortical and lamellar actin, with polarized localization most pronounced at the rear of the cell, where actin and p-ERM strongly colocalized (Figure 7.5B). This observation is reminescent of recent findings suggesting that the actin–membrane crosslinker accumulation marks specialized cortical actin networks associated with morphological rounding and increased cortical tension[55]. In contrast, elongated cells displayed a smoother p-ERM distribution, enriched in front membrane ruffles, suggest-

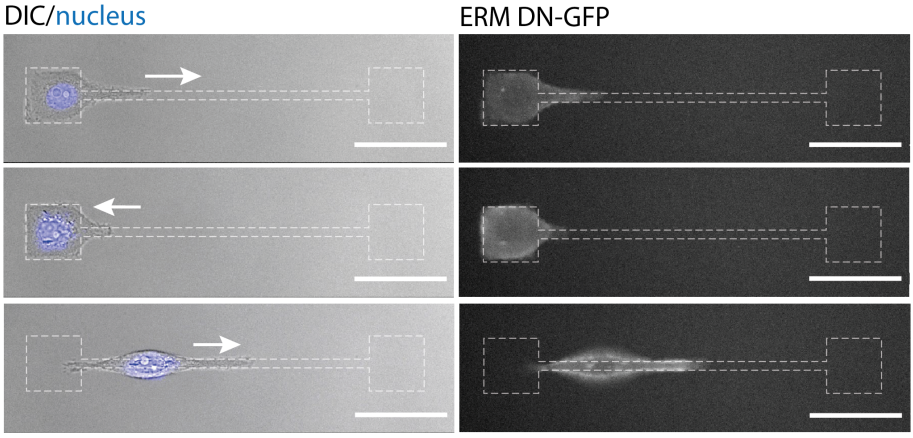

Figure 7.6: *Representative frames from a time-lapse of MCF-10A cells expressing Ezrin dominant negative–GFP on fibronectin micro-dumbbell featuring 30 x 30 µm islands. Left, DIC images with nuclei stained in blue; arrows indicate migration direction. Right, corresponding Ezrin DN–GFP signal showing cortical distribution during cell movement. Scale bars, 50 µm.*

ing distinct ERM roles in organizing actin structures across different migration states (Figure 7.5C).

Functional perturbations of ERM activity further reinforce their role in cell migration under confinement and shape maintenance. Both dominant-negative ezrin constructs (Figure 7.6) and pharmacological inhibition of ERM phosphorylation using NSC668394 (Figure 7.7) induced increased spreading and cellular elongation, revealed by reduced circular shape index (CSI), together with protrusion extension on bridges, translated by increased major axis (Figure 7.8A-C). By stabilizing ERM proteins in their closed, inactive conformation, NSC668394 effectively decouples the plasma membrane from the underlying F-actin cortex (Figure 7.7). Consistently, treated cells lost their compacted morphology, displayed reduced protrusion stability, and showed a decrease in motility and directionality, with migration resembling microtubule-disrupted phenotypes (Figure 7.9A-C).

Further quantitative analyses revealed a significant decrease in SSD (sliding standard deviation) values, consistent with a failure to maintain persistent mi-

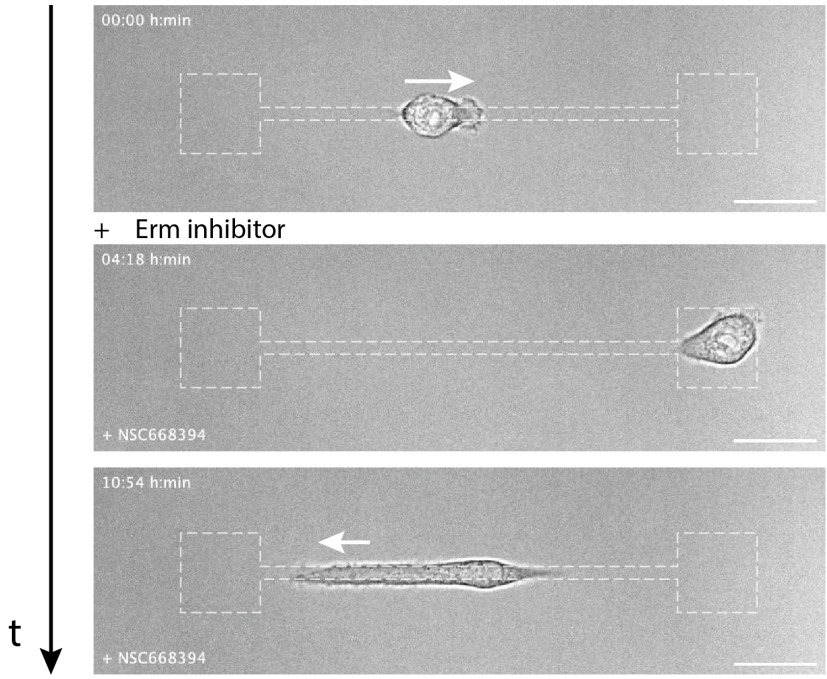

Figure 7.7: *Representative frames from a time-lapse of MCF-10A cells treated with the ERM inhibitor (NSC668394) on fibronectin micro-dumbbell featuring 30 × 30 µm islands. Arrows indicate migration direction. Scale bars, 30 µm.*

gration. The sliding SD corresponds to the variation in the relative position of the cell center of mass over time, calculated within a 1-hour sliding window, which is relevant to the typical timescale required for cells to cross the bridge (Figure 7.9A-C). Together, these results suggest that ERM depletion compromises polarity, morphology maintenance, and leading-edge organization, effectively abolishing the memory of confinement-induced compaction.

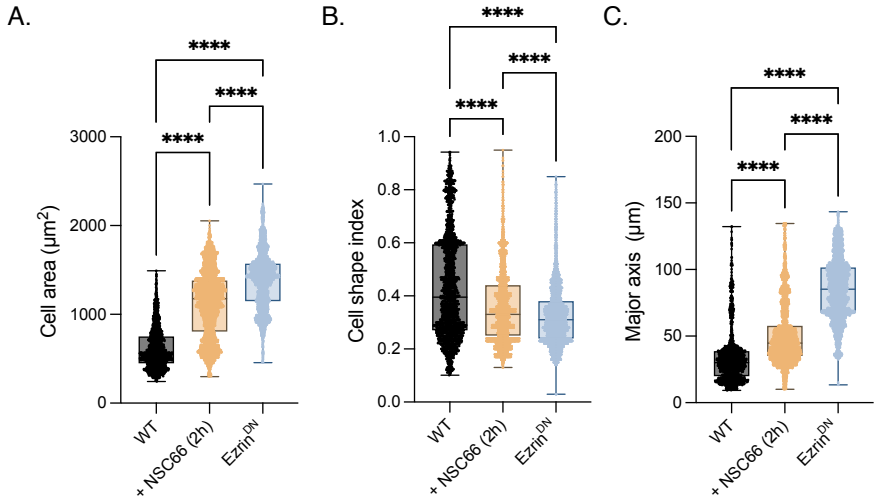

Figure 7.8: *ERM depletion or inhibition alters cell morphology under confinement. (A) quantification of cell area, (B) cell shape index (CSI) and (C) major axis length in wild-type (WT) MCF-10A (n = 23 cells, N = 2 replicates), WT treated with ERM phosphorylation inhibitor NSC668394 (after 2 h drug treatment) (n = 23 cells, N = 2 replicates), and Ezrin dominant-negative (Ezrin DN) cells (n = 10 cells, N = 1 replicates).****p < 0.0001 (Kruskal-Wallis test).*

Translational perspectives

These findings open promising translational perspectives. Indeed, ERM proteins are frequently upregulated in cancers, and their mislocalization has been linked to impaired adhesion, disrupted receptor signaling, and enhanced invasiveness [208, 57]. Ezrin, in particular, is overexpressed in aggressive breast cancers and correlates with poor prognosis, while moesin expression is upregulated during TGF-β–induced epithelial-to-mesenchymal transition (EMT), where it contributes to the assembly of contractile actin structures and invasive behavior [209]. Based on our preliminary results, we could speculate that ERM proteins play a central role in coupling the actin cortex to polarity signals, highlighting their necessity for efficient confined migration and the establishment of mechanical memory. However, further characterization is required, including quantitative measurements of the actin cortex and structural visualization

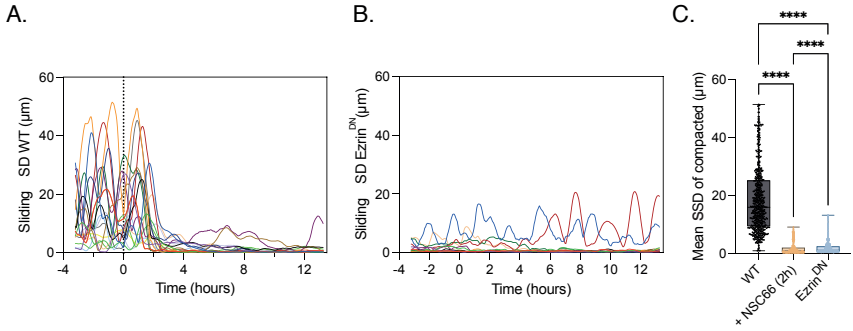

Figure 7.9: *ERM activity is required for persistent migration under confinement. (A) Sliding standard deviation (SSD) of the center-of-mass coordinates of wild-type MCF-10A cells over 12 hours time-lapse, calculated over a 1-hour moving window at each time point. Data compromises both compacted and elongated cell morphology. NSC668394 addition is indicated by a dashed vertical line. (B) Sliding SD analysis of Ezrin DN cells over 12 hours time-lapse.(C) Mean SSD of compacted cells calculated for wild-type (WT) MCF-10A (n = 23 cells, N = 2 replicates), WT treated with ERM phosphorylation inhibitor NSC668394 (after 2 h drug treatment) (n = 23 cells, N = 2 replicates), and Ezrin dominant-negative (Ezrin DN) cells (n = 10 cells, N = 1 replicates). ****p < 0.0001 (Kruskal-Wallis test).*

under conditions of impaired ERM function, in order to establish their link with the proposed mechanism. We hypothetize that expressing high levels of ERM proteins may give tumor cells an advantage in adapting to confinement and migrating through complex environments. We aim to further explore this direction in the near future.

A promising future perspective is to exploit our micropattern confinement system across the MCF-10A progression series starting with MCF10DCIS.com invasive derivatives (Figure 7.10). MCF-DCIS are breast cancer cell line derivatives that model ductal carcinoma in situ (DCIS), representing a pre-invasive, early stage of breast cancer progression situated between normal/atypical hyperplasia and invasive carcinoma. These experiments would allow us to test whether ERM-dependent memory mechanisms become progressively amplified during tumor evolution. Such experiments could help determine whether ERM-mediated cortical memory is a driver of invasive transitions, particularly during EMT, and whether targeting ERM function, via inhibitors of ERM phosphorylation such as NSC668394 or dominant-negative constructs, could reduce

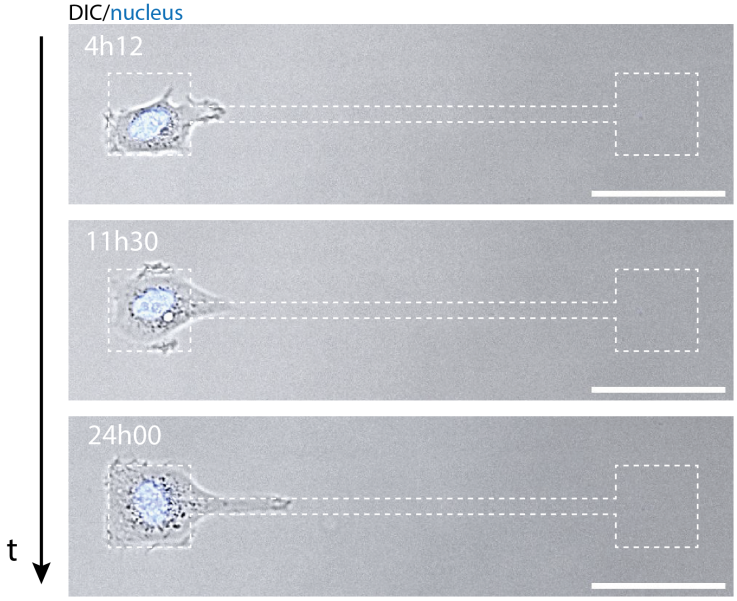

Figure 7.10: *Representative frames from a time-lapse of MCF10DCIS.com cells on fibronectin micro-dumbbell featuring 30 × 30 µm islands. Scale bar, 50 µm*

metastatic efficiency.

We are currently exploring this perspective. We have performed time-lapse experiments with MCF10DCIS.com cells provided by Giorgio Scita on micro-dumbbells featuring 900 μm^2 islands in order to establish a direct comparison with MCF-10A cells in which ERM function is impaired (Figure 7.10). In parallel, we carried out staining of wild-type MCF-10A cells, Ezrin dominant-negative cells, cells treated with the ERM phosphorylation inhibitor NSC668394 and MCF10DCIS.com, focusing on the actin cortex, phosphorylated ERM, and non-muscle myosin II. At this stage, these experiments remain preliminary, and detailed quantitative analyses are still required to determine how ERM impairment reshapes cortical organization and how this relates to the buildup of mechanical memory. This ongoing work will be essential to support the hypothesis that ERM proteins act as molecular encoders of cortical memory with potential relevance to tumor progression.

PROTOCOLS

PRIMO ALVEOLE MICROPATTERNING DUMBBELL PROJECT

This is a user-friendly version of the protocol

Created by Daniel Selma (daniel.selma-herrador@univ-grenoble-alpes.fr) **on Feb 13, 2023**
Edited by Yohalie Kalukula (yohalie.kalukula@umons.ac.be) on May 26, 2025
Edited by Robin Deschamps (robin.deschamps@student.umons.ac.be) on July 24, 2025

This protocol has been adapted from Daniel Selma's and Alvéole's.

Last edit by RD on July 24, 2025

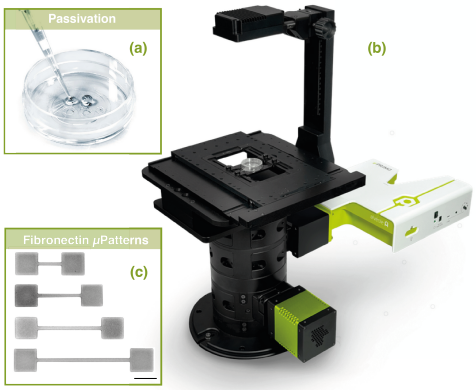

Protocol purpose:
This protocol describes how to obtain protein micro patterns on glass of your own design for the study and assessment of epithelial cell migration.

PROTOCOL

Step 1 [Time required 30 minutes]

FluoroDish and PDMS stencils cleaning

✎ Note:

The protocol has been adapted for use with FluoroDishes (glass-bottom dishes) instead of glass coverslips. Unlike coverslips, which require a cleaning step to remove a non-adhesive coating used to prevent sticking, FluoroDishes are ready to use and do not need cleaning. For optimal results, an additional 15 min UV treatment can be applied to the FluoroDishes prior to plasma activation.

- Peel off (n) PDMS stencils from the "stock" sheet.
- Cut-off edges of the stencils to fit the bottom of the dishes.
- Place them in a 70% IPA solution (use a beaker).
- Leave the beaker in a ultrasonic bath for 15 min.
- Take (n) FluoroDishes and place them under UV germicidal irradiation for 15 min.
  → **Meanwhile, go to step 3, prepare the material required to move quickly from step 2 to 3.**
- Dry stencils one-by-one with the nitrogen flux.
- Place them one-by-one on the lid of the FluoroDishes and close them.
- Seal them with Parafilm and store them until next use or continue to Step 2.

EQUIPMENT

Plasma Cleaner | MCF10A Cells | Nitrogen Gun | Biological Hood | Fluorescence microscope | Parafilm | Ultrasonicator | Tweezers | Beaker | Isopropanol, IPA | Petri dishes | Falcon tubes | PRIMO Photopatterning | 0.22 µm Filters | Clean room wipers | pH meter | Incubator (37°C & 5% CO_2) | *(n) glass bottom dish D35-28-1.5-N*, FluoroDishes | Black eppendorfs

Micromanager | Leonardo

CHEMICALS

99% Isopropanol (IPA) | 70% Ethanol | 0.1% (m/v) Poly-L-lysin | mQ water | 20 µM PEG-SVA | 0.1 M HEPES pH 8.3 | 0.1 M Sodium Bicarbonate ($NaHCO_3$) | PBS | DMEM | 1 mg/mL Fibronectin | horse serum | insulin | hydrocortisone | cholera toxin | Rhodamine Fibronectin | EGF | Streptomycin/penicillin | PLPP | Surfactant | Hoescht reagent

PROTECTIVE GEAR

Lab Coat | Gloves | Goggles

PROTOCOL

Step 2 [Time required 15 minutes]

Plasma activation

✎ Note:

Starting Step 2 implies having to do also the next two, Step 3 Step 4; thus, it is strongly recommended to take now all the necessary chemicals and equipment (see section "Aliquot Preparation"). The plasma effect lasts for one minute, therefore, incubation with PLL must be done immediately after, and followed by PEG-SVA passivation. At the same time, PEG-SVA is degraded very easily in presence of Oxygen, light and at room temperature; for that reason, aliquoting is not recommended. Also, its half-life in 0.1 M HEPES at pH 8.4 is around 10 minutes, so it should be prepared right before using it.

- Open the plasma cleaner door (air valve should be horizontal)
- Place open FluoroDishes face up as well as the PDMS stencils. Do not overcrowd the chamber. Ex : 4 dishes at a time.

  → **Trick: While using glass-bottom dishes, place the stencils on the lid and place the lid face up in the chamber during plasma treatment.**

- Close the chamber (air valve should be vertical). Turn on the vacuum pump.
- Turn on the plasma and turn the RF knob to high level.
- Turn carefully the air valve clockwise until the plasma is stabilized (characteristic purple color).
- Enable intense plasma for 3 min.
- Turn off the plasma and vacuum pump.
- Gently open the air valve to let air enter the chamber.
- Remove all items from the chamber and quickly transition under the biological hood.

Step 3 [Time required 40 minutes]

PLL Incubation

- Peel off stencils from lids and return them on the glass part of the FluoroDishes. Make sure to remove bubbles with tweezer.
  → **This step should be perform quickly after plasma treatment under the biological hood.**
- Divide a volume of 100 µL of 0.1% PLL solution among each well of the stencil. Repeat this for each dish.
- Incubate 30 min in wet chamber (place wet pieces of clean room wipers between the lid of the FluoroDishes and the Petri dish in which they are placed) at room temperature.
- Rinse each dish 3 times, gently, with 2 mL of HEPES.
- Dry the stencils after the third rinsing.

NOTES

PROTOCOL

Step 4 [Time required 1.5 hours]

PEG-SVA incubation

- Take the PEG-SVA bottle from the freezer, warm it up with your hands for a while and weight 10 mg per FluoroDish. Measure also 100 µL of HEPES per FluoroDish, to obtain a final concentration of PEG-SVA@HEPES of 100 mg/mL. For instance, if there are 4 FluoroDishes, weight 40 mg of PEG-SVA and then add 400 µL of HEPES.
- Reflow the mixture until full homogenisation.
- Divide a volume of 100 µL of the PEG-SVA@HEPES solution among each well of the stencil. Repeat this for each dish.
- Put wet pieces of clean room wipers between the lid of the FluoroDishes and the Petri dish.
- Let passivate for 60 min at room temperature.
- At the end of the incubation, rinse each FluoroDish 5 times, gently, with 1 mL of HEPES. Pay attention not to suck up inside the squares before the last rinse, which should be carried out very gently.
- Dry the FluoroDishes one-by-one with the air gun.
- Seal them with Parafilm and put them in a Petri dish. Store it in a dark and fresh place (fridge) until next use, or continue to Step 5.

Step 5 [Time required 0.5 - 1 hours]

PLPP-Gel Solution

✎ Note:

Starting Step 5 implies having to do also the next one, Step 6; thus, it is strongly recommended to take now all the necessary chemicals and equipment (see section "Aliquot Prepartion").

PLPP is photoactivatable reagent and the mix should be prepared right before the patterning. Step 7 can be followed as well if there are available cells (Step 8); otherwise, it is recommended to store the stencils in $NAHCO_3$ and wait for the cells.

- Under the fume hood and in the dark, prepare the PLPP-gel solution in a black eppendorf (note that you need around 3 µL per stencil):
  - 80 µL of 70 % EtOH
  - 8 µL of PLPP-gel solution from Alvéole
  - 3 µL of surfactant from Alvéole
- Vortex the solution for full homogenisation.
- Drop a volume of 3 µL of the solution on each well. That is to say that you will require 27 µL of the solution for each stencil since there are 9 wells on a stencil.
- Let the FluoroDishes open and put them at the back of the fume hood under a 100% ventilation flow.
- Let them dry for 30 min, still in the dark.
- Once they are dry, seal the FluoroDishes with Parafilm and cover the Petri dish with aluminium to avoid light exposure.

NOTES

PROTOCOL

Step 6 [Time required 0.5 - 1 hours]

PRIMO Patterning

> ✎ Note:
>
> The CAMERA CALIBRATION of the PRIMO must be done once a week. Be sure to calibrate it before the PRIMO CALIBRATION stage.

- Turn on the multi-socket, the microscope, the camera, the PRIMO, the lasers and the computer.
- On the computer, open "Micro-Manager 2.0", select "Plugins" → "Leonardo" and choose "Micropatterning".
- Place the x20 lens (top right button on "Ultimeyes" controller).
- Put the calibration sample on the microscope.
- ***If not done yet this week***, calibrate the camera, follow the instructions on the screen.

- Calibrate the PRIMO before every patterning, set the Laser Power on 6 mW and the intensity on 5%. Follow the instructions on the screen.
- Replace the calibration sample by one of your FluoroDish. Make sure to clean its surface with a lens cleaning tissue.
- Select 🗁"Load Template" and load your template file. Turn on the light and move the template correctly on the stencil. Turn off the light.
- Select "Add Pattern" and load your pattern file.
- Once your patterns are correctly positioned. Place the camera in a non-used side of a well (a corner for instance). Click on "preview", then click on the "sun" and adjust the focus (with the "Ultimeyes" joystick) to see the upper cross.
- Click on "run", stay in place to check if the focus is evetually lost, to immediately refocus.
  → **Turn off the LASER if not done automatically, close Micro-manager and repeat the procedure for each FluoroDish.**

- Once the patterning is done, retrieve the FluoroDish from the holder and rinse 5 times with 2 mL of 0.1 M $NaHCO_3$ to remove the PLPP. Before rinsing, the patterns shoud be slighty visible against the light. Again, do not dry directly in the squares and let the last rinsing during 5 min.

NOTES

PROTOCOL

Step 7 [Time required 30 minutes]

Fibrinogen/Fibronectin Protein Coating

- In the dark, prepare the protein suspension in a black eppendorf. **Do not vortex it.**
  → **If doing a Time-lapse recording:**
  - 985 µL of 0.1 M $NaHCO_3$
  - 10 µL 1 mg/mL Fibronectin
  - 5 µL of 1 mg/mL Rhodamine Fibronectin

  → **If doing an immunostaining:**
  - 985 µL of 0.1 M $NaHCO_3$
  - 15 µL 1 mg/mL Fibronectin
- Peel now the Parafilm and, for each FluoroDish, place a 100 µL drop of the protein suspension (distribute the 100 µL on the wells, connect the bubbles and make "up and downs" with the pipette).
- Let incubate for 5 min.
- Rinse each FluoroDish 5 times, gently with 1 mL of $NaHCO_3$.

→ **At this point, FluoroDishes can be stored in the fridge with 3 mL of $NaHCO_3$ and sealed with Parafilm. Otherwise, go to Step 8 for cell seeding the patterns.**

Step 8 [Time required 1 hour]

Seeding cells on your patterns

✎ Note:

Prepare the cells medium consisting of Dulbecco's modified Eagle's medium (DMEM), 5% horse serum, 1% penicillin/streptomycin, 0.1% Insulin, 0.05% hydrocortisone, 0.02% EGF and 0.01% cholera toxin. Remember always to have enough

cells for your patterns but also to pass them. Avoid seeding cells that have been passed recently (same day or the day before) as they are more stressed and prone to death.

- Preheat for 10 minutes the medium and the 0.25% Trypsin, in the warm bath.
- Put the DPBS aliquot in the biological hood.
- Take the flask with cells from the incubator (37°C & 5% CO_2), the medium and the Trypsin from the warm bath, and the FluoroDishes from the fridge. Put everything inside the hood.
- Remove the old medium and rinse the cells with 10 mL of DPBS.
- Remove the DPBS and add 2 mL Trypsin (for a T75 flask). Place the flask in the incubator for 5-15 minutes, to detach the cells from the surface. Check the cells frequently, if necessary, hit the flask consistently against the table to fully detach them.
- **Meanwhile**, remove the $NaHCO_3$ from the FluoroDishes. Take also a new T75 flask for cell culture, label it and add 10 mL of medium. In this way, cells have fresh medium when they are transferred.
- Add 4 mL medium and "flush" the cells in order to create a single-cell suspension.
- Transfer the cell suspension to a 15 mL Falcon and centrifuge it for 3 minutes at 1500 rpm (150 G).
- Aspirate supernatant and resuspend pellet in 1 mL medium.

NOTES

PROTOCOL

- Count the cells with the LUNA automated cell counter and calculate the needed volume to have 500 µL with 25 000 - 35 000 cells **per FluoroDish**.
- **In the new culture flask**, seed 20 000 cells/cm².
- T25 ⇒ 500 000 cells
- T75 ⇒ 1 500 000 cells
- Put back in the incubator the passed cells.
- After 2-4 hours of seeding: complete your FluoroDishes with medium to a volume of 3mL.

→ **If doing a Time-lapse recording:**

- Vortex Hoescht reagent, add 1 µL of it per FluoroDish, and make "up and downs" with a 1 mL pipette in order to homogeneise the mix.
- After 15 min, rinse the FluoroDishes with 1 - 2 mL PBS.
- Add 3mL of medium per FluoroDish.

→ **If doing an immunostaining:**

- Let incubate the cells on the patterns for 24 hours before proceeding with your immunostaining protocol.
- This protocol ends here for you.

Step 9 [Time required XX hours]

Time-lapse recording

- Tag each region to be recorded, adjust the focus with the PFS, set up the time-lapse conditions.
- Launch the time-lapse for XX hours with X minutes of frame rate.

NOTES

ALIQUOT PREPARATION

Step i [Time required 15 minutes]

PLL Solution

- Take a 10 mL Falcon tube and label it accordingly.
- Under the hood, pour maaximum 5 mL of the 0.1% (m/v) Poly-L-lysine (PLL) solution, straight from the bottle.
- Seal the tube with Parafilm and store it at 4°C in the dark.

Step ii [Time required 45 minutes]

HEPES Solution

- In a 1 L beaker, make a 0.1 M HEPES solution by dissolving 11.92 g of solid HEPES in 0.5 L of milliQ water.
- At 25°C the pH should be around 5 - 6.5, and it needs to be adjusted to 8 - 8.4. To do so, do real-time pH monitoring of the solution and pour slowly 5 - 5.5 mL of 10 M NaOH solution, while continuously stirring with a magnetic stir bar.
- Once the pH is adjusted to 8 - 8.4, take 10 syringes of 50 mL, 10 filters of 0.2 µm and 10 Falcon tubes of 50 mL. One-by-one, filter and fill up the 50 mL Falcon tubes with the 0.1 M HEPES solution at pH 8 - 8.4. **Syringes and filters are single-use.**
- Seal the Falcon tubes with Parafilm and label them properly, keeping 2 aliquots exclusively for the PEG-SVA@HEPES incubation (see Protocol Step 2) and the other 8 aliquots for rinsing processes. In this way, the incubation steps are better preserved from external contamination. Store them at 4°C in the dark up to one month, for optimal performance.

Step iii [Time required 30 minutes]

Bicarbonate Solution

- In a 1 L beaker, make a 0.1 M Sodium Bicarbonate ($NaHCO_3$) solution by dissolving 4.2 g of $NaHCO_3$ in 0.5 L of milliQ water.
- As for HEPES aliquots, take 10 syringes of 50 mL, 10 filters of 0.2 µM and 10 Falcon tubes of 50 mL. One-by-one, filter and fill up the 50 mL Falcon tubes with the 0.1 M $NaHCO_3$ solution. **Syringes and filters are single-use**
- Seal the Falcon tubes with Parafilm and label them properly, keeping 2 aliquots exclusively for the protein incubation (see Protocol Step 7) and the other 8 aliquots for rinsing processes. In this way, the incuvation steps are better preserved from external contamination. Store them at 4°C in the dark up to one month, for optimal performance.

SOURCES

NOTES

CHAPTER 8

SUPPLEMENTARY MOVIES

Supplementary Movie 1 – Representative time-lapse sequences (t=20 hours) showing the elongated and compacted morphologies adopted by an individual MCF-10A epithelial cell during its back-and-forth motion on a dumbbell-shaped fibronectin micropattern with a bridge length of 160 μm. The cell is imaged using Differential Interference Contrast (DIC) microscopy, with the micropattern labeled with rhodamine-conjugated fibronectin and the nucleus stained with Hoechst. The scale bar represents 20 μm, and images were captured at 3-minute intervals.

Figure 8.1: *Movie S1*

Supplementary Movie 2 – Time-lapse sequence in DIC mode of an epithelial cell (MCF10-A) migrating on a dumbbell-shaped fibronectin micropattern, featuring a bridge 160 μm in length and 6 μm in width, with square ends measuring 30 μm $\times$ 30 μm (t= 20 hours). The fibronectin micropattern is red and the nucleus in blue. The scale bar represents 20 μm.

Figure 8.2: *Movie S2*

Supplementary Movie 3 – Time-lapse sequence in DIC mode of an epithelial cell (MCF10-A) migrating on a dumbbell-shaped fibronectin micropattern, featuring a bridge 160 μm in length and 6 μm in width, with square ends measuring 50 μm $\times$ 50 μm (t = 20 hours). The fibronectin micropattern is depicted in red, and the nucleus is stained blue. The scale bar represents 20 μm.

Figure 8.3: *Movie S3*

Supplementary Movie 4 – Time-lapse sequences in DIC mode of an MCF10A cell migrating on interconnected dumbbell-shaped micropatterns with 160 μm-long bridges and square deconfinement zones of 2500 μm^2 (first sequence) and 900 μm^2 (second sequence). The first sequence spans 59 hours and 54 minutes, and the second sequence lasts 17 hours and 30 minutes. The nucleus is stained blue with Hoechst. Scale bar: 100 μm.

Figure 8.4: *Movie S4*

Bibliography

[1] Eva Bianconi, Allison Piovesan, Federica Facchin, Alina Beraudi, Raffaella Casadei, Flavia Frabetti, Lorenza Vitale, Maria Chiara Pelleri, Simone Tassani, Francesco Piva, et al. An estimation of the number of cells in the human body. *Annals of Human Biology*, 40(6):463–471, 2013.

[2] Marine Luciano, Marie Versaevel, Eléonore Vercruysse, Anthony Procès, Yohalie Kalukula, Alexandre Remson, Amandine Deridoux, Sylvain Gabriele, et al. Appreciating the role of cell shape changes in the mechanobiology of epithelial tissues. *Biophysics Reviews*, 3(1):011305, 2022.

[3] Miguel Vicente-Manzanares, Donna J Webb, and A Rick Horwitz. Cell migration at a glance. *Journal of Cell Science*, 118(21):4917–4919, 2005.

[4] Satoshi Kurosaka and Anna Kashina. Cell biology of embryonic migration. *Birth Defects Research Part C: Embryo Today: Reviews*, 84(2):102–122, 2008.

[5] Pablo Vargas, Lucie Barbier, Pablo José Sáez, and Matthieu Piel. Mechanisms for fast cell migration in complex environments. *Current Opinion in Cell Biology*, 48:72–78, 2017.

[6] A. Haeger, A. Kashyap, C. Kevin, et al. Collective cancer invasion forms an integrin-dependent tissue niche that promotes radiation resistance. *Communications Biology*, 3(1):1–13, 2020.

[7] Peter Friedl and Katarina Wolf. Tumour-cell invasion and migration: diversity and escape mechanisms. *Nature Reviews Cancer*, 3(5):362–374, 2003.

[8] Thomas D Pollard, Laurent Blanchoin, and R Dyche Mullins. Molecular mechanisms controlling actin filament dynamics in nonmuscle cells. *Annual review of biophysics and biomolecular structure*, 29(1):545–576, 2000.

[9] Laurent Blanchoin, Rajaa Boujemaa-Paterski, Cécile Sykes, and Julie Plastino. Actin dynamics, architecture, and mechanics in cell motility. *Physiological reviews*, 94(1):235–263, 2014.

[10] Frederick Gittes, Brian Mickey, Jilda Nettleton, and Jonathon Howard. Flexural rigidity of microtubules and actin filaments measured from thermal fluctuations in shape. *The Journal of Cell Biology*, 120(4):923–934, 1993.

[11] David C. Morse. Viscoelasticity of concentrated isotropic solutions of semiflexible polymers. 2. linear response. *Macromolecules*, 31(20):7044–7067, 1998.

[12] Hiroaki Kojima, Akihiko Ishijima, and Toshio Yanagida. Direct measurement of stiffness of single actin filaments with and without tropomyosin by in vitro nanomanipulation. *Proceedings of the National Academy of Sciences*, 91(26):12962–12966, 1994.

[13] Alphée Michelot, Julien Berro, Christophe Guérin, Rajaa Boujemaa-Paterski, Christopher J Staiger, Jean-Louis Martiel, and Laurent Blanchoin. Actin-filament stochastic dynamics mediated by adf/cofilin. *Current Biology*, 17(10):825–833, 2007.

[14] Sunny S. Lou, Alba Diz-Muñoz, Orion D. Weiner, Daniel A. Fletcher, and Julie A. Theriot. Myosin light chain kinase regulates cell polariza-

tion independently of membrane tension or rho kinase. *Journal of Cell Biology*, 209(2):275–288, 2015.

[15] Christophe Le Clainche and Marie-France Carlier. Regulation of actin assembly associated with protrusion and adhesion in cell migration. *Physiological reviews*, 88(2):489–513, 2008.

[16] Bruce Alberts. *Molecular Biology of the Cell*. CRC Press, New York, 6 edition, 2017.

[17] M Amanda Hartman and James A Spudich. The myosin superfamily at a glance. *Journal of cell science*, 125(7):1627–1632, 2012.

[18] James R Sellers. Myosins: a diverse superfamily. *Biochimica et Biophysica Acta (BBA)-Molecular Cell Research*, 1496(1):3–22, 2000.

[19] Miguel Vicente-Manzanares, Xuefei Ma, Robert S Adelstein, and Alan Rick Horwitz. Non-muscle myosin ii takes centre stage in cell adhesion and migration. *Nature reviews Molecular cell biology*, 10(11):778–790, 2009.

[20] Melissa A Quintanilla, John A Hammer, and Jordan R Beach. Non-muscle myosin 2 at a glance. *Journal of cell science*, 136(5):jcs260890, 2023.

[21] Megan R Chastney, Jasmin Kaivola, Veli-Matti Leppänen, and Johanna Ivaska. The role and regulation of integrins in cell migration and invasion. *Nature Reviews Molecular Cell Biology*, 26(2):147–167, 2025.

[22] Mohammad R.K. Mofrad and Roger D. Kamm. *Cellular Mechanotransduction: Diverse Perspectives from Molecules to Tissues*. Cambridge University Press, Cambridge, 2009.

[23] Yoshikazu Takada, Xiaojing Ye, and Scott Simon. The integrins. *Genome biology*, 8(5):215, 2007.

[24] Catherine G Galbraith, Kenneth M Yamada, and Michael P Sheetz. The relationship between force and focal complex development. *The Journal of cell biology*, 159(4):695–705, 2002.

[25] Pakorn Kanchanawong, Gleb Shtengel, Ana M Pasapera, Ericka B Ramko, Michael W Davidson, Harald F Hess, and Clare M Waterman. Nanoscale architecture of integrin-based cell adhesions. *Nature*, 468(7323):580–584, 2010.

[26] Daniel Riveline, Eli Zamir, Nathalie Q Balaban, Ulrich S Schwarz, Toshimasa Ishizaki, Shuh Narumiya, Zvi Kam, Benjamin Geiger, and Alexander D Bershadsky. Focal contacts as mechanosensors: externally applied local mechanical force induces growth of focal contacts by an mdia1-dependent and rock-independent mechanism. *The Journal of cell biology*, 153(6):1175–1186, 2001.

[27] Nathalie Q Balaban, Ulrich S Schwarz, Daniel Riveline, Polina Goichberg, Gila Tzur, Ilana Sabanay, Diana Mahalu, Sam Safran, Alexander Bershadsky, Lia Addadi, et al. Force and focal adhesion assembly: a close relationship studied using elastic micropatterned substrates. *Nature cell biology*, 3(5):466–472, 2001.

[28] Colin K Choi, Miguel Vicente-Manzanares, Jessica Zareno, Leanna A Whitmore, Alex Mogilner, and Alan Rick Horwitz. Actin and α-actinin orchestrate the assembly and maturation of nascent adhesions in a myosin ii motor-independent manner. *Nature cell biology*, 10(9):1039–1050, 2008.

[29] Catherine G Galbraith, Kenneth M Yamada, and James A Galbraith. Polymerizing actin fibers position integrins primed to probe for adhesion sites. *Science*, 315(5814):992–995, 2007.

[30] Buzz Baum and Patricia Kunda. Actin nucleation: spire—actin nucleator in a class of its own. *Current biology*, 15(8):R305–R308, 2005.

[31] R Dyche Mullins, John A Heuser, and Thomas D Pollard. The interaction of arp2/3 complex with actin: nucleation, high affinity pointed end capping, and formation of branching networks of filaments. *Proceedings of the National Academy of Sciences*, 95(11):6181–6186, 1998.

[32] Thomas D Pollard and Gary G Borisy. Cell motility and the cytoskeleton. *Cell*, 112(4):453–465, 2003.

[33] Tatyana Svitkina. The actin cytoskeleton and actin-based motility. *Cold Spring Harbor perspectives in biology*, 10(1):a018267, 2018.

[34] Dan Cojoc, Francesco Difato, Enrico Ferrari, Rajesh B Shahapure, Jummi Laishram, Massimo Righi, Enzo M Di Fabrizio, and Vincent Torre. Properties of the force exerted by filopodia and lamellipodia and the involvement of cytoskeletal components. *PloS one*, 2(10):e1072, 2007.

[35] TJ Mitchison and LP Cramer. Actin-based cell motility and cell locomotion. *Cell*, 84(3):371–379, 1996.

[36] Erik S Welf, Christopher E Miles, Jaewon Huh, Etai Sapoznik, Joseph Chi, Meghan K Driscoll, Tadamoto Isogai, Jungsik Noh, Andrew D Weems, Theresa Pohlkamp, et al. Actin-membrane release initiates cell protrusions. *Developmental cell*, 55(6):723–736, 2020.

[37] Anjali Bisaria, Arnold Hayer, Damien Garbett, Daniel Cohen, and Tobias Meyer. Membrane-proximal f-actin restricts local membrane protrusions and directs cell migration. *Science*, 368(6496):1205–1210, 2020.

[38] Guillaume Salbreux, Guillaume Charras, and Ewa Paluch. Actin cortex mechanics and cellular morphogenesis. *Trends in cell biology*, 22(10):536–545, 2012.

[39] Priyamvada Chugh and Ewa K Paluch. The actin cortex at a glance. *Journal of cell science*, 131(14):jcs186254, 2018.

[40] Romain Levayer, Anne Pelissier-Monier, and Thomas Lecuit. Spatial regulation of dia and myosin-ii by rhogef2 controls initiation of e-cadherin endocytosis during epithelial morphogenesis. *Nature cell biology*, 13(5):529–540, 2011.

[41] Michael Murrell, Patrick W Oakes, Martin Lenz, and Margaret L Gardel. Forcing cells into shape: the mechanics of actomyosin contractility. *Nature reviews Molecular cell biology*, 16(8):486–498, 2015.

[42] Priyamvada Chugh, Andrew G Clark, Matthew B Smith, Davide AD Cassani, Kai Dierkes, Anan Ragab, Philippe P Roux, Guillaume Charras, Guillaume Salbreux, and Ewa K Paluch. Actin cortex architecture regulates cell surface tension. *Nature cell biology*, 19(6):689–697, 2017.

[43] Miia Bovellan, Yves Romeo, Maté Biro, Annett Boden, Priyamvada Chugh, Amina Yonis, Malti Vaghela, Marco Fritzsche, Dale Moulding, Richard Thorogate, et al. Cellular control of cortical actin nucleation. *Current Biology*, 24(14):1628–1635, 2014.

[44] Anumita Jawahar, Joseph Vermeil, Julien Heuvingh, Olivia Du Roure, and Matthieu Piel. The third dimension of the actin cortex. *Current Opinion in Cell Biology*, 89:102381, 2024.

[45] Binh An Truong Quang, Ruby Peters, Davide AD Cassani, Priyamvada Chugh, Andrew G Clark, Meghan Agnew, Guillaume Charras, and Ewa K Paluch. Extent of myosin penetration within the actin cortex regulates cell surface mechanics. *Nature communications*, 12(1):6511, 2021.

[46] Alba Diz-Muñoz, Michael Krieg, Martin Bergert, Itziar Ibarluceа-Benitez, Daniel J Muller, Ewa Paluch, and Carl-Philipp Heisenberg. Control of directed cell migration in vivo by membrane-to-cortex attachment. *PLoS biology*, 8(11):e1000544, 2010.

[47] Andrew G Clark, Kai Dierkes, and Ewa K Paluch. Monitoring actin cortex thickness in live cells. *Biophysical journal*, 105(3):570–580, 2013.

[48] Mathias P Clausen, H Colin-York, Falk Schneider, Christian Eggeling, and Marco Fritzsche. Dissecting the actin cortex density and membrane-cortex distance in living cells by super-resolution microscopy. *Journal of physics D: Applied physics*, 50(6):064002, 2017.

[49] Gijsje H Koenderink and Ewa K Paluch. Architecture shapes contractility in actomyosin networks. *Current opinion in cell biology*, 50:79–85, 2018.

[50] Richard G Fehon, Andrea I McClatchey, and Anthony Bretscher. Organizing the cell cortex: the role of erm proteins. *Nature reviews Molecular cell biology*, 11(4):276–287, 2010.

[51] Alexis Gautreau, Patrick Poullet, Daniel Louvard, and Monique Arpin. Ezrin, a plasma membrane–microfilament linker, signals cell survival through the phosphatidylinositol 3-kinase/akt pathway. *Proceedings of the National Academy of Sciences*, 96(13):7300–7305, 1999.

[52] Soren Prag, Maddy Parsons, Melanie D Keppler, Simon M Ameer-Beg, Paul Barber, James Hunt, Andrew J Beavil, Rosy Calvert, Monique Arpin, Borivoj Vojnovic, et al. Activated ezrin promotes cell migration through recruitment of the gef dbl to lipid rafts and preferential downstream activation of cdc42. *Molecular biology of the cell*, 18(8):2935–2948, 2007.

[53] Ferran Valderrama, Subangi Thevapala, and Anne J Ridley. Radixin regulates cell migration and cell–cell adhesion through rac1. *Journal of cell science*, 125(14):3310–3319, 2012.

[54] Seph Marshall-Burghardt, Rodrigo A Migueles-Ramírez, Qiyao Lin, Nada El Baba, Rayan Saada, Mustakim Umar, Kian Mavalwala, and Arnold Hayer. Excitable rho dynamics control cell shape and motility by sequentially activating erm proteins and actomyosin contractility. *Science Advances*, 10(36):eadn6858, 2024.

[55] Besaiz J Sánchez-Sánchez, Stefania Marcotti, David Salvador-Garcia, María-del-Carmen Díaz-de-la Loza, Mubarik Burki, Andrew J Davidson, Will Wood, and Brian M Stramer. Moesin integrates cortical and lamellar actin networks during drosophila macrophage migration. *Nature Communications*, 16(1):1414, 2025.

[56] G Bulut, SH Hong, K Chen, EM Beauchamp, S Rahim, GW Kosturko, E Glasgow, S Dakshanamurthy, HS Lee, I Daar, et al. Small molecule inhibitors of ezrin inhibit the invasive phenotype of osteosarcoma cells. *Oncogene*, 31(3):269–281, 2012.

[57] Abdi Ghaffari, Victoria Hoskin, Gulisa Turashvili, Sonal Varma, Jeff Mewburn, Graeme Mullins, Peter A Greer, Friedemann Kiefer, Andrew G Day, Yolanda Madarnas, et al. Intravital imaging reveals systemic ezrin inhibition impedes cancer cell migration and lymph node metastasis in breast cancer. *Breast Cancer Research*, 21(1):12, 2019.

[58] Ana Estecha, Lorena Sánchez-Martín, Amaya Puig-Kroger, Rubén A Bartolomé, Joaquín Teixidó, Rafael Samaniego, and Paloma Sánchez-Mateos. Moesin orchestrates cortical polarity of melanoma tumour cells to initiate 3d invasion. *Journal of cell science*, 122(19):3492–3501, 2009.

[59] Michael Abercrombie, JEM Heaysman, and SM Pegrum. The locomotion of fibroblasts in culture: A study of locomotory paths and the proposed model of movement. *Experimental Cell Research*, 59:393–398, 1970.

[60] Michael Abercrombie. The croonian lecture, 1978: The crawling movement of metazoan cells. *Proceedings of the Royal Society of London. Series B. Biological Sciences*, 207(1167):129–147, 1980.

[61] Douglas A Lauffenburger and Alan F Horwitz. Cell migration: A physically integrated molecular process. *Cell*, 84(3):359–369, 1996.

[62] Anne J Ridley, Martin A Schwartz, Keith Burridge, Richard A Firtel, Mark H Ginsberg, Gary Borisy, Jonathan T Parsons, and Alan R Horwitz. Cell migration: integrating signals from front to back. *Science*, 302(5651):1704–1709, 2003.

[63] Michael P Sheetz, Dan Felsenfeld, Catherine G Galbraith, and Daniel Choquet. Cell migration as a five-step cycle. In *Biochemical Society Symposium*, volume 65, pages 233–243, 1999.

[64] Danahe Mohammed, Guillaume Charras, Eléonore Vercruysse, Marie Versaevel, Joséphine Lantoine, Laura Alaimo, Céline Bruyère, Marine Luciano, Karine Glinel, Geoffrey Delhaye, et al. Substrate area confinement is a key determinant of cell velocity in collective migration. *Nature Physics*, 15(8):858–866, 2019.

[65] Benjamin Geiger, Joachim P Spatz, and Alexander D Bershadsky. Environmental sensing through focal adhesions. *Nature Reviews Molecular Cell Biology*, 10(1):21–33, 2009.

[66] Miguel Vicente-Manzanares, Catherine K Choi, and Alan R Horwitz. Actin dynamics and the regulation of cell migration. *Trends in Cell Biology*, 19(7):362–369, 2009.

[67] Alberto Elosegui-Artola, Ignacio Andreu, Amy E M Beedle, Ane Lezamiz, Marina Uroz, Anita J Kosmalska, Rosa Oria, Jenny Z Kechagia, Patricia Rico-Lastres, Anne-Laure Le Roux, et al. Mechanical regulation of a molecular clutch defines force transmission and transduction in response to matrix rigidity. *Nature Cell Biology*, 20(3):271–281, 2018.

[68] Guillaume Giannone, Benjamin J Dubin-Thaler, Hans-Günther Doberei-ner, Nadine Kieffer, Anne R Bresnick, and Michael P Sheetz. The molec-ular clutch model for the formation of actin-based lamellipodia. *Cell*, 128(3):561–575, 2009.

[69] Benjamin L Bangasser and David J Odde. Determinants of maximal force transmission in a motor–clutch model of cell traction in a compliant microenvironment. *Nature Communications*, 4:1–9, 2013.

[70] Anita J Kosmalska, Laura Casares, Alberto Elosegui-Artola, Joseph J Thottacherry, Raquel Moreno-Vicente, Vanesa Gonzalez-Tarrago, Miguel A Del Pozo, Pere Roca-Cusachs, Nils C Gauthier, et al. Physi-cal principles of membrane remodelling during cell mechanoadaptation. *Nature Communications*, 6:7292, 2015.

[71] Arik D Lieber, Sarit Yehudai-Resheff, Elizabeth L Barnhart, Julie A Theriot, and Kinneret Keren. Membrane tension governs cell motility by controlling lamellipodium organization and dynamics. *Cell Reports*, 5(3):611–622, 2013.

[72] Alba Diz-Muñoz, Kevin Thurley, Swetha Chintamen, Steven J Altschuler, Lani F Wu, Orion D Weiner, and Daniel A Fletcher. Control of directed cell migration in vivo by membrane-to-cortex attachment. *PLoS Biology*, 11(11):e1001720, 2013.

[73] Nils C Gauthier, Thomas A Masters, and Michael P Sheetz. Mechanical feedback between membrane tension and dynamics. *Trends in cell biology*, 22(10):527–535, 2012.

[74] Pierre Sens and Matthew S Turner. Membrane tension and the organi-zation of cell shape and motility. *Journal of Physics: Condensed Matter*, 27(27):273103, 2015.

[75] Meghan K Driscoll and Gaudenz Danuser. Cell shape dynamics: from waves to migration. *Developmental Cell*, 23(2):196–209, 2012.

[76] Catherine D Nobes and Alan Hall. Rho, rac, and cdc42 gtpases regulate the assembly of multimolecular focal complexes associated with actin stress fibers, lamellipodia, and filopodia. *Cell*, 81(1):53–62, 1995.

[77] Sarah J Heasman and Anne J Ridley. Mammalian rho gtpases: new insights into their functions from in vivo studies. *Nature reviews Molecular cell biology*, 9(9):690–701, 2008.

[78] Alan Hall. Rho gtpases and the actin cytoskeleton. *Science*, 279(5350):509–514, 1998.

[79] Johannes L Bos, Holger Rehmann, and Alfred Wittinghofer. Gefs and gaps: critical elements in the control of small g proteins. *Cell*, 129(5):865–877, 2007.

[80] Matthew Machacek, Louis Hodgson, Christine Welch, Heather Elliott, Olivier Pertz, Petra Nalbant, Amy Abell, George L Johnson, Klaus M Hahn, and Gaudenz Danuser. Coordination of rho gtpase activities during cell protrusion. *Nature*, 461(7260):99–103, 2009.

[81] Amine Sadok and Christopher J Marshall. Rho gtpases: masters of cell migration. *Small GTPases*, 5(4):e983869, 2014.

[82] Rana El Masri and Jerome Delon. Rho gtpases: from new partners to complex immune syndromes. *Nature Reviews Immunology*, 21(8):499–513, 2021.

[83] Sarah E Siegrist and Chris Q Doe. Microtubule-induced cortical cell polarity. *Genes & development*, 21(5):483–496, 2007.

[84] Eric R Gomes, Sonal Jani, and Gregg G Gundersen. Centrosome positioning in migrating cells. *Nature Cell Biology*, 7(11):1194–1201, 2005.

[85] Masaki Fukata, Shun Kuroda, Masatoshi Nakagawa, Ayako Kawajiri, Norihiko Itoh, Akihiko Iwamatsu, and Kozo Kaibuchi. Rac1 and cdc42 capture microtubules through iqgap1 and clip-170. *Cell*, 109(7):873–885, 2002.

[86] Jörg Birkenfeld, Perihan Nalbant, Benjamin P Bohl, Olivier Pertz, Klaus M Hahn, and Gary M Bokoch. Gef-h1 modulates localized rhoa activation during cytokinesis under the control of mitotic kinases. *Developmental cell*, 12(5):699–712, 2007.

[87] Sandrine Etienne-Manneville. Microtubules in cell migration. *Annual review of cell and developmental biology*, 29(1):471–499, 2013.

[88] Takashi Watanabe, Jun Noritake, and Kozo Kaibuchi. Regulation of microtubules in cell migration. *Trends in cell biology*, 15(2):76–83, 2005.

[89] Robert J Ju, Alistair D Falconer, Christanny J Schmidt, Marco A Enriquez Martinez, Kevin M Dean, Reto P Fiolka, David P Sester, Max Nobis, Paul Timpson, Alexis J Lomakin, et al. Compression-dependent microtubule reinforcement enables cells to navigate confined environments. *Nature cell biology*, 26(9):1520–1534, 2024.

[90] Marileen Dogterom and Gijsje H Koenderink. Actin–microtubule crosstalk in cell biology. *Nature reviews Molecular cell biology*, 20(1):38–54, 2019.

[91] Jonathon Howard and Anthony A Hyman. Growth, fluctuation and switching at microtubule plus ends. *Nature Reviews Molecular Cell Biology*, 10(8):569–574, 2009.

[92] Stefanie Gossen, Sarah Gerstner, and Annette Borchers. The rhogef trio is transported by microtubules and affects microtubule stability in migrating neural crest cells. *Cells & development*, 177:203899, 2024.

[93] Flora Llense and Sandrine Etienne-Manneville. Front-to-rear polarity in migrating cells. In *Cell Polarity 1: Biological Role and Basic Mechanisms*, pages 115–146. Springer, 2015.

[94] Clare Garcin and Anne Straube. Microtubules in cell migration. *Essays in biochemistry*, 63(5):509–520, 2019.

[95] Shailaja Seetharaman and Sandrine Etienne-Manneville. Cytoskeletal crosstalk in cell migration. *Trends in cell biology*, 30(9):720–735, 2020.

[96] M Angeles Juanes, Daniel Isnardon, Ali Badache, Sophie Brasselet, Manos Mavrakis, and Bruce L Goode. The role of apc-mediated actin assembly in microtubule capture and focal adhesion turnover. *Journal of Cell Biology*, 218(10):3415–3435, 2019.

[97] Yamini Ravichandran, Bruno Goud, and Jean-Baptiste Manneville. The golgi apparatus and cell polarity: Roles of the cytoskeleton, the golgi matrix, and golgi membranes. *Current opinion in cell biology*, 62:104–113, 2020.

[98] Kotryna Vaidžiulytė, Anne-Sophie Macé, Aude Battistella, William Beng, Kristine Schauer, and Mathieu Coppey. Persistent cell migration emerges from a coupling between protrusion dynamics and polarized trafficking. *Elife*, 11:e69229, 2022.

[99] Benoit Ladoux, René-Marc Mège, and Xavier Trepat. Front–rear polarization by mechanical cues: from single cells to tissues. *Trends in cell biology*, 26(6):420–433, 2016.

[100] Desirée Kroll and Julia Renkawitz. Organelle positioning as a regulated driver of cell migration. *Nature Reviews Molecular Cell Biology*, 25(2):123–138, 2024.

[101] Julien Elric and Sandrine Etienne-Manneville. Centrosome positioning in polarized cells: common themes and variations. *Experimental cell research*, 328(2):240–248, 2014.

[102] Ryan J Petrie, Andrew D Doyle, and Kenneth M Yamada. Random versus directionally persistent cell migration. *Nature reviews Molecular cell biology*, 10(8):538–549, 2009.

[103] Hervé De Belly, Claudia Thomas, Ana Zorzano, and Nils C Gauthier. Optogenetic dissection of cortical force propagation via membrane tension. *Cell Reports*, 40(1):111047, 2023.

[104] Hervé De Belly, Andreu Fernández Gallen, Evelyn Strickland, Dorothy C Estrada, Patrick J Zager, Janis K Burkhardt, Hervé Turlier, and Orion D Weiner. Long-range mutual activation establishes rho and rac polarity during cell migration. *bioRxiv*, page 2024.10.01.616161, 2024.

[105] Peter Friedl and Darren Gilmour. Collective cell migration in morphogenesis, regeneration and cancer. *Nature reviews Molecular cell biology*, 10(7):445–457, 2009.

[106] Ryan J Petrie and Kenneth M Yamada. Multiple mechanisms of 3d migration: the origins of plasticity. *Current opinion in cell biology*, 42:7–12, 2016.

[107] Rizwan Farooqui and Gabriel Fenteany. Multiple rows of cells behind an epithelial wound edge extend cryptic lamellipodia to collectively drive cell-sheet movement. *Journal of cell science*, 118(1):51–63, 2005.

[108] Andrew D Doyle, Nicole Carvajal, Albert Jin, Kazue Matsumoto, and Kenneth M Yamada. Local 3d matrix microenvironment regulates cell migration through spatiotemporal dynamics of contractility-dependent adhesions. *Nature communications*, 6(1):8720, 2015.

[109] Katarina Wolf, Markus Te Lindert, Mirjam Krause, Stefan Alexander, Joost Te Riet, Alan L Willis, Robert M Hoffman, Carl G Figdor, Stephan J Weiss, and Peter Friedl. Physical limits of cell migration: control by ecm space and nuclear deformation and tuning by proteolysis and traction force. *Journal of Cell Biology*, 201(7):1069–1084, 2013.

[110] Kenneth M Yamada and Michael Sixt. Mechanisms of 3d cell migration. *Nature Reviews molecular cell biology*, 20(12):738–752, 2019.

[111] Guillaume T Charras, Margaret Coughlin, Timothy J Mitchison, and L Mahadevan. Life and times of a cellular bleb. *Biophysical journal*, 94(5):1836–1853, 2008.

[112] Katarina Wolf, Irina Mazo, Harry Leung, Katharina Engelke, Ulrich H Von Andrian, Elena I Deryugina, Alex Y Strongin, Eva-B Brocker, and Peter Friedl. Compensation mechanism in tumor cell migration: mesenchymal–amoeboid transition after blocking of pericellular proteolysis. *The Journal of cell biology*, 160(2):267–277, 2003.

[113] Hong-pyo Lee, Farid Alisafaei, Kolade Adebawale, Julie Chang, Vivek B Shenoy, and Ovijit Chaudhuri. The nuclear piston activates mechanosensitive ion channels to generate cell migration paths in confining microenvironments. *Science advances*, 7(2):eabd4058, 2021.

[114] Vincent Hakim and Pascal Silberzan. Collective cell migration: a physics perspective. *Reports on Progress in Physics*, 80(7):076601, 2017.

[115] Peter Friedl and Katarina Wolf. Plasticity of cell migration: a multiscale tuning model. *Journal of Cell Biology*, 188(1):11–19, 2010.

[116] Kerry Wilson, Alexandre Lewalle, Marco Fritzsche, Richard Thorogate, Tom Duke, and Guillaume Charras. Mechanisms of leading edge protrusion in interstitial migration. *Nature communications*, 4(1):2896, 2013.

[117] Martin Bergert, Anna Erzberger, Ravi A Desai, Irene M Aspalter, Andrew C Oates, Guillaume Charras, Guillaume Salbreux, and Ewa K Paluch. Force transmission during adhesion-independent migration. *Nature cell biology*, 17(4):524–529, 2015.

[118] Anne Reversat, Florian Gaertner, Jack Merrin, Julian Stopp, Saren Tasciyan, Juan Aguilera, Ingrid De Vries, Robert Hauschild, Miroslav Hons, Matthieu Piel, et al. Cellular locomotion using environmental topography. *Nature*, 582(7813):582–585, 2020.

[119] Yan-Jun Liu, Maël Le Berre, Franziska Lautenschlaeger, Paolo Maiuri, Andrew Callan-Jones, Mélina Heuzé, Tohru Takaki, Raphaël Voituriez, and Matthieu Piel. Confinement and low adhesion induce fast amoeboid migration of slow mesenchymal cells. *Cell*, 160(4):659–672, 2015.

[120] Elena Cambria, Mark F Coughlin, Marie A Floryan, Giovanni S Offeddu, Sarah E Shelton, and Roger D Kamm. Linking cell mechanical memory and cancer metastasis. *Nature Reviews Cancer*, 24(3):216–228, 2024.

[121] Jia Wen Nicole Lee and Andrew W Holle. Engineering approaches for understanding mechanical memory in cancer metastasis. *APL bioengineering*, 8(2), 2024.

[122] Polina G. Gritsenko, Olga Ilina, and Peter Friedl. Interstitial guidance of cancer invasion. *The Journal of Pathology*, 226(2):185–199, 2012.

[123] Karuna Ganesh and Joan Massagué. Targeting metastatic cancer. *Nature medicine*, 27(1):34–44, 2021.

[124] John Condeelis and Jeffrey E Segall. Intravital imaging of cell movement in tumours. *Nature Reviews Cancer*, 3(12):921–930, 2003.

[125] Olga Ilina, Pavlo G Gritsenko, Simon Syga, Jurgen Lippoldt, Caterina AM La Porta, Oleksandr Chepizhko, Steffen Grosser, Manon Vullings, Gert-Jan Bakker, Jorn Starruß, et al. Cell–cell adhesion and 3d matrix confinement determine jamming transitions in breast cancer invasion. *Nature cell biology*, 22(9):1103–1115, 2020.

[126] Oleksandr Chepizhko, Josep-Maria Armengol-Collado, Stephanie Alexander, Nicholas A. Kurniawan, and Ovijit Chaudhuri. Confined cell migration along extracellular matrix space in vivo. *Proceedings of the National Academy of Sciences*, 122(1):e2414009121, 2025.

[127] Bettina Weigelin, Gert-Jan Bakker, and Peter Friedl. Intravital third harmonic generation microscopy of collective melanoma cell invasion: Principles of interface guidance and microvesicle dynamics. *IntraVital*, 1(1):32–43, 2012.

[128] Paolo P Provenzano, Kevin W Eliceiri, Jay M Campbell, David R Inman, John G White, and Patricia J Keely. Collagen reorganization at the tumor-stromal interface facilitates local invasion. *BMC medicine*, 4(1):38, 2006.

[129] Matthew W Conklin, Jens C Eickhoff, Kristin M Riching, Carolyn A Pehlke, Kevin W Eliceiri, Paolo P Provenzano, Andreas Friedl, and Patricia J Keely. Aligned collagen is a prognostic signature for survival in human breast carcinoma. *The American journal of pathology*, 178(3):1221–1232, 2011.

[130] Wei Han, Shuo Chen, Wenzhen Yuan, Qiang Fan, Jian Tian, Xing Wang, Xiang Zhang, Lin Chen, Yu Zhang, and Liyun Liu. Oriented collagen fibers direct tumor cell intravasation. *Proceedings of the National Academy of Sciences*, 113(40):11208–11213, 2016.

[131] Matthew R. Zanotelli, Joseph P. Miller, Wenjun Wang, and Cynthia A. Reinhart-King. Tension directs cancer cell migration over fiber alignment through energy minimization. *Biomaterials*, 311:122682, 2024.

[132] Azarnoosh Foroozandehfar, Shayan Tohidi, Shafayet Ahmed Siddiqui, Fred Rogers Namanda, and Ian C. Schneider. Branched and linear f-actin

networks control directional migration switching behavior on aligned collagen fibrils. *bioRxiv*, 2025.01.03.631234, 2025. Preprint.

[133] Colin D. Paul, Panagiotis Mistriotis, and Konstantinos Konstantopoulos. Cancer cell motility: lessons from migration in confined spaces. *Nature Reviews Cancer*, 17(2):131–140, 2017.

[134] Anna Haeger, Marina Krause, Katarina Wolf, and Peter Friedl. Cell jamming: collective invasion of mesenchymal tumor cells imposed by tissue confinement. *Biochimica et Biophysica Acta (BBA)-General Subjects*, 1840(8):2386–2395, 2014.

[135] Ge al Berx, AM Cleton-Jansen, F Nollet, WJ De Leeuw, M Van de Vijver, C Cornelisse, and Frans Van Roy. E-cadherin is a tumour/invasion suppressor gene mutated in human lobular breast cancers. *The EMBO journal*, 14(24):6107–6115, 1995.

[136] Guillaume Duclos, Santiago Garcia, Hannah G. Yevick, and Pascal Silberzan. Perfect nematic order in confined monolayers of spindle-shaped cells. *Soft Matter*, 10(14):2346–2353, 2014.

[137] Ravi S Kane, Shuichi Takayama, Emanuele Ostuni, Donald E Ingber, and George M Whitesides. Patterning proteins and cells using soft lithography. *Biomaterials*, 20(23-24):2363–2376, 1999.

[138] Marine Luciano and Sylvain Gabriele. Designing hydrogel dimensionality to investigate mechanobiology. *Soft Matter*, 21(23):4551–4572, 2025.

[139] Martin Reifarth. (sub-) microscale patterning via microcontact printing (μcp): Recent advances, applications and future perspectives. *Soft Matter*, 2025.

[140] Cornelis J Weijer. Collective cell migration in development. *Journal of cell science*, 122(18):3215–3223, 2009.

[141] Peter Friedl, Peter B Noble, Paul A Walton, Dale W Laird, Peter J Chauvin, Roger J Tabah, Martin Black, and Kurt S Zänker. Migration of coordinated cell clusters in mesenchymal and epithelial cancer explants in vitro. *Cancer research*, 55(20):4557–4560, 1995.

[142] Kevin J Cheung and Andrew J Ewald. A collective route to metastasis: Seeding by tumor cell clusters. *Science*, 352(6282):167–169, 2016.

[143] Eléonore Vercruysse, David B Brückner, Manuel Gómez-González, Alexandre Remson, Marine Luciano, Yohalie Kalukula, Leone Rossetti, Xavier Trepat, Edouard Hannezo, and Sylvain Gabriele. Geometry-driven migration efficiency of autonomous epithelial cell clusters. *Nature Physics*, 20(9):1492–1500, 2024.

[144] Medhavi Vishwakarma, Joachim P Spatz, and Tamal Das. Mechanobiology of leader–follower dynamics in epithelial cell migration. *Current opinion in cell biology*, 66:97–103, 2020.

[145] Leone Rossetti, Steffen Grosser, Juan Francisco Abenza, Léo Valon, Pere Roca-Cusachs, Ricard Alert, and Xavier Trepat. Optogenetic generation of leader cells reveals a force–velocity relation for collective cell migration. *Nature Physics*, 20(10):1659–1669, 2024.

[146] Jessanne Y. Lichtenberg, Ella Ramamurthy, Anna D. Young, and Ian Y. Wong. Leader cells mechanically respond to aligned collagen architecture to direct collective migration. *PLOS ONE*, 19(1):e0296153, 2024.

[147] Kandice Tanner, Hidetoshi Mori, Rana Mroue, Alexandre Bruni-Cardoso, and Mina J Bissell. Coherent angular motion in the establishment of multicellular architecture of glandular tissues. *Proceedings of the National Academy of Sciences*, 109(6):1973–1978, 2012.

[148] Saori L Haigo and David Bilder. Global tissue revolutions in a morphogenetic movement controlling elongation. *Science*, 331(6020):1071–1074, 2011.

[149] Shreyansh Jain, Victoire ML Cachoux, Gautham HNS Narayana, Simon de Beco, Joseph D'alessandro, Victor Cellerin, Tianchi Chen, Mélina L Heuzé, Philippe Marcq, René-Marc Mège, et al. The role of single-cell mechanical behaviour and polarity in driving collective cell migration. *Nature physics*, 16(7):802–809, 2020.

[150] Chao Jiang, Hong-Yu Luo, Xinpeng Xu, Shuo-Xing Dou, Wei Li, Dongshi Guan, Fangfu Ye, Xiaosong Chen, Ming Guo, Peng-Ye Wang,

et al. Switch of cell migration modes orchestrated by changes of three-dimensional lamellipodium structure and intracellular diffusion. *Nature communications*, 14(1):5166, 2023.

[151] David B Brückner, Alexandra Fink, Christoph Schreiber, Peter JF Röttgermann, Joachim O Rädler, and Chase P Broedersz. Stochastic nonlinear dynamics of confined cell migration in two-state systems. *Nature Physics*, 15(6):595–601, 2019.

[152] Alexandra Fink, David B Brückner, Christoph Schreiber, Peter JF Röttgermann, Chase P Broedersz, and Joachim O Rädler. Area and geometry dependence of cell migration in asymmetric two-state micropatterns. *Biophysical journal*, 118(3):552–564, 2020.

[153] Andrew D Doyle, Francis W Wang, Kazue Matsumoto, and Kenneth M Yamada. One-dimensional topography underlies three-dimensional fibrillar cell migration. *Journal of cell biology*, 184(4):481–490, 2009.

[154] Ryan J Petrie and Kenneth M Yamada. At the leading edge of three-dimensional cell migration. *Journal of cell science*, 125(24):5917–5926, 2012.

[155] Charlotte Guetta-Terrier, Pascale Monzo, Jie Zhu, Hongyan Long, Lakshmi Venkatraman, Yue Zhou, PeiPei Wang, Sing Yian Chew, Alexander Mogilner, Benoit Ladoux, et al. Protrusive waves guide 3d cell migration along nanofibers. *Journal of Cell Biology*, 211(3):683–701, 2015.

[156] Erdem D Tabdanov, Vikram Puram, Alexander Zhovmer, and Paolo P Provenzano. Microtubule-actomyosin mechanical cooperation during contact guidance sensing. *Cell reports*, 25(2):328–338, 2018.

[157] K Hennig, I Wang, P Moreau, L Valon, S DeBeco, M Coppey, YA Miroshnikova, C Albiges-Rizo, Cyril Favard, R Voituriez, et al. Stick-slip dynamics of cell adhesion triggers spontaneous symmetry breaking and directional migration of mesenchymal cells on one-dimensional lines. *Science Advances*, 6(1):eaau5670, 2020.

[158] Kirstine Lavrsen, Girish Rajendraprasad, Marcin Leda, Susana Eibes, Elisa Vitiello, Vasileios Katopodis, Andrew B Goryachev, and Marin

Barisic. Microtubule detyrosination drives symmetry breaking to polarize cells for directed cell migration. *Proceedings of the National Academy of Sciences*, 120(22):e2300322120, 2023.

[159] Puja Sharma, Colin Ng, Aniket Jana, Abinash Padhi, Paige Szymanski, Jerry SH Lee, Bahareh Behkam, and Amrinder S Nain. Aligned fibers direct collective cell migration to engineer closing and nonclosing wound gaps. *Molecular biology of the cell*, 28(19):2579–2588, 2017.

[160] Hannah G Yevick, Guillaume Duclos, Isabelle Bonnet, and Pascal Silberzan. Architecture and migration of an epithelium on a cylindrical wire. *Proceedings of the National Academy of Sciences*, 112(19):5944–5949, 2015.

[161] William Y. Wang, Carla D. Davidson, Doris Lin, and Brendon M. Baker. Actomyosin contractility-dependent matrix stretch and recoil induces rapid cell migration. *Nature Communications*, 10(1):1186, 2019.

[162] Samila Nasrollahi, Chad Walter, Anthony J. Loza, Gregory V. Schimizzi, Gregory D. Longmore, and Apurva Pathak. Past matrix stiffness primes epithelial cells and regulates their future collective migration through a mechanical memory. *Biomaterials*, 146:146–155, 2017.

[163] José A. Almeida, Jenna L. Balestrini, James P. O'Donnell, Brian Peña, Sanjay Kumar, and Ovijit Chaudhuri. Mechanically primed cells transfer memory to fibrous matrices for invasion across environments of distinct stiffness and dimensionality. *Molecular Biology of the Cell*, 34(6):ar54, 2023.

[164] Oscar Maiques, Rachel Chen, Kian F. Wong, Skyler D. Conner, Denis Wirtz, and Andrew J. Ewald. Matrix mechano-sensing at the invasive front induces a cytoskeletal and transcriptional memory supporting metastasis. *Nature Communications*, 16(1):1394, 2025.

[165] Joseph D'Alessandro, Alex Barbier-Chebbah, Victor Cellerin, Camille Allier, Timo Betz, and Alexandre Nicolas. Cell migration guided by long-lived spatial memory. *Nature Communications*, 12(1):4118, 2021.

[166] Jenna A. Mosier, Emily D. Fabiano, Catherine M. Ludolph, Marja C. Lampi, and Cynthia A. Reinhart-King. Confinement primes cells for faster migration by polarizing active mitochondria. *Nanoscale Advances*, 6(1):209–220, 2024.

[167] Matthew R. Zanotelli, Aniqua Rahman-Zaman, Jacob A. VanderBurgh, Paul V. Taufalele, Aadhar Jain, David Erickson, François Bordeleau, and Cynthia A. Reinhart-King. Energetic costs regulated by cell mechanics and confinement are predictive of migration path during decision-making. *Nature Communications*, 10:4185, 2019.

[168] Ying Qu, Bingchen Han, Yi Yu, Weiwu Yao, Shikha Bose, Beth Y Karlan, Armando E Giuliano, and Xiaojiang Cui. Evaluation of mcf10a as a reliable model for normal human mammary epithelial cells. *PloS one*, 10(7):e0131285, 2015.

[169] Pierre-Olivier Strale, Ammar Azioune, Ghislain Bugnicourt, Yohan Lecomte, Makhlad Chahid, and Vincent Studer. Multiprotein printing by light-induced molecular adsorption. *Advanced materials*, 28(10):2024–2029, 2016.

[170] Thomas Grevesse, Marie Versaevel, Géraldine Circelli, Sylvain Desprez, and Sylvain Gabriele. A simple route to functionalize polyacrylamide hydrogels for the independent tuning of mechanotransduction cues. *Lab on a Chip*, 13(5):777–780, 2013.

[171] Thomas Grevesse, Marie Versaevel, and Sylvain Gabriele. Preparation of hydroxy-paam hydrogels for decoupling the effects of mechanotransduction cues. *Journal of Visualized Experiments: JoVE*, (90):51010, 2014.

[172] Giuseppe Ciccone, Mariana Azevedo Gonzalez-Oliva, Marie Versaevel, Marco Cantini, Massimo Vassalli, Manuel Salmeron-Sanchez, and Sylvain Gabriele. Epithelial cell mechanoresponse to matrix viscoelasticity and confinement within micropatterned viscoelastic hydrogels. *Advanced Science*, 12(18):2408635, 2025.

[173] Sandrine Morlat and Jean-Luc Gardette. Phototransformation of water-soluble polymers. part ii: photooxidation of poly (ethylene oxide) in aqueous solution. *Polymer*, 44(26):7891–7897, 2003.

[174] Carsen Stringer, Tim Wang, Michalis Michaelos, and Marius Pachitariu. Cellpose: a generalist algorithm for cellular segmentation. *Nature methods*, 18(1):100–106, 2021.

[175] Utku Horzum, Berrin Ozdil, and Devrim Pesen-Okvur. Step-by-step quantitative analysis of focal adhesions. *MethodsX*, 1:56–59, 2014.

[176] Matthew E. Berginski and Shawn M. Gomez. The focal adhesion analysis server: a web tool for analyzing focal adhesion dynamics. *F1000Research*, 2:68, 2013. v1; ref status: indexed.

[177] RD Allen and GB David. The zeiss-nomarski differential interference equipment for transmitted-light microscopy. *Zeitschrift fur wissenschaftliche Mikroskopie und mikroskopische Technik*, 69(4):193–221, 1969.

[178] Bruce Alberts, Rebecca Heald, Alexander Johnson, David Morgan, Martin Raff, Keith Roberts, and Peter Walter. *Molecular biology of the cell: seventh international student edition with registration card*. WW Norton & Company, 2022.

[179] Jeff W Lichtman and José-Angel Conchello. Fluorescence microscopy. *Nature methods*, 2(12):910–919, 2005.

[180] D Lansing Taylor. Basic fluorescence microscopy. *Methods in cell biology*, 29:207–237, 1988.

[181] Marvin Minsky. Memoir on inventing the confocal scanning microscope. 1988.

[182] David B Brückner, Nicolas Arlt, Alexandra Fink, Pierre Ronceray, Joachim O Rädler, and Chase P Broedersz. Learning the dynamics of cell–cell interactions in confined cell migration. *Proceedings of the National Academy of Sciences*, 118(7):e2016602118, 2021.

[183] David B Brückner, Pierre Ronceray, and Chase P Broedersz. Inferring the dynamics of underdamped stochastic systems. *Physical review letters*, 125(5):058103, 2020.

[184] Marie Versaevel, Thomas Grevesse, and Sylvain Gabriele. Spatial coordination between cell and nuclear shape within micropatterned endothelial cells. *Nature communications*, 3(1):671, 2012.

[185] Paolo Maiuri, Jean-François Rupprecht, Stefan Wieser, Verena Ruprecht, Olivier Bénichou, Nicolas Carpi, Mathieu Coppey, Simon De Beco, Nir Gov, Carl-Philipp Heisenberg, et al. Actin flows mediate a universal coupling between cell speed and cell persistence. *Cell*, 161(2):374–386, 2015.

[186] Yohalie Kalukula, Marine Luciano, Gleb Simanov, Guillaume Charras, David B Brückner, and Sylvain Gabriele. The actin cortex acts as a mechanical memory of morphology in confined migrating cells. *Nature Physics*, pages 1–11, 2025.

[187] David B Brückner and Chase P Broedersz. Learning dynamical models of single and collective cell migration: a review. *Reports on Progress in Physics*, 87(5):056601, 2024.

[188] François Pouthas, Philippe Girard, Virginie Lecaudey, Thi Bach Nga Ly, Darren Gilmour, Christian Boulin, Rainer Pepperkok, and Emmanuel G Reynaud. In migrating cells, the golgi complex and the position of the centrosome depend on geometrical constraints of the substratum. *Journal of cell science*, 121(14):2406–2414, 2008.

[189] Alexander S Zhovmer, Alexis Manning, Chynna Smith, Ashley Nguyen, Olivia Prince, Pablo J Sáez, Xuefei Ma, Denis Tsygankov, Alexander X Cartagena-Rivera, Niloy A Singh, et al. Septins provide microenvironment sensing and cortical actomyosin partitioning in motile amoeboid t lymphocytes. *Science Advances*, 10(1):eadi1788, 2024.

[190] Congying Wu, Sreeja B Asokan, Matthew E Berginski, Elizabeth M Haynes, Norman E Sharpless, Jack D Griffith, Shawn M Gomez, and

James E Bear. Arp2/3 is critical for lamellipodia and response to extracellular matrix cues but is dispensable for chemotaxis. *Cell*, 148(5):973–987, 2012.

[191] Thomas D Pollard and Gary G Borisy. Cellular motility driven by assembly and disassembly of actin filaments. *Cell*, 112(4):453–465, 2003.

[192] Johannes Flommersfeld, Stefan Stöberl, Omar Shah, Joachim O Rädler, and Chase P Broedersz. Geometry-sensitive protrusion growth directs confined cell migration. *Physical review letters*, 132(9):098401, 2024.

[193] Christanny J Schmidt and Samantha J Stehbens. Microtubule control of migration: Coordination in confinement. *Current Opinion in Cell Biology*, 86:102289, 2024.

[194] Kevin J Chalut and Ewa K Paluch. The actin cortex: a bridge between cell shape and function. *Developmental cell*, 38(6):571–573, 2016.

[195] Jian Zhang, Wei-Hui Guo, and Yu-Li Wang. Microtubules stabilize cell polarity by localizing rear signals. *Proceedings of the National Academy of Sciences*, 111(46):16383–16388, 2014.

[196] Henry De Belly, Shannon Yan, Hudson Borja da Rocha, Sacha Ichbiah, Jason P Town, Patrick J Zager, Dorothy C Estrada, Kirstin Meyer, Hervé Turlier, Carlos Bustamante, et al. Cell protrusions and contractions generate long-range membrane tension propagation. *Cell*, 186(14):3049–3061, 2023.

[197] M Fritzsche, D Li, H Colin-York, VT Chang, E Moeendarbary, JH Felce, E Sezgin, G Charras, E Betzig, and C Eggeling. Self-organizing actin patterns shape membrane architecture but not cell mechanics. *Nature communications*, 8(1):14347, 2017.

[198] Martin Bergert, Stanley D Chandradoss, Ravi A Desai, and Ewa Paluch. Cell mechanics control rapid transitions between blebs and lamellipodia during migration. *Proceedings of the National Academy of Sciences*, 109(36):14434–14439, 2012.

[199] Agathe Chaigne, Clément Campillo, Nir S Gov, Raphaël Voituriez, Jessica Azoury, Claudia Umaña-Diaz, Maria Almonacid, Isabelle Queguiner, Pierre Nassoy, Cécile Sykes, et al. A soft cortex is essential for asymmetric spindle positioning in mouse oocytes. *Nature cell biology*, 15(8):958–966, 2013.

[200] Yohalie Kalukula, Andrew D Stephens, Jan Lammerding, and Sylvain Gabriele. Mechanics and functional consequences of nuclear deformations. *Nature reviews Molecular cell biology*, 23(9):583–602, 2022.

[201] David M Graham, Tomas Andersen, Lisa Sharek, Gunes Uzer, Katheryn Rothenberg, Brenton D Hoffman, Janet Rubin, Martial Balland, James E Bear, and Keith Burridge. Enucleated cells reveal differential roles of the nucleus in cell migration, polarity, and mechanotransduction. *Journal of Cell Biology*, 217(3):895–914, 2018.

[202] Aleksi Isomursu, Jonna Alanko, Sara Hernández-Pérez, Karla Saukkonen, Markku Saari, Pieta K Mattila, and Johanna Ivaska. Dynamic micropatterning reveals substrate-dependent differences in the geometric control of cell polarization and migration. *Small Methods*, 8(1):2300719, 2024.

[203] Eva Crosas-Molist, Vittoria Graziani, Oscar Maiques, Pahini Pandya, Joanne Monger, Remi Samain, Samantha L George, Saba Malik, Jerrine Salise, Valle Morales, et al. Ampk is a mechano-metabolic sensor linking cell adhesion and mitochondrial dynamics to myosin-dependent cell migration. *Nature Communications*, 14(1):2740, 2023.

[204] AJ Lomakin, CJ Cattin, Damien Cuvelier, Zahraa Alraies, Marc Molina, GPF Nader, Nishit Srivastava, PJ Sáez, JM Garcia-Arcos, IY Zhitnyak, et al. The nucleus acts as a ruler tailoring cell responses to spatial constraints. *Science*, 370(6514):eaba2894, 2020.

[205] Audrey Prunet, S Lefort, Hélène Delanoë-Ayari, B Laperrousaz, Gilles Simon, Catherine Barentin, S Saci, Françoise Argoul, Boris Guyot, J-P Rieu, et al. A new agarose-based microsystem to investigate cell response to prolonged confinement. *Lab on a Chip*, 20(21):4016–4030, 2020.

[206] Valeria Venturini, Fabio Pezzano, Frederic Catala Castro, Hanna-Maria Häkkinen, Senda Jiménez-Delgado, Mariona Colomer-Rosell, Monica Marro, Queralt Tolosa-Ramon, Sonia Paz-López, Miguel A Valverde, et al. The nucleus measures shape changes for cellular proprioception to control dynamic cell behavior. *Science*, 370(6514):eaba2644, 2020.

[207] Harrison V Prentice-Mott, Yasmine Meroz, Andreas Carlson, Michael A Levine, Michael W Davidson, Daniel Irimia, Guillaume T Charras, Lakshminarayanan Mahadevan, and Jagesh V Shah. Directional memory arises from long-lived cytoskeletal asymmetries in polarized chemotactic cells. *Proceedings of the National Academy of Sciences*, 113(5):1267–1272, 2016.

[208] Jarama Clucas and Ferran Valderrama. Erm proteins in cancer progression. *Journal of cell science*, 127(2):267–275, 2014.

[209] Jennifer Haynes, Jyoti Srivastava, Nikki Madson, Torsten Wittmann, and Diane L Barber. Dynamic actin remodeling during epithelial–mesenchymal transition depends on increased moesin expression. *Molecular biology of the cell*, 22(24):4750–4764, 2011.

PUBLICATIONS AND COMMUNICATIONS

Peer-Reviewed Publications

9. *Unlocking the therapeutic potential of cellular mechanobiology*
   Y. Kalukula*, G. Ciccone*, D. Mohammed, A. Procès, M. Versaevel, A. Deridoux, L. Ergot, Z. Barbier, M. Mansy, R. Aucouturier, R. Tranzer, M. Surin, S. Gabriele and M. Luciano
   Science Advances **11**, eaea6817 (2025)

8. *How squeezed cells remember their shape to migrate efficiently*
   D. B. Brückner, Y. Kalukula and S. Gabriele
   Nature Physics (*Research Briefing*) **21**, 1359–1360 (2025)

7. *The actin cortex acts as a mechanical memory of morphology in confined migrating cells*
   Y. Kalukula, M. Luciano, G. Charras, D. B. Brückner and S. Gabriele
   Nature Physics **21**, 1451–1461 (2025)

6. *Geometry-driven migration efficiency of autonomous epithelial cell clusters*
   E. Vercurysse, D. B Brückner, M. Gómez-González, A. Remson, M. Luciano, **Y. Kalukula**, L. Rossetti, X. Trepat, E. Hannezo and S. Gabriele
   Nature Physics **20**, 1492-1500 (2024)

5. *Mechanoresponse of curved epithelial monolayers lining bowl-shaped 3D microwells*
   M. Luciano*, M. Versaevel*, **Y. Kalukula** and S. Gabriele
   *These authors contributed equally to this work
   Advanced Healthcare Materials **13**, 2303377 (2024)

4. *Translating cell mechanobiology and nuclear deformations to the clinics*
   Y. Kalukula*, M. Luciano* and S. Gabriele
   *These authors contributed equally to this work
   Clinical and Translational Medicine **12**, e1000 (2022)

3. *Mechanics and functional consequences of nuclear deformations*
   Y. Kalukula, A.D. Stephens, J. Lammerding and S. Gabriele
   Nature Reviews Molecular Cell Biology **23**, 583-602 (2022)

2. *Multiscale Mechanobiology in Brain Physiology and Diseases*
   A Procès, M Luciano, **Y. Kalukula**, L Ris and S. Gabriele
   Frontiers in Cell and Developmental Biology **10**, 823857 (2022)

1. *Appreciating the role of cell shape changes in the mechanobiology of epithelial tissues*
   M. Luciano, M. Versaevel, E. Vercruysse, A. Procès, **Y. Kalukula**, A. Remson, A. Deridoux and S. Gabriele
   Biophysics Reviews **3**, 011305 (2022)

Oral Presentations in International Conferences

- Rising Stars in Soft and Biological Matter Symposium — December 2024
  UChicago & USCD, online.
- GRC Mechanochemistry and Mechanobiology — July 2024
  Lewiston, USA
- 9th Biennal European Cell Mechanics Meeting — September 2023
  Marseille, France
- GDR Quantitative Approaches to Living Systems — May 2023
  Oléron, France
- 9th World Congress of Biomechanics — July 2022
  Taipei, Taiwan

Seminars

- Max-Planck-Zentrum für Physik und Medizin — November 2025
  Erlangen, Germany (Prof. Benoît Ladoux)
- Mechanobiology Seminar Series - UMONS — December 2023
  Mons, Belgium (Prof. Sylvain Gabriele)
- University of California, Berkeley — September 2022
  San Francisco, USA (Prof. Sanjay Kumar)
- University of Vanderbilt, Nashville — November 2021
  Nashvilles, USA (Prof. Cynthia Reinhart-King)

Poster Presentations

- Physics of life, Harrogate (UK) — March 2025
- Gordon Research Conference in Mechanobiology (USA) — July 2024
- GDR AQV 3070 (CNRS) (France) — May 2024
- 90th Harden Conference, Birmingham (UK) — April 2024

- Plenary days GDR B2i, Louvain la neuve (Belgium) June 2023
- GDR AQV 3070 (CNRS), Oléron (France) May 2023
- GDR AQV 3070 (CNRS), Paris (France) January 2022
- RBSCDB, Ghent (Belgium) October 2021
- GDR AQV 3070 (CNRS), Online January 2021

Distinctions and Awards

- Young Researcher Poster Prize June 2023
  Plenary days of the GDR B2i, Leuven (BE)
- Best Poster Prize, AQV days 2023 May 2023
  GDR AQV, Oléron (France)
- FRMH Research Grant November 2021
  Fund for Medical Research in Hainaut (BE)
- FRIA-FNRS Doctoral Fellowship October 2020
  National Fund for Fundamental Research, FNRS (BE)

Academic Activities

- CellMech 2025 organizing committee 2025
  10th Biennial European Cell Mechanics Meeting, Leuven (BE)
- Member of the Prelights community 2022-Now
  The Company of Biologists, link to Prelights

Popularization activities

- "Octobre Rose au SPARKOH!", Public conference — October 2025
  SPARKOH, Frameries (Belgium)

- Soapbox Science Speaker — September 2024
  3nd edition - Planetarium, Brussels (Belgium)

- Soapbox Science Speaker - Brussels event — June 2022
  Science outreach initiative for Women in STEM visibility
  Brussels (Belgium)

- "Nuclear deformations in confined cells" — May 2022
  Interview with S. Gabriele, RTBF - La Première, Emission Les Eclaireurs by Fabienne Vande Meerssche

Scientific training

- "Mastering cell culture" training BIOCEL-3.1.2 (ULB) — May 2021